Tidal energy theory and turbine array design in constricted channels

Malcolm Smeaton

A thesis submitted for the degree of

Doctor of Philosophy

at the University of Otago, Dunedin, New Zealand.

18th December, 2019

Acknowledgments

I would like to acknowledge the support and guidance given to me by my supervisors Dr. Ross Vennell and Dr. Alice Harang during this thesis. Ross' overarching vision and advice paired with Alice's technical expertise have been fundamental to the completion of this work.

I have been incredibly fortunate to gain exposure to many overseas researchers and industry during my thesis thanks in large to the New Zealand Marsden Fund (Grant 12-UO-101). Additional financial assistance from Dr. Elman Poole and the Otago Energy Research Committee allowed me to complete trips to both Stanford University and the Bay of Fundy - these have been invaluable to my career development and I thank both parties. I thank the University of Otago Marine Science Department for hosting me at the start of this project and the Cawthron Institute for hosting me at the end. I also thank the University of Otago Marine Science Department for an international travel grant to attend a conference in Singapore.

Some people went out of their way to assist me during the course of this work. In particular, Dr. Richard Karsten facilitated a visit to Nova Scotia and Dr. Margot Gerritsen hosted me during two visits to Stanford University. Both Richard and Margot have been influential to my career in terms of professional advice, establishing an international network and, unwittingly, some recent life decisions.

This thesis has been trying at times and I would like to thank my friends and family for their support. I am especially grateful to my parents for their encouragement and support to pursue a tertiary education. Not everyone has such opportunity.

Abstract

This thesis extends existing tidal energy theory to include the effects of channel constriction - previous general theoretical works have been limited to unconstricted rectangular channel geometries. This work uses a combination of 1-D and 2-D mathematical modelling to explore how channel constriction affects the upper-limits of tidal energy generation, how turbine arrays should be designed in constricted channels and how turbine arrays will affect constricted channels when they are operational. 1-D modelling is fast and efficient and is particularly suitable for performing a broad systematic study. However, flow in constricted channels is a multi-dimensional phenomenon. Thus, a 2-D depth-averaged model is adopted to examine how 2-D flow, more realistic geometries, and more realistic tidal forcing impact on the derived 1-D theory. A comparison is done between the 1-D and 2-D models. As the 1-D model used here is similar to models used to build the foundations of tidal energy theory for unconstricted channels, this comparison serves to validate findings in these works also.

Initial work treats turbines as an arbitrary amount of drag in a basic 1-D channel model, this drag is increased in a myriad of test channels with differing degrees of constriction. Both channels connecting two ocean bodies (regular channels), and channels connecting an ocean body to a lagoon or bay (lagoon channels) are tested. Findings show that for channels of similar size, more constriction in the channel results in less power available for extraction (channel potential). Faster flows in the constricted region result in greater energy loss to friction and less energy is available for electricity generation. Lagoon channels can be geometrically modified (by increasing/decreasing the degree of constriction) to increase channel potential. A simple approximation for channel potential in the literature is extended to constricted channels.

An analytical turbine model is then nested into the 1-D channel model. This allowed for a systematic exploration of array design in a myriad of channel geometries. Power generation

was maximised by placing one row of turbines in the smallest cross-section and filling it to maximum blockage. Arrays built outside of the constriction can generate the same amount of power as arrays in the constriction but use more turbines. Using the power-to-force ratio as an economic indicator, building stronger turbines to withstand the forces of the constriction are worthwhile in terms of enhanced power generation. Results from the 2-D model showed that large amounts of kinetic energy are lost from constricted small channels in the constriction jet. In larger channels, the jet can mix in with the surrounding flow before the channel exit. Adding turbines dampens the jet by reducing flow through the channel, this allows more of this lost energy to be captured. Turbines were found to have an effect on the channel head difference driving flow. This was not accounted for in the 1-D model. When accounted for, the 1-D model showed good agreement for large channels. Agreement was within 40% for smaller channels but the 1-D model could not account for the kinetic energy loss in the jet.

Contents

List of Figures

List of Tables

Nomenclature

Common to all chapters

$\bar{P}_{\mathrm{T}}^{\mathrm{avail}}$	Mean power available from isolated turbine
$\bar{P}_{\mathrm{farm}}^{\mathrm{opt}}$	Channel potential
β	Lagoon factor
Δ	Amplitude of the head difference across channel ends
ϵ_{R}	Ratio of turbine-row area to cross-sectional area
ϵ_{T}	Ratio of turbine area to cross-sectional area
η	Free surface deviation from mean depth
γ	GC05 potential multiplier
$\hat{\alpha}$	Arbitrary non-dimensional parameter
λ_0	Non-dimensional seabed drag
λ_{F}	Non-dimensional farm-related drag
Fr	Froude number
PFR	Power to force ratio, mean power per turbine divided by mean load per turbine
ω	Tidal frequency (1E-4 rad/s)
ρ	Density of seawater
A	Cross-sectional area of the channel
A_0	Maximum channel cross-sectional area
A_3	Cross-sectional area of through-flow stream before mixing zone
A_{F}	Cross-sectional area at row location
A_{R}	Cross-sectional area of channel at turbine row location
A_{T}	Blade-swept area of single turbine (400 m)
c	Coefficient used to control broadness of constriction (0.1)

C_{D} Seabed bottom drag coefficient (0.0025)

C_{F} Drag coefficient of farm

C_{R} Drag coefficient of row of turbines

F_{T} Force of flow on turbine

F_{T} Total force from turbine array

g Acceleration due to gravity

G_{w} Gaussian curve used to create one half of the width constriction

h Channel depth

h_0 Maximum channel depth

L Channel length

n_{R} Number of rows of turbines

p_0 Pressure far upstream of turbine row

p_1 Pressure directly upstream of turbines

p_2 Pressure directly downstream of turbines

p_3 Pressure of turbine through-flow before mixing zone

p_4 Pressure of turbine bypass-flow before mixing zone

Q Channel transport

Q_0 Amplitude of the channel transport

$Q_{0\mathrm{u}}$ Amplitude of the peak undisturbed transport

Q_{IU} Amplitude of channel transport in frictionless 1-D channel model

r_1 u_1/u_0

r_2 u_2/u_0

r_3 Row tuning parmameter u_3/u_0

r_4 u_4/u_0

t Time

u x-velocity component

u_0 Free-stream velocity far upstream of turbines

u_1 Velocity directly upstream of turbines

u_2 Velocity directly downstream of turbines

u_3 Velocity in turbine through-flow before mixing zone

u_4 Velocity in turbine bypass-flow before mixing zone

v y-velocity component

W Channel width

W_0 Maximum channel width

W_c Width constriction factor

x Axis of the channel's length-wise direction

x_R x-coordinate of turbine row

y Axis of the channel's width-wise direction

$P_\mathrm{T}^\mathrm{avail}$ Instantaneous power available from isolated turbine

r_3^opt Optimal row tuning that maximises power

Specific to Chapter 2

γ Potential approximation coefficient

κ Drag approximation coefficient

A_S Surface area of lagoon as viewed from above

B Non-dimensional equivalent of b

b One of two geometric factors in 1-D channel model

G_h Gaussian curve used to create depth constriction

h_c Depth constriction factor

I Non-dimensional equivalent of i

i One of two geometric factors in 1-D channel model

Specific to Chapter 3

Δx Minimum row spacing constraint ($0.1L$)

$\mathrm{k_c}$ Dollar cost per Newton load of one turbine

$\mathrm{k_p}$ Dollar income per watt of power generated

TEEI Turbine economic efficiency index

P_1 Power generation in watts of one turbine

r_W Relative downstream velocity of turbines calculated from wake model

S Steepness constant for wake activation functions

$Z^\pm$ Activation function to ensure correct wake direction

Z_i Activation function to turn on wake

Specific to Chapter 4

$\bar{u}$	Mean velocity over strip dy
$\boldsymbol{F}_i$	Force of turbines on flow
$\check{\mathbf{n}}$	Unit-vector normal to seafloor $\check{\mathbf{n}} = (\partial h_0/\partial x, \partial h_0/\partial y, -1)$
Δt	2-D model time step (1s)
Δt_{R}	Duration of drag ramp-up process
Δx_{R}	Effective turbine row length (200 m)
η_0	Amplitude of boundary tides
$\hat{\mathbf{F}}$	Force component of flow that contributes to power generation
$\mathbf{u}$	Velocity vector
P	Power generated by row of turbines
ϕ	Phase difference between boundary tides
τ	Reynolds stress tensor
θ	Steepness constant for coastline smoothing function
A_{xy}	Effective turbine row-area
$C_{\mathrm{R,xy}}$	xy-drag coefficient of turbine row
$C_{\mathrm{R,yz}}$	yz-drag coefficient of turbine row, called C_{R} elsewhere
F_{b}	Undisturbed bottom drag force
h_{cor}	2-D domain depth correction for coastline smoothing
R_{P}	Steepness coefficient of turbine drag ramp-up function (8)
t_{R0}	Starting time of drag ramp-up process
t_{R}	Turbine drag ramp-up function
w	Vertical velocity component
x_{W}	Gaussian drag smoothing function
z	Axis of the channel's depth-wise direction

Chapter 1

Tidal Energy as a Resource

Earth's fossil fuel reserves are finite but global energy demand continues to grow (Lloyd, 2007).

Climate change threatens to irreversibly alter our environment (IPCC, 2013).

Uptake of existing, and the discovery of new, renewable energy technology is an essential part of the solution to these crises and tidal energy is one of the largest untapped sources of renewable energy on Earth. To give this resource some perspective, total global energy use in 2017 was 623 EJ (EIA, 2017) which corresponds to an average draw of 19.8 TW. The total energy input from astronomical forcing of the tides is 2.35 TW - about 12% of global energy draw (Le Provost and Lyard, 1997).

Extracting energy from the tides is complex and so humans should not expect to harness this energy resource in its entirety. Existing technology can generate electricity from tides in only a handful of geographically favourable sites on Earth but many of these sites have the potential to contribute a significant portion of their country's current energy demand. Cook Strait, New Zealand is the world's largest tidal stream energy resource and could theoretically supply 14 GW of electrical energy (Vennell, 2011a), equal to over three times New Zealand's electricity consumption, and 70% of the country's total energy consumption in 2017 (MBIE,

2017). Realising all 14 GW would require a wall of turbines completely blocking a cross-section (Garrett and Cummins, 2005) of Cook Strait, which is probably not possible. However, even harnessing only 10% of the Cook Strait tidal energy resource could generate enough electricity to power the city of Auckland.

Tidal energy as an industry is young but developing. A handful of prototype tidal energy conversion devices (turbines or turbines) have been deployed and are supplying electricity to local or national grids in the UK and Canada. Several multi-turbine arrays are planned and have passed through their local regulatory systems. An array of four turbines in the United Kingdom has been supplying electricity to the national grid for some months[1]. For tidal energy to significantly contribute to world energy supplies, turbine arrays need to generate gigawatts of power - 1000 times more than what is currently operational (Vennell *et al.*, 2015). This scale of development requires turbine arrays that contain hundreds, if not thousands, of individual turbine devices (Willden *et al.*, 2014). As an industry, tidal energy is far away from realising its potential.

A lack of confidence is holding back an industry that requires high capital investment. To remedy this, it is critical for researchers to develop confidence in, and increase the efficiency of, resource assessment methods. Developers and investors need to understand both how much power one can generate, how to efficiently generate that power and how to do so in a feasible way. To make sophisticated decisions, one also needs to know how the power generated from a turbine array scales as more turbines are added to the array. As most turbine arrays will be developed in stages, understanding the likely returns on investment over the various stages will be critical to planning. This thesis aims to better our understanding of the tidal energy resource by adding to this field of knowledge.

Many of the world's most promising tidal energy resources are channels that contain a constriction (to name a few: Tory Channel, New Zealand; Minas Passage, Canada; Petit Passage and Grand Passage, Canada). A constriction is a section of channel where the cross-section narrows then widens, which causes flow to accelerate. Constricted areas within channels appear lucrative to tidal energy developers due to the prospects of placing turbines in higher speed flows and also being able to block more of the channel's cross-section. Despite this, major works that

[1] https://simecatlantis.com/projects/meygen/

form the backbone of turbine array theory have mostly limited their analysis to non-constricted rectangular channels (Vennell, 2010, 2011b,a, 2012; Garrett and Cummins, 2005; Karsten *et al.*, 2008; Blanchfield *et al.*, 2008; Houlsby *et al.*, 2008; Whelan *et al.*, 2009). There are few, if any, studies that systematically explore how deviating from a perfect rectangular channel to one of varying geometry may affect both the power output and optimal array layout of a turbine farm. It is thus the focus of this thesis to look specifically at how tidal energy theory changes in constricted channels compared to unconstricted channels. This knowledge can inform engineers, scientists, policy makers and financial planners in their decision-making regarding development strategies and future work.

In the absence of real world examples and thus real data, resource assessment studies and much tidal energy theory must be studied using mathematical modelling. Mathematical modelling uses the laws of physics to describe a system. One can then use this description (the mathematical model) to make predictions about how the system may respond to change. In the case of this thesis, mathematical modelling is used to systematically explore how tidal power production is affected by the presence of a channel constriction and what one can do to produce more power in a constricted channel. Extracting energy from tidal currents is a process that spans multiple spatio-temporal scales from wakes forming behind turbine blades to spring/neap tidal variability in ocean basins (Adcock *et al.*, 2015). Resolving all relevant hydrodynamic processes and length scales would require a 3-D model covering the size of the continental shelf with cell sizes small enough to capture the turbulent wake around each turbine (Divett, 2013). Spanning all relevant scales in a single model is not currently computationally possible. Selecting the correct model scale and making appropriate assumptions is imperative to getting realistic results.

1.1 The tide

The tide is the name given to the oscillating rise and fall of sea level around the world due to rotational and gravitational forces of the Earth and nearby celestial bodies - mainly the Moon and the Sun. On average this oscillation has a period of 12.4 hours (a lunar day) giving rise to two low tides and two high tides per day. Although the Sun is four hundred times more massive

than the Moon, its relative distance means that the effect of the Sun on Earth's tides is 2.2 times less than that of the Moon (Butikov, 2002). The gravitational pulls of the Sun and the Moon constructively and destructively interact depending on their relative positions causing the spring/neap tidal fluctuation which has a period of roughly 14 days. Local conditions further influence the tide, resulting in a near infinite myriad of different tidal patterns throughout the world's oceans.

The rise and fall of tides was a well observed phenomenon by prehistoric coastal populations who recognised that local tidal fluctuations were somehow associated with astronomical events and developed crude techniques to predict the tidal sequence (Pond and Pickard, 1983). Correctly estimating tidal elevation at a given location can require the consideration of hundreds of individual constituents each with a respective amplitude, frequency and phasing (Consoli *et al.*, 2014). Additionally, sea level can be affected by environmental factors such as air pressure and temperature. These can contribute up to 30% of total sea level in certain places (Pond and Pickard, 1983).

Tides can be considered as gravity-driven, long, shallow-water waves - even in the deepest location in the ocean (Toffoli and Bitner-Gregersen, 2017). When a tidal pulse hits a land mass, some of its energy is lost while the remainder is reflected. The combination of this reflection effect and the Coriolis effect causes the tides to oscillate around ocean basins as a Kelvin wave. These Kelvin waves rotate around amphidromic points which are points in the ocean that have a tidal range of zero e.g. no change in sea level. Amphidromic systems occur in all ocean basins except the Southern Ocean where tides simply move from east to west.

While deep ocean basins such as the Atlantic and Pacific respond more or less directly to gravitational forcing, the adjacent seas of continental shelves are too small to be directly influenced by the gravitational pulls of the Moon and Sun. Tidal waves in coastal regions can hence be regarded as a forced oscillation sub-system of these larger-scale, gravity-driven systems that starts at the continental shelf. In shallow water, drag from the seafloor acts to slow down the wave. Tidal ranges observed along the coast (1.5-2 m) are typically larger than those observed in the open ocean (0.5-1 m) (Kowalik, 2004).

When a constituent frequency of a deep ocean tidal wave is close to the natural period of oscillation of the continental shelf, a phenomenon called tidal resonance occurs. This results

in enhanced tides at the coast (Garrett, 1972) and occurs in both the Bay of Fundy, Canada (Garrett, 1972) and the Severn Estuary, United Kingdom (Liang *et al.*, 2014). When a tidal crest enters one of these resonant channels from the ocean, it travels through the channel until it reaches the channel-end where it is then reflected back. If the conditions are right, as the tidal crest returns to the open ocean interface, the next tidal crest comes past and pushes it back through the channel towards the bay. This is analogous to pushing somebody on a swing. The effects of this can be incredible. For instance, the 16 m tidal range in the Bay of Fundy (Scott and Greenberg, 1983) is attributed to the Gulf of Maine - Bay of Fundy system having a natural period of oscillation (13.3 hours) close to the period of lunar tidal constituent (12.4 hours) (Garrett, 1972). Tidal currents in Minas Passage that are driven by this oscillation can reach depth-averaged velocities of up to 3 ms^{-1}(Cornett *et al.*, 2015) and velocities as high as 6 ms^{-1}.

1.1.1 Tidal streams in channels

Where differences in amplitude and phase of tides occur within a short distance of each other, tidal currents may develop (Pugh, 1987). Most favourable tidal energy sites are in regions where different tidal range conditions occur between two landmasses separated by a narrow strait or channel. Differences in sea level at either end of the channel translate to differences in hydrostatic pressure and so a pressure gradient occurs across the channel length. For cases where the channel length is short compared to the tidal wavelength, the magnitude of the currents is determined by the balance between the hydrostatic pressure gradient and the retarding drag force from the seafloor and channel walls (Pugh, 1987). These currents also occur in narrow strait or channels that connect the open ocean to an embayment such as a harbour or fjord. In this case, water entering the terminal embayment affects the water elevation of the embayment. In turn, this changes the pressure gradient that drives the flow.

1.2 Extracting energy from tides

There are essentially two ways that humans have thus far managed to generate electricity from the tides: (1) using a tidal barrage or tidal lagoon and (2) using tidal energy conversion devices

(turbines) otherwise called tidal turbines (Adcock *et al.*, 2015). The first method of generation extracts energy from the water level difference or "head" across a barrier and is similar to hydropower. The latter method extracts energy from tidal currents and is similar to wind energy.

1.2.1 Tidal head generation: barrages and lagoons

The tidal head approach to tidal energy generation requires a large tidal head and necessitates the construction of a barrier that obstructs the flow. Within this barrier is a passage or multiple passages containing turbines through which tidal flows are forced. In a sense, building barrages and lagoons is effectively the same as artificially adding a constriction to a tidal channel.

In most instances, water is left to accumulate on one side of the barrier until the head difference across the barrier is maximised. The passage is then opened, allowing movement of water from the high pressure side of the barrier to the low pressure side which causes a turbine, or turbines, to spin. This approach to generating electricity is advantageous in the sense that most of the power arising from the hydrostatic pressure difference is captured. Flow has no other option but to pass through turbines. The large tidal head required for this style of generation greatly limits its suitability. Tidal ranges at some existing and planned sites are 10.5 m in Swansea, UK (Waters and Aggidis, 2016); 13.5 m in La Rance, France (Gorlov *et al.*, 2001); and 16 m in Bay of Fundy, Canada (Scott and Greenberg, 1983).

Traditionally, tidal head generation has used *tidal barrages* (e.g. La Rance, France and Annapolis Royal, Canada) that completely block the cross-section of the channel. Barrages restrict the circulation of water and sediment in the tidal system which can have ecological consequences. In more recent times, the tidal energy industry has looked towards *tidal lagoons* as an alternative approach to tidal head generation.

While barrages and tidal lagoon systems operate on the same principle of forcing water through a turbine via a barrier, tidal lagoons block off an enclosed area within the channel or bay (rather than the whole channel/bay). This allows water to continue to flow freely in and out of the ecosystem. A pilot tidal lagoon project[2] in Swansea, United Kingdom (part of the Severn

[2]http://www.tidallagoonpower.com/

Estuary) has had its resource consent granted. This project is estimated to cost a total of $2.3 billion dollars (NZD) and will supply 320 MW of electricity to the UK national grid (Waters and Aggidis, 2016). For comparison, a failed Central Otago, New Zealand wind energy project (Project Hayes) was budgeted at around $2 billion dollar (NZD) and had a projected generation of 630 MW (Manins, 2008, 2009). The Swansea lagoon project has backing from environmental lobbyist groups Greenpeace and the World Wildlife Foundation but was put on hold in 2018 due to being denied a necessary government subsidy (Vaughan, 2019). Developers of the lagoon now intend to add floating solar panels to the lagoon to increase energy output and believe they have sufficient capital to proceed without government assistance (Vaughan, 2019). Several complementary lagoon developments in the Severn Estuary and other parts of the United Kingdom have been proposed.

1.2.2 Tidal current generation: turbine arrays

The tidal current approach to tidal energy generation involves placing tidal energy conversion devices (turbines) into tidal flow. These are essentially underwater wind farms. This unconstrained generation is advantageous in the sense that it has less of an impact on sediment transport. Furthermore, passage through the developed section of ocean can be maintained. A major disadvantage is that not all flow passes through the turbine(s) and, depending on the array design, much of the flow may bypass the turbines (Garrett and Cummins, 2007). While the hydrodynamic and environmental impacts of this approach to energy conversion are less significant than those associated with the construction of a barrage or lagoon, they are not negligible. Turbine arrays result in local flow changes and as they get larger, can have significant effects on far-field tidal dynamics (Polagye and Malte, 2011).

1.2.3 Promising turbine array sites

1.2.3.1 Bay of Fundy, Canada (7GW, Karsten *et al.*, 2008)

The Bay of Fundy in Nova Scotia, Canada has the highest tidal range in the world due to resonance occuring between the tidal signal at the outside of the bay and the reflecting tidal pulse returning from the northern end of the bay. The majority of power can be generated by

exploiting the Minas Passage (a constricted region of channel in the Northern end of the bay) although several smaller developments are being pursued along other constricted passages at the southern end of the Digby Peninsula. The Bay of Fundy has an existing 20 MW tidal barrage built in 1984 in Annapolis Royal. The Fundy Ocean Research Centre for Energy (FORCE) was established [2009] in the Minas Passage to allow for testing of prototype devices. Large armoured sub-sea cables extend out to the Passage and developers are able to connect their turbine devices to the local grid. OpenHydro deployed a unit in 2009, gravity anchored to the seabed, that ultimately failed and another improved unit in 2016 (Quon, 2018). The deployment of a 2 MW turbine in 2016 was deemed successful and retrieved in 2017 (Carlson and Adams, 2020). On the 24th July, 2018 a third turbine was deployed and three days later OpenHydro declared insolvency and entered bankruptcy proceedings (Carlson and Adams, 2020). The device ceased to function in 2018 due to internal component failure (Carlson and Adams, 2020) and could not be retrieved off the seafloor (Quon, 2018) - at the time of writing, this device is still there. There are many citizens concerned by the possible impacts that tidal energy in Minas Passage will have on the Bay of Fundy environment - particularly the impact it may have on local fisheries which are a vital part of the struggling regional economy (*pers. obs.* author).

Smaller developments on the Digby Peninsula include Grand Passage and Petit Passage. The devices intended for use in these areas differ from that deployed in the Minas Passage in that they are suspended mid water column from a floating platform. These projects are still being pursued.

1.2.3.2 Pentland Firth and Orkney, United Kingdom (4GW, Draper *et al.*, 2014)

The Pentland Firth is a constricted channel separating the north of Scotland from the Orkney Islands. (Draper *et al.*, 2014) estimated the potential resource in the Pentland Firth to be 4 GW while (Adcock *et al.*, 2013) estimated 2 GW of power could be generated if turbines were allowed to block up to 40% of the channel's cross-section. The European Marine Energy Centre (EMEC), established in 2003, is a facility similar to FORCE in the Bay of Fundy (see previous section) where marine energy converter devices (both wave and tidal) can be tested

Figure 1.1: Map of Bay of Fundy, Canada annotated with relevant tidal stream energy areas

and connected to an electrical grid. The MeyGen project of Simec Atlantis Energy[3], based off the northern coast of Scotland, is an operational array of four 1.5 MW turbines. This array was built primarily as a proof of concept project to demonstrate the commercial and technical feasibility of turbine arrays. MeyGen had exported 17GWh to the UK national grid as of June 2019 and construction for the second phase of the project (Phase 1B or Project Stroma) is underway. Project Stroma will add an additional two turbines to the array and a 'sub-sea hub' which will allow for power to be transmitted onshore via a single power cable. Phase 1C has been granted consent and plans for a further 49 turbines to be added to the array (73.5MW) while Phases 2 and 3 may boost array output to 398 MW total.

The Brims tidal array[4] at the south-western point of the Orkney Islands is a planned array of up to 200 turbines with a combined output of 200 MW. This "almost fully consented" project is a joint venture between OpenHydro and SSE Renewables and was set to commence this year (2019) but this is now uncertain as OpenHydro declared bankruptcy in 2018. Another project in Lashy Sound[5] is currently seeking consent for 10 MW of generation and is in the process of gathering environmental data to inform their application. A series of tidal energy projects

[3]https://simecatlantis.com/projects/meygen/
[4]https://tethys.pnnl.gov/annex-iv-sites/brims-tidal-array
[5]https://orbitalmarine.com/projects/lashy-sound

Figure 1.2: Map of Pentland Firth, United Kingdom annotated with relevant tidal stream energy areas

along West Orkney and Costa Head have been abandoned.

Elsewhere in the United Kingdom, a prototype turbine (SeaGen) was successfully deployed in Strangford Lough (east coast of Northern Ireland) that provided more than 11.6 GWh of generation to the national grid[6] over the course of eleven years. Simec Atlantis Energy has expresed interest in further developing this area.

1.2.3.3 Cook Strait, New Zealand (14GW, Vennell 2011a)

Cook Strait separates the two major islands of New Zealand and could potentially supply up to 14GW of electricity (Vennell, 2011a). Generating 14GW would necessitate a wall of turbines spanning the full width of the strait and is therefore unlikely due to environmental and socioeconomic reasons. Nonetheless, several areas within Cook Strait are promising for tidal energy generation including but not limited to the immediate area off Cape Terawhiti (Vennell *et al.* in review) and the greater Karori Rip (Stevens *et al.*, 2012) which sits between Cape Terawhiti and Tory Channel. Using a simple one-dimensional model, (Vennell, 2010) predicted the maximum power that could be generated from Tory Channel alone to be 105MW

[6] https://simecatlantis.com/2019/07/26/meygen-operational-update-3-2/

Figure 1.3: Map of Cook Strait, New Zealand annotated with relevant tidal stream energy areas

and (Plew and Stevens, 2013) used a more realistic model to show that an array of turbines in Tory Channel could generate 33MW.

Energy Pacifica announced in 2008 that they would be applying for a resource consent to develop an array of 10 turbines in Tory Channel after Neptune Energy Ltd. gained resource consent to test a prototype turbine in the Karori Rip in 2009 (Fleisher, 2016). After ten years, neither of these projects have come to fruition. A barrier to the growth of the tidal energy industry in New Zealand is the lack of demand for electricity and the vast number of readily available alternatives. New Zealand generated 82% of its electricity from renewable energy in 2017 (MBIE, 2017) and has an abundance of untapped wind, geothermal, solar and hydro-kinetic energy resources. A consequence of this is a lack of urgency or immediate need to develop the country's tidal energy resources. In the future, effectively taxing greenhouse gas emissions on top of the inevitable uptake of electric vehicles and alternative industrial heating systems may cause demand for electricity to increase to a point where New Zealand will need to exploit their tidal energy resource.

1.3 Resource assessment and tidal energy modelling

1.3.1 A problem spanning many scales

Tidal current energy resource assessment is a problem that spans multiple spatial scales, each scale interacts with the spatial scales directly above and below. Adcock *et al.* (2015) believe this to be the key difficulty in accurately modeling tidal stream turbines and define five characteristic length scales shown below in Figure 1.4. The length scales prescribed by Adcock *et al.* (2015) are broad-ranging and there is significant overlap between them - including one length scale (10 - 20 m or an approximate turbine diameter) which overlaps all other scales (the array scale). Modeling the output of a turbine array that contains multiple turbine devices and its effect on regional hydrodynamics while still accounting for structures seen at the blade scale requires enormous computational effort and at the time of writing is unfeasible for practical research purposes. Thus, the length scales that one chooses to model will depend on the objective of the particular study. Often key processes seen in adjacent length scales can be accounted for by creating simplified, lower-order models that can then be fed into the governing higher-order model. Here, three custom length scales are discussed by combining some of those given in 1.4. These are: (1) the turbine/blade scale, (2) the small array scale and (3) the large array scale. An overview of relevant findings and methods pertaining to each of these three scales is given below before defining this work's position amongst existing literature.

1.3.2 Blade scale/turbine scale

Although separated by Adcock *et al.* (2015), there is significant overlap between the blade scale and turbine scale in Figure 1.4. Fortunately, there is great commonality between tidal turbine blade design and wind turbine blade design and methods for this latter field are well established. Turbine/blade scale modeling aims to understand the effects of local flow around an individual device (including the trailing wake). This geometric scale of interest is sufficiently small that modelling work can be validated using lab-scale experiments (Malki *et al.*, 2013) or ocean-scale prototype tests (Ahmed *et al.*, 2017). This scale of modelling is not only useful for testing and optimising design features for a specific turbine or turbine blade, but additionally for developing simplified lower-order models that can be used within larger scale models (Garrett

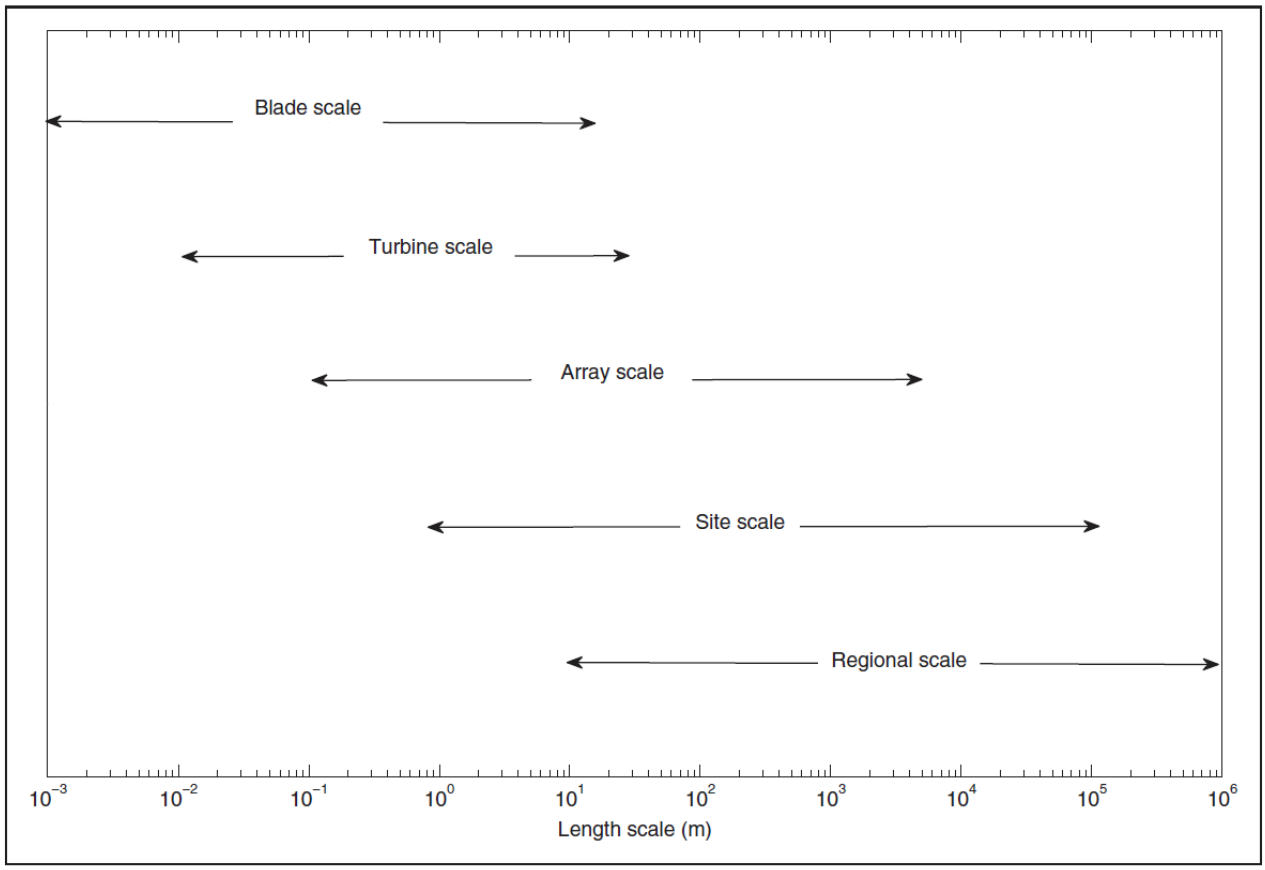

Figure 1.4: Different scales in hydrodynamic modelling of tidal stream power generation (Source: Adcock *et al.* (2015))

and Cummins, 2007; Houlsby *et al.*, 2008; Churchfield *et al.*, 2013). Lower-order models are models which simplify a physical process such that important phenomena of the process are accounted for but not necessarily the finer details. These models are simple and fast; their development is critical for completing larger-scale works (using higher-order coastal models) where resolving small-scale processes is non-important, computationally expensive or otherwise impossible.

Blade element momentum theory (BEMT) is a well established method used for engineering modelling of wind turbines that is readily transferable to turbine devices (Adcock *et al.*, 2015). BEMT is an amalgamation of two different turbine models: (1) a model that treats the turbine as a collection of blade elements which generate lift and drag forces from the flow they are subjected to and (2) a model that deals with the absorption and transmission of linear momentum (on the turbine from the flow) to angular momentum that causes a wake in the downstream flow (Masters *et al.*, 2015). Modelling flow separation and turbulent mixing behind the blades and in the boundary layer attached to the blades requires significant computational resource (Adcock *et al.*, 2015) which makes it impractical for modelling more than few turbines. Building a lower order turbine model that accurately accounts for wake dynamics is one of the greatest challenges of blade scale/turbine scale research.

Perhaps the most commonly used lower order turbine model (Draper *et al.*, 2010; Houlsby *et al.*, 2008; Vennell, 2010; Blunden and Bahaj, 2007), and the model used in this thesis, is the actuator disc. This approach to modelling turbines was first derived by Lanchester (1915) for the application of a screw propeller and then later applied to the case of an isolated wind turbine (Betz, 1920). Garrett and Cummins (2007) extended this work (Figure 1.5) for a tidal turbine within a bounded channel (wind turbine flow can usually be considered unbounded). The work of Garrett and Cummins (2007) was then applied to large arrays of turbines by Vennell (2010). Variants of this model exist to account for non-zero Froude number effects such as free-surface deformation (Houlsby *et al.*, 2008; Whelan *et al.*, 2009). The model has also been extended to account for support structure drag (Vennell, 2012) and turbine arrays that occupy only part of the channel cross-section (Nishino and Willden, 2012, 2013).

The actuator disc representation models a spinning turbine rotor as a stationary, semi-porous disc through which some flow passes while the remaining flow goes around the disc. By com-

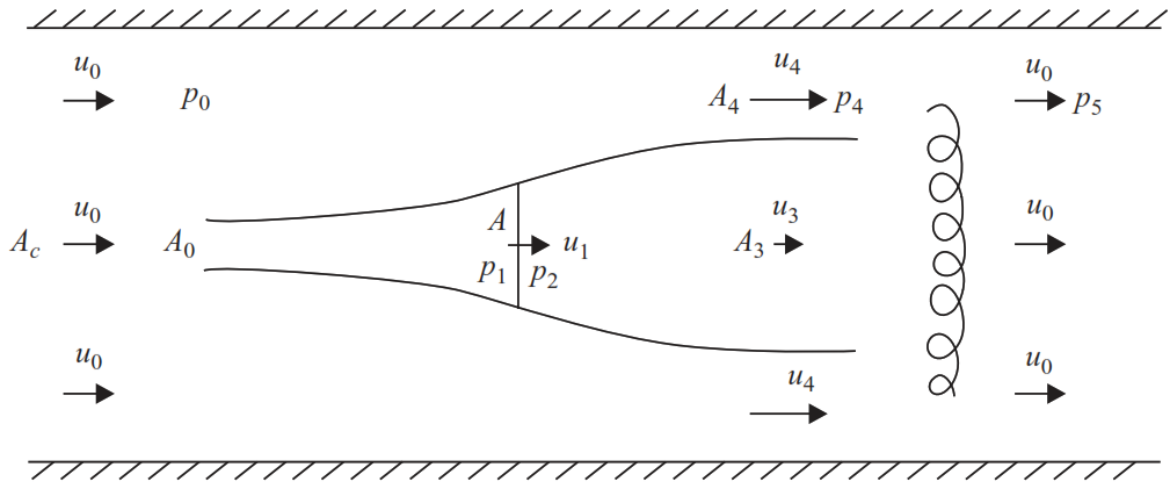

Figure 1.5: Diagram showing the actuator-disc model for a single turbine in an unconstricted channel. (Taken from Garrett and Cummins (2007))

bining the Bernoulli equation with mass continuity, the force and power on the disc can be expressed as a function of the disc's surface area (in Figure 1.5, A - throughout the rest of this thesis, A_T), the cross-sectional area of the channel at the turbine location (A_c), and the ratio of the velocity downstream of the turbine to the upstream undisturbed velocity before the turbine ($r_3 = u_3/u_0$). The application of this work to a higher order channel model is discussed later in Chapters 3 and 4 of this thesis.

An alternative BEMT-based, lower-order model is the actuator line method where rather than uniformly distributing the turbine load over a circular disc, the load is distributed along rotating lines representing individual turbine blades. Each line is divided into a number of segments for which physical data is known. The lift and drag forces experienced by each turbine segment are calculated using look up tables for the device and are then projected onto the fluid flow as a point force. Much like the actuator disc model, this model was developed for wind turbines by Sorensen and Shen (2002). It was first used in tidal energy research by Churchfield *et al.* (2013). The actuator line method is advantageous in the sense that it considers the rotating motion of the turbine and can thereby account for rotation in the downstream wake. That said, the accuracy of this wake representation remains questionable (Kang *et al.*, 2014; Adcock *et al.*, 2015).

Kang *et al.* (2014) present a numerical study comparing the wake predictions of the actuator disc model and the actuator line model and then compared both turbine models to one that resolved

the actual geometry of a lab-tested prototype device. Kang *et al.* (2014) found good agreement between both near-wake and far-wake dynamics for the resolved geometry case but the two actuator models underpredicted the turbulent intensity of the far wake region. Structures in the near-wake region that are dependent on turbine geometry were found to greatly impact the far-wake dynamics (important in arrays where turbines sit downstream of each other). Kang *et al.* (2014) also note that their chosen grid resolution was significantly finer than most array-scale/site-scale models which must often use a coarse resolution for computational feasibility reasons. While these findings infer that neither method satisfactorily reproduces the wake dynamics behind a turbine device, using a mesh small enough to resolve turbine geometries in a large array simulation is too computationally expensive. At the array/site/regional scale, the size of the domain necessary to capture the relevant physics and high-resolution modeling of individual turbine devices is prohibitive.

In summary, while work done at the blade/turbine scale is used for turbine design it also assists modelling efforts at larger scales. Computational resource limitations often prohibit the resolution of a model beyond a certain cell size which prevents flow features smaller than this scale from being resolved. Lower-order models that account for the dominant physical behaviour observed at the blade/turbine scale can be used to account for sub-mesh phenomena in larger models.

1.3.3 Channel feedback: energy extraction reduces flow

Adding turbine devices to a channel not only changes flow velocities in the near-vicinity of the turbines but also through the channel as a whole (Garrett and Cummins, 2005). Tidal currents in channels are driven by the pressure gradient which results from a difference in sea level between the channel ends (Pugh, 1987). Turbine devices are sources of drag on the channel flow that act to transfer energy from the flow to the rotational motion of a turbine. The addition of turbines to a channel acts to retard the flow and causes a pressure drop in the immediate vicinity of the turbines (Vennell, 2011a). In smaller drag-dominated channels, this pressure drop causes the driving pressure gradient, and thus flow acceleration, to decrease (Vennell, 2012). This results in flow reduction everywhere in the channel which in turn reduces the power available for electricity generation. In large, inertia-dominated channels, the addition

of few turbine devices can actually increase flow by bringing the tidal current more in phase with the head difference that drives it (Vennell, 2012). However, as more turbines are added to these large channels, flow reduction effects eventually kick in (Vennell, 2012). Garrett and Cummins (2005) were the first to show that turbine devices could influence channel transport by representing an array of turbines as an impulse function of drag force in a simple 1-D numerical model for a rectangular channel. Vennell *et al.* (2015) approximate that arrays can become large enough for channel feedback to be important once they start occupying between 2 and 3% of a channel's cross-sectional area. For smaller channels this would require only a single turbine device [based on a 400m^2 frontal area (Vennell *et al.*, 2015)].

1.3.4 Small arrays: where channel feedback does not matter

By definition, two or more turbines constitute an array and Adcock *et al.* (2015) define array scale modelling as modelling where the focus is on the interactions between turbines. For the purposes of this review, small arrays are considered to be arrays that have local effects on channel flow such as wake formation and flow separation but are sufficiently small that they do not impact the channel flow rate or head (see Section 1.3.3).

For small arrays, studies have mostly focused on optimising the positions of turbines relative to each other with a particular emphasis on turbines downstream of each other. The focus of these works is on the effects of bypass flows between turbines and wake recovery directly behind turbines. Modelling of wakes is usually achieved using high resolution computational fluid dynamics (CFD) models often with a rotating mesh to account for the rotation of the turbine blades (Masters *et al.*, 2015). The computational requirements for direct numerical solution (DNS) of the turbulent processes in the wake make it impractical for larger scale simulations due to the large number of cells required. Wake turbulence is often modelled using LES (large-eddy simulations) (Kang *et al.*, 2014; Gebreslassie *et al.*, 2013; Afgan *et al.*, 2013) or by taking a RANS (Reynolds averaged Navier Stokes) approach. The LES method considers only turbulence above a certain length scale which thereby increases the simulation efficiency by removing the computational cost of resolving smaller smaller turbulent features (as would be done in a direct numerical simulation method, or DNS). The RANS approach works by first decomposing the flow into mean and varying components, the latter of which contain the

turbulent fluctuations of the fluid. Rather than solving for the turbulent variables, an additional model (a turbulence closure scheme) is used to approximate them. Afgan *et al.* (2013) compared LES and RANS model outputs against experimental data for a three-bladed horizontal axis turbine measured by Bahaj *et al.* (2005). When operating the turbine at high tip-speed ratio (the ratio of the flow speed to the tangential speed of the spinning turbine blade), thrust and power calculations were within 3% of measured data. At lower tip-speed ratios, the LES method continued to show good agreement with measured data while the RANS model underpredicted power extraction by 10%. Afgan *et al.* (2013) concluded that LES was a more appropriate tool for examining turbines operating away from their design point. Masters *et al.* (2015) state that the LES method is more rigorous than the RANS method despite the latter being more prolific in current literature. While the RANS and LES methods for modelling turbulence are useful, further simplification of the modelled physics is often necessary. Additional simplifications made in recent works include the assumption of fixed upstream flow (Malki *et al.*, 2014), the assumption of a rigid free surface (Churchfield *et al.*, 2013; Malki *et al.*, 2014) or reducing the flow model from 3-D to 2-D (Divett *et al.*, 2013).

Numerous modelling studies (Hunter *et al.*, 2015; Draper and Nishino, 2014; Churchfield *et al.*, 2013; Stansby and Stallard, 2016; Malki *et al.*, 2014) have examined the use of staggering turbines in two-rows with some optimal spacing so downstream turbines can reap benefits from high-speed bypass flows. Many of these modelling exercises have been supported by scaled-down experimental works (Stallard *et al.*, 2013; Myers and Bahaj, 2012). Findings from these works generally converge on an optimal spacing distance of two turbine diameters in both the spanwise and streamwise directions (Malki *et al.*, 2014; Turnock *et al.*, 2011; Lee *et al.*, 2010). Most works show that staggering turbines in consecutive rows can increase power generation by between 10-20% (Malki *et al.*, 2014; Turnock *et al.*, 2011). Perhaps more importantly, findings across multiple studies suggest that packing turbines into a single row (still with some optimal intrarow spacing) was preferential to a staggered two-row configuration (Hunter *et al.*, 2015; Myers and Bahaj, 2012).

When arrays reach a critical size they start interacting with the hydrodynamics of the channel they are placed in by decreasing the flow rate through the whole channel (described further in Section 1.3.3). This effect is a key mechanism when considering large arrays at the site/regional

scales. While many studies at this scale are too small to impact channel dynamics, Vennell *et al.* (2015) pointed out that some works have neglected this mechanism when it should have probably been included (Churchfield *et al.* (2013); Turnock *et al.* (2011)). Small array scale studies have been useful for obtaining important information regarding the relative spacing of few turbines in an array but their complexity makes them computationally unfeasible for larger turbine arrays where the effects of channel geometry and channel dynamics become significant.

1.4 Large arrays: where channel feedback does matter

Following from Section 1.3.4, a large array is an array that is sufficiently large to affect the flow rate of the channel.

As array size increases, it is important to model a large region around the array as its hydrodynamic impact is not necessarily limited to the immediate locale (Polagye and Malte, 2011; Vennell *et al.*, 2015). The total area modelled must be large enough so that the presence of the array does not affect the forcing boundary conditions of the model (Garrett and Greenberg, 1977; Carter and Merrifield, 2007). The necessarily large domain of the problem requires further computational effort and thus additional simplifications of the physics must be made in comparison to works described above in Section 1.3.4. Larger array modelling studies can be broadly categorised into two different types: (1) multi-dimensional studies of specific geographic locations that look promising for tidal energy (Draper *et al.*, 2014; Polagye and Malte, 2011; Hasegawa *et al.*, 2011; Stevens *et al.*, 2012; Plew and Stevens, 2013; Sutherland *et al.*, 2007) and (2) general studies that systematically explore the underlying concepts and fundamental theory of tidal turbine array design (Adcock and Draper, 2014; Vennell, 2010, 2011b, 2012, 2013; Karsten *et al.*, 2008; Blanchfield *et al.*, 2008). The former studies come at higher computational cost and are thereby usually limited by testing fewer scenarios than is possible using simplified dynamics. The latter studies come at the cost of being overly simplified and risk missing or ignoring important details and phenomena.

Common across both study types is the need to use a lower-order turbine model derived using methods above to represent turbines within a tidal flow model. Turbines are usually modelled as a single source or multiple sources of increased bottom drag on the seabed - the magnitude

of this increase can be calculated using a lower order turbine model. These drags are either applied at discrete points each representing an individual turbine device (Divett *et al.*, 2013; Funke *et al.*, 2014) or across a broader area that is representative of a turbine array or part of a turbine array (Plew and Stevens, 2013; Vennell, 2010, 2011b; Sutherland *et al.*, 2007).

1.4.1 Systematic resource assessment studies

Aside from demonstrating that turbine devices could influence channel transport, Garrett and Cummins (2005) also showed there is a theoretical upper limit to the amount of power that can be generated in any given channel and a corresponding optimal array-drag force. Further adding drag (turbines) beyond this optimal array-drag force reduces flow in the channel to the point that power output also decreases. Thus there is an optimal number of turbines that one can place in a channel. The maximum amount of power (termed the channel potential) that can be generated from a rectangular channel connecting two ocean bodies can be approximated using the theoretically derived expression of Garrett and Cummins (2005):

$$P_{\text{farm}}^{\text{opt}} = \gamma \rho g \Delta Q_{0\text{u}}. \tag{1.1}$$

Where ρ is the density of seawater, g is the acceleration due to gravity, Δ is the amplitude of the head difference across the channel ends and Q_{0u} is the peak undisturbed flow rate of the channel. The coefficient γ is a multiplier that changes from 0.24 to 0.21 from inertia dominated channels to channels that are dominated by drag effects. Equation 1.1 was derived by fitting a curve of best-fit to 1-D numerical model data.

Blanchfield *et al.* (2008); Karsten *et al.* (2008) reworked the model of Garrett and Cummins (2005) to apply to uniform rectangular channels connecting the open ocean to an inlet (henceforth referred to as lagoon channels). In lagoon channels, the pressure head (or sea elevation) of the lagoon is dependent on the flow rate of the channel connecting the ocean to the lagoon. In some instances, adding turbines to the channel can bring it closer to resonance causing flow rate to increase which allows more power to be generated from the array. Karsten *et al.* (2008) present an approximate analytical solution to the lagoon channel version of the Garrett and Cummins (2005) channel model which they apply to the Minas Passage, Bay of Fundy.

They show that adding turbines could push the Bay of Fundy-Gulf of Maine system closer to resonance. Blanchfield *et al.* (2008) extended the potential approximation of (Garrett and Cummins, 2005) to lagoon channels by varying the γ between values of 0.19 to 0.26 depending on a lagoon geometry factor β (discussed in more detail in Chapter 2). These fundamental theoretical studies (Garrett and Cummins, 2005; Blanchfield *et al.*, 2008; Karsten *et al.*, 2008) are limited to unconstricted rectangular geometries. This thesis extends the methods developed in these works to constricted channels in order to determine the effects of channel constriction on maximum power limits in both regular channels and lagoon channels.

The impulse function application method was made more sophisticated by adopting the actuator disc method of Garrett and Cummins (2007) to relate a given turbine configuration to an equivalent amount of bottom drag. The methods produced by Garrett and Cummins (2007) for a single isolated turbine can be extended to arrays under the assumptions that turbines are evenly spaced in rows and that these rows span the full cross-section of the channel (Vennell, 2010). The actuator disc model is applied to each respective row of turbines in the array to give a drag impulse function for each row. This model was first combined with the channel model of Garrett and Cummins (2005) by Vennell (2010) to provide a simple means of calculating flow-rate-corrected power output. (Vennell, 2010) also showed that turbines should be "tuned" in order to maximise power output. Draper *et al.* (2013) provided an equivalent model to Garrett and Cummins (2007) for a partial row extending outwards from a headland.

The combined Garrett and Cummins (2005) and Garrett and Cummins (2007) model has been the foundation of many systematic analytical resource assessment studies on array design and array tuning (Vennell, 2011b,a, 2012, 2013, 2016). These works all discuss the importance of tuning turbines in an array and do so via a tuning factor ($r_3 = u_3/u_0$, see Figure 1.5) which can be correlated to turbine blade pitch. By adjusting the blade pitch of turbines in the array, it is possible to achieve the optimal velocity ratio r_3 which maximises the power generated by the array. Optimal tuning is dependent on channel dynamics, the size of the array and how turbines are positioned within rows in the array (Vennell, 2010, 2011b). These studies agree with findings from small-array works that a single row with more turbines is preferential to an array of multiple rows. They found that there is a diminishing return on power per row of turbines as rows are added to an array (Vennell, 2012) and found that adding turbines to a row

may cause power to increase or decrease depending on the dynamics of the channel (Vennell, 2012). Major limitations of these works are that they assume flow is one-dimensional and that they consider only uniform channels with rectangular geometry. Extending these theoretical works to look at optimal array design and tuning is in a spatially varying channel is part of this thesis.

Nishino and Willden (2012, 2013) extended the simple actuator disc model of Garrett and Cummins (2007) by applying it at two problem scales: the device scale and the array scale. This model, named partial row theory, allows for an array of tidal turbines that only partially blocks a channel. The original model (Nishino and Willden, 2012) is based on the logic that the length scales of the device scale mixing processes are much smaller than those of the array and thus it follows that the mixing processes behind the device will occur much faster than the expansion of the array wake - that is, that the mixing processes of the two scales are fully independent. This is a good assumption provided the number of the turbines in the row is sufficiently large that the two mixing processes do not merge. Nishino and Willden (2013) extend the model's suitability for smaller arrays by accounting for array flow expansion on the device scale. This is achieved by introducing array-scale flow expansion factors which are based on a simple power law. These outputs are then compared to results from a higher order 3-D RANS simulation. Knowing the wake structure of an actuator disc can vary considerably from that of an actual device (as discussed in Section 1.3.2) the authors modified the turbulence production term in their RANS closure model. Finally, in the absence of real data, the two models were compared but both with approximated variables used to describe flow expansion and turbulence. Agreement between the two was deemed satisfactory; however, the added complexity of the model, the lack of information over the flow expansion coefficients, and the additional computational expense of optimising two variables makes it of questionable usefulness in comparison to the more computationally efficient model of Garrett and Cummins (2007).

1.4.1.1 Higher-order resource assessment studies.

Higher-order works are useful for validating the vast body of theory that has been completed using one-dimensional models. However, few generalised and systematic style studies using higher-order models have been completed that examine the fundamental theory of large-array

design. These works tend to focus on assessing the potential energy extraction from few specified array designs in an oceanographically promising area e.g. four designs in the Pentland Firth, United Kingdom (Adcock *et al.*, 2013) or two designs in Ria de Ortigueira, Spain (Sanchez *et al.*, 2014). This is likely because of the increased computational expense associated with simulating a turbine array scenario in multi-dimensional flow.

Divett *et al.* (2013) used a 2-D depth-averaged LES approach with an adaptive mesh to look at turbine tuning in a rectangular channel. They found a strong linear relationship between power extracted by an array and the resultant flow reduction which validated findings in lower order works (Vennell, 2011a). Karsten *et al.* (2008) validated their extension of channel potential theory for lagoon channels using a 2-D hydrodynamic model of the Bay of Fundy with a line discontinuity model representing a row of turbines. Karsten *et al.* (2008) defined the properties of the line discontinuity using the actuator disc model of Garrett and Cummins (2007) discussed in preceding sections. Draper *et al.* (2010) validated findings of Garrett and Cummins (2005, 2007) for a single row of turbines using a 2-D model in an idealised rectangular channel connecting two large ocean bodies.

Works pertinent to a specific geographic location can often still provide some validation to 1-D theoretical predictions by including a validation for their specific site. Sutherland *et al.* (2007) for example, validated the 1-D channel potential theory of Garrett and Cummins (2005) for Johnstone Strait, Canada against a 2-D hydrodynamic simulation by including an additional (but unrealistic) simulation where all flow was forced through a strip of high blockage. They found that the channel potential estimate provided by 1-D theory was within 10% of the higher order model. Adcock *et al.* (2013) showed that multi-row arrays placed in different parts of Pentland Firth interacted with each other, which was implicitly predicted by Vennell (2011b) using a lower order model to show rows of turbines in the same channel need to be tuned 'in concert'.

Important works completed using higher order models are those of Funke *et al.* (2014, 2016) who use adjoint methods to significantly reduce the computational effort required to complete optimisation. Adjoint methods involve finding a second [adjoint] model that provides the solver with the gradient of the objective function (the function that one wishes to maximise or minimise). They found for a farm containing M turbines that using an adjoint approach reduces

the time taken to find the gradient by a factor of M. Funke *et al.* (2014) used their model to optimise both the tuning and location of 50 turbines in the relatively complex flows around the island of Stroma (in the Pentland Firth). They found that the optimal arrangement for a 16-turbine array was a single row of turbines in the narrowest cross-section of the channel but five turbines within the array were producing little power. By examining how the power output scaled with the number of turbines, they showed that the 16-turbine array was only 10% more powerful than the optimal 11-turbine design which provides valuable information to industry - particularly if array development is to be staged. Findings in Funke *et al.* (2014) confirm results found in many of the lower order works mentioned above (Hunter *et al.*, 2015; Myers and Bahaj, 2012) that more power is extracted from the same number of turbines in a single row rather than a pair of staggered rows.

1.5 This thesis

This thesis aims to identify and describe the fundamental theory of tidal energy generation and turbine array design in constricted channels with a focus on large scale generation. It thereby fits into the large-array scale discussed above.

A series of works using one-dimensional methods has provided most existing tidal energy theory. Theory regarding channel potential was completed by Karsten *et al.* (2008); Blanchfield *et al.* (2008); Garrett and Cummins (2005) and Vennell (2010, 2011b, 2012) have provided theory regarding optimal array design. All these works have been limited to uniform rectangular channels. The quantitative inclusion of channel constriction into fundamental tidal energy theory and a systematic exploration of the topic has not yet been undertaken. This thesis explores how channel constriction affects the theoretical upper limits of tidal energy generation and looks at how turbine array design aspects such as row location, turbine tuning and how turbines are distributed between rows will affect power generation and relevant hydrodynamics. Model data is analysed and ways which findings may influence developmental and operational decisions are discussed.

Higher-order studies have been completed on some specific channels that contain constrictions using higher order models (Funke *et al.*, 2014) but no higher order works exist that have

systematically explored aspects of array design and developed generalised tidal energy theory in constricted channels (or unconstricted channels for that matter). Such works are critical to building investor confidence in the industry and informing decision-makers about social, economic and technological aspects of tidal energy generation. This thesis aims to fill this void in the literature by performing a systematic exploration of tidal array design using a higher order 2-D model. To date, no generalised works on fundamental tidal energy theory have been completed using multi-dimensional hydrodynamic models except for perhaps Funke *et al.* (2014, 2016) who still applied their work to a specific promising location (Pentland Firth).

Additionally, there are few works that perform a systematic validation on results seen at the one-dimensional level in higher order models. By adopting a 2-D flow model, this work hopes to validate findings for the constricted channel theory it develops in early chapters but also validate array design theory produced in Vennell (2010, 2011b, 2012). The explicit aims for this thesis are presented below.

1.5.1 Research questions

1. How are theoretical limits on tidal energy generation such as channel potential and maximum available power affected by channel constriction?

2. How does channel constriction affect the extent of tidal energy related flow reduction?

3. How should arrays be arranged in constricted channels to maximise energy output?

4. How do channel constrictions affect how power scales with the number of turbines in an array or across multiple arrays in the same channel?

5. How might flow separation and jet formation downstream of a constriction influence energy output and array design?

6. How suitable are 1-D models for performing exploratory studies on tidal energy resource assessment relative to 2-D modelling?

1.5.2 Structure

This thesis consists of three major parts. The first, Chapter 2 (published as (Smeaton *et al.*, 2016)), looks at how the degree of constriction in a channel affects the theoretical upper limit of tidal energy generation (channel potential). This work forms a theoretical foundation for subsequent work and addresses Research Questions 1 & 2 of this thesis. A one-dimensional model (Garrett and Cummins, 2005) and analytical solution (Karsten *et al.*, 2008; Vennell, 2010) are extended and applied to both regular channels and lagoon channels. The model is then used to explore how channel potential and flow rate reduction are affected by both the degree of constriction and the balance of drag in the channel. An analytical approximation for channel potential first given in Garrett and Cummins (2005), then extended in Blanchfield *et al.* (2008) is further adapted to apply to constricted channels.

Chapter 3 builds upon work presented in Chapter 2 by incorporating the actuator disc model as a means for exploring array design scenarios in constricted channels. Work in this chapter addresses thesis Research Questions 2, 3 and 4. Six idealised example channels are defined of varying size and dynamics, each with differing degrees of channel constriction and natural bottom drag regimes. Isolated rows and multi-row arrays are explored. Features such as number of rows, turbines in each row, tunings of each row and most importantly, row location were explored. The trade-off of high velocity flow in the constriction requiring better engineered turbine devices versus the energetic gains of generating power from these forces is discussed. A simple velocity deficit penalty is applied to the model to examine how downstream wakes may influence optimal row spacing in multi-row arrays.

Through the adoption of a higher order 2-D numerical model (namely SUNTANS), Chapter 4 seeks to identify two-dimensional features that may influence the power production of optimal array layouts not predicted by the 1-D theory derived in previous chapters. This chapter aims to address Research Questions 1 - 6 and validate findings from earlier chapters. Additionally, this chapter performs a broad validation of already existing 1-D array theory derived for rectangular channels.

Chapter 5 concludes the thesis with a general discussion.

Chapter 2

Channel Potential Theory in Constricted Channels

2.1 Foreword

Work contained in this chapter has been published in Renewable Energy (Smeaton *et al.*, 2016). Co-authors of this work include Ross Vennell and Alice Harang. The contribution of these authors was purely supervisional. Minor changes have been made from the original manuscript - the original manuscript referred to channels connecting two large water bodies as Type I channels and channels connecting a large water body to an embayment/lagoon as Type II channels. For the sake of consistency, these have been renamed to 'regular channels' and 'lagoon channels' respectively. At times, the original manuscript referred to work contained within itself as a paper, manuscript or work. These have been reworded using the term 'chapter' or 'thesis'.

This chapter aims to address Research Questions 1 and 2 of this thesis:

1. How are theoretical limits on tidal energy generation such as channel potential and maximum available power affected by channel constriction?

2. How does channel constriction affect the extent of tidal energy related flow reduction?

2.2 Introduction

This work extends tidal energy theory beyond the case of an unconstricted, rectangular channel. The works of Blanchfield *et al.* (2008); Karsten *et al.* (2008); Garrett and Cummins (2005) made several conclusions about the potential and flow rate within unconstricted, rectangular channels but did not explore the effect of channel constriction or variable cross-section. Furthermore, the studies of Garrett and Cummins (2005); Blanchfield *et al.* (2008); Karsten *et al.* (2008) did not describe the relationship between channel potential and geometry nor identify with any certainty how a constriction may be used to advantage.

Channel potential is the theoretical upper limit to the amount of power that can be lost by a channel to a tidal turbine array and can be realised by occupying the channel's cross-section with a wall of turbines (Garrett and Cummins, 2007). While this is likely to be an unattainable goal in most parts of the world due to environmental, economic and social reasons; channel potential provides a useful first indication of the amount of available power at a given site.

Multi-dimensional modelling of different geometries has been completed for site-specific resource assessment studies in the past (Draper *et al.*, 2014; Carballo *et al.*, 2009; Easton *et al.*, 2012; Stevens *et al.*, 2012); however, little work has been completed on exploring the general relationship between channel geometry and tidal power. While complex numerical models can provide a great deal of information to a reasonably high degree of accuracy, they are usually computationally demanding and gathering results is time consuming. One-dimensional (1-D) modelling allows for results to be collected quickly for a myriad of conditions. Although less realistic and detailed, 1-D modelling is particularly suitable for systematic studies such as this one. This chapter applies the models derived in Garrett and Cummins (2005); Blanchfield *et al.* (2008); Karsten *et al.* (2008) to an unconstricted channel and derives analytical solutions similar to that given in Vennell (2012) for constricted regular channels and lagoon channels. This framework is then used to examine the effect of channel constriction on channel potential and channel dynamics.

A derivation and outline of the model used for this study is given below in Section 2.3 and an analytical approximation to this model is provided in Section 2.4. The effects of channel constriction on channel potential are then presented in Section 2.5 for both channel types. Section

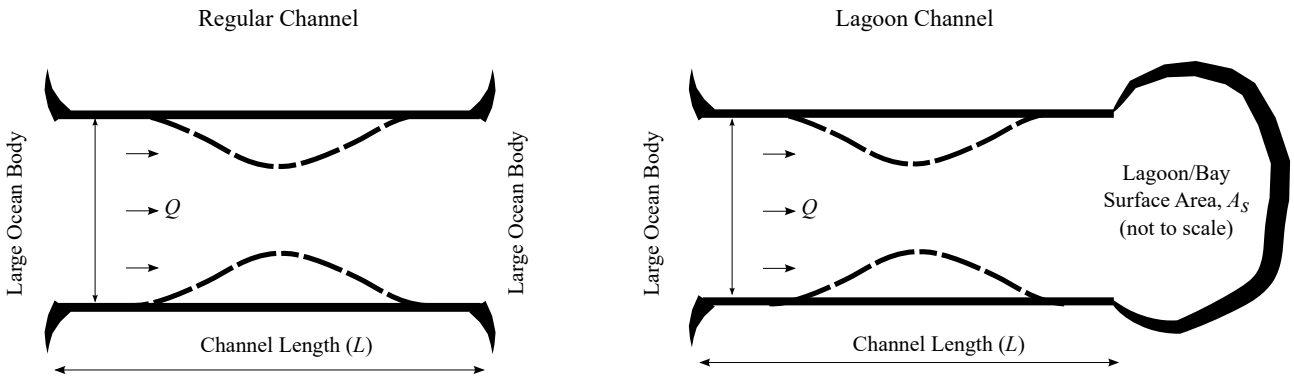

Figure 2.1: Illustrations showing a *regular* channel connecting two infinitely large water bodies (left) and a *lagoon* channel connecting one infinitely large water body to a prismatic lagoon of surface area A_s (right). The dashed line shows how a width constriction is built into the channels. Q is the time varying transport through the channel and L is the channel's length.

2.6 then proceeds to look at how the degree of channel constriction influences flow through the channel and how the flow reduction required to achieve potential varies with channel geometry. Finally, a simple approximation provided in Garrett and Cummins (2005) for unconstricted regular channels - extended by Blanchfield *et al.* (2008) to apply to unconstricted lagoon channels - is then further extended here to apply to constricted cases. A similar approximation is also presented that allows the farm drag required at potential to be quickly approximated for shallow, friction dominated channels.

2.3 Tidal model

2.3.1 Dynamic model for regular channels

Consider a shallow water tidal channel connecting two large water bodies (a regular channel) of variable rectangular cross-section $A(x)$. The x-axis spans the length of the channel beginning at the first water body ($x = 0$) and terminating at the second water body ($x = L$). Constant density (barotropic) tidal currents are driven by the difference in free surface elevation between the two water bodies. Seawater density varies with temperature and salinity normally between values of 1020 and 1029 kgm^{-3}. The assumption of barotropic currents is suitable for this thesis as real tidal channels such as Cook Strait are generally well mixed (Garner, 1969). In some environments, such as the equator, thermal forcing is the dominant driver of transport. However, this forcing is negligible compared to tidal forcing in locations suitable for tidal energy

generation. Starting with the dynamical governing equation as given in Garrett and Cummins (2005):

$$\frac{\partial u}{\partial t} + u\frac{\partial u}{\partial x} = -g\frac{\partial \eta}{\partial x} - \frac{C_{\mathrm{D}}}{h}\left|u\right| u - F_{\mathrm{T}}. \tag{2.1}$$

Where $u(x,t)$ is the velocity of the flow which is assumed to be uniform at any given cross-section of the rectangular channel, g is the acceleration due to gravity, $\eta(x,t)$ is the displacement of the water's free surface from depth $h(x)$, C_{D} is the background bottom drag coefficient and F_{T} is an additional force associated with the presence of a turbine farm. The momentum balance for the channel as a whole can be found by multiplying by $\rho A(x)$ and integrating across the length of the channel.

$$\rho\int_0^L A\frac{\partial u}{\partial t}dx + \rho\int_0^L Au\frac{\partial u}{\partial x}dx = -\rho g\int_0^L A\frac{\partial \eta}{\partial x}dx - \rho C_{\mathrm{D}}\int_0^L \frac{A}{h}\left|u\right| u dx - \rho\int_0^L AF_{\mathrm{T}}dx. \tag{2.2}$$

If the channel is "dynamically short" then the volume flow rate of the channel is approximately constant across its length and varies only with time e.g. $Q(t) = u(x,t)A(x)$ (Vennell, 1998a,b). Expressing the velocity in (2.1) with respect to flow rate and cross-sectional area then gives the energy balance of the channel:

$$\left(\int_0^L \frac{dx}{A}\right)\frac{dQ}{dt} + \frac{Q^2}{2}\left[\frac{1}{A_{\mathrm{L}}^2} - \frac{1}{A_0^2}\right] = g\left[\eta_0 - \eta_{\mathrm{L}}\right] - C_{\mathrm{D}}\left(\int_0^L \frac{dx}{hA^2}\right)\left|Q\right| Q - \int_0^L F_{\mathrm{T}}dx. \tag{2.3}$$

The turbine farm is assumed to obey a quadratic drag law, thus the integral of F_{T} may be defined as:

$$\int_0^L F_{\mathrm{T}}dx = \frac{C_{\mathrm{F}}}{A_{\mathrm{R}}^2}\left|Q\right| Q. \tag{2.4}$$

Where A_{R} is the cross-sectional area at the location of the farm and C_F is the gross farm drag coefficient. Substituting this into (2.3) gives:

$$\left(\int_0^L \frac{dx}{A}\right)\frac{dQ}{dt} + \frac{Q^2}{2}\left[\frac{1}{A_{\mathrm{L}}^2} - \frac{1}{A_0^2}\right] = g\left[\eta_0 - \eta_{\mathrm{L}}\right] - \left(C_{\mathrm{D}}\left(\int_0^L \frac{dx}{hA^2}\right) + \frac{C_{\mathrm{F}}}{A_{\mathrm{R}}^2}\right)\left|Q\right| Q. \tag{2.5}$$

For simplicity, it is assumed that the cross-sectional areas at both ends of the channel are

the same and thus the advection term in (2.5) vanishes. The two remaining integrals in (2.5) are referred to in the literature as the channel's geometric factors; $i = \int_0^L \frac{dx}{A}$and $b = \int_0^L \frac{dx}{hA^2}$. Expressing the difference in free surface between the two terminal water bodies as a sinusoidal function of time (t) with angular frequency (ω) and amplitude (Δ), Equation (2.5) becomes:

$$i\frac{dQ}{dt} = g\Delta\sin(\omega t) - \left(bC_D + \frac{C_\mathrm{F}}{A_\mathrm{R}^2}\right)|Q|\,Q. \tag{2.6}$$

In the absence of friction, for an unconstricted channel of uniform rectangular cross-section, Equation (2.6) has an exact solution $Q(t) = Q_\mathrm{IU}\cos(\omega t)$ where $Q_\mathrm{IU} = \frac{g\Delta A_0}{\omega L}$. Flow rate can be non-dimensionalised using this value and time using $t' = t\omega$. Depth and area can then be non-dimensionalised with respect to h_0 and A_0 (their maximum values that occur outside of the constricted zone). Using the non-dimensional parameter $\hat{\alpha} = 8g\Delta/3\pi\omega^2L^2$ (Vennell, 2012) then allows the non-dimensional bottom drag and farm drag to be defined as $\lambda_0 = \hat{\alpha}LC_\mathrm{D}/h_0$ and $\lambda_\mathrm{F} = \hat{\alpha}C_\mathrm{F}/A_\mathrm{R}'^2$ respectively. The effective bottom drag is defined as $B\lambda_0$ which when added to the farm drag constitutes the total drag coefficient of the channel: $\lambda_\mathrm{T} = B\lambda_0 + \lambda_\mathrm{F}$. Equation (2.6) in non-dimensional form is thus:

$$I\frac{dQ'}{dt'} = \sin(t') - \frac{3\pi}{8}\lambda_\mathrm{T}|Q'|\,Q'. \tag{2.7}$$

The $\frac{3\pi}{8}$ factor is introduced for mathematical convenience at a later point and $I = \int_0^1 \frac{dx'}{A'}$ and $B = \int_0^1 \frac{dx'}{h'A'^2}$ are the non-dimensional equivalents of the geometric factors introduced in (2.6).

2.3.2 Dynamic model for lagoon channels

For channels connecting a large water body to a bay of finite volume as described in Blanchfield *et al.* (2008); Karsten *et al.* (2008), the tidal head difference driving transport through the channel is now dependent on the water level inside the bay which is dependent on the flow rate itself. Following the same derivation as described in Section 2.3.1, Equation (2.8) is the lagoon channel equivalent to (2.6). If the embayment is assumed to be prismatic then the free surface elevation inside the bay is related to flow rate and its surface area A_s by (2.9)

$$i\frac{dQ}{dt} = g(\eta_{\text{ocean}} - \eta_{\text{bay}}) - \left(bC_{\text{D}} + \frac{C_{\text{F}}}{A_{\text{R}}}\right)|Q|\,Q, \tag{2.8}$$

$$\frac{d\eta_{bay}}{dt} = \frac{Q}{A_{\text{s}}}. \tag{2.9}$$

Here, $\eta_{\text{ocean}} = \eta_0 \sin(\omega t)$ is the sinusoidally varying free surface elevation of the large water body and η_{bay} is the time varying free surface of the bay. Introducing the parameter $\hat{\alpha}^* = 8g\eta_0/3\pi\omega^2 L^2$ allows for the non-dimensional bottom drag and farm drag for lagoon channels to be expressed as $\lambda_0^* = \hat{\alpha}^* L C_{\text{D}}/h_0$ and $\lambda_F = \hat{\alpha}^* A_0 C_{\text{F}}/A'_{\text{R}}$ respectively. The total drag in the channel is then $\lambda_{\text{T}}^* = B\lambda_0^* + \lambda_{\text{F}}^*$. Non-dimensionalising against an unconstricted, frictionless regular channel, Equations (2.8) and (2.9) are respectively:

$$I\frac{dQ'}{dt'} = \sin(t') - \eta'_{\text{bay}} - \frac{3\pi}{8}\lambda_{\text{T}}^*\,|Q'|\,Q', \tag{2.10}$$

$$\frac{d\eta'_{\text{bay}}}{dt'} = \beta Q'. \tag{2.11}$$

Where $\beta = (g/\omega^2)(A_0/LA_{\text{s}})$ is referred to as the lagoon factor and is the ratio of the Helmholtz frequency of the basin to the frequency of the forcing tides. From here onward the * is dropped from the dimensionless drag coefficients for lagoon channels and it is assumed that the subtle differences in drag coefficient definitions are understood i.e. the lagoon channel has dependence on η_0 rather than Δ.

2.3.3 Channel constrictions

Constrictions used in this study are Gaussian-shaped. A width constriction is made of two symmetrical Gaussian curves with the line of symmetry spanning the length of the channel at $W/2$. Depth constrictions are based on a single Gaussian sill. Both width and depth constrictions are formulated so that their respective curves peak halfway along the channel's

length at $x = L/2$. The curve used to constrict the channel width is:

$$G_{\mathrm{w}}(x') = \frac{W_{\mathrm{c}}}{2} \exp\left[\frac{-(x' - \frac{1}{2})^2}{c^2}\right]. \tag{2.12}$$

Where W_{c} is the width constriction factor and is the width of the "land mass" at the most constricted point of the channel relative to the flow width outside of the constriction (W_0). Thus, for a constriction that at most blocks the channel by 60%, $W_{\mathrm{c}} = 0.6$. The $\frac{1}{2}$ in the numerator of the exponential function ensures the curve peaks at the midpoint of the channel length. Finally, the factor c controls the broadness of the constriction such that as $c \to \infty$, $G_{\mathrm{w}}(x') \to \frac{W_{\mathrm{c}}}{2}$. In this study, c is set at 0.1. As the width constriction consists of two of these curves, the non-dimensionalised width of the channel flow area at any point is $W'(x') = 1 - 2G_{\mathrm{w}}(x')$.

Depth constrictions are based on a similar curve:

$$G_{\mathrm{h}}(x) = h_{\mathrm{c}} \exp\left[\frac{-(x' - \frac{1}{2})^2}{c^2}\right]. \tag{2.13}$$

Here h_{c} is the depth constriction factor and is analogous to the width constriction factor but in the depth axis. The remaining variables in (2.13) are the same as in (2.12). As the depth constriction consists of only one of these curves (Figure 2.2), the total depth at any point in the channel is given by $h'(x') = 1 - G_{\mathrm{h}}(x')$. Again, a value of $c = 0.1$ is used. Note that a width constriction factor and depth constriction factor of equal value will result in the same flow area reduction along the channel length and decrease the overall flow volume of the channel by the same amount. Furthermore, any specific constriction factor will result in the same flow area and flow volume reductions regardless of whether the channel is a regular or lagoon type.

2.3.3.1 Flow separation

As the 1-D model does not consider the effects of flow separation, it is only applicable to gradual constrictions. Flow separation may occur at the lee side of the constriction where the expanding cross-section will result in an adverse pressure gradient which will cause flow in the boundary layer to decelerate to the point of reversal. The presence of bottom drag will further enhance this effect. Depending on the aspect ratio of the constriction geometry, the frictional

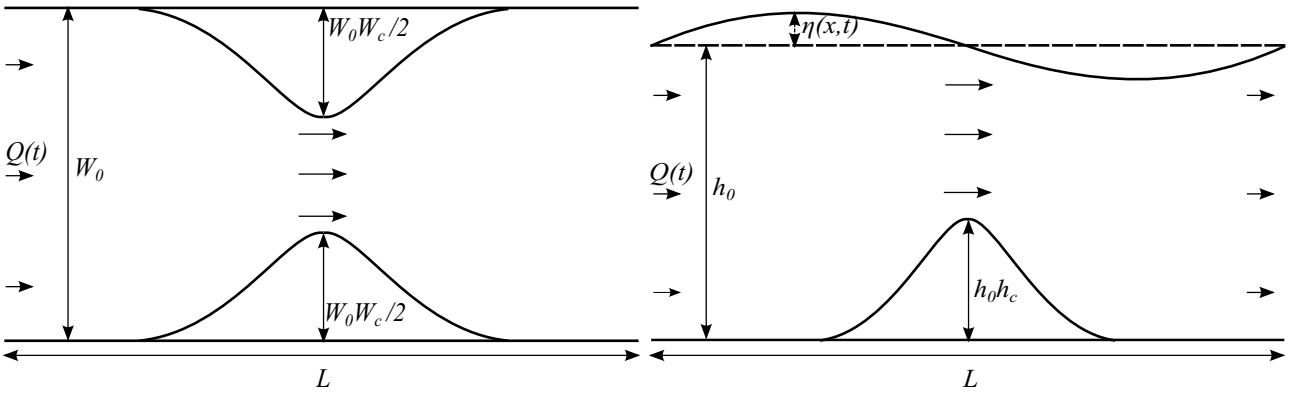

Figure 2.2: Examples of width (left) and depth (right) constriction formulations used in this study. Width constrictions are based on symmetric Gaussian curves (Equation 2.12) and depth constrictions a single Gaussian sill (Equation 2.13). Constriction factors (W_c and h_c) determine the extent to which the constriction occupies the cross-section at the channel's narrowest point.

Reynolds number and the Keulegan-Carpenter number – this separated flow may cause eddies to form (Signell and Geyer, 1991). Both flow separation alone and flow separation leading to eddy formation will result in a loss of energy in the channel. Quantifying this energy loss is beyond the scope of this chapter and is investigated using a 2-D model in Chapter 4 of this thesis.

2.3.3.2 Channel geometric factors (I and B) and multiple constrictions

The channel geometric factors both increase from an initial value of 1 where the channel is unconstricted to a value of infinity when the channel is fully blocked off (Figure 2.3). The geometric factor I is the same for both constriction types (e.g. depth or width). The factor B is more sensitive to constriction factor than I due to its dependence on the square of the area and is also sensitive to depth constriction due to its dependence on h. This study has limited itself to looking at channels with a single Gaussian-shaped constriction as described in the preceding section. The effect of having multiple constrictions within this one-dimensional model would cause the I and B factors to further increase. Thus, with respect to the channel potential and transport, the effect of several small constrictions would be identical to that of a single large constriction that produced the same values of I and B.

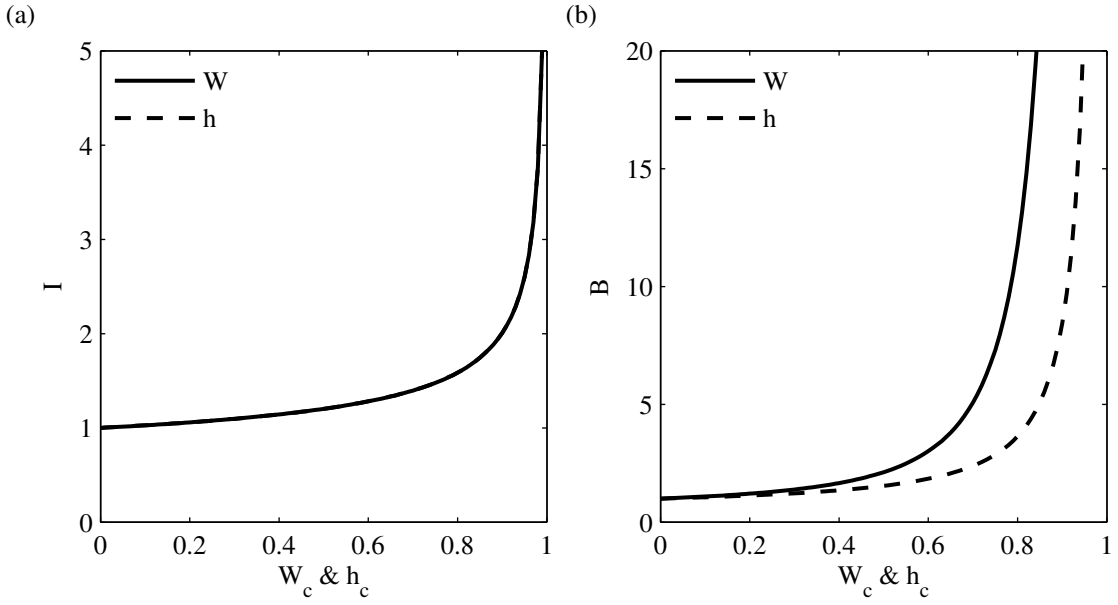

Figure 2.3: Effect of depth (h_c) and width (W_c) constrictions on a channel's non-dimensional geometric factors $I = \int_0^1 \frac{dx'}{A'}$ and $B = \int_0^1 \frac{dx'}{h'A'^2}$.

2.3.3.3 Constriction and Froude Number

This model is also only valid for small Froude numbers. In some extreme constriction cases the Froude number ($\mathrm{Fr} = u/\sqrt{gh}$) might approach a value of 1, resulting in near-critical flow in the channel. When flow turns super-critical, where $\mathrm{Fr} > 1$, hydraulic jumps can occur where there is a rapid transition of potential energy to kinetic energy - observable as a sudden drop in free-surface. As flow accelerates through the constricted region, Fr will increase via an increase in the flow velocity (u). This increase will be more profound if the constriction is a depth constriction as not only will the velocity of the flow increase, but the depth (h) of the channel will decrease. As is discussed later on in this work (Section 2.6), provided $I > \beta$, increasing the degree of constriction in a channel will cause the transport to decrease. This effect may partially offset the increase in Fr. The sensitivity of accounting for non-zero Froude number effects is tested in Appendix 5.3 of this thesis and was found to be negligible except in very extreme cases.

2.4 Analytical approximation

Vennell (2012) provides an approximate analytical solution to (2.7) that agrees closely with solutions obtained through numerical methods (Karsten *et al.*, 2008; Garrett and Cummins, 2005; Blanchfield *et al.*, 2008). The analytical solution considers only the M2 (semi-diurnal lunar) constituent and assumes the transport can be expressed as a single frequency sinusoidal current:

$$Q' = Q_0 \sin(t' - \phi_\mathrm{u}). \tag{2.14}$$

Where ϕ_u is the phase difference between the channel transport and the channel forcing. This forcing is driven by differences in phase and amplitude of the water surface at the ends of the channel. The non-linearity of the bottom friction term introduces higher harmonics which distort the transport function from a perfect sine wave. This distortion becomes important when analysing power over a full spring/neap cycle and this effect is explored in detail by Adcock *et al.* (2013). The error in using this analytical approximation instead of solving the problem numerically is less than 4% (Vennell, 2012).

Substituting (2.14) into (2.7) and using the approximation $|Q|\,Q \approx \frac{8}{3\pi} Q_0^2 \sin(t' - \phi_\mathrm{u})$ (Vennell, 2011a) yields two simultaneous equations of which the first can be solved to give an expression for ϕ_u. This can subsequently be used with the second equation to obtain an expression for Q_0. Similarly, substituting (2.14) into (2.10) gives an analytical solution for lagoon channels (Equations (2.15) and (2.16)). The analytical approximation for lagoon channels can be used for regular channels by setting $\beta = 0$. Equations (2.15) and (2.16) are a generalised forms of those given in Blanchfield *et al.* (2008) who considered only an unconstricted, rectangular channel where $I = 1$:

$$\phi_\mathrm{u} = \tan^{-1}\left(\frac{I - \beta}{\lambda_\mathrm{T} Q_0}\right), \tag{2.15}$$

$$Q_0 = \frac{\sqrt{2}}{\sqrt{\sqrt{4\lambda_\mathrm{T}^2 + (I-\beta)^4} + (I-\beta)^2}}. \tag{2.16}$$

2.5 Effects of channel constriction on channel potential

Channel potential is the theoretical upper limit for power generation in a tidal channel and can be achieved with a single row of turbines occupying 100% of the channel's cross-section. Channel potential considers the power in the channel that can be lost to all sources of farm related drag and therefore includes power production, mixing losses behind the turbines, structural drag related losses and electromechanical losses (Vennell, 2012). The amount of channel potential that can actually be realised is dependent on turbine array design and configuration (Vennell *et al.*, 2015). The number of rows of turbines, the number of turbines in each row, how the turbines are laid out in these rows and the blade pitch of the turbines have all been shown to have significant influence on the amount of power lost to a turbine array (Vennell, 2012; Vennell *et al.*, 2015; Vennell, 2011a). While channel potential does give an overestimate of the power that can be generated by an array, it is a useful quantity for the purpose of observing channel scale responses to changes in channel geometry. The non-dimensionalised potential ($\overline{P}'^{\text{opt}}_{\text{farm}}$) is calculated by finding the optimal non-dimensional farm drag ($\lambda_{\text{F}}^{\text{opt}}$) which maximises the average power lost to the farm over a tidal cycle for some geometric factors I and B (2.17).

$$\overline{P}'^{\text{opt}}_{\text{farm}} = \frac{1}{2\pi}\int_0^{2\pi} \lambda_{\text{F}}^{\text{opt}} \left|Q'(t')\right|^3 dt'. \tag{2.17}$$

Defining $P_{\text{IU}} = \frac{2\rho Q_{\text{IU}}^3}{3\pi\hat{\alpha}A_0^2}$ such that $\overline{P}^{\text{opt}}_{\text{farm}} = P_{\text{IU}}\overline{P}'^{\text{opt}}_{\text{farm}}$ and using Equation 2.14, then Equation 2.17 can be rewritten as:

$$\overline{P}'^{\text{opt}}_{\text{farm}} = 2(\lambda_{\text{T}}^{\text{opt}} - B\lambda_0)Q_0^3. \tag{2.18}$$

2.5.1 Increasing constriction reduces the potential of regular channels

This study was done entirely in non-dimensional variables for a hypothetical channel. Although this study did not model any specific channels, Table 2.1 supplies values for Cook Strait, New Zealand and Minas Passage, Canada to give some perspective to the figures we have used throughout this work.

Table 2.1: Approximate geometry values for the Cook Strait and Minas Passage. The lagoon factor for the Minas Passage was taken from Karsten *et al.* (2008) while the rest of the data was taken by projecting the channels onto a regular xy-grid. Data for the Cook Strait assumes a flat seafloor*

Channel	Cook Strait	Minas Passage
L, W_0, h_0	117km, 125km, 100m	9km, 7.1km, 71m
Mean W, h	77km, 100m*	5.9km, 59m
W_c, h_c	0.60, 0*	0.35, 0.28
$\lambda_0 = \hat{\alpha} L C_D / h_0$	0.13	7.00
I, B, β	1.76, 3.31, -	1.15, 1.59, 12.9
$B\lambda_0$	0.43	11.1

Figure 2.4(a) shows the response of channel potential to increases in constriction for three different values of bottom friction coefficient (λ_0) with thick lines used for width constricted channels and thin lines for depth constricted channels. It can be seen in Figures 2.4 (a) and (b) that an increase in either bottom drag or constriction factor of a regular channel will cause the potential to diminish in all instances. This decrease in potential is primarily due to an enhancement in sea floor related drag and the associated decrease in channel flow rate. Bottom drag is proportional to the local velocity squared and hence a localised region of high velocity within a channel will cause the effective bottom drag coefficient of the channel as a whole to increase significantly (Figure 2.4(d)). As more power is consequently lost to drag from the sea floor, less power is then available for the production of electricity.

The second contributing factor to this decrease in potential with constriction is channel transport. Transport through the channel decreases with constriction due to this aforementioned increase in bottom drag and geometric factor I. This is discussed further in Section 2.6 below. Results here suggest that a trade-off exists in regular channels between having a local zone of high velocity and having a high channel potential.

Figure 2.4 demonstrates that depth constricted channels always have lower potentials than channels constricted in their width to the same degree. Making a channel shallower causes a greater increase in effective bottom drag than does making the channel narrower (Figure 4). Mathematically, this is due to the $1/h$ component of the effective bottom drag term. Physically, it's due to the boundary layer associated with the seafloor extending vertically through a greater percentage of the total water column. As the channel is made shallower, a greater percentage of the channel transport is affected by this boundary layer. Although beyond the scope of

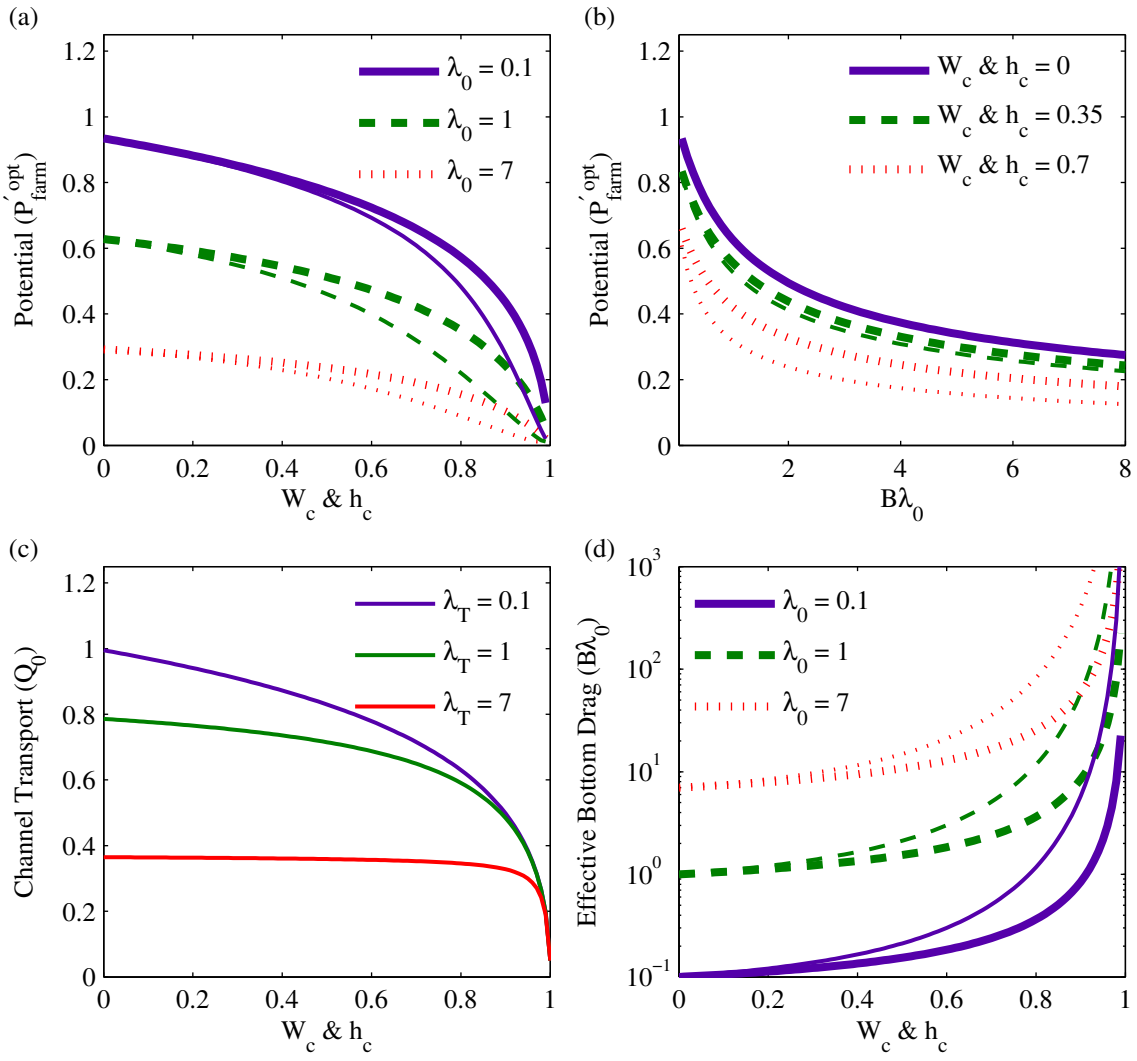

Figure 2.4: The effect of constriction and bottom drag in a regular (open ended) channel on (a,b) channel potential, and (c) channel transport. Figure (d) shows how constriction enhances the effective bottom drag of the channel through increases in geometric factor B - note the log scale on the y axis of (d). Thick lines have been used for width constricted channels while thin lines have been used for depth constrictions. Both channel potential and transport values are relative to an unconstricted, frictionless channel.

this study, the presence of this boundary layer will have implications for turbines mounted on the seafloor and, in the case of shallow channels with strong tidal flows, will also affect tidal turbines floating on the surface.

The above finding suggests that, although a radical idea in principle, if a channel were to be geometrically modified to create a local zone of high velocity, it would be preferential to constrict the channel's width rather than its depth. This would create a high velocity region that may allow developers to generate power using fewer turbines. It would also, however, come at the expense of lowering the potential of the channel. Note that this study has assumed the aspect ratio of the channel is such that the channel's width is significantly greater than its depth and thus does not consider drag from the lateral walls of the channel. In deep, thin channels where the depth is of similar or greater magnitude to the channel width, this drag source will not be negligible and may in fact dominate.

2.5.2 Potential of lagoon channels

Figure 2.5 shows the channel potential in lagoon channels versus channel geometric factor I. Geometric factor was used instead of constriction factor here as it better demonstrated the "power peaks" that can be observed in the figure. The three coloured lines correspond to bottom drag values of $\lambda_0 = 0.1$ (purple), $\lambda_0 = 1$ (green) and $\lambda_0 = 7$ (red). Recall that for an unconstricted channel, the geometric factor $I = 1$ and as the degree of constriction is increased, the geometric factor I approaches infinity (when the channel is totally blocked off).

Figure 2.5 shows that the potential of a lagoon channel with low bottom drag can exceed that of an unconstricted frictionless regular channel (e.g. $\overline{P}'^{\text{opt}}_{\text{farm}} > 1$) for certain combinations of channel geometry I and lagoon geometry β. This is a consequence of feedback between channel flow rate and the free surface elevation of the terminal embayment. Certain channel dynamics and geometries give rise to enhanced head differences across the channel and consequently flow rates that are not possible in regular channels. This feedback mechanism is believed to be the primary reason for the power peaks observed in Figure 2.5.

The power peaks in Figures 2.5 (c) and (d) are clearly visible. The potential of these channels increases with constriction to some peak value and then diminishes as the channel is further

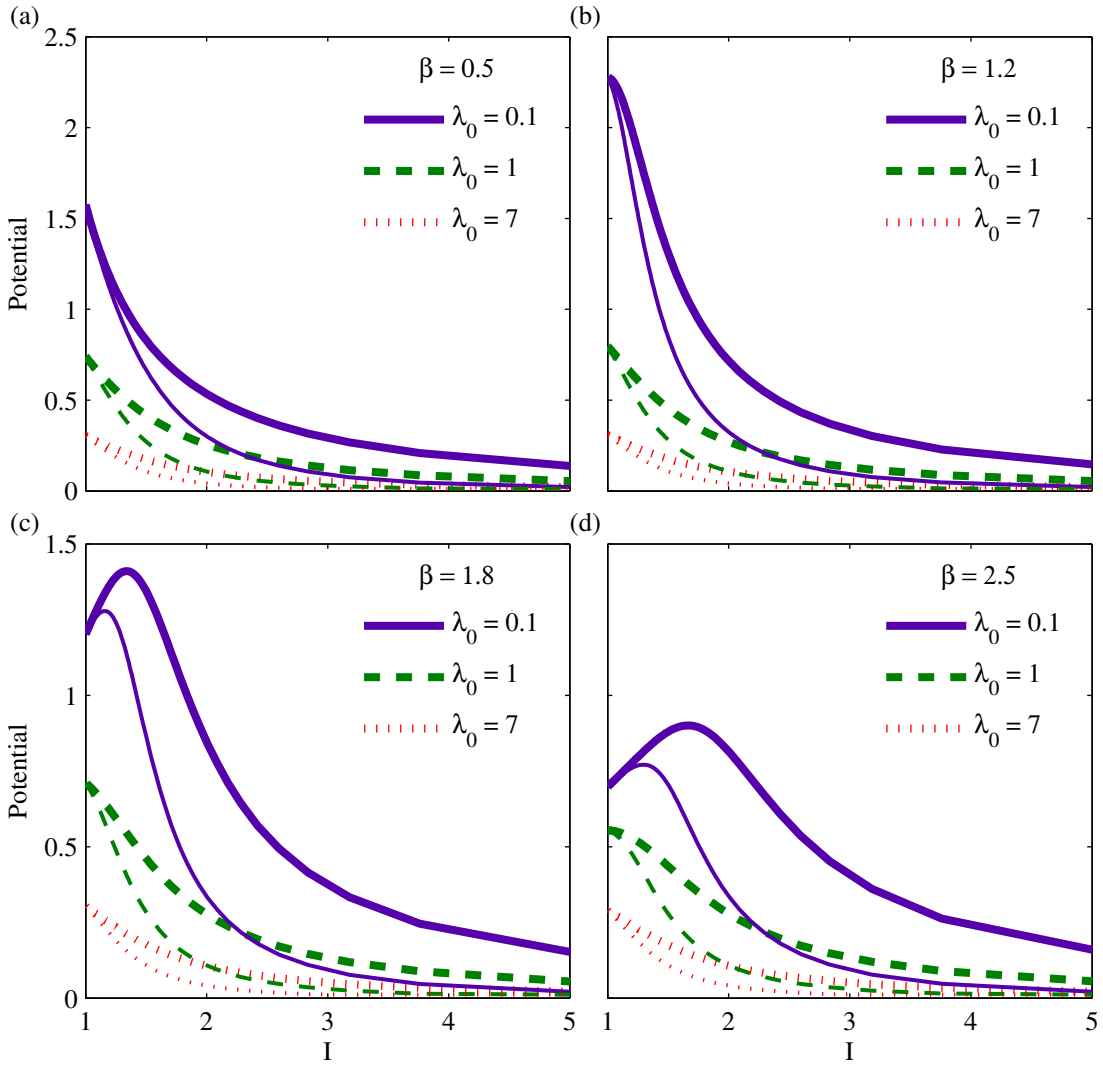

Figure 2.5: Line plots of channel potential versus geometric factor I for various lagoon channels of differing lagoon factors (β) and bottom friction (λ_0) configurations. Width constricted channels are denoted with thick lines while depth constricted channels are denoted with thin lines. Channel potential refers to the maximum amount of power that can be lost in a channel to turbine farm related drag and the geometric factor $I = \int_0^1 \frac{dx'}{A'}$ is determined by the amount of constriction within the channel, for an unconstricted channel $I = 1$ and this factor increases with an increase in constriction. All potential values are relative to the channel potential of a frictionless regular channel of the same maximum dimensions.

constricted. The peak in the upper left plot (a) lies to the left of the y-axis and cannot be seen. This would suggest that channel potential could be increased by widening the channel to achieve a value of $I < 1$. Plot (b) is essentially peaking around $I = 1$ although a slight widening may possibly cause further increase in potential.

The location of these peaks on the I-axis is dependent on the lagoon geometric factor (β) of the channel and the fact that these peaks exist is an interesting result. Although an extreme proposition, the presence of these peaks suggests that lagoon channels can be geometrically "tuned" to increase potential. This process could involve either constricting or widening the channel to cause an increase or decrease in the channel's I value respectively. In cases where I is below its optimal value, further constricting the channel would simultaneously increase the total power and increase the velocity in the constricted area. Such an operation is likely to be unfeasible for large scale channels such as Minas Passage, Bay of Fundy but may be feasible in smaller channels.

Analogous to observations made for regular channels in Section 2.5.1 above, increasing the bottom drag coefficient of lagoon channels results in a lower potential regardless of channel geometry or lagoon geometry. Again, depth constricted channels have less available power than width constricted channels of the same constriction factor.

2.6 Effects of constriction on flow

The degree of constriction present within a channel affects the dynamical balance of forces which has implications for the channel transport. Power is proportional to the channel's flow rate cubed and consequently the behaviour of the channel transport is pertinent to that of the potential. The approximate analytical solution described in Section 2.4 is a useful tool for demonstrating flow rate behaviour and is shown again below for convenience:

$$Q_0 = \frac{\sqrt{2}}{\sqrt{\sqrt{4\lambda_T^2 + (I-\beta)^4} + (I-\beta)^2}}.$$

2.6.1 Regular channels

By setting $\beta = 0$, the analytical approximation above can be used for a regular channel (Equation 2.16). It is clear from (2.19) that both increases in drag and constriction factor (and therefore an increase in I) will cause the peak flow rate through the channel to diminish. Channel drag and channel constriction both act to retard the flow rate through a regular channel (Figure2.4(c)). Channel drag acts to retard the flow via an increase in the λ_T term in the denominator of (2.19). Due to the quadratic dependence of drag on velocity, the zone of high velocity flow through the constricted passage equates to a zone of high drag:

$$Q_0 = \frac{\sqrt{2}}{\sqrt{\sqrt{4\lambda_{\mathrm{T}}^2 + I^4} + I^2}}. \tag{2.19}$$

The presence of the constriction decreases the flow through the channel via an increase in geometric factor I. The presence of a constriction reduces the total volume of water in the channel as some of the water volume is now occupied by land. As the degree of forcing in the channel is unaffected by the channel's geometry, this suggests that the flow rate should increase. However, more of the channel's forcing is now expended by accelerating the flow through the constricted passage. This latter effect dominates the volume reduction effect and while a channel constriction causes local velocity to increase, this comes at the cost of lower transport throughout the channel as a whole.

2.6.2 Lagoon channels

As was the case for power, the relationship for lagoon channels is made more complex by the feedback mechanism between channel flow rate and the free surface of the lagoon (Figures 2.6 (a) - (d)). "Flow peaks" result for specific combinations of channel geometry and lagoon geometry as certain values of Q can increase the head difference at the channel ends and alter the channel forcing. Channel transport in lagoon channels can exceed that of a frictionless, unconstricted regular channel as demonstrated by peak flows greater than $Q_0 > 1$ (Figure 2.6(a) - (d)). The flow rate of lagoon channels is maximised when the channel's geometric factor I is equal to the lagoon geometric factor β which, in the case of zero friction, corresponds to a resonant mode in

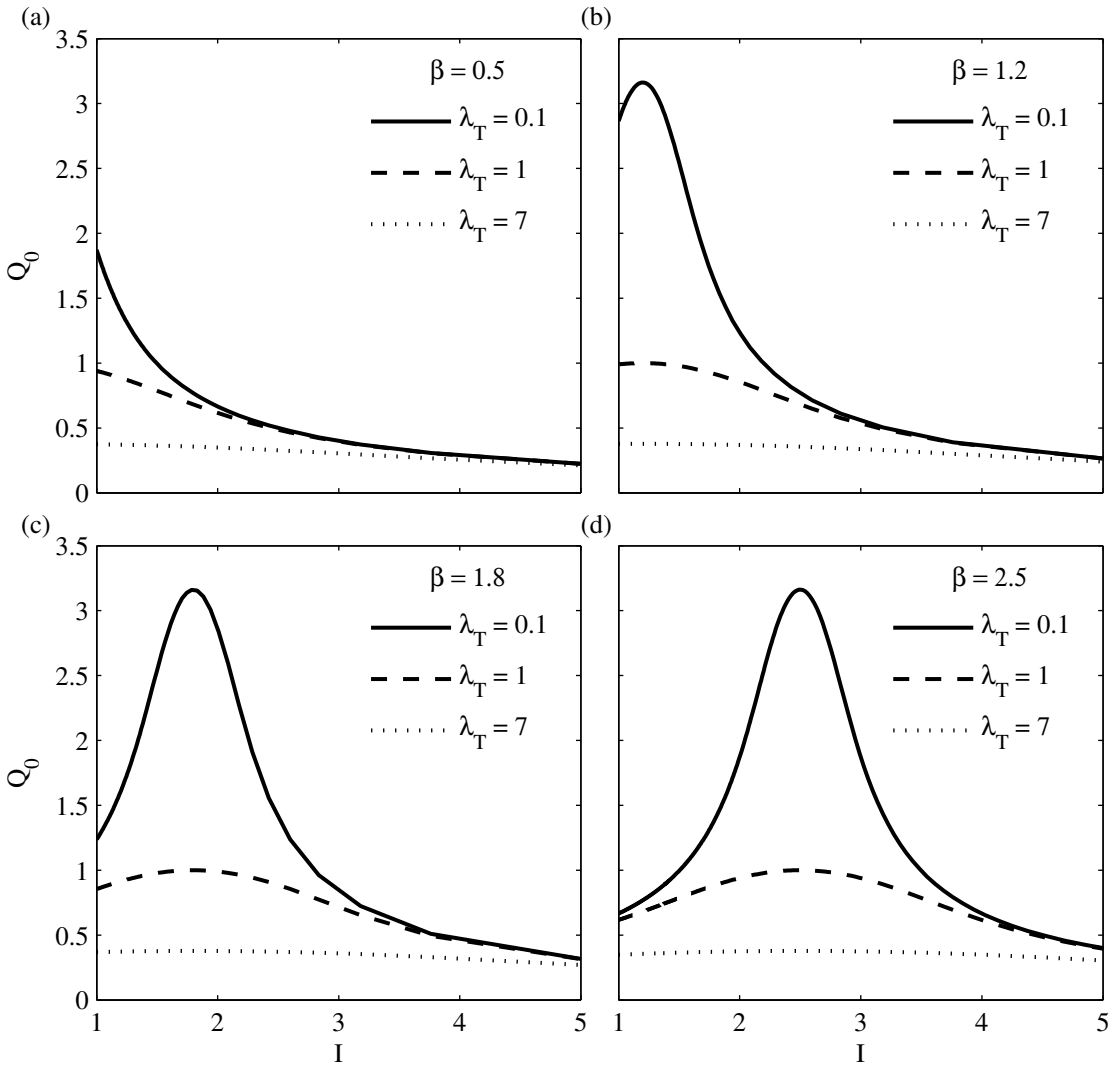

Figure 2.6: Plots of the peak undisturbed flow rate $Q_{0\mathrm{UD}}$ versus geometric factor I for various lagoon channels of differing lagoon factors (β) and total drag (λ_T) values. Note that total drag may constitute drag from both the seafloor and a turbine array. All flow rates are relative to an unconstricted, frictionless channel of the same maximum dimensions. Flow rates peak in channels where the channel geometric factor I is equal to the lagoon geometric factor β for a given value of total drag

the channel-lagoon system. Although this rather elegant condition will maximise the channel's flow rate, it will not necessarily maximise the channel's potential (Figure 2.5).

Applying the condition $\beta = I$ to the analytical approximation yields (2.20). At this condition, transport through the channel is maximised as $\lambda_T \to 0$. Increasing the amount of drag in the channel results in a decrease in flow rate for all geometric combinations. Any deviation from the optimum geometric condition seen in (2.20) causes peak flow rate to decrease:

$$Q_0 = \frac{1}{\sqrt{\lambda_T}}. \tag{2.20}$$

2.6.3 Flow reduction at potential

The negative feedback effect of adding turbines on channel flow rate is well known (Vennell, 2010, 2011a, 2012; Garrett and Cummins, 2005; Karsten *et al.*, 2008; Blanchfield *et al.*, 2008). Equations (2.19) and (2.20) both show adding turbines (and hence adding sources of drag) to a channel will cause a decrease in peak flow rate in all instances. Figure 2.7 shows the reduction in flow rate required to achieve potential in a regular channel (a) and several lagoon channels of differing lagoon geometries (b) - (f). Surprisingly, the reduction in flow rate at maximum power extraction is reasonably invariant to channel type and constriction factor. The reduction in flow rate at potential for all channels increases rapidly with small increases in effective bottom drag initially but eventually plateaus to a constant value. This trend is observed in all instances where β is less than about 3 (Figure 2.7 (a) - (e)). Beyond this value of β, channels exhibit more erratic behaviour (Figure 2.7 (f)) and the relationship between constriction, lagoon geometry and the balance of forces in the channel is unclear. Despite this, the flow rate reduction observed in these high β channels remains in the ballpark range of 0.6 - 0.7, the same range as all plots shown in Figure 2.7. All the flow rate reductions shown in Figure 2.7 would probably be considered unacceptable for environmental reasons (Shields *et al.*, 2011). Due to the obvious barriers to achieving channel potential and the relatively insignificant change in the values of flow rate reduction at high β, we have chosen not to investigate this detail any further in this work.

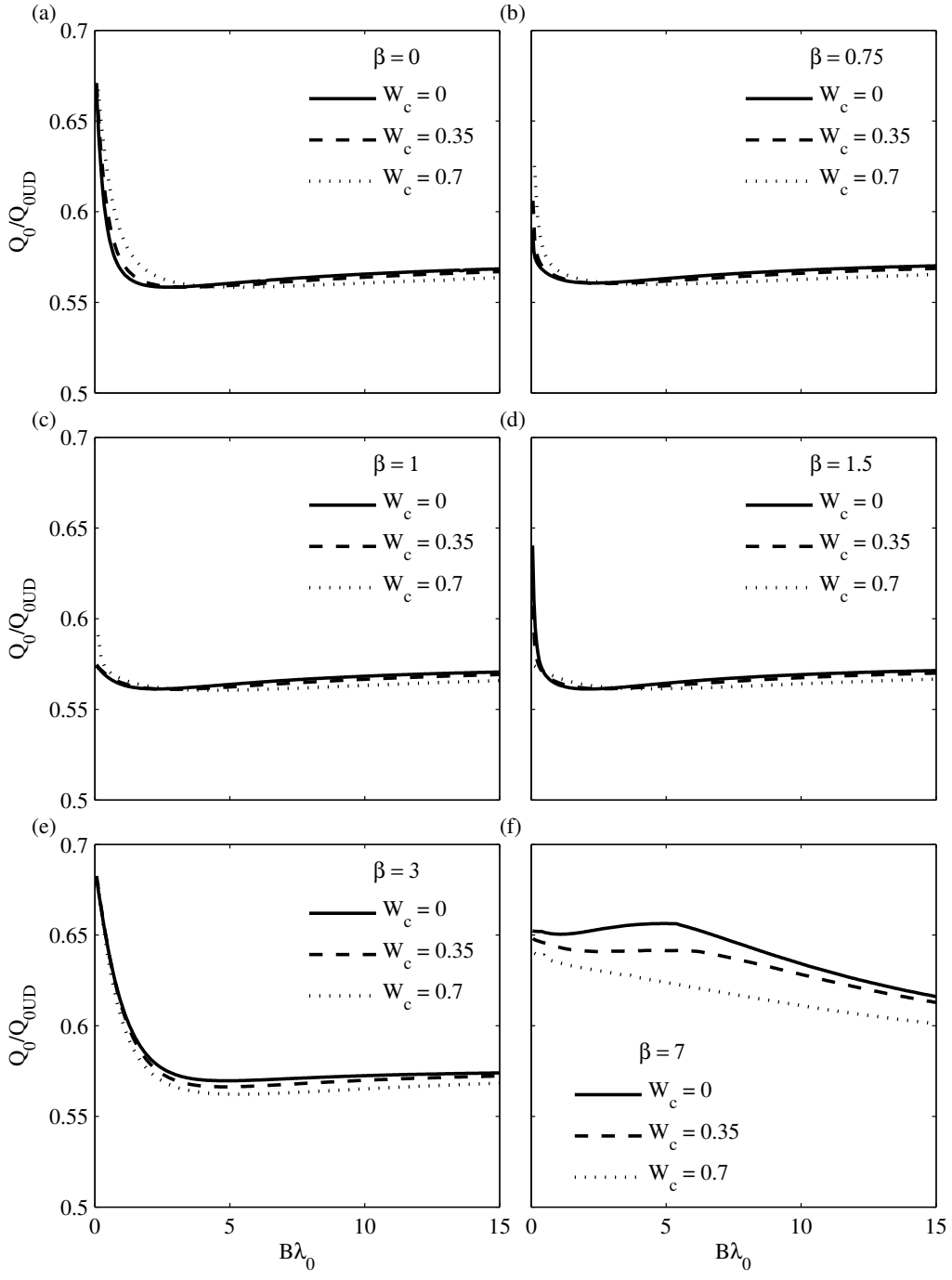

Figure 2.7: Plots showing the percentage reduction in peak transport at channel potential (maximum power) for a regular channel (a) and various lagoon channels (b-f) with various constriction factors. Surprisingly, the percentage reduction does not vary significantly with constriction factor and is relatively invariant to lagoon geometry provided $\beta \lesssim 3$. Plots are shown only for width constrictions as the flow reduction showed little to no sensitivity to constriction type.

2.7 Extending the GC05 approximation

Garrett and Cummins (2005) provided a simple approximation for the potential of unconstricted channels which uses only the amplitude of the tidal forcing (or difference in head between the two water bodies) Δ and the undisturbed flow rate $Q_{0\mathrm{UD}}$ of the channel. Blanchfield *et al.* (2008) extended this approximation to an unconstricted channel connecting a bay to the open ocean:

$$\bar{P}^{\max}_{\mathrm{farm}} \simeq \gamma \rho g \Delta Q_{0\mathrm{UD}}. \tag{2.21}$$

Depending on the level of bottom friction in the channel, Garrett and Cummins (2005) found that the multiplier γ varies between 0.21 and 0.24 for a regular channel and findings in Blanchfield *et al.* (2008) found that for a lagoon channel this coefficient varies between 0.19 and 0.26 depending on bottom friction and the β parameter. Both studies find that as bottom friction increases, γ converges to near 0.22, and suggest that this value may be used as a reasonable guess without any need to understand the influence of friction within the channel.

Here, this approximation was investigated for regular and lagoon channels of varying constriction factor and was found to hold with approximately the same ranges of γ given by Blanchfield *et al.* (2008); Garrett and Cummins (2005). The multiplier (Figure 2.8) was invariant to constriction type as the channel constriction is accounted for in the calculation of B and hence the effective bottom drag ($B\lambda_0$) of the channel.

Gamma values consistently converged to a value of approximately 0.22 until β was increased beyond a value of around 7. Past this point, both the range of the multiplier and the point of convergence increased slightly.

The range of the multiplier seems to depend on how close the lagoon geometry is to the case of $\beta = 1$. Values closer to this point have a smaller range and all multiplier values lie around the convergent value of $\gamma = 0.22$ while other cases can vary by up to 0.06. As most channels lie beyond this inertial domain of bottom drag coefficients, these findings reaffirm the statement given in Blanchfield *et al.* (2008); Garrett and Cummins (2005) that a multiplier value of 0.22 can be used with (2.21) as a rough approximation to the channel potential.

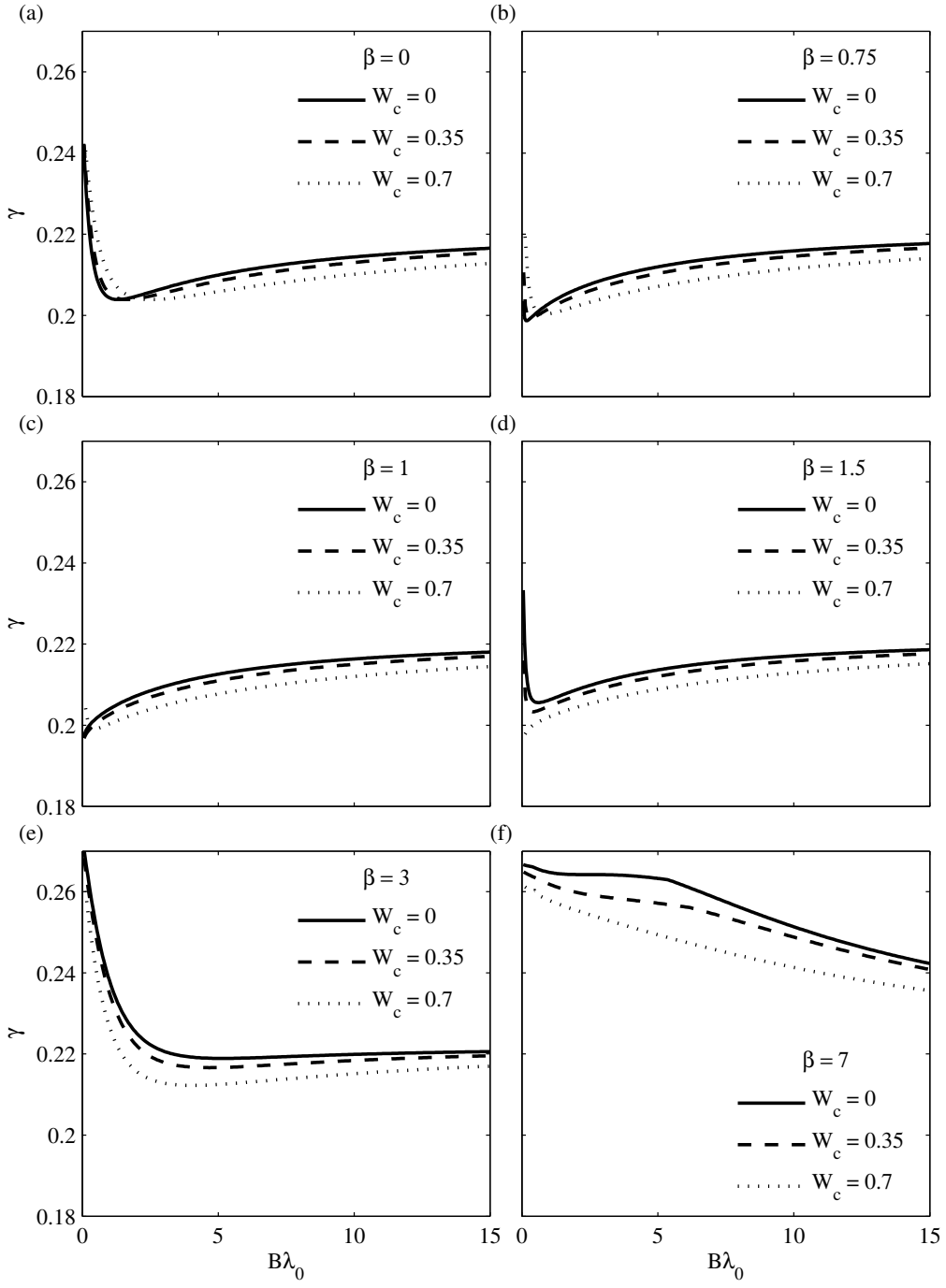

Figure 2.8: Plots of the multiplier γ as introduced in Equation 2.21 for a variety of β values, effective bottom drag values and constriction factors. Plot (a) corresponds to a regular channel while the remaining plots (b-f) correspond to lagoon channels with different lagoon geometries. Plots are shown only for width constrictions as little to no sensitivity was observed between the multiplier γ and constriction type.

2.8 Predicting the drag coefficient at potential

At potential, the ratio of the channel bottom drag coefficient to the total drag coefficient (termed $\kappa = B\lambda_0/\lambda_T$) exhibits similar behaviour to that of the multiplier mentioned above in Section 2.7. That is, this ratio tends to converge to a given value (0.32) as the effective bottom drag coefficient of the channel ($B\lambda_0$) increases. As was the case for the γ multiplier, the range of this value is smaller and the values of κ converge faster when the lagoon geometry factor β is close to $\beta = 1$. It can be seen in Figure 2.9(f) for the lagoon channel where $\beta = 7$ that the ratio does not converge in the bottom drag coefficient range shown although may do so at higher effective bottom drag. While this drag approximation is not useful for inertia dominated channels it does allow for rapid approximation of the required farm drag coefficient for shallower friction dominated channels - or at least rapid calculation of a good first guess for an optimisation routine. The total drag required to optimise a friction dominated channel can be approximated using (2.22) and the required drag coefficient of the turbine farm can be approximated using (2.23):

$$\lambda_T \approx \frac{B\lambda_0}{\kappa} \tag{2.22}$$

$$\lambda_F \approx \frac{B\lambda_0 - \kappa}{\kappa} \tag{2.23}$$

Little distinction can be made between width constricted and depth constricted channels in the value of κ.

2.9 Conclusion

This chapter has used a 1-D shallow water model to investigate the effects of channel constriction on the maximum available power in tidal channels connecting two large water bodies (regular channels) and a large water body connected to an embayment (lagoon channels). Findings from this study indicate that increasing the degree of constriction in a regular channel decreases the potential of the channel to produce power, which partially addresses the first aim of this thesis. This reduction in potential is due to an increase in the effective bottom drag of the channel and an associated decrease in the peak flow rate of the channel. As drag force is proportional to the

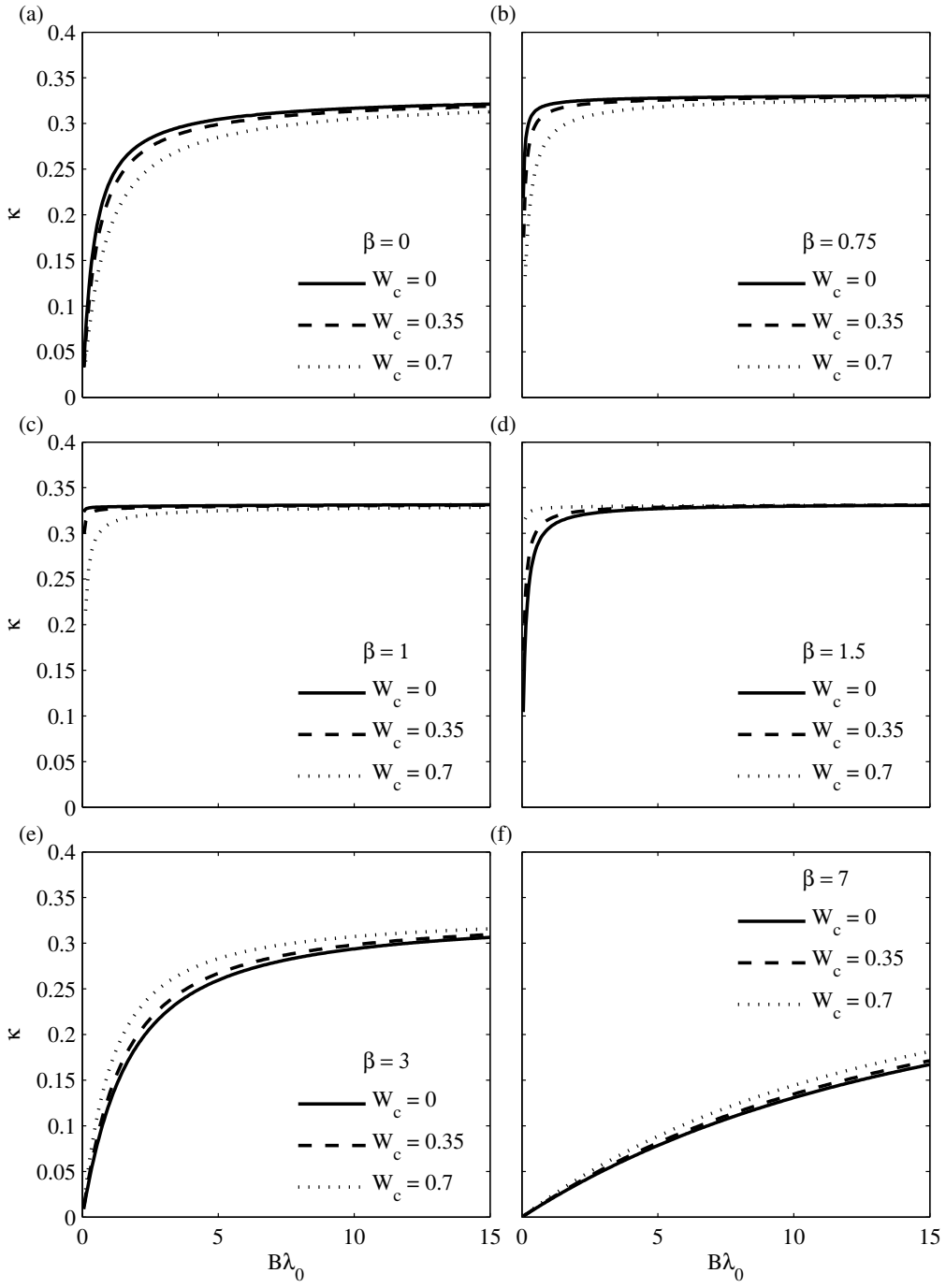

Figure 2.9: Plots showing the ratio $\kappa = B\lambda_0/\lambda_T$. This value converges to a value of about 0.32 which allows for quick calculation of the farm drag coefficient required to achieve potential in shallow friction dominated channels. It can be seen in plots (b), (c) and (d) that κ also can be used for inertia dominated channels with some caution provided the β factor is close to a value of $\beta = 1$. Much like the multiplier γ, as lagoon factors deviated away from $\beta = 1$, κ was more dependent on the effective bottom drag of the channel. Plots are shown only for width constrictions as κ exhibited little or no sensitivity to constriction type

square of the velocity, the enhanced velocities through the narrow constricted zone result in an increase in effective bottom drag coefficient of the channel. More power is expended overcoming seafloor related drag and less is then available for electricity generation, lowering the channel's potential.

The addition of a constriction also results in a smaller flow volume through the channel, which answers the second aim of this thesis. This is due to the aforementioned increase in effective bottom drag through the channel and the fact that more of the channel's forcing is now expended by accelerating the flow through the constriction. This decrease in transport through the channel further reduces channel power. Findings from this chapter suggest a trade-off exists between having a constricted channel with a local zone of high velocity and having an unconstricted channel with a high potential.

The relationship between channel potential and constriction in lagoon channels is more complicated because the free surface elevation in the terminal bay and the channel flow rate are mutually dependent. This feedback loop means that increasing the degree of constriction in the channel can cause the maximum power and flow rate of a lagoon channel to either increase or decrease depending on the relative geometries of the channel and the bay. Although a somewhat radical proposition, this suggests that the channel geometry and lagoon geometry of lagoon channels may be "tuned" to increase the channel's maximum power output. Furthermore, in certain instances this would have the dual effect of increasing the channel's potential as well as creating a localised zone of high velocity. The behaviour of peak flow rate in lagoon channels was analogous to the behaviour of potential in these channels. The transport of lagoon channels peaks when the channel geometric factor I is equal to the lagoon geometric factor β. The geometric condition that maximises channel potential is not clear.

For both types of channel examined, negative effects on potential were more profound for depth constrictions than width constrictions of equal magnitude (in terms of constriction volume). This suggests that artificially constricting a channel would preferentially be done by modifying its width rather than depth. This would create a localised zone of high velocity which may be advantageous for power extraction but would come at the cost of lowering the upper power limit of the channel as a whole.

The degree of constriction was found to have little to no effect on the flow rate reduction

required to achieve channel potential in regular channels, and, lagoon channels with small β values ($\beta < 3$). For channels with low effective bottom friction coefficients ($B\lambda_0 < 3$), the necessary flow rate reduction to achieve potential increased rapidly from a value of about 33% in the near frictionless case to a value of about 43%. For higher levels of effective bottom friction ($B\lambda_0 \geq 3$), the flow rate reduction at potential for these channels exhibited little sensitivity to constriction factor, did not necessarily increase with greater effective bottom drag coefficient and did not converge to a constant value within the range tested.

Finally, the simple approximation for channel potential provided by Blanchfield *et al.* (2008); Garrett and Cummins (2005) was found to hold for constricted channels of both regular type and lagoon type and a similar relationship was found to approximate the drag coefficient required by a turbine farm to achieve potential for a friction dominated channel ($B\lambda_0 > 3$). Both relationships, particularly the latter, were found to be poorer approximations for lagoon channels with particularly high lagoon geometric factors ($\beta > 6$).

This chapter has taken what may be the first systematic look at the effects of channel constriction on the upper limit of tidal power production. The focus of Chapter 3 will be on determining more realistic values of available power and looking at how array design influences power production by building a turbine model into the pre-existing model. Further work is then undertaken in Chapter 4 to expand analysis into two dimensions.

Chapter 3

1-D Turbine Array Theory in Constricted Channels

3.1 Foreword

This chapter is the first work of its kind to systematically explore and quantify different aspects of turbine array design in constricted channels. It extends and complements the one-dimensional theoretical works of Vennell (2011a, 2012, 2010) to cases where channel geometry is non-rectangular and uniform. The velocity deficit component of this chapter was partially completed under the supervision of Margot Gerritsen at Stanford University, USA thanks to the Elman Poole Scholarship. This chapter has been submitted to Journal of Renewable and Sustainable Energy where it is currently undergoing revision. Ross Vennell, Alice Harang and Margot Gerritsen will be co-authors of these papers - their contribution has been purely supervisional.

This work addresses Research Questions 1 to 4 of this thesis:

1. How are theoretical limits on tidal energy generation such as channel potential and **maximum available power** affected by channel constriction?
2. How does channel constriction affect the extent of tidal energy related flow reduction?
3. How should arrays be arranged in constricted channels to maximise energy output?
4. How does power scale with the number of turbines in a constricted channel?

3.2 Introduction

It is important to understand how constrictions affect power generation and how turbine arrays should be designed in constricted channels. Environmental effects and engineering limitations also need to be considered. These and other factors may require developers to deviate from the array design that maximises power output. This chapter performs a systematic exploration of turbine array design in constricted channels to build upon existing 1-D tidal energy theory. Findings from this work can inform decisions made regarding tidal energy developments in constricted channels.

Several prototype turbine devices (0.1 to 1.2MW) have successfully supplied electricity to local grids in Canada, France and the United Kingdom. Additionally, a collection of small array projects ($\leq$10 turbines, 3 to 30MW) have now passed the planning and consent process. Small array developments (such as the MeyGen array in Pentland Firth) are critical for the progression of the industry. However, looking forward into the future, much larger arrays containing hundreds of turbines (100 to 1000 MW capacity) will be necessary if tidal stream energy is to significantly contribute to global energy supply. Array theory developed for unconstricted channels indicates arrays this large will significantly alter the tidal resource (Vennell *et al.*, 2015) and affect both near and far-field hydrodynamics (Hasegawa *et al.*, 2011; Vennell, 2010; Polagye and Malte, 2011). Although industry is far from developing arrays large enough to influence channel dynamics, knowing how these arrays will function and how they should be designed is a critical first step towards their realisation.

As discussed in the introductory chapter of this thesis, large array scale resource assessment studies can be categorised into two types. The first type is generalised systematic studies that mostly use one-dimensional modelling to test a broad range of scenarios and develop generalised tidal energy theory (Vennell, 2011b, 2012; Karsten *et al.*, 2008; Blanchfield *et al.*, 2008). These works aim to examine the overarching behaviour of turbine-ocean systems. The second type of study uses multi-dimensional numerical models that are usually applied to a specific development and geography and use complex geometry (Carballo *et al.*, 2009; Draper and Nishino, 2014; Easton *et al.*, 2012; Polagye and Malte, 2011). This style of work provides detailed and accurate information pertaining to specific development scenarios that are useful

for assessing a project's feasibility and environmental impact. These latter studies are less computationally efficient and are therefore limited by the number of scenarios they can test. They are hence less suitable for exploratory studies. Theory derived from the first type of study (1-D modelling) is useful for informing modellers and researchers on what scenarios would be useful to test in these higher order modelling works and can increase their efficiency. The next chapter (Chapter 4) extends analysis to 2-D flow and is one of few existing studies that systematically explores array design using a higher order model.

This chapter here undertakes a systematic exploration of turbine array design in constricted channels using a 1-D model. Quantitative large array studies of this nature have so far been applied only to unconstricted channels with rectangular geometries (Karsten *et al.*, 2008; Garrett and Cummins, 2005; Blanchfield *et al.*, 2008; Vennell, 2011a) although Vennell (2010) qualitatively discusses how varying the channel geometry may change results. Despite this, many favourable tidal energy sites contain channel constrictions. Work completed in the past chapter (published as Smeaton *et al.* (2016)) examined how varying the channel cross-section of an idealised constricted channel in both the width and depth affected the potential of the channel. This last chapter allowed the total drag in the channel to vary arbitrarily. Work presented here uses a 1-D analytical turbine model to derive drag coefficients for particular turbine array designs that can then be used as input to the 1-D channel model. This attaches a description of a turbine array layout to the channel drag coefficient which allows for a systematic investigation of turbine array design in constricted channels. Using this model, this chapter explores how arrays should be built in constricted channels by looking at factors such as: how turbines are packed into rows, where these rows should be positioned and how these rows should be optimally tuned. This work looks at how power generation scales with the number of turbines in different turbine array designs in constricted channels and extends existing turbine array theory. Findings here can be used to make informed decisions regarding turbine array development.

While it may seem intuitive that placing turbines in the narrowest cross-section of a channel will generate more power than placing turbines elsewhere in a channel - this has not been formally tested. Furthermore, if economic feasibility or regulatory measures prohibit developing the smallest cross-section, one needs to know the consequences of developing outside of this region. If multiple arrays are developed in the same channel, the arrays may interact with each other.

This could cause one array to be more productive than the other. In this case, policy will be required to prevent monopolisation of power, encourage investment in the industry and ensure early pioneers of the technology are not disadvantaged.

This chapter starts with a brief overview of the mathematical model that was used to complete this work (Section 3.3). Section 3.4 then looks at the relationship between channel constriction and the design of a single row of turbine devices (row location, device tuning, number of turbines) and how these factors influence the total available power from the array, how power scales as turbines are added to the array, what the average loads are on the turbines and uses the power to force ratio (PFR) as an indicator of economic feasibility. The end of this section looks at how channel constriction and row placement influence the optimal tuning of turbines in the row and the reduction in flow. Analysis is then extended in Section 3.5 to multi-row arrays and examines how rows should be arranged subject to some minimum row spacing constraint. Finally, Section 3.5.2 applies a simple velocity deficit model behind rows of turbines in a two-row array to investigate what effect this has in both constricted and unconstricted channels.

3.3 Methods

This study uses the 1-D depth averaged shallow water model presented in the preceding chapter to simulate the behaviour of a constricted tidal channel. Turbines are built into this model as additional sources of drag. Methods developed here allow for the magnitude of this drag force to be related to specific turbine array configurations. These two models were first combined in Vennell (2010) for unconstricted rectangular channels and have since been used in other works to develop fundamental turbine array theory for unconstricted rectangular channels (Vennell, 2010, 2011b, 2013, 2011a, 2012). Here this combined model is applied to constricted channels for the first time. In order to nest the turbine model into the channel model it is assumed that the cross-sectional area of the channel does not vary significantly over the turbine scale.

3.3.1 Channel types and constriction shapes

Three hypothetical channel examples were used in this study: (1) a large, inertia-dominated regular channel; (2) a small, friction-dominated regular channel; and (3) a large, inertia-dominated

Table 3.1: Details of the channel examples used in Chapter 3

Parameter	**Small channels**	**Large channels**	**Lagoon channels**
Length (L)	2 km	50 km	50 km
Max. Width (W_0)	500 m	10 km	10 km
Depth (h_0)	20 m	100 m	100 m
Max. Tidal head difference (Δ)	0.17 m	1.4 m	1.4 m
$\lambda_0 = C_\mathrm{D} L\hat{\alpha}/h_0$	4.5	0.30	0.30
Max. Transport (Q_0)	25.2 $\times 10^3 \mathrm{m^3 s^{-1}}$	$1.87 \times 10^6 \mathrm{m^3 s^{-1}}$	$1.19 \times 10^6 \mathrm{m^3 s^{-1}}$
$\hat{\alpha} = 8g\Delta/(3\pi\omega^2 L^2)$	18.1	0.24	0.24
Average potential ($\overline{P}^{\mathrm{max}}_{\mathrm{farm}}$)	3.4 MW	5.3 GW	3.9 GW
Turbines to fill (A_0/A_T)	25	2,500	2,500
A_s/β	0	0	$6 \times 10^9 \mathrm{m^2}/1.67$

lagoon channel (see Table 3.1).

The lagoon channel's parameters were specifically chosen to demonstrate that the potential of lagoon channels can increase with constriction factor (Chapter 2 and (Smeaton *et al.*, 2016)). This specific channel's potential peaks when the geometric factor $I \approx 1.33$ which corresponds to a constriction factor of $W_\mathrm{c} \approx 0.65$. The large and small regular channels are based on the unconstricted rectangular channels provided in Vennell (2012) but have Gaussian-shaped constrictions applied mid-length.

Constrictions are formulated using two symmetric Gaussian curves centered halfway along the channel's length (see Figure 3.2). These curves are similar to those used in Chapter 2 but have been expressed in dimensional units:

$$G_\mathrm{w}(x) = \frac{W_0 W_\mathrm{c}}{2} \exp\left[\frac{-25(L-2x)^2}{2L^2}\right]. \tag{3.1}$$

As in Chapter 2, W_c is the width constriction factor and is the width of "land mass" at the most constricted point of the channel relative to the channel width outside of the constriction (W_0). Thus, for a constriction that, at most, blocks the channel cross-section by 70%: $W_\mathrm{c} = 0.7$. As the constriction is made up of two of these curves (see Figure 3.2), the width of the channel at any point is $W = W_0 - 2G_\mathrm{w}(x)$.

In this study, the head difference across the channel ends is assumed to be constant and the flow velocity is allowed to vary. This results in unusually high velocities in some cases (4.4 $\mathrm{ms^{-1}}$ and 5.8 $\mathrm{ms^{-1}}$ for the most constricted cases tested). Another way of comparing channels

in this study would be to hold the peak-velocity constant by lowering the head difference accordingly. Additional simulations were conducted for this alternative problem formulation and are presented in Appendix A. They show that while this alternative formulation changes absolute power values, the trends and shapes of the power curves are unaffected.

Jet formation and flow separation effects (Old and Vennell, 2001) occurring at the exit of the constriction cannot be accounted for using our one-dimensional model but are addressed and quantified in Chapter 4 using a higher-order flow model.

3.3.2 Analytical turbine model

3.3.2.1 Isolated turbine in a channel

This section provides an overview of relevant methods derived in Garrett and Cummins (2007) for an isolated turbine in bounded channel flow.

Flow upstream of a turbine at Point 0 (Figure 3.1) has uniform velocity u_0 and uniform pressure p_0. As the flow passes in and around the turbine, it can be modelled as two streams: a through-turbine stream that passes through Points 1, 2, 3 and a bypass stream that passes through Point 4. Downstream of the turbines, the two streams mix together in a 'mixing zone'. Downstream of this mixing zone, at Point 5, uniform velocity and pressure are re-established.

This model developed for uniform, rectangular channels can be applied to constricted channels by assuming that the change in area across the row of turbines is negligible. This is an adequate assumption for the large channel where the cross-sectional area changes slowly with respect to channel length. This assumption may be less appropriate for small channels - an attempt to improve the accuracy of this model is provided at the end of these methods in Section 3.3.3 and results obtained using these methods are presented in Section 3.5.2.

Within the through-turbine stream, Point 1 is taken directly upstream of the turbine and Point 2 directly downstream of the turbine. Velocity is assumed to be constant between these points but there is a pressure drop across the turbine e.g. $u_1 = u_2$ and $p_1 > p_2$. Pressure of the through-turbine stream and bypass stream is assumed to be constant at Point 3 and Point 4 although the bypass flow will be faster than the through-turbine flow e.g. $u_4 > u_3$ and $p_3 = p_4$.

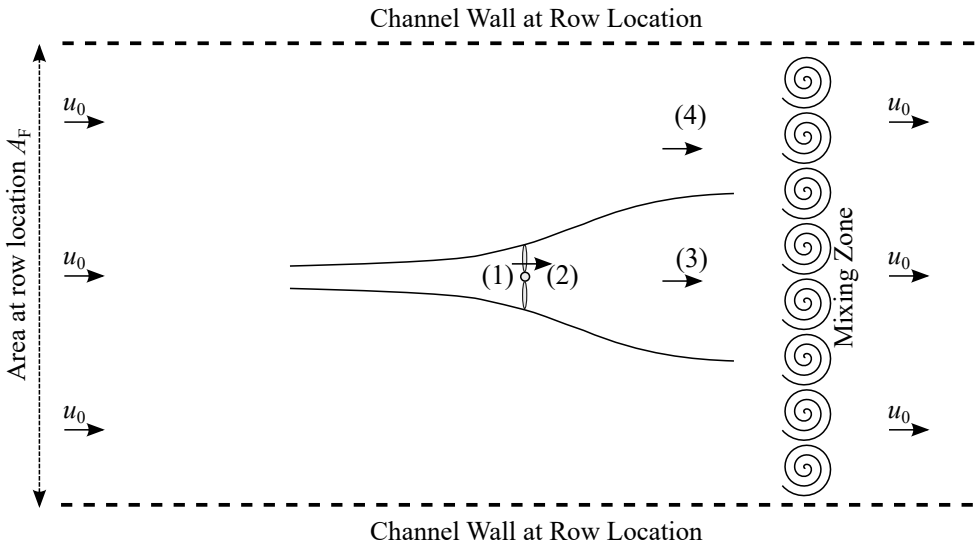

Figure 3.1: Actuator disc model for a single isolated turbine in a channel.

Continuity relationships for the through-turbine stream and bypass stream are respectively:

$$A_{\mathrm{T}}u_1 = A_{\mathrm{T}}u_2 = A_3u_3, \tag{3.2}$$

$$A_{\mathrm{R}}u_0 = A_3u_3 + (A_{\mathrm{R}} - A_3)u_4. \tag{3.3}$$

The latter relationship can be written as:

$$A_R(u_4 - u_0) = A_3(u_4 - u_3). \tag{3.4}$$

The force on the turbine can be calculated in two ways. The first way is by calculating the difference in the flow's momentum upstream of the turbine (Point 0) and downstream of the turbine (Points 3, 4):

$$F_{\mathrm{T}} = \rho(A_{\mathrm{R}}u_0^2 - (A_{\mathrm{R}} - A_3)u_4^2 - A_3u_3^2) + A_{\mathrm{R}}(p_0 - p_4). \tag{3.5}$$

An expression for $(p_0 - p_4)$ is obtained by taking Bernoulli at Points 0 and 4:

$$(p_0 - p_4) = \frac{1}{2}\rho(u_4^2 - u_0^2). \tag{3.6}$$

This can be substituted into (3.5) to give:

$$F_{\mathrm{T}} = \rho \left[\frac{1}{2} A_{\mathrm{R}} (u_0^2 - u_4^2) + A_3 (u_4^2 - u_3^2) decisions \right],$$

which after expansion gives:

$$F_{\mathrm{T}} = \rho \left[\frac{1}{2} A_{\mathrm{R}} (u_0 + u_4)(u_0 - u_4) + A_3 (u_4 + u_3)(u_4 - u_3) \right]. \tag{3.7}$$

Equation (3.4) can then be used to give:

$$F_{\mathrm{T}} = \frac{1}{2} \rho A_{\mathrm{R}} (u_4 - u_0) \left[u_4 + 2u_3 - u_0 \right] \tag{3.8}$$

The second way to calculate the force on the turbines is to take the pressure difference at Points 1 and 2 and multiply this by the cross-sectional area of the turbine:

$$F_{\mathrm{T}} = \rho A_{\mathrm{T}} (p_1 - p_2)$$

Expressions for p_1 and p_2 can be obtained by taking Bernoulli at Points 0 and 1, and Points 2 and 3 to give:

$$F_{\mathrm{T}} = \rho A_{\mathrm{T}} (\left[p_0 + \frac{1}{2} u_0^2 - \frac{1}{2} u_1^2 \right] - \left[p_3 + \frac{1}{2} u_3^2 - \frac{1}{2} u_2^2 \right]).$$

Knowing that $u_1 = u_2$, $p_3 = p_4$ and using relationship (3.6) yields:

$$F_{\mathrm{T}} = \frac{\rho}{2} A_{\mathrm{T}} \left(u_4^2 - u_3^2 \right) \tag{3.9}$$

Defining the blockage ratio of the turbine as the fraction of the channel's cross-sectional area that is blocked by the turbine device (e.g.$\epsilon_{\mathrm{T}} = A_{\mathrm{T}}/A_R$), and expressing velocities relative to the upstream velocity at Point 0 such that $r_k = u_k/u_0$ (where k corresponds to the point in Figure 3.1) gives:

$$F_{\mathrm{T}} = \frac{\rho}{2} \epsilon_{\mathrm{T}} A_{\mathrm{R}} \left(r_4^2 - r_3^2 \right) u_0^2. \tag{3.10}$$

This formula will be returned to later.

Meanwhile, the force expression of Equation (3.8) can be equated to (3.9) and solved for the relative velocity immediately upstream of the turbine:

$$r_1 = \frac{r_3(r_4 + r_3)}{r_4 + 2r_3 - 1}. \tag{3.11}$$

To find an equation for the relative velocity of the bypass flow, Equation (3.2) is first rearranged for A_3 and substituted into (3.3):

$$r_3(r_4 - 1) = \epsilon_{\mathrm{T}} r_1 (r_4 - r_3), \tag{3.12}$$

Then, Equation (3.11) is substituted into 3.12 to provide an expression for r_4 as a function of ϵ_{T} and r_3 only (Garrett and Cummins, 2007):

$$r_4 = \frac{1 - r_3 + \sqrt{\epsilon_{\mathrm{T}} - 2\epsilon_{\mathrm{T}} r_3 + (1 - \epsilon_{\mathrm{T}} + \epsilon_{\mathrm{T}}^2) r_3^2}}{1 - \epsilon_{\mathrm{T}}} \tag{3.13}$$

Now, returning to Equation 3.10, this can be rewritten in terms of channel flow rate Q and blockage ratio such that:

$$F_{\mathrm{T}} = \frac{\rho \epsilon_{\mathrm{T}}}{2A_{\mathrm{R}}} \left(r_4^2 - r_3^2\right) |Q| \, Q = \frac{\rho C_{\mathrm{F}}}{A_{\mathrm{R}}} |Q| \, Q \tag{3.14}$$

where $C_{\mathrm{F}} = \frac{\epsilon_{\mathrm{T}}}{2}(r_4^2 - r_3^2)$. The instantaneous power lost by the flow to the single turbine (available power) is this force multiplied by the velocity at Point 1:

$$P_{\mathrm{avail,T}} = \rho r_1 \frac{C_{\mathrm{F}}}{A_{\mathrm{R}}^2} Q^3. \tag{3.15}$$

Averaging over a tidal cycle and expressing with non-dimensional variables gives:

$$\overline{P}_{\mathrm{avail,T}} = \frac{\rho}{2\pi} r_1 \frac{C_{\mathrm{F}}}{A\prime_{\mathrm{R}}^2 A_0^2} Q_{IU}^3 \int_0^{2\pi} |Q'(t')|^3 \, dt', \tag{3.16}$$

which when assuming Q' has form $Q\prime = Q_0 \sin t\prime$ integrates to:

$$\overline{P}_{\text{avail,T}} = \frac{4\rho r_1 C_F Q_{IU}^3 Q_0^3}{3\pi A_R{}'^2 A_0^2} \tag{3.17}$$

Defining $P_{IU} = \frac{2\rho Q_{\text{IU}}^3}{3\pi\hat{\alpha}A_0^2}$ such that $\overline{P}_{\text{avail,T}} = \overline{P}'_{\text{avail,T}} P_{IU}$ can be rearranged to give the simple expression:

$$\overline{P}'_{\text{avail,T}} = 2r_1\lambda_{\text{F}}Q_0^3. \tag{3.18}$$

where $Q_{\text{IU}} = \frac{g\Delta A_0}{\omega L}$ and $\hat{\alpha} = 8g\Delta/3\pi\omega^2 L^2$.

3.3.2.2 Application to multiple rows of multiple turbines

Provided turbines are evenly spaced in a row along a cross-section and flow is uniform, the above methods can be applied to multiple turbines in the same row. The bypass velocity u_4 effectively creates a virtual wall on adjacent turbines and methods for bounded flow still apply (Figure 3.2). Additionally, assuming the velocity recovers between upstream/downstream rows, this model can be applied to a multi-row array and used in the channel model as a sum of force impulse functions. Figure 3.2 provides a schematic overview of how the single actuator disc model is used to model a row of M turbines and how this is in turn used in the channel model.

The drag coefficient ($C_{\text{R}i}$) [Equation 3.19] for the i^{th} row of turbines in an array constituting n_{R} rows of turbines is thus:

$$C_{\text{R}i} = \frac{\epsilon_i}{2}(r_{4i}^2 - r_{3i}^2) \tag{3.19}$$

where the row blockage factor $\epsilon_i = M_i A_{\text{T}}/A_{\text{R}i}$ is used and M_i is the number of turbines in the i^{th}row. A_{T} is the blade swept area of one turbine which is set to 400m^2 [based on the SeaGen turbine (Douglas *et al.*, 2008)]. Note that the calculation of the drag coefficient is insensitive to the turbine area because it depends only on the row blockage factor. Changing the blade swept area would change only the theoretical number of turbines required to achieve a given blockage ratio. The relative velocity in the bypass flow of the i^{th} wake, r_{4i} is then (Garrett and Cummins, 2007):

$$r_{4i} = \frac{1 - r_{3i} + \sqrt{\epsilon_i - 2\epsilon_i r_{3i} + (1 - \epsilon_i + \epsilon_i^2)r_{3i}^2}}{1 - \epsilon_i}. \tag{3.20}$$

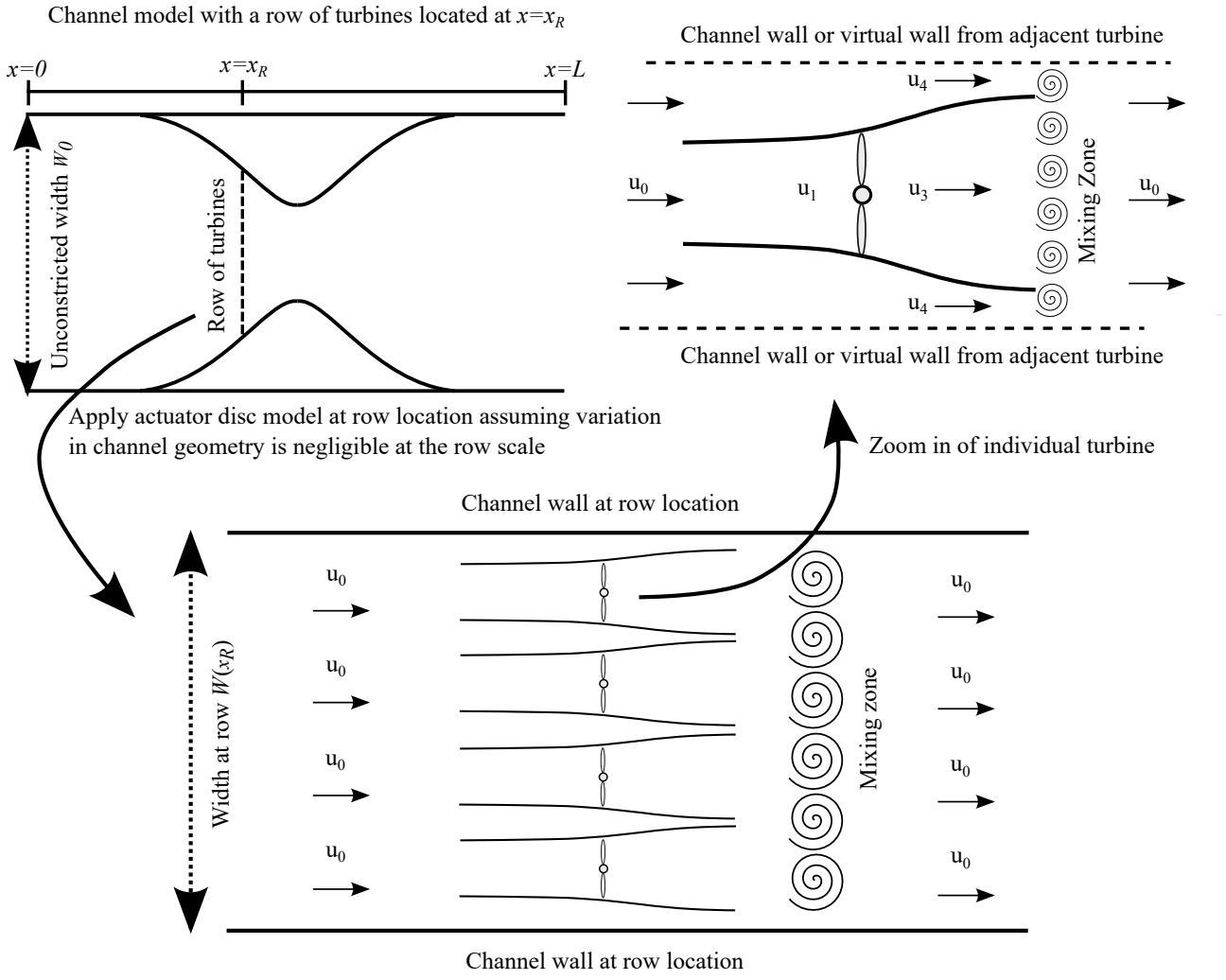

Figure 3.2: Application of the actuator disc model into the constricted channel model. Velocities in the zoomed-in view of the row of turbines show the points of reference referred to in the actuator disc equations

Note the singularity at the point where the blockage ratio equals 1. Subsequently, the model was only run with blockage values of up to $\epsilon_i = 0.99$. The relative velocity through the turbines is then:

$$r_{1i} = \frac{r_{3i}(r_{4i} + r_{3i})}{r_{4i} + 2r_{3i} - 1}. \tag{3.21}$$

By combining these equations with the channel model, the non-dimensional power available for electricity generation averaged over a tidal cycle for the array of n_{R} rows is:

$$\overline{P}'_{\mathrm{avail}} = \left(\sum_{i=1}^{n_R} 2r_{1i} \frac{C_{\mathrm{R}i}}{A'^2_{\mathrm{R}i}} \right) \hat{\alpha} Q_0^3, \tag{3.22}$$

which again can be converted into dimensional units using:

$$\overline{P}_{\mathrm{avail}} = \frac{2\rho Q_{\mathrm{IU}}^3}{3\pi \hat{\alpha} A_0^2} \overline{P}'_{\mathrm{avail}}, \tag{3.23}$$

Figure 3.3 shows, that as blockage ratio increases for a row of turbines, the optimal tuning changes to minimise the force put on the turbine devices. The difference between the upstream and downstream velocity gets smaller (r_3 increases). Increases in blockage ratio without tuning cause the force on the turbines to become too great, resulting in a reduction in flow rate. Turbines must be tuned, or their design changed to achieve the optimal r_3 when increasing the blockage of a row. In contrast to what one would necessarily think, decreasing the thrust coefficient increases the power generated by the row of turbines (Figure 3.3)

Note that Vennell (2012) also calculates the power lost to support structures on the turbines which are not accounted for here - Vennell (2012) estimates these losses can be between 10 and 15% of the power available. A further potential caveat is that the derivation of these equations is for an unconstricted channel and assumes that the Froude number of the flow is small e.g. $\mathrm{Fr} = u/\sqrt{gh} \ll 1$. In this study, velocities in the constricted region, particularly those in the turbine by pass flow, may be sufficiently high that this is not the case. Whelan *et al.* (2009) and Houlsby *et al.* (2008) derive similar actuator disc models which account for non-zero Froude number flow. A summary of these equations and a sensitivity analysis of these results and the model used here is given in Appendix 5.3. Non-zero Froude number effects were found to be insignificant except at high blockage ratios.

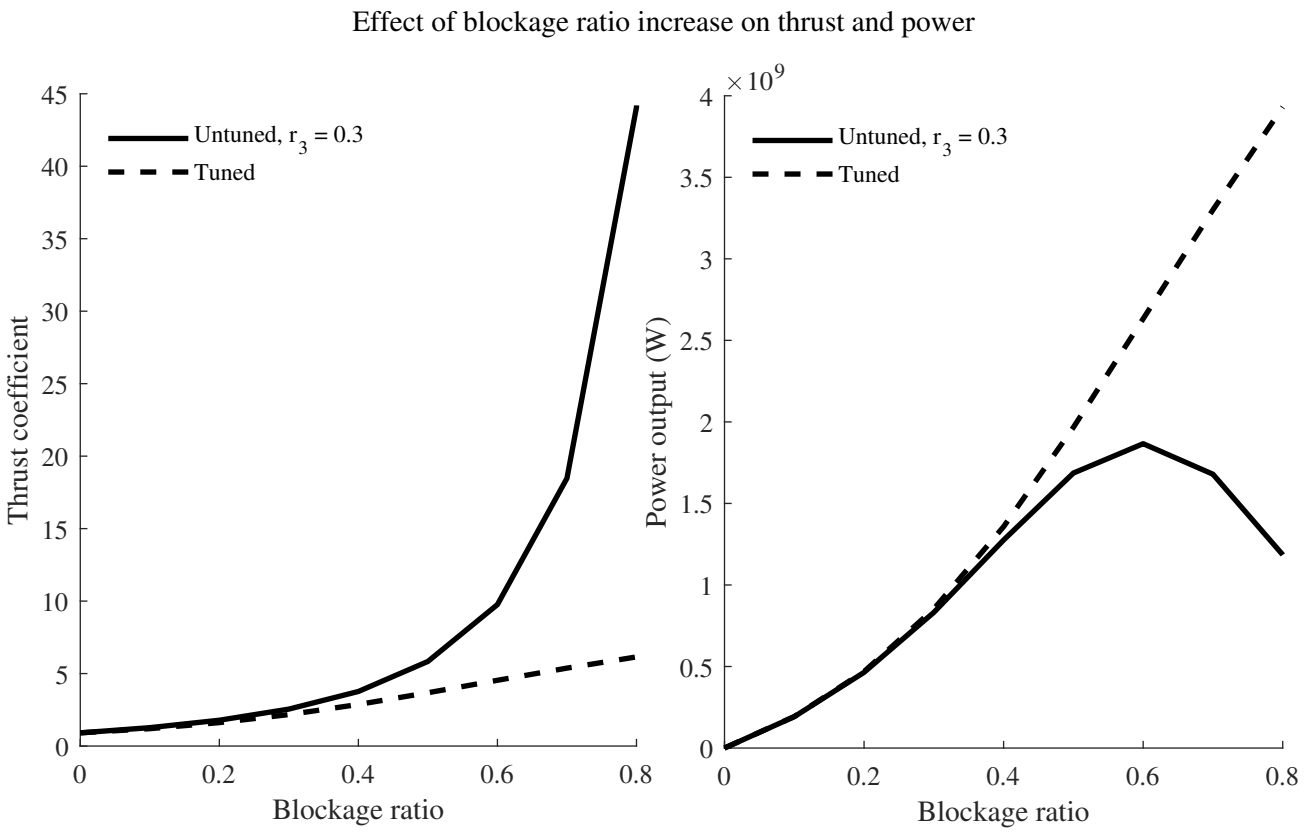

Figure 3.3: Thrust coefficient and row power output for an untuned and tuned row of turbines in a large, constricted channel ($W_c = 0.4$) using methods described here and the preceding section.

3.3.3 Multi-row velocity deficit model

In the last section of this chapter, a downstream velocity deficit is applied to the upstream turbine row to look at how this may influence results. Downstream of a row of turbines, the flow that passes through the blade-swept area and the bypass flow mix together until uniform flow is re-established. Throughout this mixing zone, relative flow velocities behind the blade-swept area recover from a value of r_3 back to 1 which indicates the point at which flow is once again fully uniform across the cross-section. Here we represent this process in its simplest form by applying a recovering velocity deficit behind the row of turbines. This is implemented by adapting a simple wake model given in Katic *et al.* (1986) for wind turbines so that the relative velocity at a distance of four turbine diameters ($4D_{\mathrm{T}}$) downstream of a row of turbines is equal to the r_3 value of that row and the velocity deficit is more or less recovered at a distance of $40D_{\mathrm{T}}$. Assuming a blade swept area of 400 m^2 (and thus a diameter of 22.6 m), these distances are approximately 90 and 900 m, respectively (c.f. channel lengths of 50 km and 2 km for the large and small channels, respectively). These values are reasonable when compared to recovery curves given in Malki *et al.* (2014) using a more sophisticated model. We do not attempt to represent the velocity of the flow any closer than four turbine diameters downstream of the turbines. The relative velocity downstream of a single row of turbines is calculated using:

$$r_{\mathrm{W}i}(x,t) = Z_i \frac{1-(1-r_{3i})}{1+(\frac{k(x_{\mathrm{D}}-Z^{\pm}4)}{\mathrm{D_T}})^2}, \tag{3.24}$$

where

$$Z_i = Z^{\pm}\frac{\tanh(S(x-x_i)+1)}{2}$$

and

$$Z^{\pm} = \tanh(SQ').$$

Here, $r_{\mathrm{W}i}$ is the varying relative velocity associated with the wake mixing process, Z_i is the activation function for the wake of the i^{th} row of turbines which oscillates between a value of 1 and 0 to switch the deficit equation on downstream of x_i (where the row of turbines generating the deficit is positioned) and $Z^{\pm}$ is a second activation function, which switches sign with the flow direction. $Z^{\pm}$ oscillates between a value of 1 and -1 when the flow is positive or negative

and ensures the wake is travelling in the correct direction. Both of these activation functions were necessary to keep the function differentiable so that optimisation could be completed. S controls the steepness of the transition in the hyperbolic functions and a greater value of S corresponds to a more instantaneous transition. A value of $S = 10^{99}$ is used to make the transition as instantaneous as possible while still keeping the function differentiable. x_{D} is the distance in turbine diameters downstream from the row of turbines inducing the wake, D_{T} is the length of one turbine diameter which is set at 22.5m (based on backwards calculation from the SeaGen turbine) and k is some constant value. Katic *et al.* (1986) use a value of $k = 0.22$ for a single isolated wind turbine which, despite the difference in applications, was also used here as it works well to give the target recovery distance of $40D_{\mathrm{T}}$. This velocity deficit model holds provided turbines in the downstream row are in line with the upstream row e.g. in a non-staggered arrangement. It is acknowledged that there are limitations to this method but for the purpose of applying a penalty for placing turbine rows too close together in a systematic 1-D study such as this, it is deemed sufficient. Typical velocity profiles for an unconstricted and a constricted channel are provided in Appendix D (Figure 5.7) with this model applied. Note that this model makes no new assumptions about the energy lost by array-wake mixing, only where it takes place.

3.4 Constriction and power from a single row

The turbine/channel model (without velocity deficit) was optimised for a single row array ($n_{\mathrm{R}} = 1$) with respect to a constant tuning parameter r_3 to maximise the average power over a tidal cycle for a given row location (x_{R}) and number of turbines (n_{T}). The row tuning parameter, r_3, was limited to a constant value for the entire row (e.g. invariant with time) for the three base channels given in Table 3.1 with three different constriction factors each. This tuning approach for constant r_3 is referred to as the patient-tuning strategy (Vennell, 2016) and has been shown to be more effective than maximising instantaneous power with time (impatient-tuning strategy) but less effective than optimising how r_3 varies in time to maximise average power (smart patient-tuning strategy). Vennell (2016) incorporated smart patient-tuning into a one-dimensional model for a uniform rectangular channel by representing the tuning as a

Fourier series in time and optimising the Fourier coefficients via adjoint methods. Due to the complexity of this procedure and the additional computational effort that would be required, this approach was not adopted here.

3.4.1 Using the smallest cross-section maximises power

In all cases, power was maximised by first placing turbines in the narrowest cross-section where they can (1) achieve the greatest blockage ratio and (2) take advantage of high flow speeds, (Figure 3.4). These are henceforth termed the *blockage advantage* and the *velocity advantage,* respectively. As more turbines were added to the array, the optimiser continued to place the row of turbines in the most constricted part of the channel until the number of turbines in the row was sufficient to completely block the cross-section. Further adding turbines to the row forced the solver to move the row outside of smallest cross-section while maintaining the condition $\epsilon = 1$.

The globally optimal solution was obtained by completely filling the smallest cross-section. Beyond this point, the output of the array ceased to increase and in some instances decreased slightly. GC07 defined the condition for channel potential as "100% blocking the cross-section with a single row of turbines" - this condition can be generalised for constricted channels to "100% blocking the *smallest* cross-section with a single row of turbines". While a blockage ratio of $\epsilon = 1$ is unrealistic, it shows how power is optimised in the absence of practical and environmental constraints. In real channels such as Cook Strait, achieving such a feat would require 8,000 turbines. Indeed, to block only 5% of the cross-section would require 403 turbines. Arrays this large are a long way away from development, but this does not mean understanding tidal energy generation at such scales is unimportant or that these blockage ratios may not be achieved using novel types of turbines.

As a general rule, power is optimised by placing a row of M turbines where it will achieve maximum blockage which, in this case, also corresponds to maximum velocity.

Figures 3.5a, b, c show the maximum power available from an optimised row of turbines (with respect to position and tuning) in the small, large and lagoon channels with constriction factors of $W_c = 0$, 0.4 and 0.7. All power curves exhibit an initial period of increase before plateauing

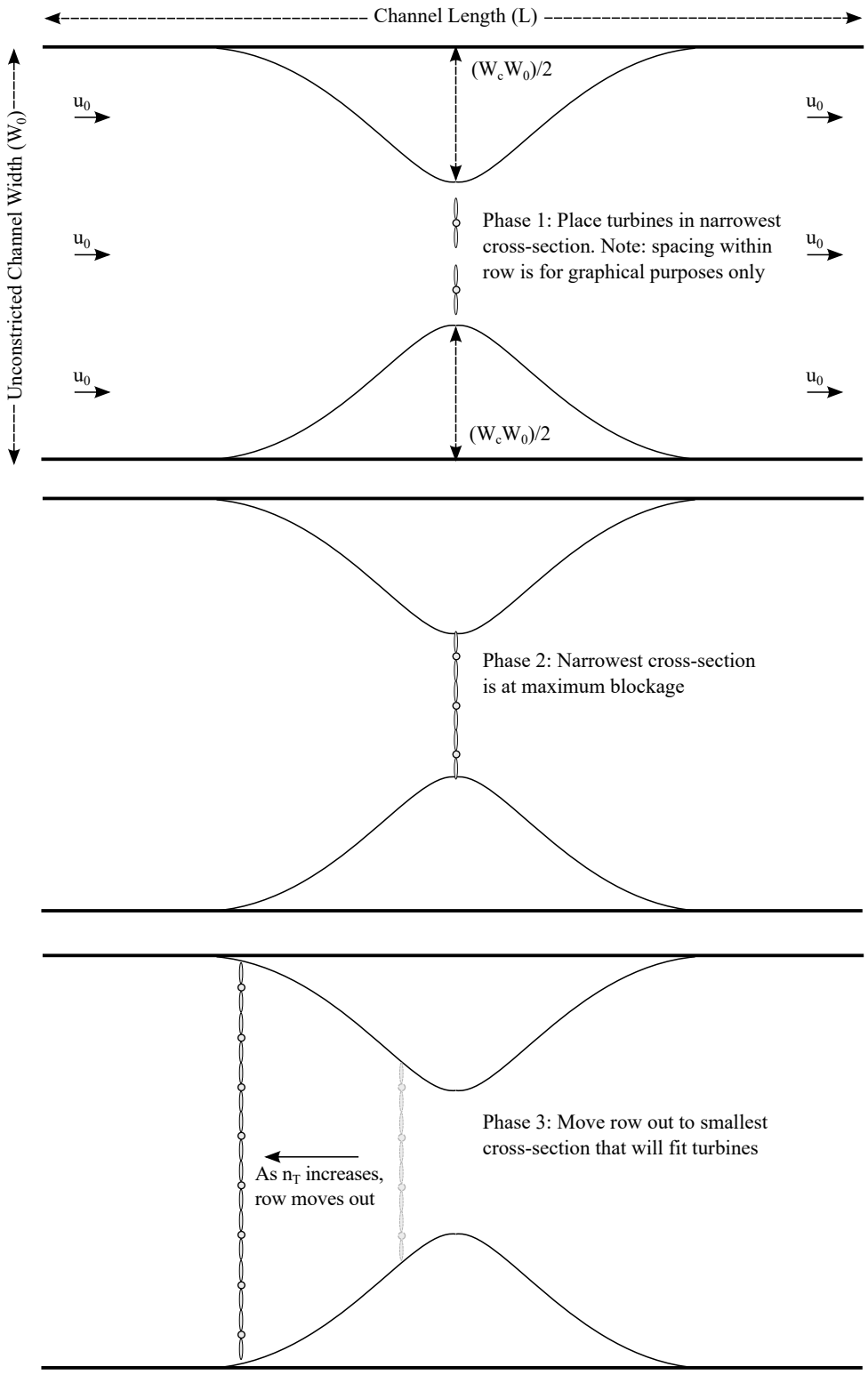

Figure 3.4: Sketch showing the optimal row location that maximises power output as the number of turbines in the row is increased

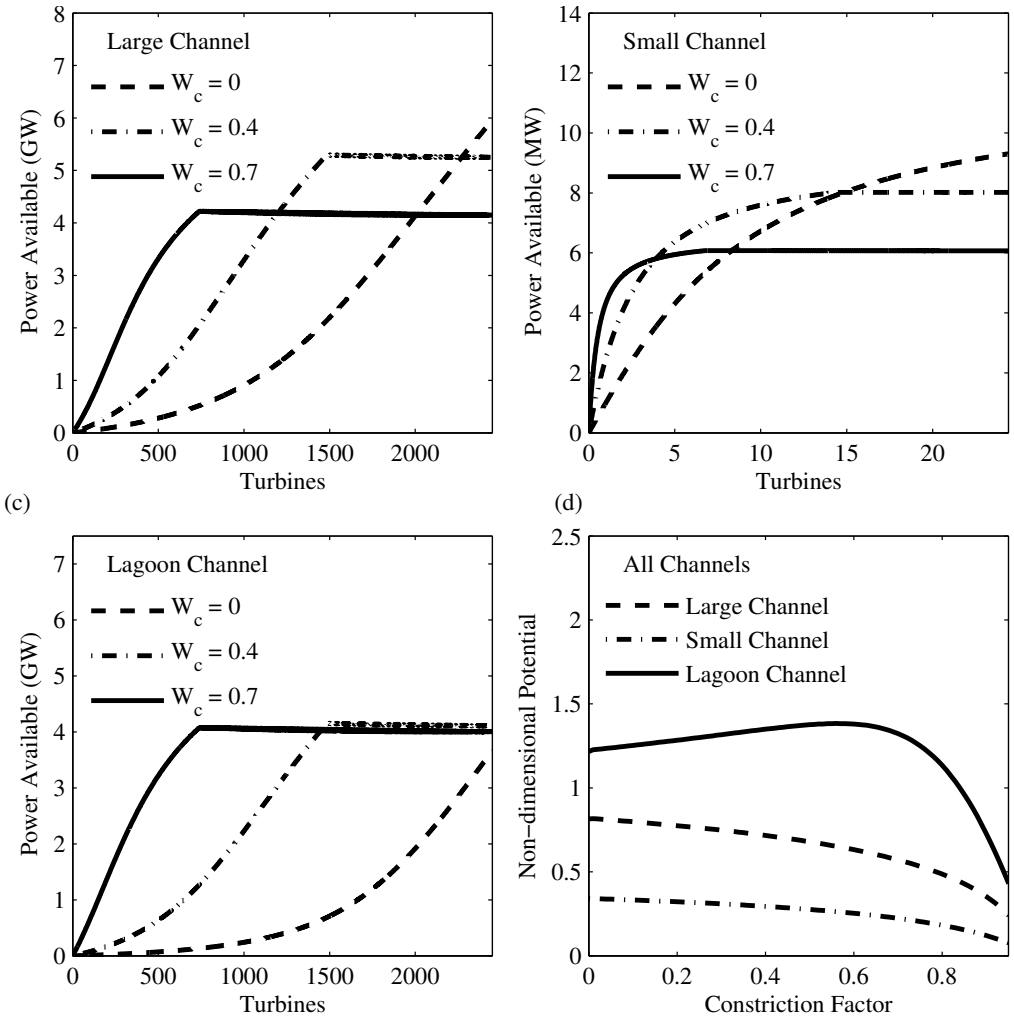

Figure 3.5: Plots (a) to (c) show the maximum available power generated by a single row of turbines for the three example base channels with the three different constriction factors. Plot (d) shows how the maximum available power varies with constriction factor for the three example channels.

Table 3.2: Optimal farm location for an array of M turbines where M_f is the number of turbines to fill the smallest cross-section and M_max is the number of turbines required to fill the largest cross-section

Number of Turbines	Optimal Row Location	Power Curve Phase
0 to $M_\mathrm{f} - 1$	smallest cross-section	Growth
M_f	smallest cross-section	Maximum
$M_\mathrm{f} + 1$ to M_max	smallest cross-section possible	Plateau/Slight Decline

at some maximum value and in some cases slightly declining. As the blockage ratio approaches $\epsilon = 1$, r_4 approaches infinity and thus to manoeuvre around this singularity, only blockages of up to 0.99 were simulated (see Equation 3.20). The slight decline in the plateau is due to the array being moved outside of the cross-section and consequently generating from lower flow velocities. That is, the velocity advantage associated with using the narrowest cross-section is lost. These results are summarised in Table 3.2 and Figure 3.4.

3.4.2 Constricted channels produce more power from fewer turbines but less at high blockage

Turbines placed in the narrowest cross-section benefit from a velocity advantage (discussed in the preceding section) but also benefit from a *blockage advantage* which is more profound. A row of M turbines placed in the smallest cross-section generates significantly less power if placed outside of this zone. The size of the blockage advantage increases with constriction factor as the difference in cross-sectional areas between the smallest cross-section and the rest of the channel becomes more stark.

Figures 3.5a, b show power curves for optimally configured arrays in the large and small regular channels. When the total number of turbines in the array is few, significantly more power is generated by arrays in the constricted channels ($W_\mathrm{c} = 0.4$, $W_\mathrm{c} = 0.7$). As turbines are added to the array, the output of these arrays becomes limited by these channels' lower potentials and this advantage is lost.

Power curves for the small channels reach their limiting potential faster than larger channels due to the difference in power curve concavities exhibited by the two different-sized channels. The consequence of a concave-down power curve (the small channels) is that most of the array power is generated from the first installments of power at the cost of diminishing return on power per

turbine added thereafter. This is beneficial to developers as it means that few turbines placed in small constricted channels will realise a significant proportion of the channel's potential. Conversely, the upwards concavity of the large channel arrays mean they experience a sort of delayed gratification. The power return from each additional turbine is relatively low at first and increases as turbines continue to be added to the row. Once a significant portion of the channel's cross-section is blocked, the power return on additional turbines (the gradient of the curve) starts to increase. This is due to less flow being able to bypass the turbine array.

The power curve for the most constricted large channel experiences a change in concavity as turbines are added to the array. This highlights the underlying mechanism that dictates the shape of these power curves: the dominance of drag in the channel. The other large channels are inertia-dominated whereas the small channels are all drag-dominated. In the modelled scenarios, two factors act to increase drag: (1) the addition of a constriction causes velocities to increase and thus drag losses and (2) the addition of more turbines to an array. The most constricted large channel is still inertia-dominated while the array is small but as turbines are added, there is a transition point (inflexion point) where the drag in the channel becomes sufficiently high that the channel behaves analogously to the small channel cases.

3.4.3 Lagoon channels behave similarly to regular channels

The above discussion does not hold for the resonant lagoon example (Figure 3.5(c, d)). As discussed in the preceding chapter, some lagoon channels can be geometrically tuned to increase power output (Smeaton *et al.*, 2016). The example lagoon channel used in this study was specifically chosen to demonstrate this. The array power for this lagoon channel was seen to peak at the same degree of constriction as did its potential ($I \approx 1.33$ or $W_c \approx 0.65$). The lagoon-potential effect distorts the relationship between the number of turbines, the available power, and constriction factor. That aside, results from the lagoon channel otherwise mirror those of the large channel in terms of curve shape and optimal array configuration. The change in concavity of the highly constricted case ($W_c = 0.7$) is also shared between regular and lagoon channels. Due to the similarity in the behaviour of these two channels the lagoon channel will be removed from further discussions and it is assumed that turbine array theory derived for regular channels is applicable to lagoon channels with the caveat that absolute power output

will depend on how geometrically tuned the channel is.

3.4.4 For reasonable blockage ratios the same power can be generated anywhere in the channel using more/fewer turbines

While the constricted region offers the most power generation per turbine, the same amount of power can be generated elsewhere using a greater number of turbines. While it may seem illogical to use more turbines than are required to generate some quantity of power, it may be necessary to do so for economic, legal or technological reasons. In particular, turbines positioned outside of the constricted area can be built to a less robust standard. The favourability of the constricted region is due to the dual benefits of the blockage effect and the velocity effect and so, outside of this region, not only is one penalised by requiring more turbines to achieve the same blockage ratio but one also needs to block more of the channel to compensate for the lack of velocity advantage. Figure 3.6 shows power curves for rows of turbines inside (black) and outside (grey) of the constriction. Blockage ratio has been plotted on the x-axis rather than the number of turbines to illustrate the magnitude of the velocity effect. At the same blockage ratio, a row of turbines in the channel narrows will generate more power than one of equal blockage ratio in the unconstricted region. Or as formulated in the discussion above, a row outside of the constriction must block more of the cross-section to achieve similar power to one inside the constriction.

Intuitively, it may seem odd that the load on the turbines can decrease while the array power increases but this is the magic of tidal turbine tuning. By tuning the row of turbines to achieve the correct ratio of downstream to upstream velocity (e.g. r_3), the force on the turbines is decreased but power output still increases as higher flows are maintained with the smaller drag coefficient (see Figure 3.3). Turbines in the fast flowing constricted region must still withstand greater loads than rows of equal blockage situated outside of the constricted region (Figure 3.6(b,d)). This is most significant in the highly constricted ($W_c = 0.7$) small channel at very low blockage ratio (i.e. the first few turbines installed). Here, the difference in power output between the inside and outside arrays is roughly a factor of three but the force per turbine differs by about a factor of five. The peaks in the load curves (Figure 3.6(b,d)) correlate to the stages of the farm's development where power return on additional turbines is highest

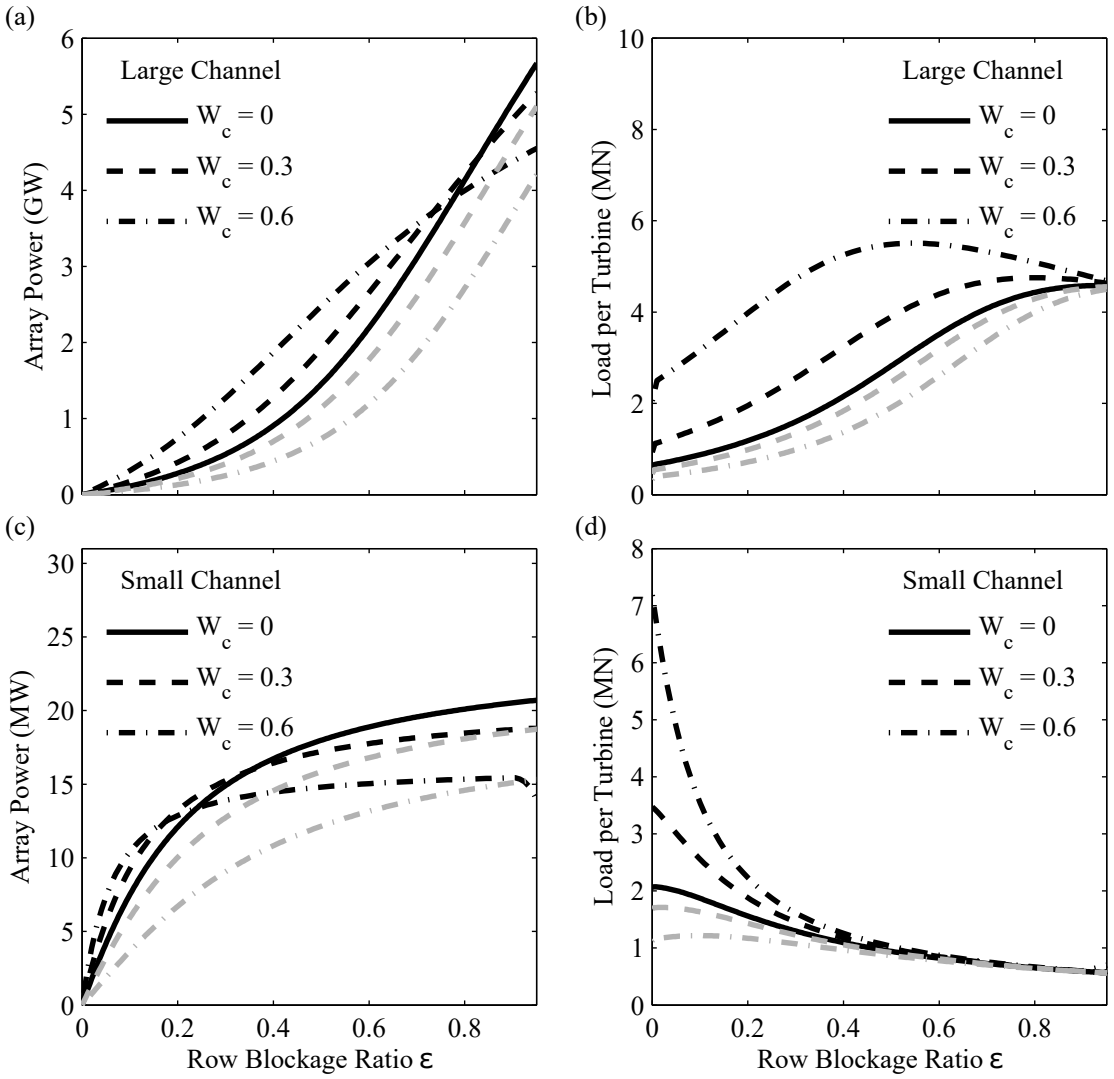

Figure 3.6: Array power and average load per turbine from arrays with a single row in the smallest cross-section (black lines) and outside of the constriction (grey lines). Row blockage ratio is plotted on the x-axis. Lines shown are for an unconstricted channel base case (solid lines), a medium degree of constriction (even dash) and a high degree of constriction (alternating dash).

(described above in Section 3.4.2). For small channels, this is close to the farm's inception. In larger channels, this occurs much later on in development process. Turbine loads converge as the cross-sections are filled and the flow in the channel is reduced. The sensitivity of load to the location of the row is more important in small channels when the blockage ratio is low but is largely insensitive to blockage ratio in larger channels.

3.4.5 Power-to-force ratio suggests the smallest cross-section is the most economic

The array design that maximises power output may not be the best array for developers. The previous section highlights that turbines must be built more strongly to withstand higher loads if placed in the narrowest cross-section. While on the surface this suggests higher construction costs, it is possible that the power returned from using this region will outweigh this cost. If all turbines have the same external dimensions (e.g. blade length, blade diameter, support structure geometry) then it follows that turbines subject to greater loads will need to have thicker external shells. These turbines will require more raw materials to build and consequently weigh more. Manwell *et al.* (2010) showed that in the wind industry, the costs of individual wind turbines were roughly proportional to their weight and it is on this premise that Vennell *et al.* (2015) introduced a turbine economic efficiency index (TEEI) which considers the power-to-force ratio of the turbines (P_1/F_1).

$$\text{TEEI} = \left(\frac{k_\text{p}}{k_\text{c}}\right)\left(\frac{P_1}{F_1}\right) \tag{3.25}$$

Here k_p is the dollar income per watt of power generated and P_1 is the power generation in watts of one turbine. k_c is the dollar cost to build a fixed size turbine per Newton load and F_1 is the load on each turbine. Although an imperfect indicator, the TEEI allows us to make a rudimentary assessment of array economics. Of course, the true economics of a project will depend on a myriad of additional factors (such as channel depth, cable lengths, grid proximity) and thus the TEEI should be viewed as a preliminary indicator of how farm design may influence economics. Quantifying the income/cost variables; k_p and k_c, is difficult and beyond the scope of this thesis. However, if one normalises the TEEI against a single isolated turbine in an unconstricted channel (denoted with subscript U) then the normalised TEEI is equivalent to the normalised power-to-force ratio (PFR). That is:

$$\text{PFR} = \left(\frac{k_\text{p}P_1}{k_\text{c}F_1}\right) / \left(\frac{k_\text{p}P_{1\text{U}}}{k_\text{c}F_{1\text{U}}}\right) = \frac{P_1/F_1}{P_{1\text{U}}/F_{1\text{U}}} = \frac{r_1}{r_{1U}}.$$

The normalised power-to-force ratio (PFR) is presented in Figure 3.7 for both the large (left

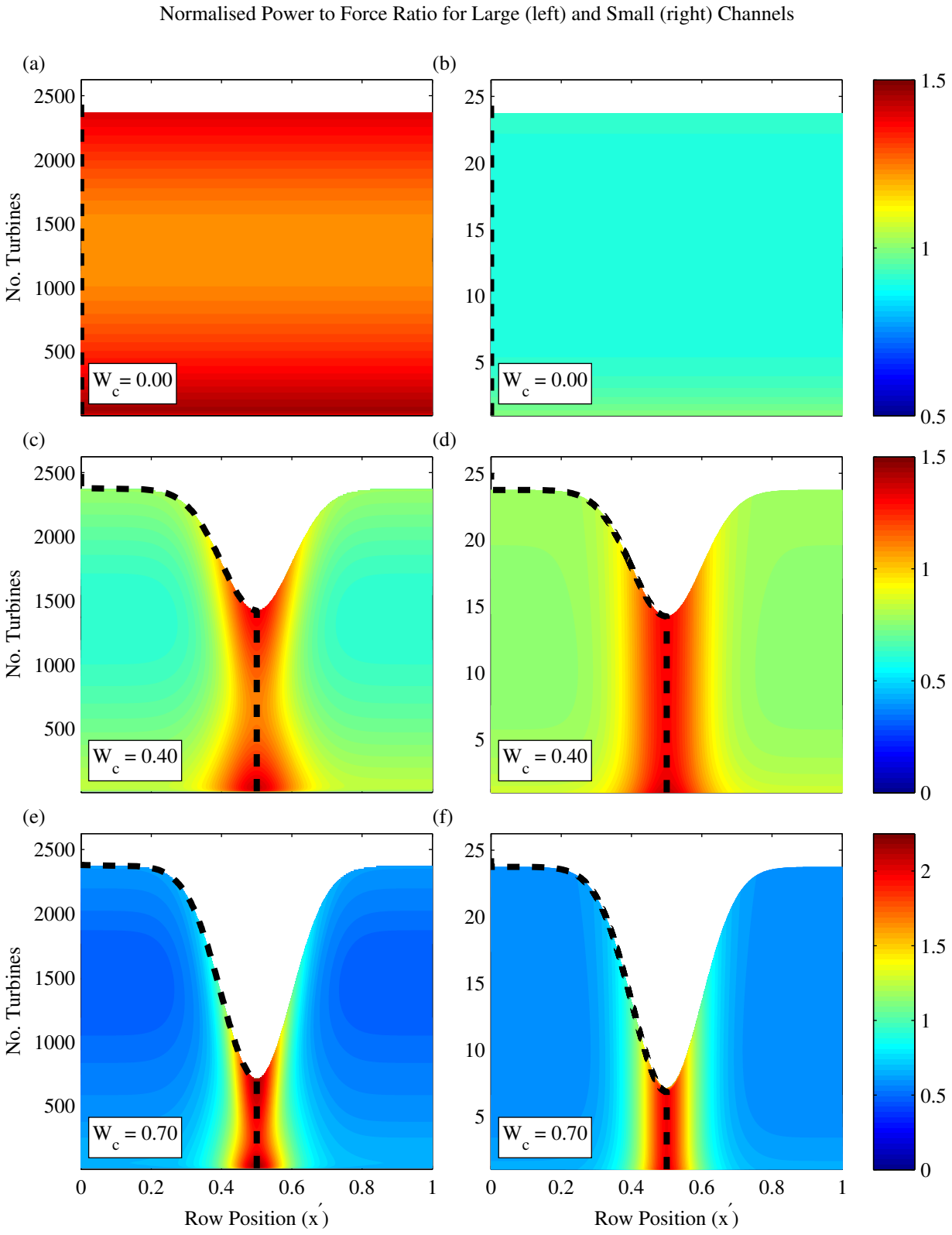

Figure 3.7: Power- to-force ratio of array configurations for large and small channels relative to that of a single isolated turbine in an unconstricted channel of the same maximum dimensions. Dashed lines show the optimal row position for a given number of turbines that maximises the ratio.

column) and small (right column) channels. The y-axis of plots in Figure 3.7 corresponds to the number of turbines in the row and the x-axis of the plots corresponds to the position of the row in the constricted channel. The optimum PFR for any number of turbines is plotted with a black dashed line. PFR is maximised by placing turbines in the most constricted region for both channels until the number of turbines exceeds the cross-sectional area of the row and then the best design is the next smallest cross-section. That is, the array configuration that maximises PFR is a mirror of that which maximises available power. This suggests that although turbines in the constriction are subject to greater loads, the additional cost of construction may well be compensated by increased power production. The lagoon channel is not shown but trends exhibited by this channel are similar to those of the big channel. Of course, the true economics will depend on the values and shape of k_p and k_c.

In large channels, Figure 3.7 shows an initial diminishing return on adding turbines to a row until the row approaches 100% blockage where the return on PFR increases again to the same value it was initially. This increase in PFR as the row is filled to 100% blockage is associated with the delayed gratification in power per turbine discussed in Section 3.4.2. In shallow, friction-dominated channels the PFR decreases suddenly as the first few turbines are added to the row before plateauing to a near-constant value due to the initial high power return period of these channels. Based on PFR, the economics of filling a smaller channel are hardly changed with respect to how much of the channel is blocked. That is, the return on adding turbines to a row in these channels is largely the same as the return on the first turbine.

3.4.6 Additional factors

This section outlines how the optimal r_3 of constricted channels differs from unconstricted channels as well as how constriction affects flow rate reduction at maximum available power.

3.4.6.1 Optimal tuning depends on the cross-section

The left hand column of Figure 3.8 shows the optimal r_3 tuning parameter for all the test channels. Black lines correspond to a single row in the narrowest cross-section while grey lines correspond to a row placed outside of the constriction. Despite these rows having different

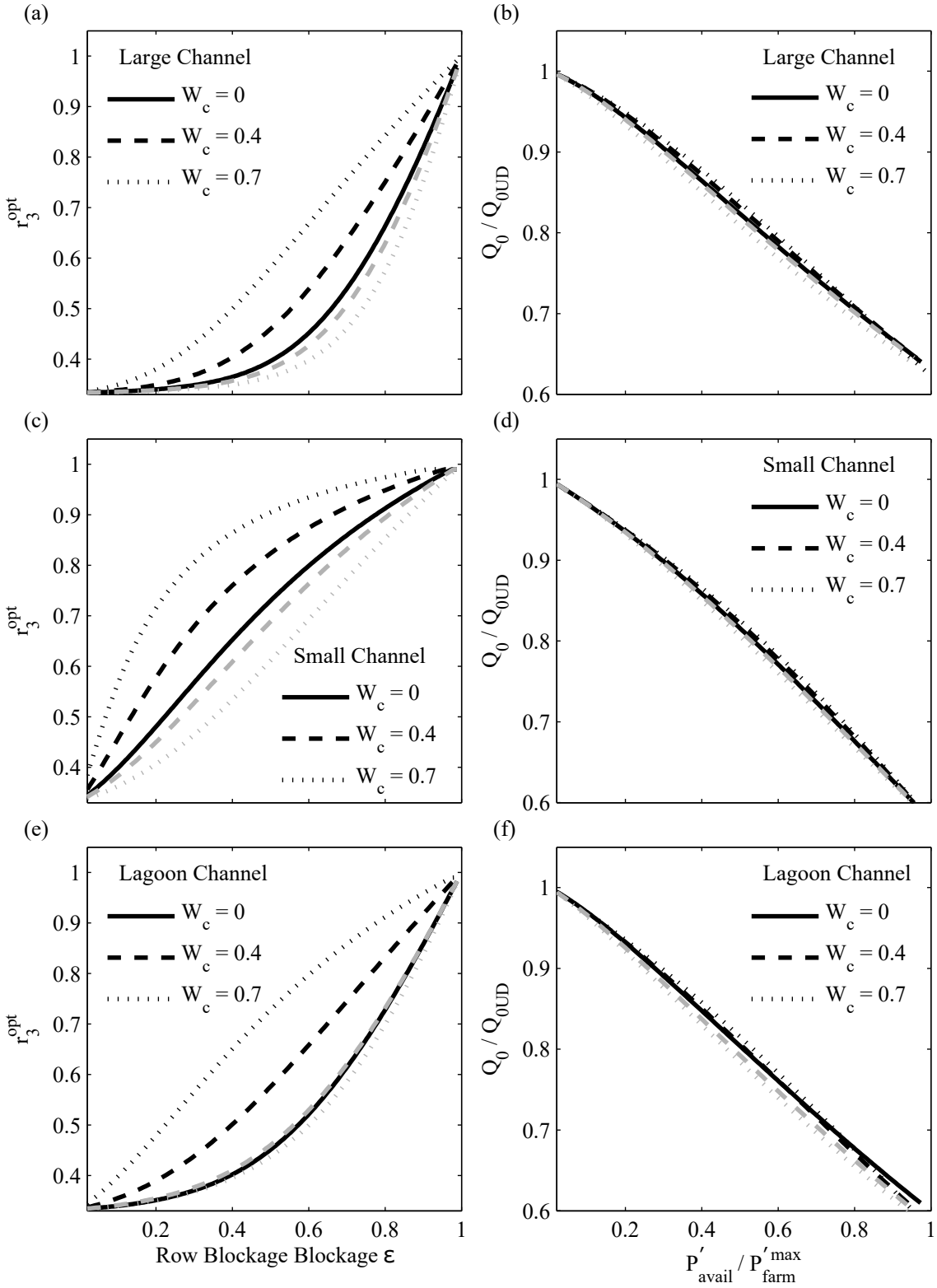

Figure 3.8: Optimal r_3 tuning for a given row blockage (left hand columns) and flow rate reduction versus relative power (right-hand columns) for the three example channels. Increasing degrees of constriction cause little change in the behaviour of optimal r_3 for a given channel blockage.

concavities for the small and large channels, the general upward nature is conserved. Analogous to results presented in Section 3.5, the highly constricted large channel behaves similarly to the small channel cases due to the increasing dominance of drag in the channel as turbines are added to the array. Rows of turbines placed inside the high velocity, constricted region of both channels require higher r_3 tuning than would be predicted by the model if the constriction was not considered. Relative to the unconstricted channel, rows of turbines positioned outside of the constricted area require slightly lower r_3 tunings except in the lagoon channel where they are slightly higher.

3.4.6.2 Flow reduction is invariant to array location

Channel transport and power production are closely interrelated. The right-hand column of Figure 3.8 shows the flow rate relative to the undisturbed flow rate versus power as a fraction of channel potential. Trends observed in Figure 3.8 show that flow rate in these channels reduces quasi-linearly as more power is extracted. Flows through these channels converge to a value 0.6 times the undisturbed value when all the available power is extracted by the farm (channel potential). The degree of flow reduction relative to power output is almost invariant to constriction factor for the three channels shown.

3.5 Constriction and power from multiple fixed rows

Analysis is now extended to arrays of multiple rows - results here also apply to situations where two developers are operating in the same channel. Results in Section 3.4 suggested that the most constricted part of the channel is the best location to place a single row of turbines for both power production and economy. Whether this still holds when more than one row of turbines is operating in the channel remains unclear. Should a two-row array place one row of turbines in the narrowest cross-section to take full advantage of the increased blockage and velocity effects? If a minimum row spacing is enforced this will mean the second row must be positioned farther away from this high value area. Perhaps a more optimal array layout is two-rows placed equidistantly from the smallest cross-section. If a navigable strip must be left open for the passage of vessels this will prevent rows from being filled. This section compares

the power production of these two scenarios. The first configuration that makes use of the smallest cross-section is referred to as the "odd" configurations while arrays that have two-rows spaced equidistantly from the smallest cross-section is referred to as the "even" configuration (Figure 3.9).

Analysis is first given to multi-row arrays in the absence of a velocity deficit penalty (Section 3.5.1). Following this, the velocity deficit model described in Section 3.3.3 is adopted for the case of two-rows.

3.5.1 Even vs. odd arrays: a trade-off between array power and turbine power

3.5.1.1 Constraining the problem

There is no merit in building a multi-row array if a single row can reach a blockage ratio of $\epsilon = 1$ as that array would be extracting the maximum power possible from the channel. However, this blockage ratio is likely unrealistic and so multi-row arrays will be of necessity to extract more energy from channels. Here, a *navigation constraint* that at least 20% of the channel's unconstricted area must remain free of turbines (e.g. $0.2A_0$) is enforced. Rows are filled consecutively in the order shown in Figure 3.9. Only after the row placed in the smallest cross-section is filled to its maximum permissible blockage ($\epsilon = 0.8$) does filling of the next row begin.

A minimum row spacing is also enforced of $\Delta x = 0.1L$, which in the small channels will likely mean that downstream turbines lie in the wake zone of upstream rows. This preliminary analysis ignores these effects for now in order to isolate analysis to large-scale channel effects (e.g. flow-rate reduction). An elementary investigation of how a downstream velocity deficit may impact on results in the small channels is provided in the following section (Section 3.5.2).

Figure 3.10 shows power curves for a four-row array but results for arrays containing fewer rows can be read off the same curves as the rows are filled consecutively. Power curves for the odd and even array designs are given in Figure 3.10(a, b) while turbine power curves (average power per turbine) are given in Figure 3.10(c, d). The odd array results are denoted with dashed lines while the even configurations use solid lines. Triangular and circular markers in

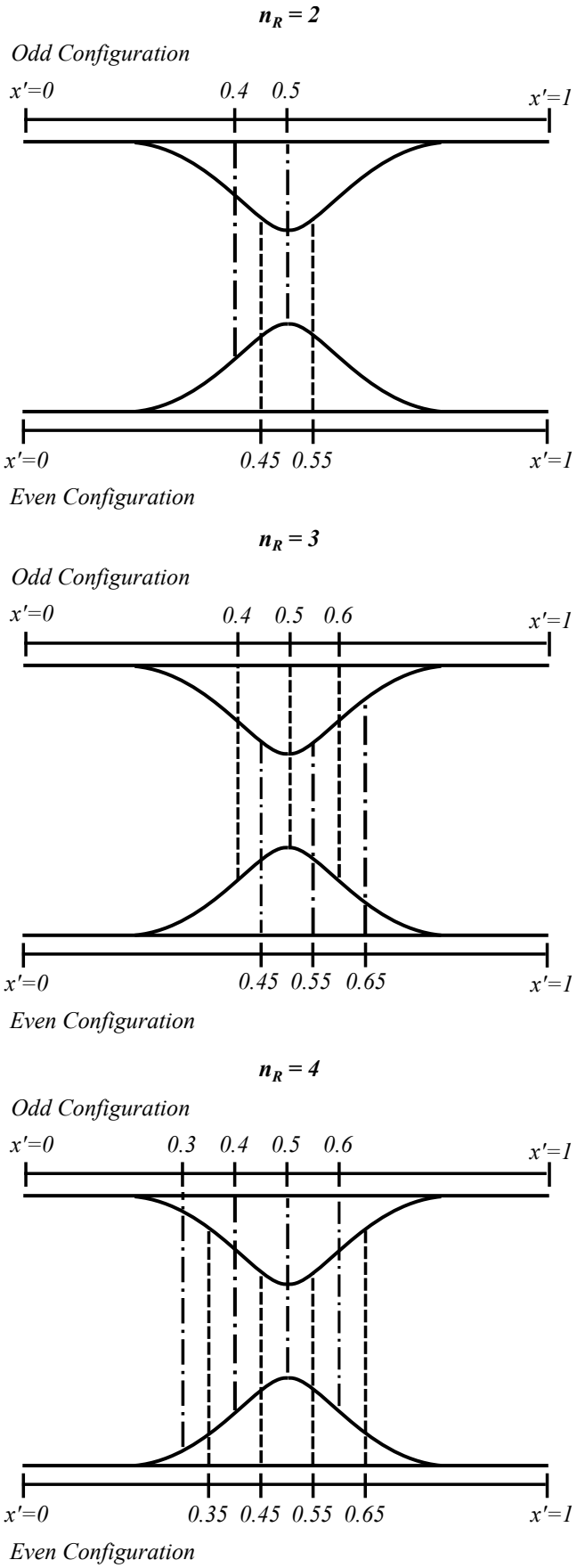

Figure 3.9: Odd and even array configurations used in Section 3.5. Rows are filled until they reach the maximum allowable blockage ratio of $\epsilon = 0.8$ from the most-centre row outwards. When rows are equidistantly outwards, the row on the left is given preference.

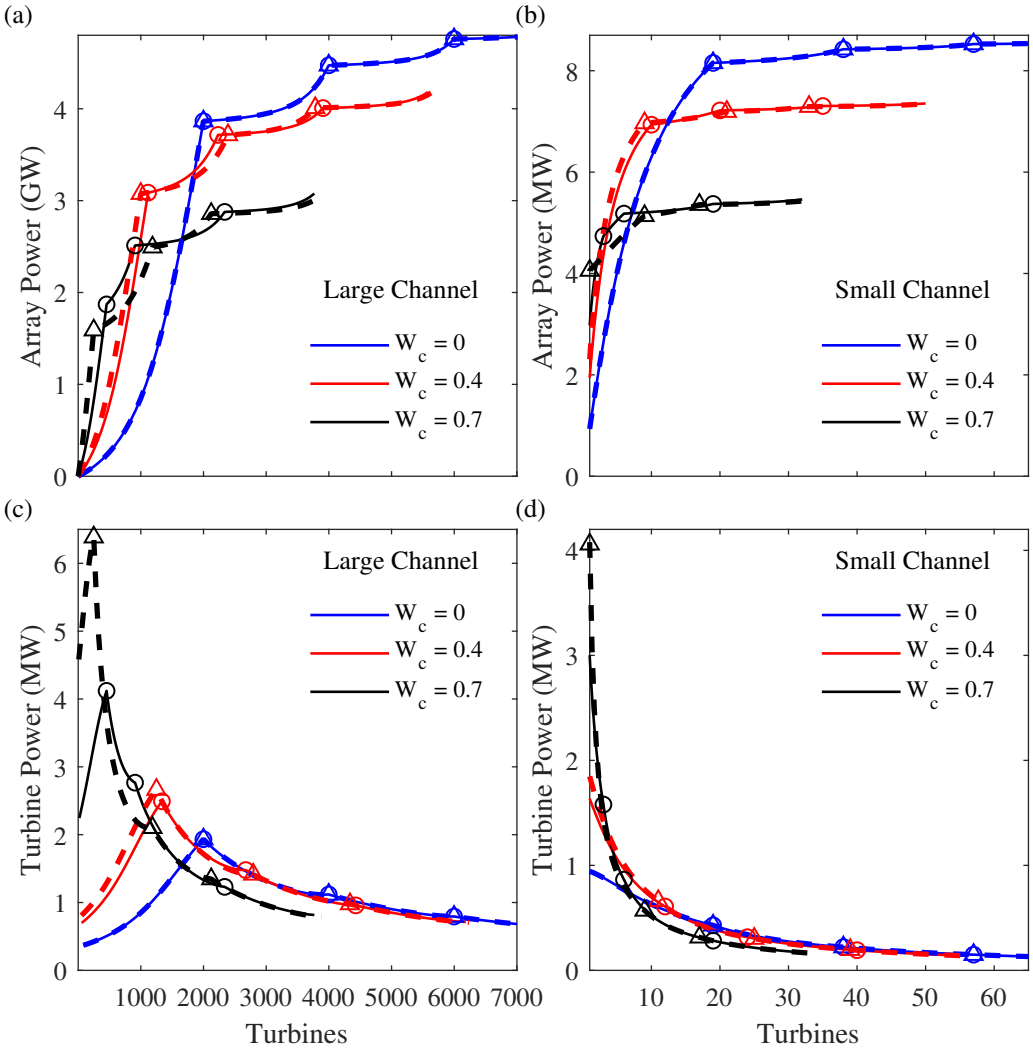

Figure 3.10: Array power and turbine power for multiple row turbine arrays in the large channel (left hand column) and small channel (right-hand column). Dashed lines correspond to the odd configuration while solid lines correspond to the even configuration. Triangles and circles mark where a row is full and the next row begins for the odd configuration and even configuration respectively. Results can be used for arrays of fewer than four rows by reading only up to the appropriate number of rows.

Figure 3.10 indicate the point where, for the odd and even arrays respectively, the row being filled has reached capacity and the filling of the next row starts. In the case of no constriction, these markers fall on the exact same point and, in the absence of turbine wakes, row location has no influence on array power or turbine power.

3.5.1.2 Turbine power vs. array power: a trade-off

In accordance with results discussed in Section 3.4, the odd configuration initially generates a greater amount of power than the even array when the number of turbines is few. Once the odd design reaches capacity, the even design surpasses its array power production due to being able to achieve greater blockage in its larger cross-section under the navigation constraint. Upon addition of a second row, the even design remains preferential as the odd design is forced into a larger cross-section. Due to the minimal row spacing constraint, $\Delta x = 0.1$, using the narrowest cross-section for the first row comes at the cost of using a larger cross-section for the next row. With each successive row thereafter, the design with the highest *array power* changes although due to diminishing returns of power on rows, this effect becomes negligible.

While array power is limited by the amount of turbines that can be packed into the row while still allowing for navigation through the channel, rows in these smaller cross-sections have higher *turbine power* (greater power output from fewer turbines). When filled, the turbines in this row are each producing more power but due to limits on their blockage ratio these arrays produce less power overall.

The velocity advantage of placing a single row in the constricted zone observed in Section 3.4 becomes less significant, if not negligible, in these multi-row arrays and channel blockage is the primary limiting factor on power production. When designing a turbine array containing more than one row of turbines in a channel of variable cross-section there is a trade-off between turbine power and row power. Favouring one of these options in one row is counterbalanced when filling the next row and counter-balanced again at each consecutive row until the array contains a certain number of rows (in this study about $n_{\mathrm{R}} = 4$) beyond which little distinction can be made the two designs.

A diminishing return on turbine power when adding additional rows to an array is a known phenomenon observed in studies of unconstricted channels (Vennell *et al.*, 2015; Vennell, 2012)

and holds for the examples studied here [Figures 3.10(c, d)]. While the absolute power of the second row can be greater than that of the first row, the addition of a second row always acts to decrease the power per turbine of all the turbines in the array. Moreover, the percentage decrease in turbine power of each row relative to the first row is greater in the constricted channels, largely because the first row of turbines in these channels produces significantly more power to begin with as it is placed in the constricted region.

Translating this to a non-Gaussian-shaped channel, these results show that using the smallest cross-sections available will grant developers the greatest power output on a per turbine basis but that a navigable strip constraint can seriously limit the total row power. If the rows of an array are to be built as close together as possible then the pros and cons of selecting the narrowest configuration or the compromised configuration will counterbalance each other as additional rows are added to the array and the globally optimal design will depend on the final number of rows in the turbine farm. The significance of these effects is proportional to the degree of constriction in the channel.

As was discussed in Section 3.4, rows of turbines placed in the constricted parts of channels generate more power using fewer turbines but their maximum power production is limited by the lower potential of the channel. This effect is demonstrated again here in Figure 3.10(a,b).

3.5.2 Effects of velocity deficit on row power and array power

3.5.2.1 Problem formulation

In this testing scenario a row of blockage ratio $\epsilon = 0.4$ is positioned at the centre of the small channel e.g. the smallest cross-section. A second row with the same number of turbines as the first row (not blockage ratio) is then added to the array and moved outwards from a row spacing of 4 diameters to 40 diameters to the right of the initial central row (which remains in the same place). The large channels were excluded from this study as the change in constriction across 40 diameters (Figure 3.11), even with $W_c = 0.7$, was insignificant and produced uninteresting results.

For each different row position combination, individual r_3 tuning values for each of the two-rows were optimised to maximise total array power. Figure 3.12 shows the power contributions of

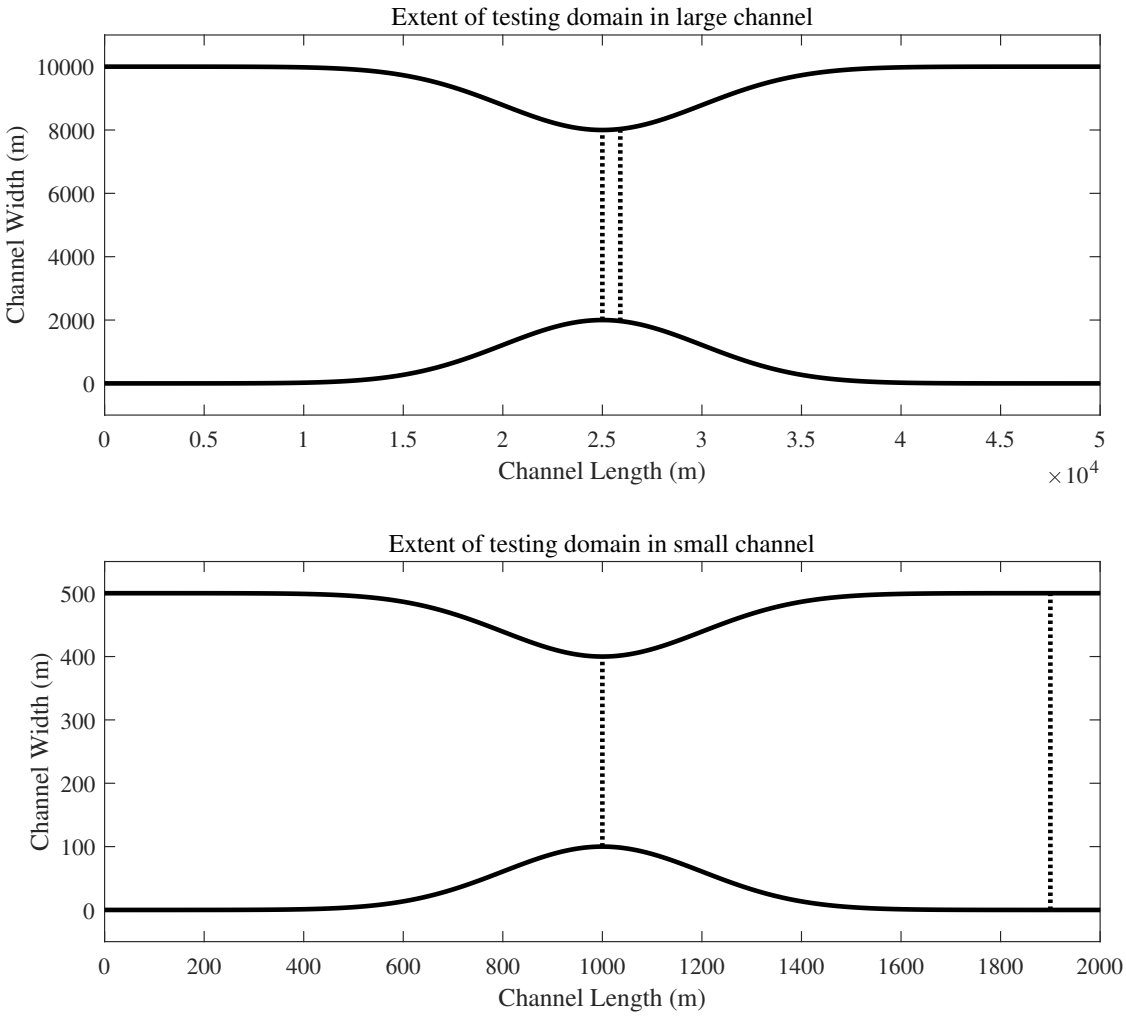

Figure 3.11: The testing range in both the large and small channels for the two-row velocity deficit scenario given in Section 3.5.2. The change in cross-section of the large channel over 40 diameters was insignificant and thus is excluded from our analysis for the sake of brevity.

both rows individually (central row with dashed lines and outer row with dotted lines), and also the total array power (denoted with solid line). Typical velocity profiles for the unconstricted and a constricted channel ($W_c = 0.4$) are provided in Appendix D (Figure 5.7) with this model applied.Three different constriction factors were tested both with no velocity deficit (left hand column) and with the velocity deficit included (right-hand column).

3.5.2.2 Results

There are two penalties against power production at work in these scenarios: (1) velocity deficit from the upstream row and (2) the decreasing blockage ratio of the outside row as it is moved further out of the constriction. Figure 3.12(a) shows the power curves for the case where neither penalty is active - an unconstricted channel with no velocity deficit. The relative power contributions from each row and the combined power do not change with row spacing which is in line with findings of other works (Vennell, 2011b).

Figures 3.12(c, f) show power curves for the two constricted cases without the application of the velocity deficit e.g. only the blockage penalty. The central row (dashed) contributes more power towards the array than the outer row and, as these rows are separated, the difference between the individual power contributions of the two-rows increases significantly. Surprisingly, the total array power remains more or less constant. For the most constricted case (Figure 3.12(e)), beyond approximately fifteen turbine diameters, the outer row is essentially contributing no power to the array and all the power is coming from the central row. The decrease in power production of the outer row is due to the diminishing blockage factor of that row as the fixed number of turbines in the row are pushed into the larger cross-sections beyond the constriction. Surprisingly, the optimiser adjusts the tuning of the central row to make up the power lost by the outer row.

Looking now at the right-hand column where both the constriction and velocity deficit penalties are applied, it is clear that the velocity deficit has little to no effect on the total array power - especially beyond approximately fifteen diameters. Comparing the individual power contributions of both rows, the tendency to favour the central row for power generation by the optimiser is amplified with the presence of the velocity deficit. As both rows mutually lie within the others wake, neither are immune from the penalty associated with the other's deficit.

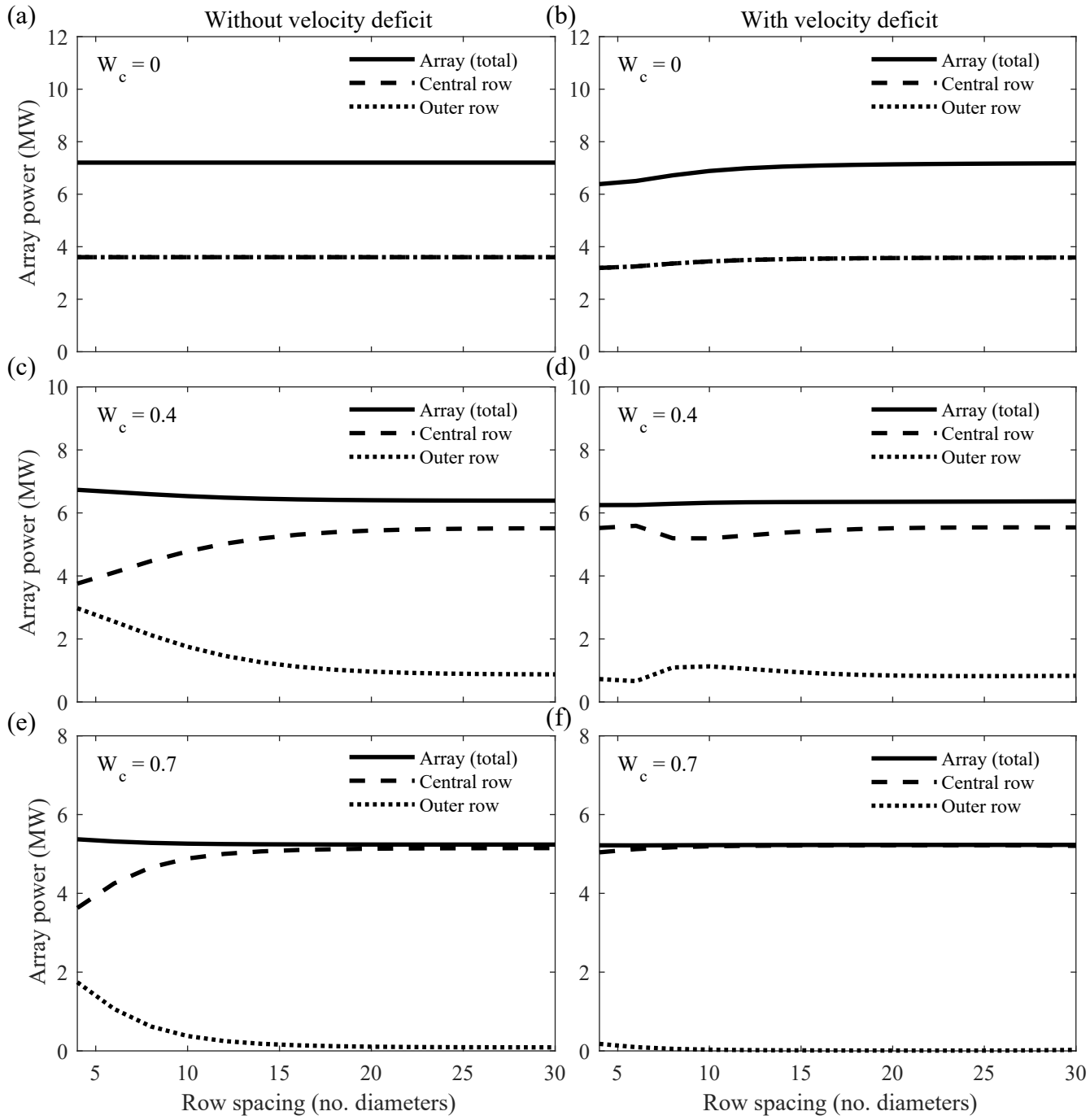

Figure 3.12: Total available power from a two-row array in the small example channel with no constriction (top row), a constriction factor of $W_c = 0.4$ (middle row) and a constriction factor of $W_c = 0.7$ (bottom row). One row is fixed in the most constricted part of the channel (dashed curves) while a second outer row of an equal number of turbines is moved outwards from 4 to 40 diameters away (dotted curves). The left hand column shows power curves in the absence of a velocity deficit while the right-hand column shows the same cases with the velocity deficit applied.

In response to this, the optimiser further reduces the output of the outer row which in turn reduces the downstream velocity deficit. Again, total array power remains unchanged as the central row's generation increases to compensate for the reduction in the outer row. The small kink in the power curves of the central and outer rows in Figure 3.12(e) shows the point in the channel where the velocity deficit penalty ceases to dominate and the blockage ratio penalty becomes more significant.

These results imply that there is little gain in building a second row of turbines in a small constricted channel, although a second row may be necessary if turbines cannot be engineered to the power rating required to fully take advantage of the channel constriction. If engineering limitations prohibit this, there may be value in adding a second row - however, this row should be placed as near to the constricted region as possible. More importantly, these results imply that if one developer has the rights to construct an array in the narrowest cross-section, unless a power cap is enforced upon them, they will capture the vast majority of tidal power in the channel and there is no motivation for a second developer to develop in the same channel.

3.6 Conclusion

This chapter used a computationally efficient 1-D model to perform a systematic study of tidal turbine array design in constricted tidal channels. Some findings in this work are intuitive while others are less obvious. This work has tested a multitude of various array design aspects and is the first work to qualitatively confirm some of these expected results, identify the less obvious and perform a qualitative exploration of of turbine array design in constricted channels.

For a row of M tidal turbines, the available power is maximised by placing the row in the smallest cross-section that it will fit in. The channel potential is realised by totally blocking the narrowest cross-section in the channel with turbines. Rows placed in the constricted zone of a channel are able to simultaneously achieve a greater blockage ratio for a given number of turbines (blockage advantage) and take advantage of high flow velocities (velocity advantage). These benefits initially significantly outweigh the lower potentials associated with the presence of the constriction until the narrowest cross-section is almost blocked with turbines.

In smaller drag dominated channels, the majority of the available power can be extracted from

the first turbines installed. Beyond this initial enhanced-growth period, the power return on additional turbines greatly diminishes. In large inertial channels, a period of increased power growth occurs later on in the row's development when it starts to block a significant portion of the channel cross-section. While the narrowest cross-section in a channel offers the greatest power output for a row of turbines, it may be impossible to build here for technological, economic or socio-environmental reasons. In this case, the same amount of power can be realised from a larger cross-section but will require a greater blockage ratio due to a diminished velocity effect. More turbines are thus required; not only because the cross-section is larger than in the channel narrows but additionally because of the higher blockage ratio required to achieve the same amount of power.

An advantage of using a larger cross-section is that turbines here will be subject to lower velocity and thus weaker loads. If all external dimensions of the turbine are the same then it follows that these turbines will require less material and be cheaper to build. Findings in this work, however, suggest that it may be worthwhile building stronger devices and taking advantage of the constricted flow. Using the power-to-force ratio as a crude indicator of array economics, the power advantage of placing turbines in the fastest flowing cross-section appears to compensate for the additional loads that these turbines must withstand. This suggests that the most constricted section of the channel is both the most productive and most economic location to build a row of turbines.

Turbines placed in a channel constriction require higher r_3 tunings than they would otherwise need if placed in an unconstricted channel. Additionally, if placed outside of the constriction, the optimal r_3 value sits slightly lower than the unconstricted equivalent. As was found in Smeaton *et al.* (2016), the effect of channel constriction on flow rate reduction was found to be mostly negligible. Array power and channel flow rate are intricately linked and thus as more power is taken out of the channel, flow rate decreases.

When building a multi-row turbine farm using the smallest cross-section for one row will come at the cost of having to use a larger cross-section for the next row, while using a larger cross-section for the first row means using a smaller cross-section (in comparison to row 2 of the first design type) for the second row. While smaller cross-sections translate to higher turbine powers, their row power is limited by the necessity of having a navigable strip in the channel.

Thus, maximising the turbine power of the first row comes at a cost of lower turbine power in the second row - however, the inverse is true for the row power of each row. The power return per turbine on each consecutive row diminishes regardless of row location and the magnitude of this effect is proportional to the degree of constriction in the channel.

If a row is present in the most constricted section of a channel, there is little value in adding a second row of an equal number of turbines to the array. The row in the most constricted part of the channel, if optimally tuned, will generate the vast majority of the total array power. The second row is disadvantaged by its lower blockage ratio in the larger cross-section. Surprisingly, the total power available is mostly unaffected by this second row's position in the channel as the same total power available can be achieved by tuning the row at the constriction to compensate for the loss in power of the outer row. The difference between the relative power contributions of the constricted row and outer row increases with the degree of constriction in the channel and the addition of a downstream velocity deficit further amplifies the disparity between the relative power production of the two-rows. This finding suggests that there is little merit in building a second row of turbines in a constricted channel unless turbines cannot be engineered to the power rating required to take advantage of the channel constriction. It also implies that if one developer has the rights to build inside the constricted part of a channel, unless a power cap is enforced upon them, there is little motivation for a second developer to build a second array in the same channel.

The one-dimensional model used here was computationally efficient and allowed the systematic exploration of many scenarios. It is limited by its inability to account for the losses and eddying effects at the constriction where jet formation is likely to occur. Furthermore, our velocity deficit model holds only if the downstream turbines are directly behind the upstream turbines and could not be used to investigate a staggered turbine arrangement. These are addressed in the proceeding chapter with the adoption of a 2-D depth-averaged hydrodynamic code (SUNTANS) which gives a more realistic representation of the flow and allows for more realistic boundary conditions and channel geometries to be used.

Chapter 4

2-D Turbine Arrays in Constricted Channels

4.1 Foreword

This chapter builds upon the previous chapters by adopting a 2-D hydrodynamic channel model to give a more realistic description of the channel geometry, flow and outer boundaries. It is unusual to use such a model for a systematic exploratory turbine array study. Divett *et al.* (2013); Divett (2013) are two of the few studies that have taken a generalised systematic approach to tidal turbine array design using higher order modelling (LES simulations in rectangular channels). While many works have been completed on specific channels such as the Pentland Firth (Funke *et al.*, 2016) or the Bay of Fundy (Polagye and Malte, 2011), few have developed overarching array design theory that applies to a set of channels (e.g. large unconstricted, small constricted etc). This chapter aims to bridge the gap between the two different types of resource assessment studies existing in literature - that is, detailed but specific multi-dimensional flow studies of few test cases, and simple but efficient 1-D studies that test a broad range of array designs in many channels. It addresses the issue of the constriction jet and quantifies the energy losses associated with this - a shortcoming of the 1-D model used in the past chapter. It also uses more realistic geometries and tidal forcing boundary conditions. This chapter forms the base of the second paper of a planned two-part series on turbine array design in constricted channels. Ross Vennell, Alice Harang and Margot Gerritsen will be co-authors of

this paper. Alice Harang was a co-developer of the model framework and assisted with nesting the turbine model into SUNTANS (Stanford Unstructured Non-hydrostatic Terrain-following Adaptive Navier-Stokes Simulator, Fringer *et al.* (2006)), writing scripts to batch process simulation runs and also with building the model meshes. The contribution of the remaining authors was purely supervisional.

This work addresses Research Questions 1 to 6 of this thesis:

1. How are theoretical limits on tidal energy generation such as channel potential and maximum available power affected by channel constriction?
2. How does channel constriction affect the extent of tidal energy related flow reduction?
3. How should arrays be arranged in constricted channels to maximise energy output?
4. How do channel constrictions affect how power scales with the number of turbines in an array or across multiple arrays in the same channel?
5. How might flow separation and jet formation downstream of a constriction influence energy output and array design?
6. How suitable are 1-D models for performing exploratory studies on tidal energy resource assessment relative to 2-D modelling?

Code from this chapter is available at https://bitbucket.org/ocean_physics_tidal/tidal_power/src/master

4.2 Introduction

The previous chapter systematically explored turbine array design in a constricted channel using a relatively simple 1-D model. This allowed for a broad investigation of the topic and permitted exploration of a large number of test cases (varying numbers of turbines, numbers of rows, row locations, row tunings and channel constriction factors). This came at the cost of neglecting more realistic aspects of flow and channel geometry. The presence of a constriction causes flow streamlines to bend and the consideration of lateral velocity components and non-homogeneous flow may be important to accurately assess the tidal energy resource. For constricted channels in

particular, the expanding cross-section downstream of the constriction can result in an adverse pressure gradient which may cause flow to decelerate to the point of reversal. This causes eddies and jets to form which may also affect turbine array performance. While the 1-D model is useful for its efficiency, it is not sophisticated enough to account for these 2-D effects.

Systematic array design studies such as this one are usually completed using simple 1-D models. It is uncommon for generalised, systematic studies to adopt higher order modelling in their methods (e.g. 2-D hydrodynamics) due to the computational demand associated with their use. These higher order models have been used prolifically in site-specific resource assessment studies (Easton *et al.*, 2012; Funke *et al.*, 2014; Polagye and Malte, 2011) and the methods used in these works for implementing turbines can be used to inform works such as this one. Past works similar to this chapter were completed by Divett *et al.* (2013) and Divett (2013) for much smaller arrays in an idealised rectangular channel. They used a 2-D LES model with an adaptive-mesh to look at four different array designs of fifteen turbines each. These works looked at optimising the location of individual turbines in an idealised rectangular channel and were the first of their kind to bridge the gap between coastal-basin scale modelling and small array modelling. Findings of this work showed a staggered array produced 54% more energy than a non-staggered array and also showed that positioning the array on the side of the channel resulted in similar power generation to positioning the array in the centre of the channel. This work differs from Divett *et al.* (2013); Divett (2013) by looking at much larger arrays in constricted channels and is also able to explore a greater breadth of array configurations by using a RANS approach to modelling turbulence instead of LES. Individual turbines are not modelled and so the effects of staggering cannot be investigated.

Other important works were completed using higher order hydrodynamic models at the same time as this thesis was written. Funke *et al.* (2014, 2016) found for a 16-turbine array in the Pentland Firth, a single row of turbines in the narrowest cross-section of the channel produced the most power, however five turbines within the array contributed very little to the array output. By examining how power output scaled with the number of turbines, they showed that the 16-turbine array was only 10% more powerful than the optimal 11-turbine design. This has implications for developers, particularly if an array development is to be staged. The works of Funke *et al.* (2014, 2016) are particularly novel in that they use adjoint methods to

quickly optimise discrete turbine locations within a higher order hydrodynamic model. This thesis examines arrays orders of magnitude larger than the scale of arrays examined in this work and so these methods may prove to be ever time-consuming despite the use of adjoint methods. Despite this, this modelling advance is promising in terms of moving away from the simpler model here which requires turbines be arranged in rows. The key finding, that the optimal array design is a single row in the narrowest cross-section does agree with the broader and more general theory presented here.

This chapter adopts the 2-D depth-averaged hydrodynamic model SUNTANS (Stanford Unstructured Non-hydrostatic Terrain-following Adaptive Navier-Stokes Simulator). This model was developed by Fringer *et al.* (2006) and has been used for various geophysical studies such as the transport of dissolved aquaculture waste (Venayagamoorthy *et al.*, 2011), intra-tidal flow on mudflats (Wang *et al.*, 2009) and particle tracking of oil spills (Feng *et al.*, 2019). The actuator disc model is applied again to calculate the drag force associated with specific turbine array configurations. This drag is applied within SUNTANS as zones of increased drag.

The computational demand of this higher order model means fewer test cases are feasible than were completed using the 1-D model. A total of four different array layouts were tested with varying blockage ratios in six different test channels. The large and small channels from the preceding chapter are used here again with three constriction factors: $W_c = [0, 0.4, 0.7]$. A more realistic boundary forcing is applied by extending the problem domain to include large coastal basins at either end of the channel. These coastal basins are given out-of-phase tidal elevations at their boundaries which forces flow to move back and forth through the channel - similar to the setup of Draper *et al.* (2010). Bathymetry at the channel edges was smoothed to remove orthogonal coastal boundaries and water depth was increased linearly from the channel-ends to the ocean-boundaries to replicate a continental shelf.

The performance of the four array designs above was explored with respect to array power, power per turbine, and average load per turbine. Additionally, this chapter explores the effects that these arrays have on the channel flow rate and free surface. Finally, a comparison is made between the 1-D model of the past chapter and this more sophisticated model.

4.3 Methods

4.3.1 Channel model and boundary conditions

Channel dynamics are modelled using the parallelised finite element coastal model SUNTANS [Stanford Unstructured Non-hydrostatic Terrain-following Adaptive Navier-Stokes Simulator] (Fringer *et al.*, 2006). Although tidal energy extraction is a 3-D phenomenon, the model was run for 2-D depth-averaged flow due to the large spatial extent of the domain, the necessarily small mesh size in the channel/jet area and the consequential necessarily small time step ($\Delta t = 1$s). SUNTANS uses a RANS (Reynolds-averaged Navier Stokes) approach to modelling flow where velocities are decomposed into a mean component and a time-varying fluctuation (denoted with $\tilde{}$). The equations are then averaged over time which yields remaining turbulent terms that cannot be explicitly solved. These terms are modelled using a turbulence closure scheme, namely the Mellor-Yamada 2.5 scheme (Mellor and Yamada, 1982). This scheme is considered suitable for shallow water flows while still being computationally efficient and is used extensively for geophysical applications (Feng *et al.*, 2019; Wang *et al.*, 2009; Venayagamoorthy *et al.*, 2011).

Formulating the total water column depth in space and time as the sum of a time-constant (h_0) and time-varying component (η):

$$z = -(h_0(x, y) + \eta(x, y, t)), \tag{4.1}$$

where $z = 0$ is the sea-surface when $\eta = 0$. Adopting Einstein-summation convention over components (x, y), the boundary condition at the free surface is:

$$w|_{z=\eta} = \frac{\partial \eta}{\partial t} + u_i \frac{\partial \eta}{\partial x_i}. \tag{4.2}$$

Here u_i is the time-averaged, depth-averaged horizontal velocity in direction x_i. Equation 4.2 states that particles at the free surface must remain at the free surface. The boundary condition applied to the seafloor is that no mass flux can occur through the boundary e.g.

$$u_i \check{n}_i|_{z=-h} = 0 \tag{4.3}$$

Here $\check{\mathbf{n}} = (\partial h_0/\partial x, \partial h_0/\partial y, -1)$ is the normal vector of the seafloor. These conditions are applied to the RANS equations which are then integrated over the water column. In this model, a uniform density ocean ($\rho = 1027\text{kgm}^{-3}$) was implemented (non-stratified, constant salinity and temperature) and atmospheric pressure at the upper boundary was assumed to be constant. In reality, temperature and salinity affect water density which in some instances (e.g. equatorial regions) can be the primary driver of water transport. The scale of this forcing is very small compared to the tidal forcing in channels suitable for energy generation e.g. temperature transects taken by Garner (1969) of Cook Strait showed thermal variability caused a density difference of 0.3 kg m^{-3} (0.3 %). Due to the small spatial extent of the domain (relative to the global scale), Coriolis force was assumed to be negligible. The governing equations are thus:

$$\frac{\partial u_i}{\partial t} + u_j \frac{\partial u_i}{\partial x_j} = -g\frac{\partial (h+\eta)}{\partial x_i} + \frac{1}{h}\frac{\partial}{\partial x_i}\left(h\left[\frac{1}{\rho}\tau_{ij} - \overline{\tilde{u}_i \tilde{u}_j}\right]\right) + \frac{1}{h\rho}\left(F_{\mathrm{B}i} + F_{\mathrm{T}i}\right) \tag{4.4}$$

$$\frac{\partial \eta}{\partial t} + \frac{\partial}{\partial x_i}(h u_i) = 0. \tag{4.5}$$

Equation 4.4 is the depth-averaged horizontal momentum equation and Equation 4.5 is the depth-averaged continuity equation. Here, g is the acceleration due to gravity, τ_{ij} is the Reynolds stress tensor and $\overline{\tilde{u}_i \tilde{u}_j}$ is the time-averaged product of the fluctuating velocity components (a residue from the Reynolds-averaging process). Collectively, the terms within the square brackets are the turbulent components of the flow which are evaluated using the aforementioned MY2.5 closure scheme. $F_{\mathrm{B}i}$ is bottom drag term, assumed to be quadratic in form such that $F_{Bi} = \rho C_d u_i |u_i|$ with constant drag coefficient $C_d = 0.0025$. $F_{\mathrm{T}i}$ is the drag force associated with the addition of a turbine array (discussed below in Section 4.3.2).

SUNTANS adopts a semi-implicit solution method (Casulli, 1999) where some of the model parameters are solved implicitly while others are solved explicitly. All flux related quantities are calculated at the edges of the triangular cells while non-flux quantities are calculated at the cells' Voronoi points (shown with circles in Figures 4.1, 4.2, and 5.5).

Open boundary conditions were applied to the outer boundaries of the ocean bodies with two sinusoidal tidal forcings (η_{L} on the left and η_{R} on the right) of equal amplitude (η_0) and phase difference (ϕ):

$$\eta_{\mathrm{R}} = \frac{\eta_0}{2}\sin(\omega t), \tag{4.6}$$

$$\eta_{\mathrm{L}} = \frac{\eta_0}{2}\sin(\omega t + \phi). \tag{4.7}$$

The tidal amplitude (η_0) was set to 0.7 m and 1 m for the large and small channels, respectively, with corresponding phase differences of 180° and 10°. The same tidal frequency was used for both channels as was used in the 1-D model ($\omega = 1.4 \times 10^{-4}$ rads^{-1}).

A wall boundary condition was applied to the channel walls e.g. the velocities at cell edges along the channel walls are equal to zero. The laminar viscosity of water was set to 10^{-4}m^{2}s^{-1} and the horizontal laminar viscosity was set to 0.1m^{2}s^{-1}. The vertical and horizontal mass diffusivities were set to zero. These values were used for all test cases.

4.3.2 Analytical turbine model

4.3.2.1 Drag application

The drag coefficient for a row of turbines (C_{R}) was calculated using methods described in the preceding chapter (Section 3.3) for 1-D flow. Rows of turbines in the past chapter, in the channel model, were treated as impulse functions of drag positioned at locations $x = x_{\mathrm{R}i}$ along the channel length. Note that the 1-D drag coefficient used in the past chapter is for turbines in the yz-plane e.g. the plane of the channel cross-section.

In the 2-D channel model, velocities are calculated at the edge-centres of the cells. A discontinuous line of turbines is not possible in SUNTANS as it caused the model to become unstable. Additionally, a discontinuous line representation is non-ideal because the line of drag will intercept multiple cells at irregular points. While it would be possible to build a grid to accommodate a straight line of turbines, testing array power sensitivity to row-location is one of the objectives of this chapter and this would have required several additional meshes to be created which would make this work less efficient. As an alternative, the turbine drag was spread over an effective xy-area that spans the entire channel-width and extends a lengthwise distance of $\Delta x_{\mathrm{R}} = 200$m, approximately 4 turbine diameters upstream/downstream in each direction,

which was the assumed distance for the flow profile to achieve r_3 in the velocity deficit model of the last chapter. This is reasonably large in the small channel; however, it was not changed for the sake of consistency across simulations. This assumption may have some implications on the free surface although comparisons between head profiles here and in literature are similar (Divett, 2013).

A Gaussian weighting function was used to smooth the drag over this area and prevent numerical instabilities from occurring. The function was designed to peak at the designated row-location ($x = x_{\mathrm{R}}$) and extend a distance of $0.5\Delta x_{\mathrm{R}}$ either way in the x-direction (e.g. $x = x_{\mathrm{R}} - 0.5\Delta x_{\mathrm{R}}$ to $x = x_{\mathrm{R}} + 0.5\Delta x_{\mathrm{R}}$). The function was made as steep as possible to accurately represent rows of turbines, while still being gradual enough to ensure numerical stability. The Gaussian weighting function x_{W} is:

$$x_{\mathrm{W}} = 1/\sqrt{2\pi}\frac{\exp\left[(-x - x_{\mathrm{R}})^2/2(\Delta x_{\mathrm{R}}/5)^2\right]}{\Delta x_{\mathrm{R}}/5}, \tag{4.8}$$

and is uniform over the row-width (y-axis) but varies over the effective row-length such that:

$$\int_{x-0.5\Delta x_{\mathrm{R}}}^{x+0.5\Delta x_{\mathrm{R}}} x_{\mathrm{W}} dx = 1. \tag{4.9}$$

The drag coefficient calculated using the 1-D analytical turbine model is for the yz-plane whereas the drag in the 2-D model must be implemented over the xy-plane. These drag coefficients are therefore not interchangeable. However, one can derive a formula to convert the yz-drag to an xy-drag. Recall, the drag force exerted by the turbines on the flow using the 1-D model is:

$$F_{\mathrm{T}}(x,t) = \rho C_{\mathrm{R,yz}} A_{\mathrm{R}}(x)\bar{u}(x,t)\left|\bar{u}(x,t)\right|, \tag{4.10}$$

where C_{R} has been rewritten as $C_{\mathrm{R,yz}}$ to emphasise it is a yz-drag coefficient. The velocity term in (4.10) is the average velocity over the cross-section which satisfies $Q = A_{\mathrm{R}}\bar{u}$.

The drag force of the turbines on the flow is calculated in the 2-D model using:

$$F_{\mathrm{T}}(x,y,t) = \rho C_{\mathrm{R,xy}} \iint x_{\mathrm{W}}(x,y)\mathbf{u}(x,y,t)\,|\mathbf{u}(x,y,t)|\,dA_{\mathrm{xy}}, \tag{4.11}$$

where $\mathbf{u}$ is the 2-D depth-averaged velocity vector and dA_{xy} is the effective turbine row area.

Now, applying (4.10) and (4.11) to an infinitesimal strip of channel width, dy, for the 1-D and 2-D drag applications respectively:

$$F_{\mathrm{T}} = (\rho C_{\mathrm{R,yz}} h\bar{u}\,|\bar{u}|)\,dy, \tag{4.12}$$

$$F_{\mathrm{T}} = \left(\rho C_{\mathrm{R,xy}} \int_{-0.5\Delta x_{\mathrm{R}}}^{0.5\Delta x_{\mathrm{R}}} x_{\mathrm{W}}\mathbf{u}\,|\mathbf{u}|dx\right) dy. \tag{4.13}$$

If the velocity does not vary considerably in the strip dy over the effective row length (Δx_R), then the error in using the mean velocity over Δx_R is small (e.g. $u \approx \bar{u}$). The integral in (4.13) becomes:

$$\int_{-0.5\Delta x_{\mathrm{R}}}^{0.5\Delta x_{\mathrm{R}}} x_{\mathrm{W}}\mathbf{u}\,|\mathbf{u}|dx = \bar{u}\,|\bar{u}| \int_{-0.5\Delta x_{\mathrm{R}}}^{0.5\Delta x_{\mathrm{R}}} dx. \tag{4.14}$$

Using this and (4.9), Equation 4.13 can be rewritten as:

$$F_{\mathrm{T}} = \rho\,(C_{\mathrm{R,xy}}\bar{u}\,|\bar{u}|\,\Delta x_R)\,dy. \tag{4.15}$$

Finally, an expression for the xy-drag coefficient is obtained by equating (4.15) to (4.12):

$$C_{\mathrm{R,xy}} = \frac{h}{\Delta x_R} C_{\mathrm{R,yz}}. \tag{4.16}$$

It should be acknowledged that this formula requires the velocity be close to constant over the effective row-length which may not always be the case - especially in constricted channels where the cross-sectional area is changing. If the cross-section is changing rapidly with respect to x, then the model here will overestimate power on one half of the tidal cycle (when the cross-section is expanding) and underestimate power during the other half of the tidal cycle (when the cross-section is contracting). The assumption of near-constant velocity over the effective

row-length is more important for the small channel examples where the full channel length is only 2000 m. For the most constricted small channel (e.g. the worst case), the channel width varies between 150 m and 243 m over the effective row-length.

The decision to only model fences of evenly spaced rows of turbines that occupy the full cross-section means wake dynamics behind the turbines cannot be properly examined here. This would require modelling discrete turbines or using partial row theory (Nishino and Willden, 2013) which requires optimising additional variables (e.g. intra-row spacing) and would ultimately limit the exploration of the chosen independent variables here. Harang *et al.* (*in prep*) have completed simulations for evenly-spaced rows of turbines that occupy only part of the channel cross-section using similar methods to those here (e.g. SUNTANS + actuator disc model). Their work looks at tidal energy generation from two partial rows in an unconstricted channel where bypass flow around the row can interact with the row's wake and the second downstream row.

In summation, for a given row of turbines, the drag coefficient of the row is calculated using the methods of Garrett and Cummins (2007); Vennell (2010) and then the total drag force from the row is calculated. This drag force is distributed over the row area in the mesh as bottom friction. This distributed bottom friction is used to calculate turbine power and thrust.

4.3.2.2 Power and force calculations

The local velocity at each edge inside the effective row-area is used to calculate the total drag force and also the power available from the i^{th} row of turbines. The force on the flow from the presence of turbines is calculated using 4.17:

$$\boldsymbol{F}_i = \rho C_{\text{R}i}^{\text{xy}} \sum_{k=1} x_{\text{W}k} |\mathbf{u}_k| \, \mathbf{u}_k, \tag{4.17}$$

where k is over all cells within the "row area" of the i^{th} row. If turbines are arranged parallel to the y-axis then the normal component of the velocity on the turbine blades is u. The normal force on the turbine blades, e.g. the force component that contributes to power generation is then:

$$\hat{\mathbf{F}}_i = \rho C_{\mathrm{R}i}^{\mathrm{xy}} \sum_{k=1} x_{\mathrm{W}k} u_k \left| u_k \right| . \tag{4.18}$$

Finally, the power generated by the i^{th}row is:

$$\mathrm{P}_i = \rho r_{1i} C_{\mathrm{R}i}^{\mathrm{xy}} \sum_{k=1} x_{\mathrm{W}k} u_k \left| u_k \right|^2 , \tag{4.19}$$

and, for an array consisting of M rows of turbines, the total array power is $P_{\mathrm{avail}} = \sum_{i=1}^{M} P_i$.

4.3.3 Limitations of actuator disc method with 2-D hydrodynamics

Treating turbines as actuator discs, while useful for macro-scale array modelling, fails to account for some aspects of turbine dynamics. For instance, it is not possible to account for individual turbine wakes and subsequent mixing processes. Additionally, the actuator disc model used here does not account for spacing between turbines within rows. Incorporating intra-turbine spacing is feasible using the partial row theory model (Nishino and Willden, 2012, 2013) but comes at additional computational expense (more variables to optimise or explore).

Limiting hydrodynamics to two dimensions (depth-averaged currents) removes any variability of water velocity with depth. This variability may be particularly important for arrays built in the near future where turbines will likely be deployed either on the seabed or floating from the sea-surface due to ease of installation (i.e. near boundaries where there are boundary layers). Additionally, the presence of wave motion will likely have some effect on surface-hanging turbines (or turbines on the seabed in shallow channels) which was not accounted for in these simulations. A more detailed discussion on the limitations of the modelling approach taken here is given in Chapter 5, Section 5.2.

4.3.4 Channels and meshes

4.3.4.1 Shape

Continuing the trend set in preceding chapters, a large inertia-dominated and small drag-dominated channel were modelled with three different constriction factors: $W_{\mathrm{c}} = [0, 0.4, 0.7]$

Table 4.1: Details of the channel examples used for this study

Parameter	**Small Channel**	**Large Channel**
Length (L)	2 km	50 km
Max. Width (W_0)	500 m	10 km
Depth (h_0)	20 m	100 m
Radius of ocean basins	28 km	165 km
Tidal amplitude at boundary (η_0)	1 m	0.7 m
Phase difference between tides	10°	180°
Min/max mesh resolution (triangle side length)		
Unconstricted ($W_c = 0$)	7 m / 7.6 km	61 m / 21 km
Moderately constricted ($W_c = 0.4$)	6 m / 6.7 km	56 m / 21 km
Highly constricted ($W_c = 0.7$)	6 m / 7.9 km	61 m / 21 km
Time step (Δt)	1 s	1 s

based on two Gaussian curves. Parameters for these channels are given in Table 4.1.

4.3.4.2 Bathymetry

Along the channel boundary, a hyperbolic tangent curve (Eq 4.20) was used to provide a more realistic boundary by smoothing the transition between the channel coastline and the seafloor:

$$z(x, y) = h_{\text{cor}}(x) \tanh\left(\frac{0.5W(x) - |y|}{\theta}\right). \tag{4.20}$$

Here $W(x)$ is the width at the lengthwise coordinate (x), y is the along-width coordinate, and θ is an arbitrary constant that controls the steepness of the transition (set at $\theta = 50$). Adding this depth transition results in a loss of total cross-sectional area at some x-values (with respect to the channels tested in the past chapter) so for the sake of consistency with the test cases used in preceding chapters, a variable $h_{\text{cor}}(x)$ was introduced to ensure that the mean cross-sectional area was conserved:

$$h_{\text{cor}}(x) = \frac{h_0}{\theta \ln\left(\cosh[0.5W(x)/\theta]/[0.5W(x)]\right)} \tag{4.21}$$

To replicate the transition from the channel to a continental shelf, the water depth was linearly increased from depths of 20 m and 100 m at the channel ends to 40 m and 400 m at the ocean boundaries for the small and large channels, respectively.

4.3.4.3 Mesh

Meshes were built using ANSYS ICEM CFD software with the same widths, mean depths, and lengths that were prescribed for the large and small channels in the previous chapter (detailed again below for reference). The origin of the meshes was positioned in the centre of the domain, which for the constricted cases is the narrowest cross-section of the channel. The outer boundaries were placed 150 km and 30 km from the large and small channel ends respectively to prevent them from artificially influencing channel dynamics. Mesh resolution was made coarse in the ocean segments and resolution was increased towards the entry and exit points of the channel before being further increased in the channel itself. Mesh resolution (triangle side length) was adjusted until the exit jets of the channels were adequately resolved and grid discretisation was no longer having a visible effect on dynamics. Parameters corresponding to the geometries and meshes of the test channels used here are given in Table 4.1 and example meshes (moderately constricted large channel e.g. $W_c = 0.4$) at different zoom-levels are provided below with shading corresponding to bathymetry below and without shading in the appendices. Images of the mesh and bathymetry are given in Figures 4.1 and 4.2, unshaded copies of these figures are given in Appendix C from which the relative mesh resolution across the domain can be seen.

4.3.4.4 Sponge layer

Despite the outer forcing boundaries being situated at distances far from the channel entry points, transient reflection was evident in early simulation runs. Wave pulses reflected off the ocean boundary back into the channel which caused artificial perturbations in the free surface within the channel. To remove these, a sponge layer was applied to the outer forcing boundaries to dampen the reflection. The sponge layer extended over a distance of 50 km and 5 km from the outer forcing boundaries for the large and small channels respectively and a sponge-decay time-scale of 1 hour was used for both channels.

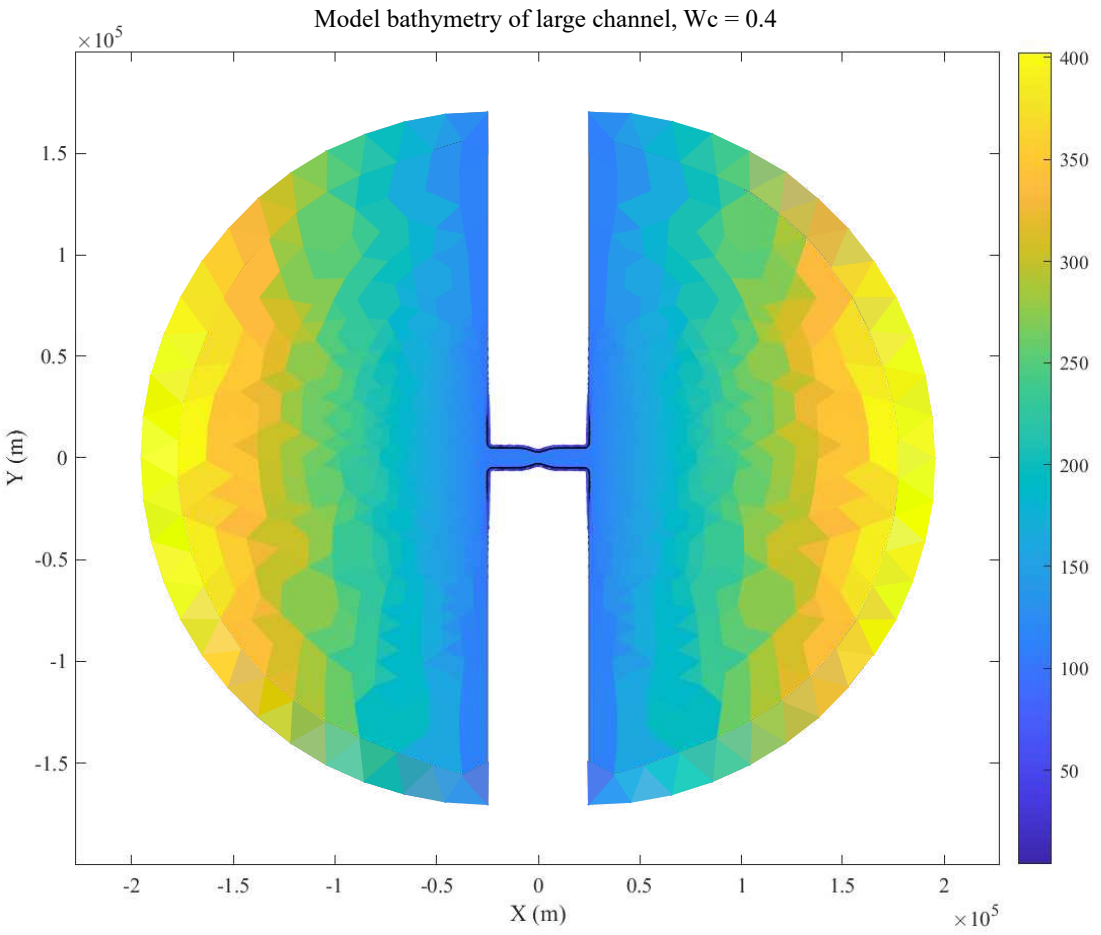

Figure 4.1: Fully zoomed out bird's eye view of mesh across whole domain for the small channel with $W_c = 0.4$. Colours denote mean water depth in cells.

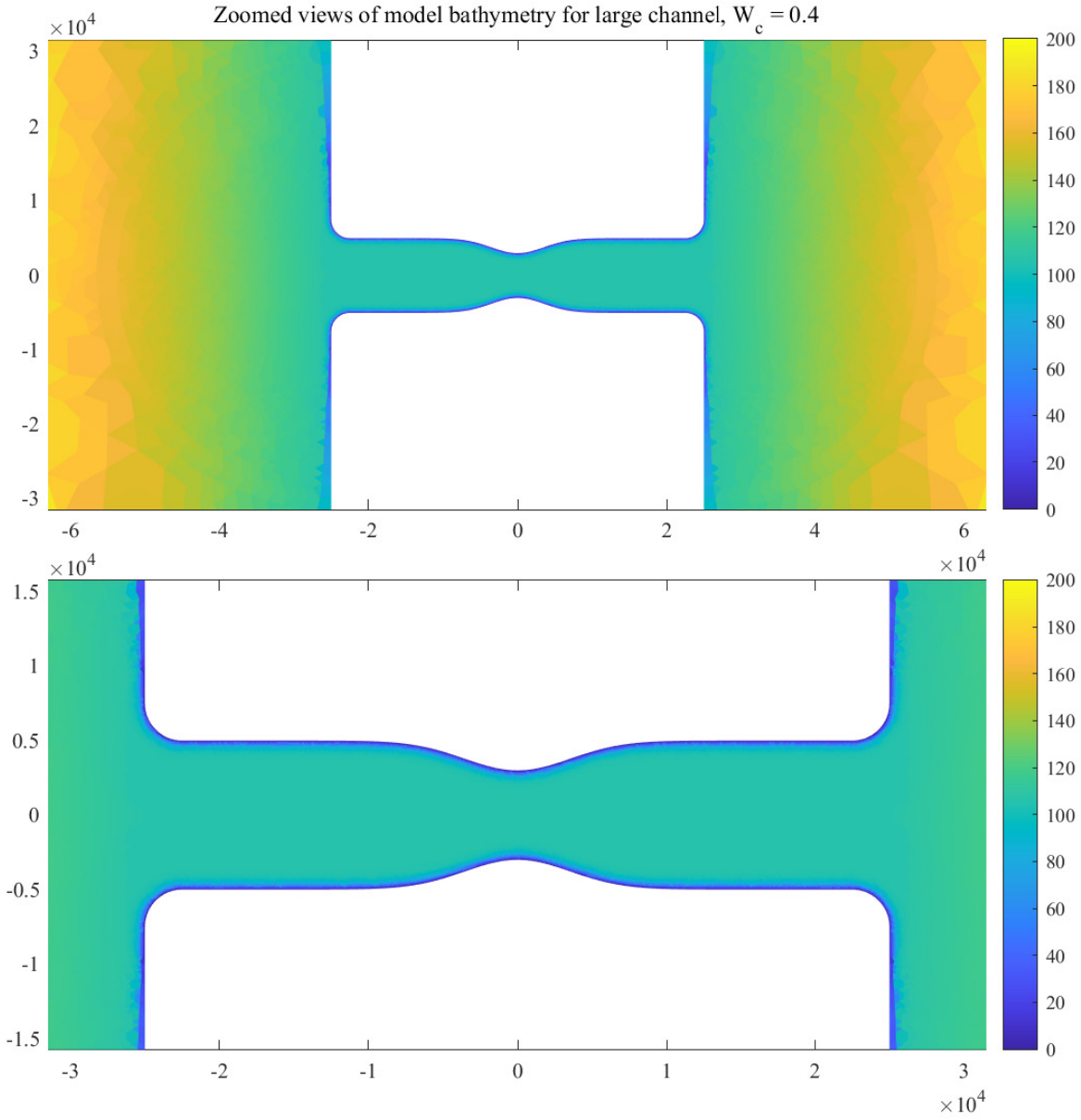

Figure 4.2: Zoomed in bird's eye views of mesh showing channel and near surroundings for the small channel with $W_c = 0.4$. Colours denote mean water depth in cells

4.3.5 Initialisation process

4.3.5.1 Boundary condition ramp-up

The model was initialised with zero velocity and zero water elevation across the entire domain. To avoid shocks and perturbations at the left boundary where the phase difference resulted in a non-zero water elevation at $t = 0$, Equation 4.7 was imposed via a linear "ramp up" during the first hour of simulation time. The model was run initially in the absence of turbines to achieve an undisturbed, natural state of the channel. Once converged, turbines were added to the channel.

4.3.5.2 Drag ramp-up

In addition to geometric smoothing, the turbine drag was increased to its final value with simulation time according to a hyperbolic tangent function (Eq 4.22). Without this ramp-up of the drag, the sudden addition of drag to the domain generated numerical waves which led to model instability.

$$t_{\mathrm{R}} = \left(\frac{1}{2} + \frac{1}{2}\tanh\left[R_{\mathrm{P}}\frac{(t - t_{\mathrm{R0}})}{(\Delta t_{\mathrm{R}} - 0.5)}\right]\right). \tag{4.22}$$

Here, t is the simulation time, $t_{\mathrm{R0}} = 172,800$s (48 hours) is the time step at which the ramping process was initiated, $\Delta t_{\mathrm{R}} = 10,800$ s (3 hours) is the duration of the ramp-up process and $R_{\mathrm{P}} = 8$ controls the steepness of the ramp.

4.3.6 Tuning optimisation

The patient-tuning strategy of Vennell (2016) was applied to the array as a whole (all rows have the same r_3). This singular parameter tuning approach is less sophisticated than the method used in the previous chapter which allowed for r_3 to vary between rows . Due to the computational demand of the SUNTANS code and the already long time required to complete simulation runs, it was decided that this tuning strategy would suffice for the purposes of this chapter (optimising the rows individually would have taken approximately twice as long per simulation). This assumption is suitable for rows with equal blockage ratio (even if the rows have different cross-sections) as Vennell (2011b) found that optimal row-turnings for rows with

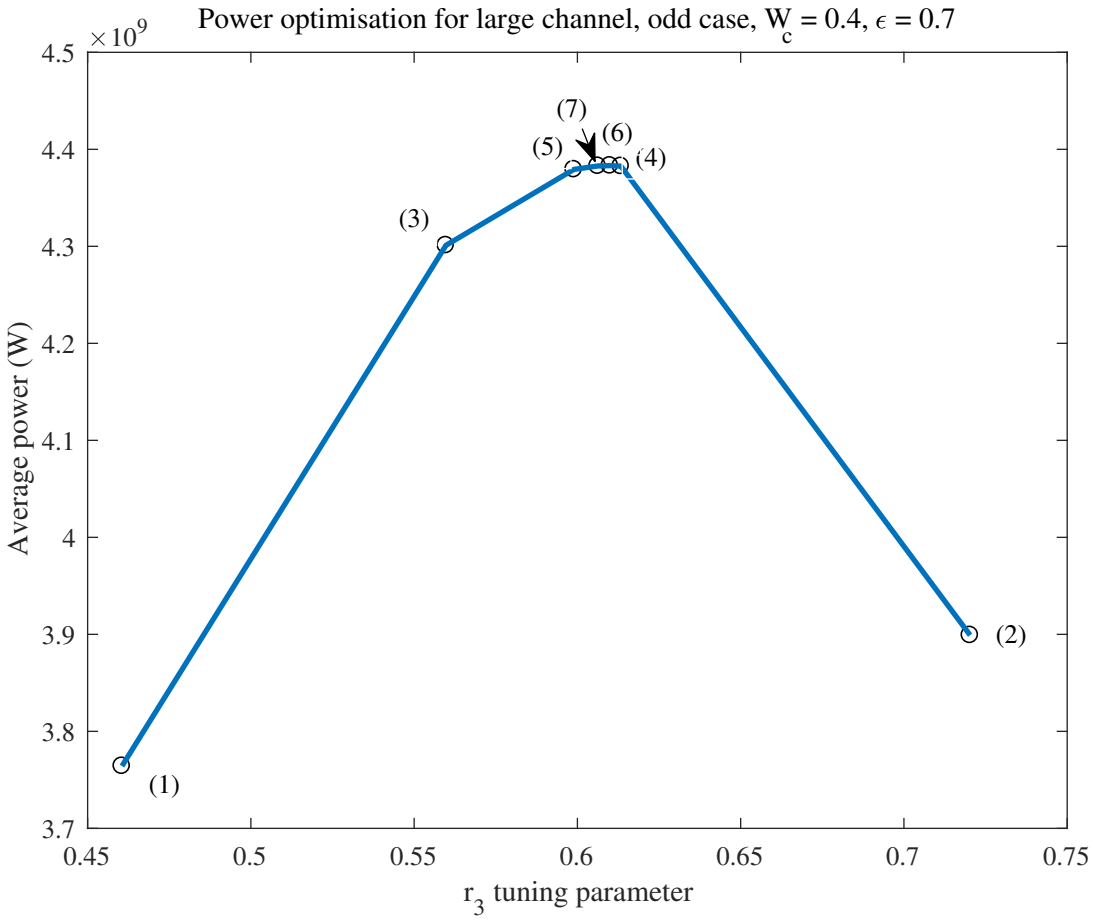

Figure 4.3: Optimisation curve showing the variation of array power with the row tuning parameter, r_3. Each circle denotes an iteration of the optimisation routine.

the same blockage ratio are near identical. Vennell (2011b) further suggests that for cases where turbine densities are near-identical, the optimisation search space can be reduced to one-dimension to more efficiently find the optimal power available from an array of turbines.

Optimisation was achieved using a Python sub-routine based on the *minimize_scalar* function in the optimisation package of the SciPy library. The tuning parameter was subject to the constraint: $0.3 < r_3 < 0.99$, and the margin of tolerance for optimal convergence was set to 0.01. The starting value for the optimisation search was taken from the 1-D model output. An example optimisation curve is shown below in Figure 4.3 for a single row in the moderately constricted large channel with blockage ratio $\epsilon = 0.7$.

For each array configuration, the simulation was run until the power computed during each half-tidal cycle converged. The power was considered converged when the fluctuations between the last two half tidal cycles were smaller than the chosen convergence criterion. Simulations were completed on the NeSI Mahuika cluster (https://www.nesi.org.nz/) using 32 cores per

run and multiple runs could be completed at the same time provided the cluster was not being used by other parties. Each run took approximately 24 - 32 hours to optimise array power with respect to r_3.

4.3.7 Array scenarios

Due to the relatively long simulation time, fewer cases are tested here with SUNTANS compared to the last chapter which used the 1-D model. Test cases were limited to four major array configurations (Figure 4.4), each of which was tested with blockage ratios between 0 and 0.8 at 0.1 intervals ($\epsilon = [0 : 0.1 : 0.8]$). Two single-row and two double-row arrays were tested. Double-row arrays were filled simultaneously e.g. turbines were added to both rows at the same time.

4.3.7.1 The "inside case"

A single row is positioned at the most constricted part of the channel (e.g. $x_{\mathrm{R}} = 0$)

4.3.7.2 The "outside case"

A single row is positioned mid-way along the constriction. In the large channel, this row is placed at the inflexion point of the Gaussian curve. In the small channel, the inflexion point fell within 200 m of the centre of the channel and for reasons pertaining to the next case, this row was moved to $x_{\mathrm{R}} = 250$ for the outside case in the small channel. In the large channel, the inflexion point was at $x_{\mathrm{R}} = 3535$.

4.3.7.3 The "odd" two-row array

This array consists of two-rows, one at the same position as the inside case and the other at the same position as the outside case. Originally, the second row was positioned at the inflexion point of the constriction in both channels, however placing, a row at the inflexion point of the small channel ($x = 141$ m) resulted in the effective turbine row-areas overlapping (rows are assumed to extend 100 m upstream/downstream of the row-centre). Accordingly, for the small channel, the second row was instead placed 250 m downstream from the first row.

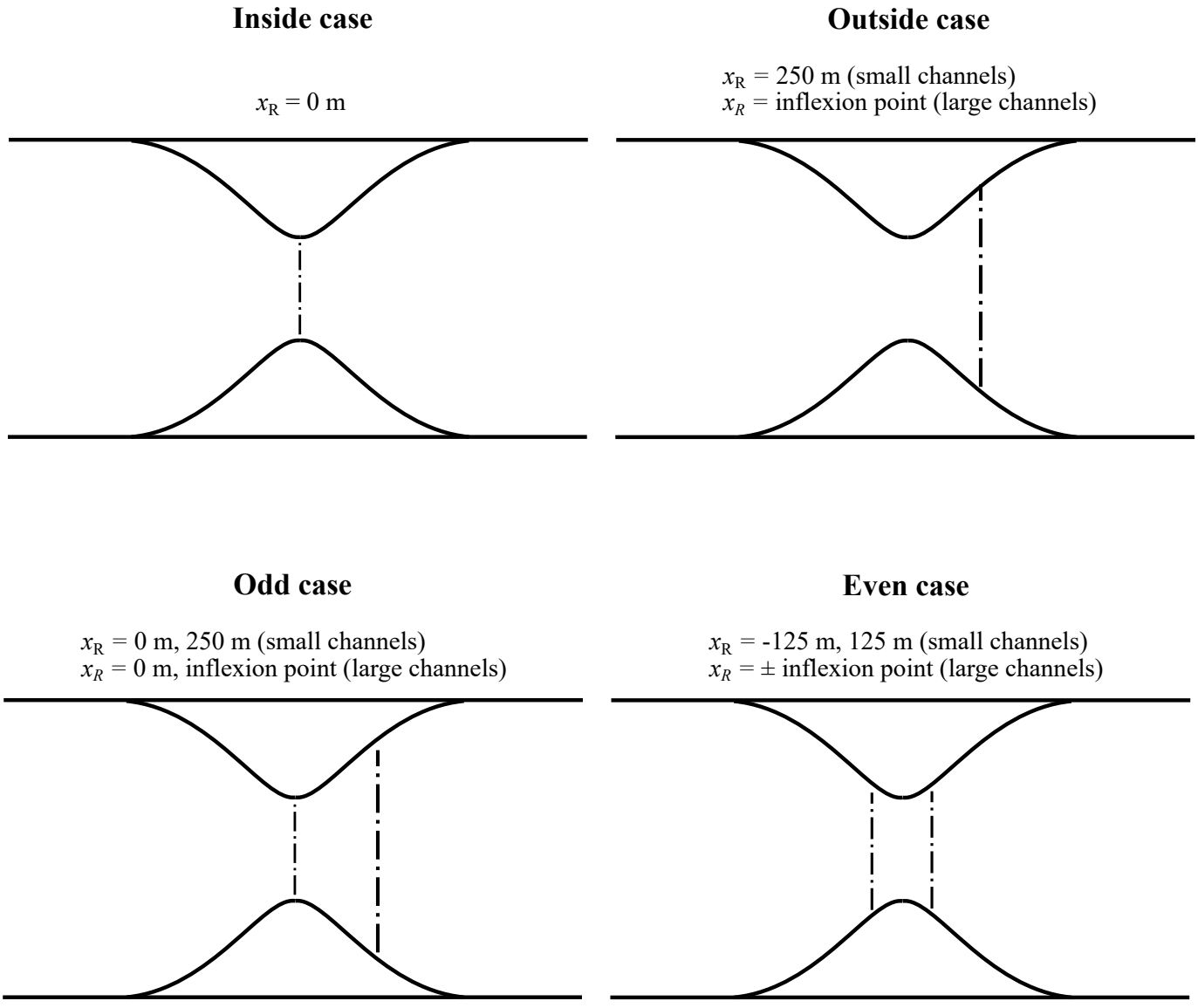

Figure 4.4: Schematic diagrams (bird's eye view) of the four array test cases presented in this chapter

4.3.7.4 The "even" two-row array

Two rows are placed either side of the constriction at a distance equal to the separation distances of the "odd" scenario. This scenario here is to test whether it is beneficial to utilise the most constricted part of the channel at the cost of placing a second row further out, or if it is preferential to take a compromised approach where rows are placed either side of the narrowest cross-section.

4.4 Undisturbed channel dynamics

Channel dynamics are presented here in the absence of turbines first to illustrate the 2-D flow regime of the idealised channels used in this thesis and how they differ from the simpler 1-D presentations of chapters precedent. The presence of a jet at the constriction (and at the channel exit for the small channel) causes flow to become non-uniform and eddies are created. These evolve and propagate which impacts upon the channel transport and available power. The following sub-sections provide a qualitative overview of macro-scale processes occurring in the highly constricted large and small channels respectively. The most constricted case was chosen because the effects are most pronounced. Similar effects happen to a lesser degree in the moderately constricted versions of these channels. A comparison to the 1-D and 2-D channel-turbine models are presented at the end of this chapter.

4.4.1 Large channel

Figure 4.5 shows the normalised head, transport and power [lost to seafloor drag] for one tidal cycle of the large, highly constricted channel (top) and small, highly constricted channel (bottom). Grey lines on Figure 4.5 mark time steps where 'snapshots' of the channel and near-channel dynamics are presented in the following sections. The following sections present a time-series of the free-surface elevation overlaid with velocity vector as well as surface elevation along three channel-wise transects. The first, central transect runs along the line $y = 0$ and then the other two are evenly spaced along lines $y = \pm 200$ and $y = \pm 4000$ for the small and large channels respectively. These two latter lines cut off where the constriction protrudes into

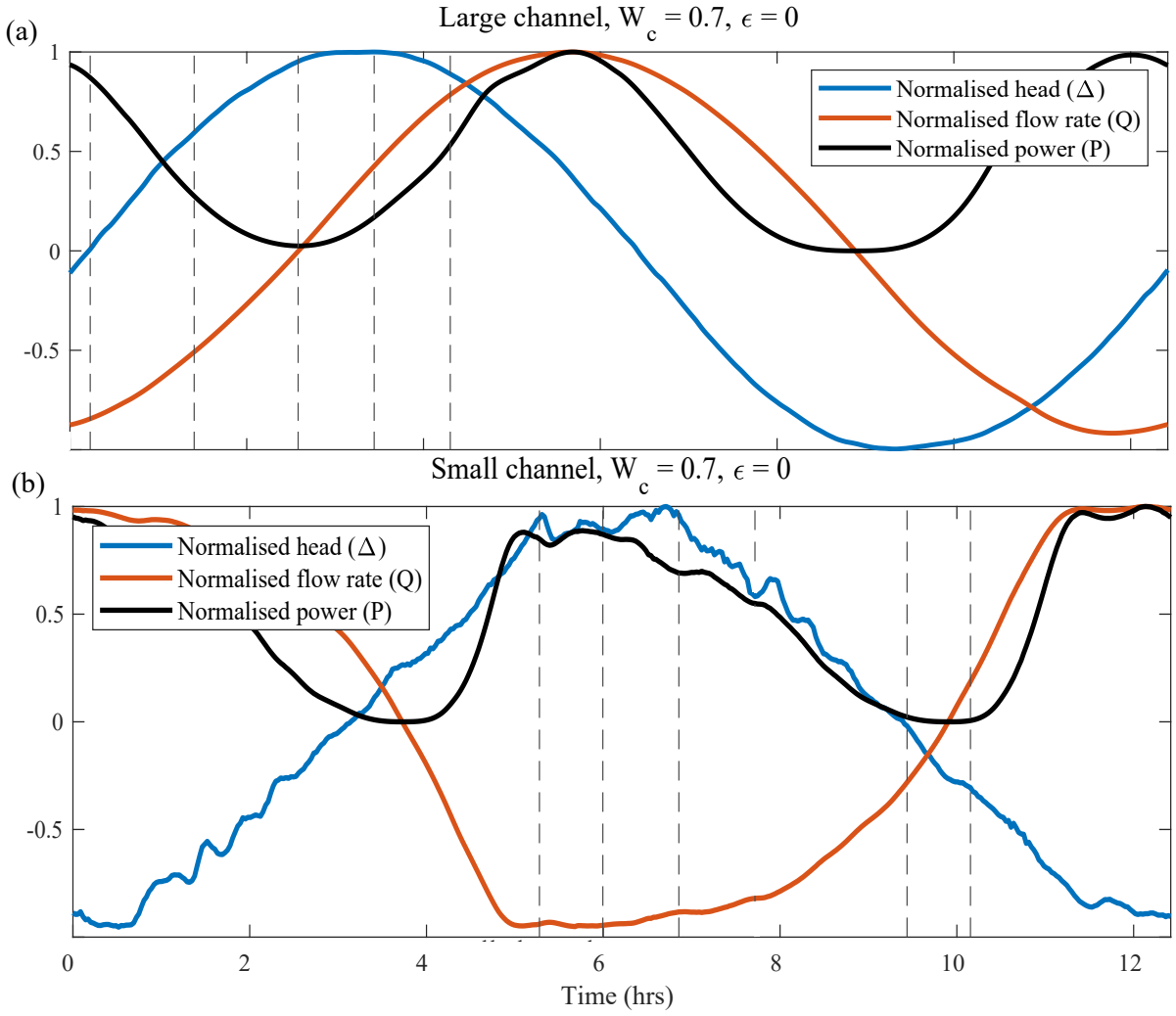

Figure 4.5: Normalised undisturbed channel head difference, flow rate and power for the large highly constricted channel (top) and small highly constricted channel (bottom). The black solid power line is the total power lost to naturally occuring bottom drag in the channel.

the channel centre.

A series of images pertaining to this discussion are shown on the following pages. Flow is typical in snapshot 1 (Figure 4.6). Tidal elevation is higher in the right-hand bay and flow is travelling according to the pressure gradient (e.g. from high to low hydrostatic pressure). Water accelerating through the constriction is matched with a corresponding sea surface drop, and then recovery as the flow expands as predicted by Bernoulli. The beginning of an eddy can be pictured on the left hand side of the constriction due to the constriction exit jet.

In snapshot 2 (Figure 4.7), approximately 1.2 hours later, the tide has changed such that the left hand side is now higher than the right. Inertia in the tidal currents means the net direction of water is against the pressure gradient which has not yet succeeded to decelerate the flow. The eddy seen in the last snapshot is now a prominent feature and a smaller eddy is forming below the upper, stronger eddy. The constriction jet flows around the stronger eddy causing it to curl upwards as it passes through the channel. The eddies cause detectable but near-negligible differences in head across the three transects. The sea surface rises and falls in the near vicinity of the constriction on the left hand side due to the competing accelerations of the constriction, flow expansion and eddies.

Snapshot 3 (Figure 4.8) is taken at still tide. Channel transport and the power lost from the flow to drag in the channel are at their minimum values. There are still remnants of the downstream eddies although these features have been largely dissipated. The head difference at the channel ends continues to increase to its maximum in snapshot 4 (Figure 4.9). In snapshot 4, the pressure gradient has overcome the inertia of the flow and water is flowing from left to right with the pressure gradient. The mostly dissipated but ever-present eddy forces flow to curl towards the bottom of the right-hand side of the channel. Free-surface perturbations are present on the upstream side of the constriction due to the slower flow velocities associated with the eddy remains.

In snapshot 5 (Figure 4.10), the eddy is nearly completely dissipated and the upstream flow is near-uniform. However, in snapshot 6 (Figure 4.11), the curved flow seen in snapshot 4 has caused a new downstream eddy to form on the top of the right-hand side of the channel (e.g. the inverse to the original eddy). This cycle of mirroring eddies repeats itself on the opposite side of the channel. Despite the peculiarities of the velocity field seen in these examples, the

macro-scale flow parameters such as head difference, power lost to drag and channel transport all behave analogously to 1-D theory (Figure 4.5(a)).

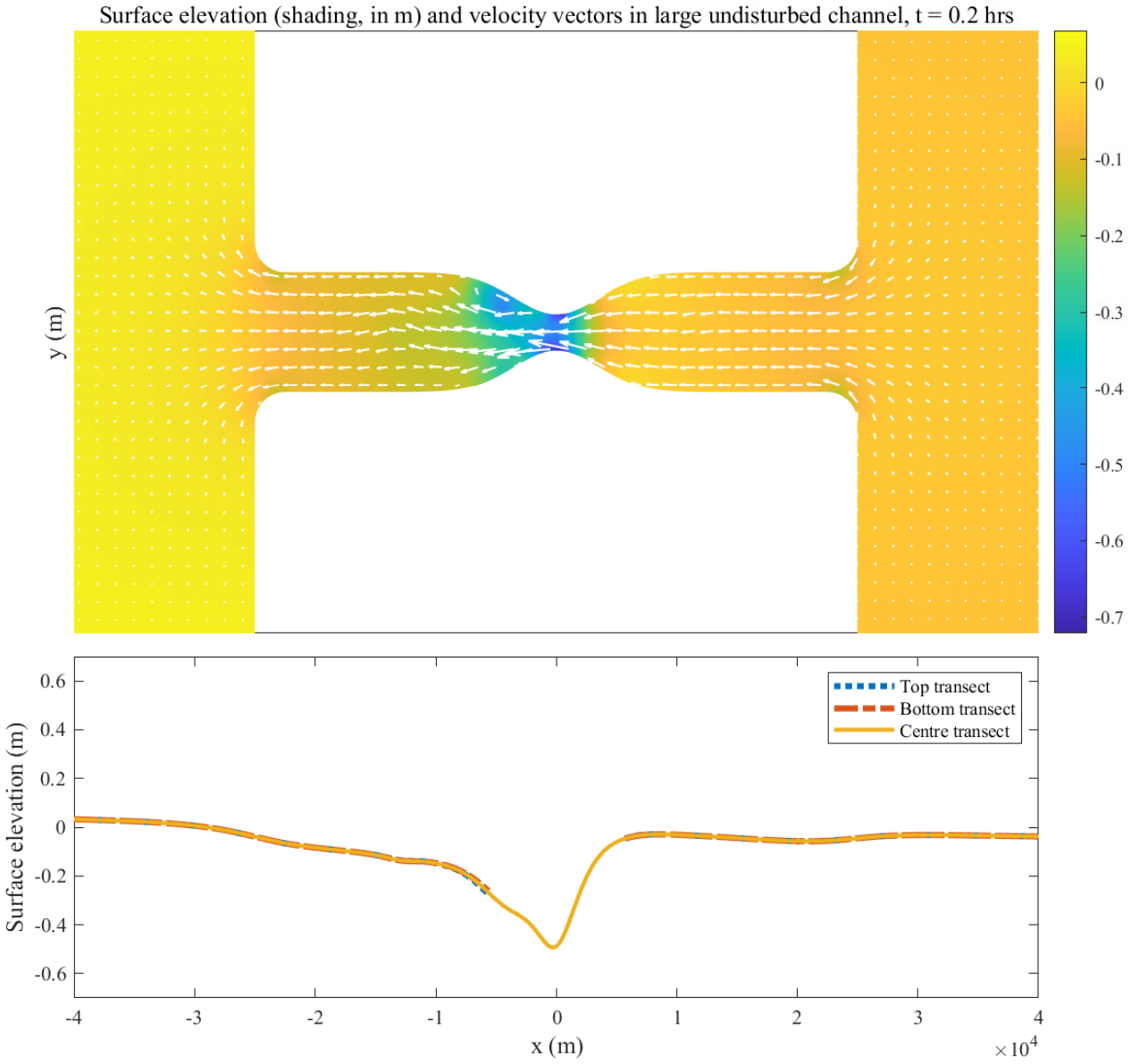

Figure 4.6: Snapshot 1 (bird's eye view) of highly constricted large channel dynamics. Shading in upper figure corresponds to surface elevation and arrows are velocity vectors. The lower line plot shows the surface elevation across three horizontal transects.

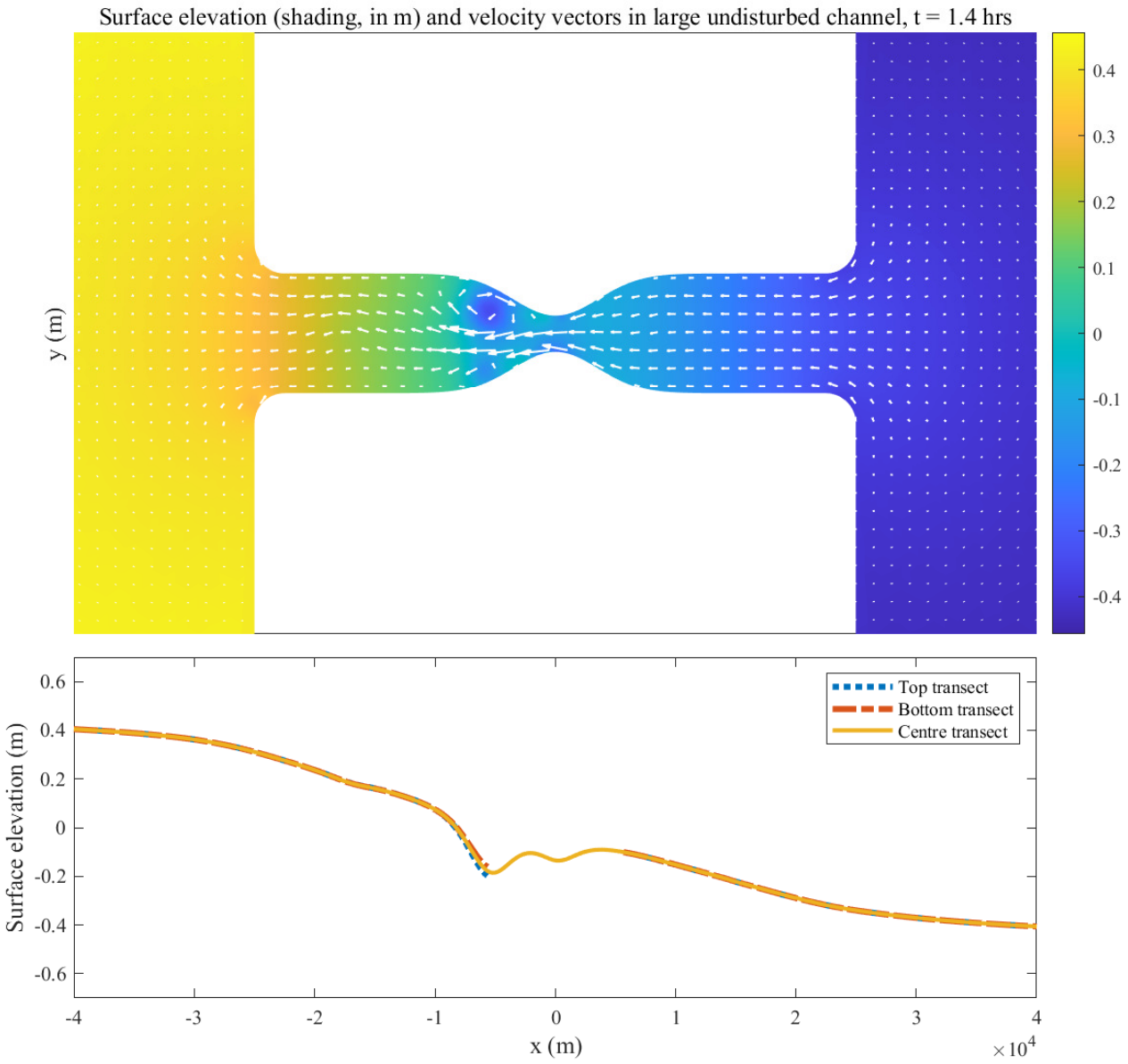

Figure 4.7: Snapshot 2 (bird's eye view) of highly constricted large channel dynamics. Shading in upper figure corresponds to surface elevation and arrows are velocity vectors. The lower line plot shows the surface elevation across three horizontal transects.

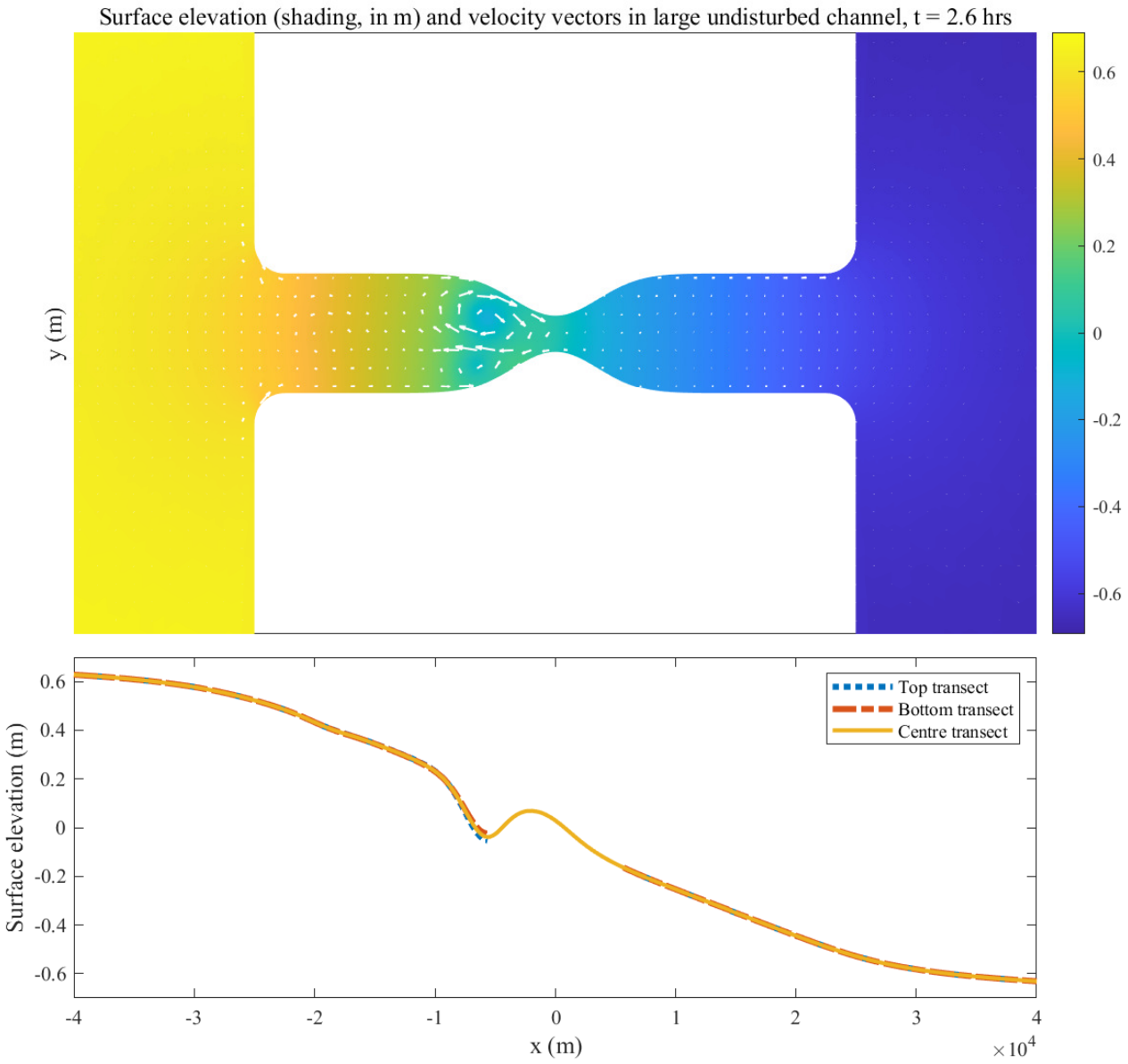

Figure 4.8: Snapshot 3 (bird's eye view) of highly constricted large channel dynamics. Shading in upper figure corresponds to surface elevation and arrows are velocity vectors. The lower line plot shows the surface elevation across three horizontal transects.

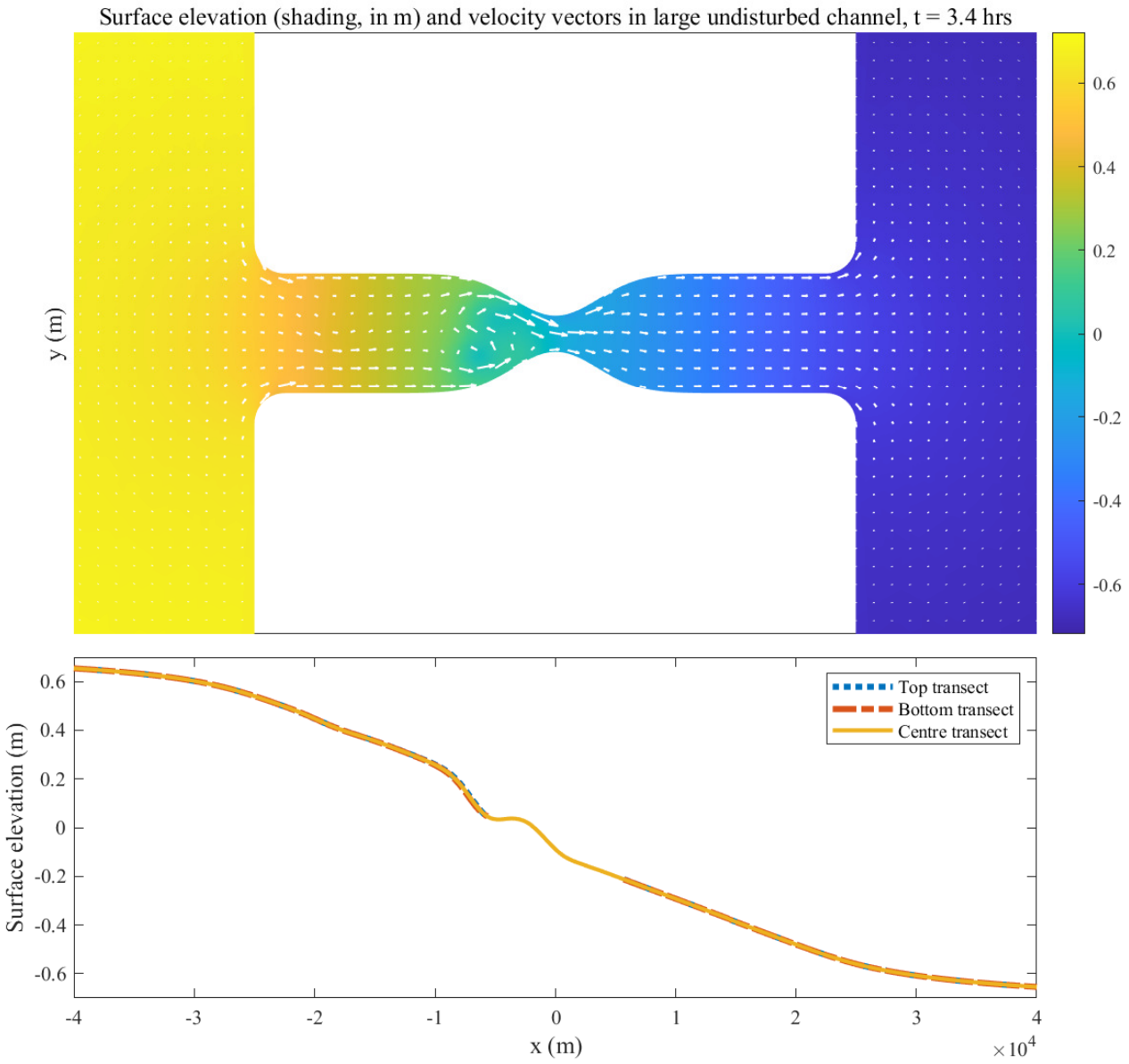

Figure 4.9: Snapshot 4 (bird's eye view) of highly constricted large channel dynamics. Shading in upper figure corresponds to surface elevation and arrows are velocity vectors. The lower line plot shows the surface elevation across three horizontal transects.

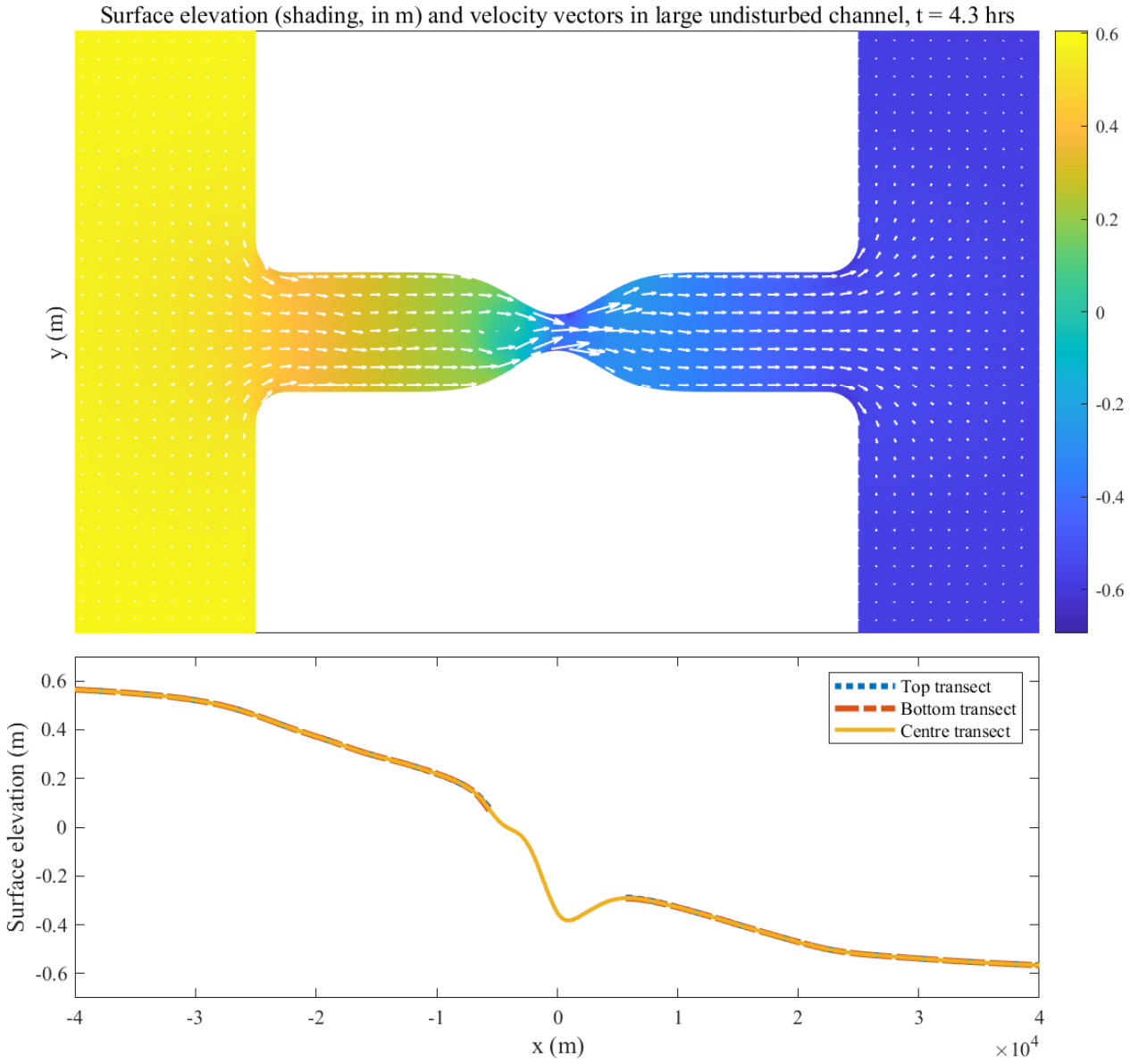

i.e

Figure 4.10: Snapshot 5 (bird's eye view) of highly constricted large channel dynamics. Shading in upper figure corresponds to surface elevation and arrows are velocity vectors. The lower line plot shows the surface elevation across three horizontal transects.

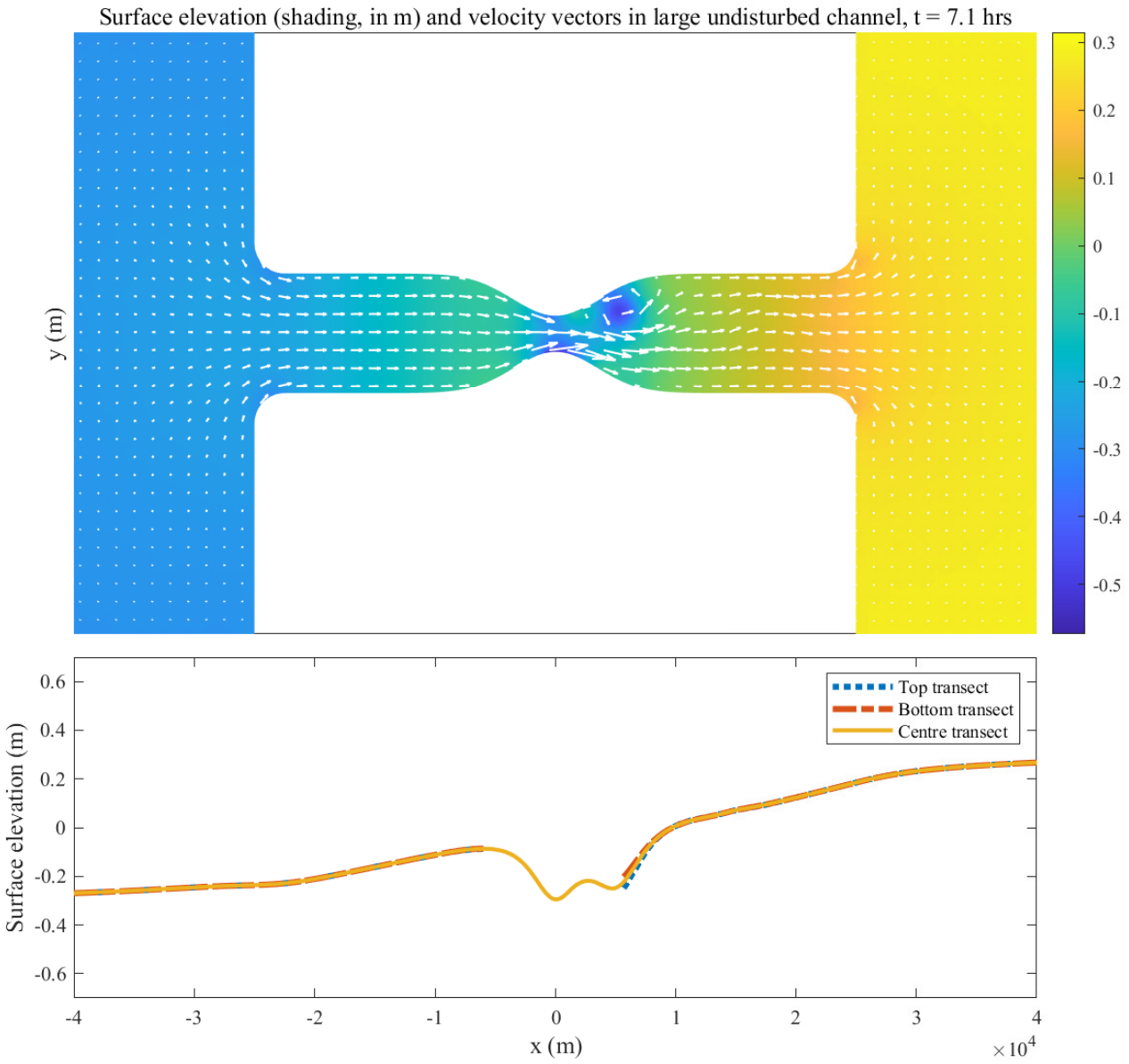

Figure 4.11: Snapshot 6 (bird's eye view) of highly constricted large channel dynamics. Shading in upper figure corresponds to surface elevation and arrows are velocity vectors. The lower line plot shows the surface elevation across three horizontal transects.

4.4.2 Small channel

The jaggedness of the normalised head curve for the small channel indicates that the macro-scale channel dynamics are being affected by the exit jet and resultant eddies. As per the large channel in the precedent section, the following figures show various snapshots in the tidal cycle (denoted by grey lines in Figure 4.5(b)) for the undisturbed, highly-constricted small channel. Again, a series of snapshots are provided on the following pages pertaining to the discussion here.

The first snapshot (Figure 4.12) is taken just after slack tide when flow has started to move with the pressure gradient from left to right. Already, an eddy is present within the channel, similar to the large channel example. In this case, however, the eddy's effects on the flow have extended beyond the channel exit and a secondary jet has formed with two eddies on each side. The bottom eddy is stronger, as flow has accelerated around the within-channel eddy and curled towards the bottom of the channel.

Flow is well established in snapshot 2 (Figure 4.13) - it is at a maximum as is the channel head difference and power loss. The internal eddy is dominating the downstream channel dynamics and the constriction jet is being forced around the eddy. The external eddies are well established and have propagated outwards into the ocean basin. The bottom eddy is significantly stronger than the top eddy. Bernoulli effects (alternate fluctuations in free-surface elevation and flow speed) can be seen along the channel transects.

At snapshot 3 (Figure 4.14), the head difference has decreased to zero. The large eddies (off screen) are still present and dominating flow in the right-hand ocean basin. The interaction with this eddy and the internal channel eddy that has now migrated to the channel exit is causing a complicated free-surface both within the channel and in the near-channel vicinity of the right-hand ocean basin - this explains the jaggedness of the head curve in Figure 4.5). In snapshot 4 (Figure 4.15), the tide has started rising on the right-hand side and flow is starting to move in the opposite direction. The remnants of an old eddy from the last tidal cycle are causing flow to curl around in one direction although by snapshot 5 (Figure 4.16) regular uniform flow has been established. Despite these channels being idealised, features seen in real channels are present. In the absence of Coriolis force, one would not expect to see irregularities (eddies) in the channels' flow. The SUNTANS model was quite sensitive to channel geometry and the implementation of turbine drag (discussed in Section 4.3.2) and so small irregularities in the mesh are likely causing these features to develop.

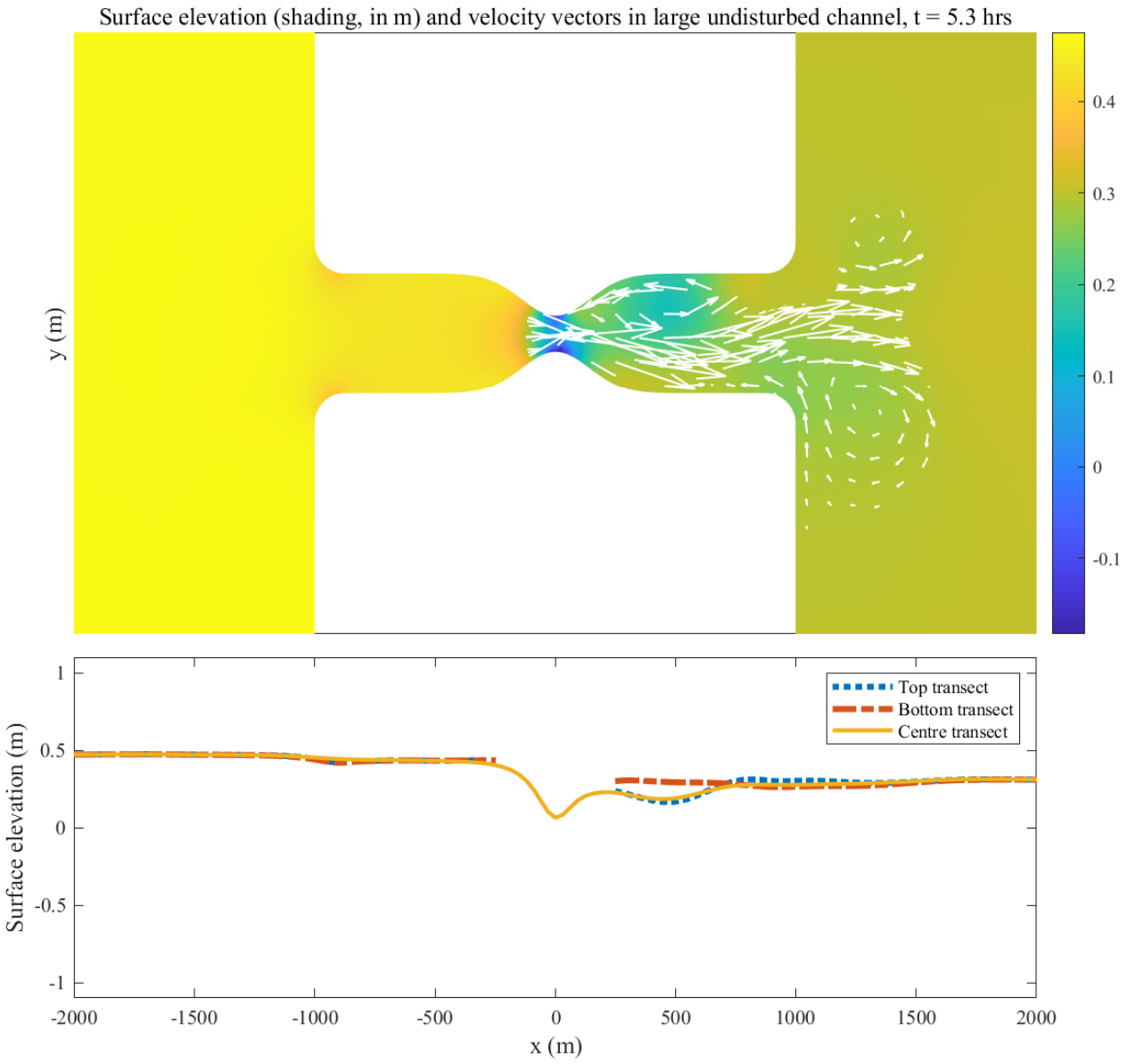

Figure 4.12: Snapshot 1 (bird's eye view) of highly constricted small channel dynamics. Shading in upper figure corresponds to surface elevation and arrows are velocity vectors. The lower line plot shows the surface elevation across three horizontal transects.

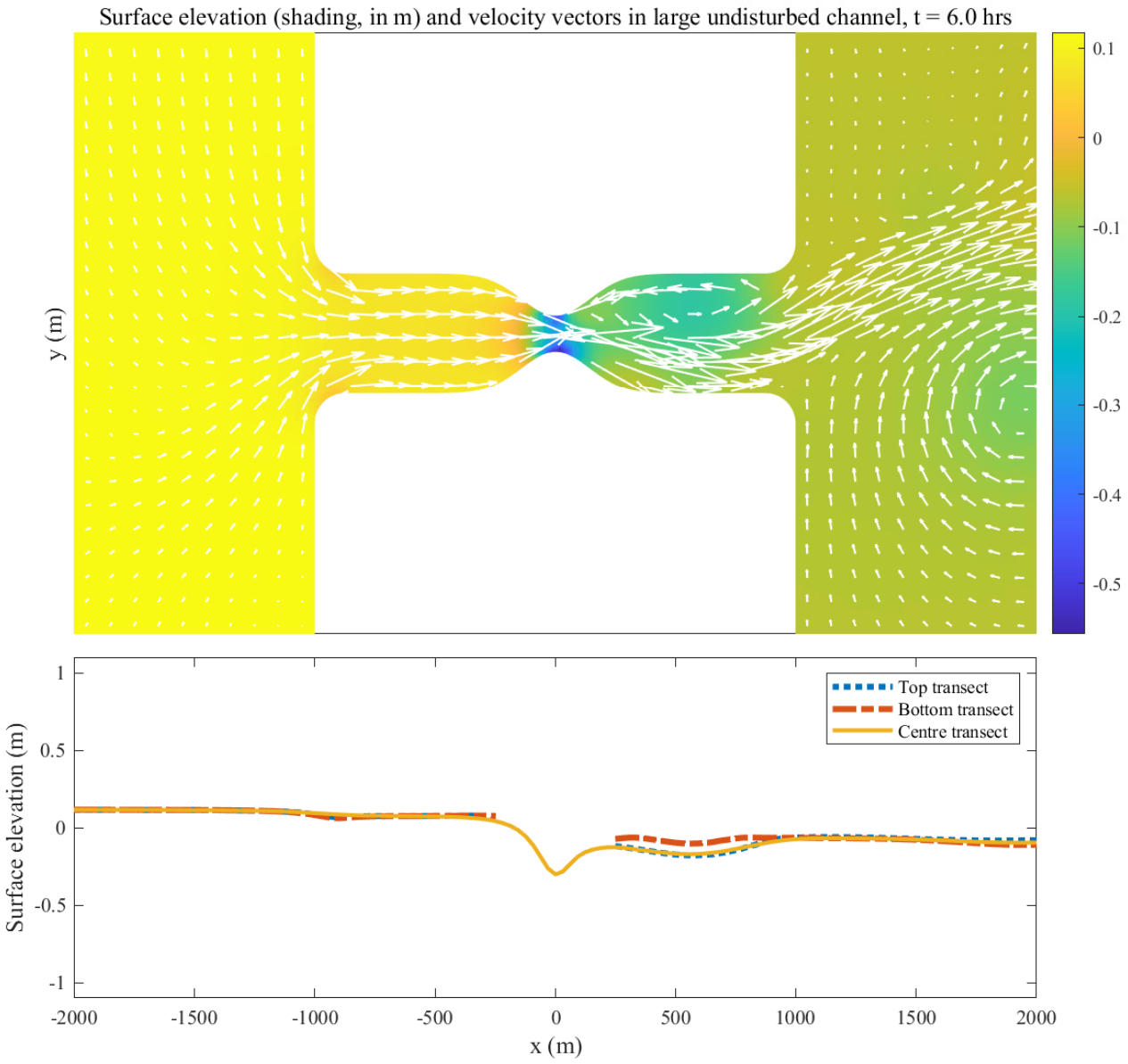

Figure 4.13: Snapshot 2 (bird's eye view) of highly constricted small channel dynamics. Shading in upper figure corresponds to surface elevation and arrows are velocity vectors. The lower line plot shows the surface elevation across three horizontal transects.

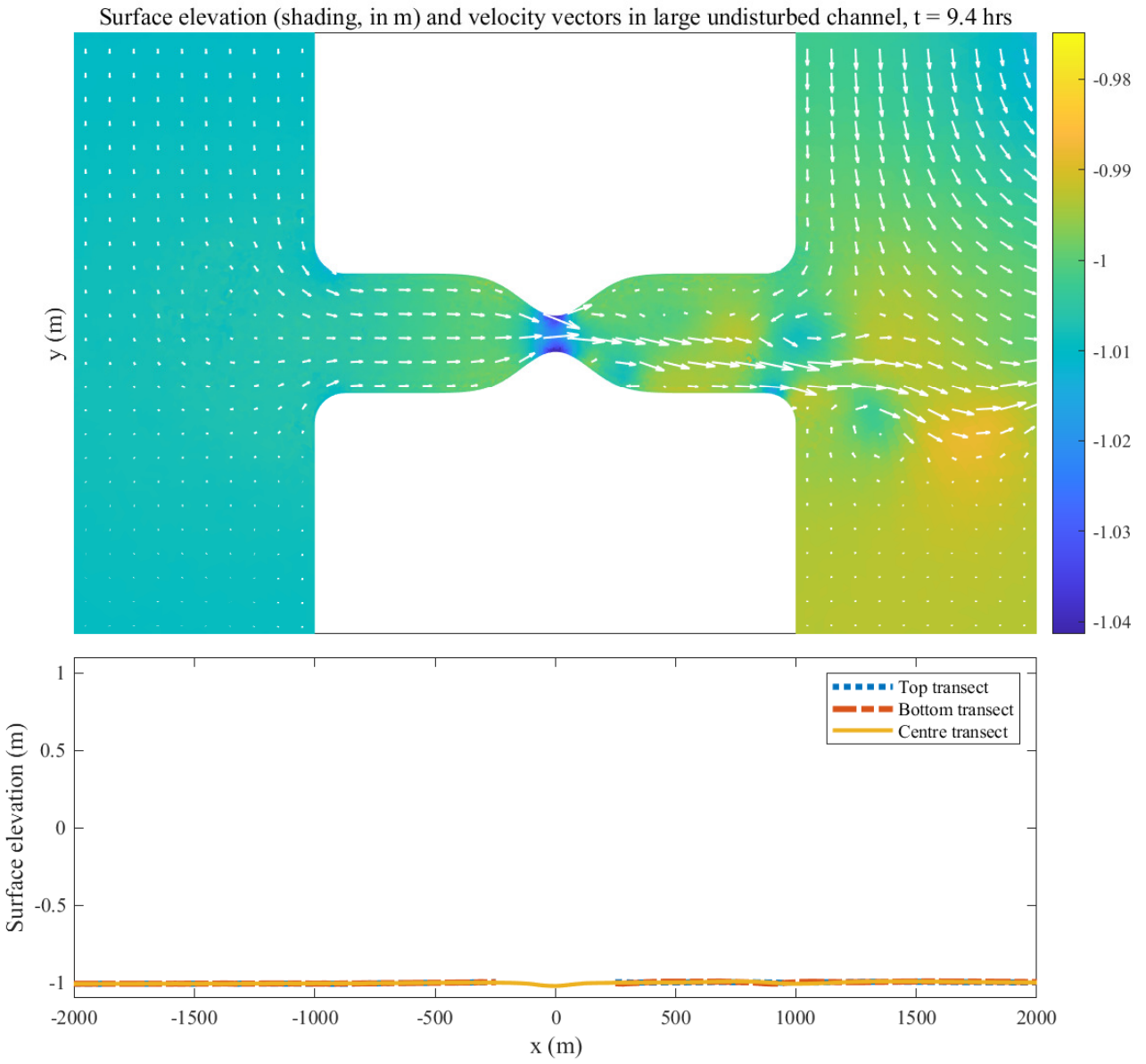

Figure 4.14: Snapshot 3 (bird's eye view) of highly constricted small channel dynamics. Shading in upper figure corresponds to surface elevation and arrows are velocity vectors. The lower line plot shows the surface elevation across three horizontal transects.

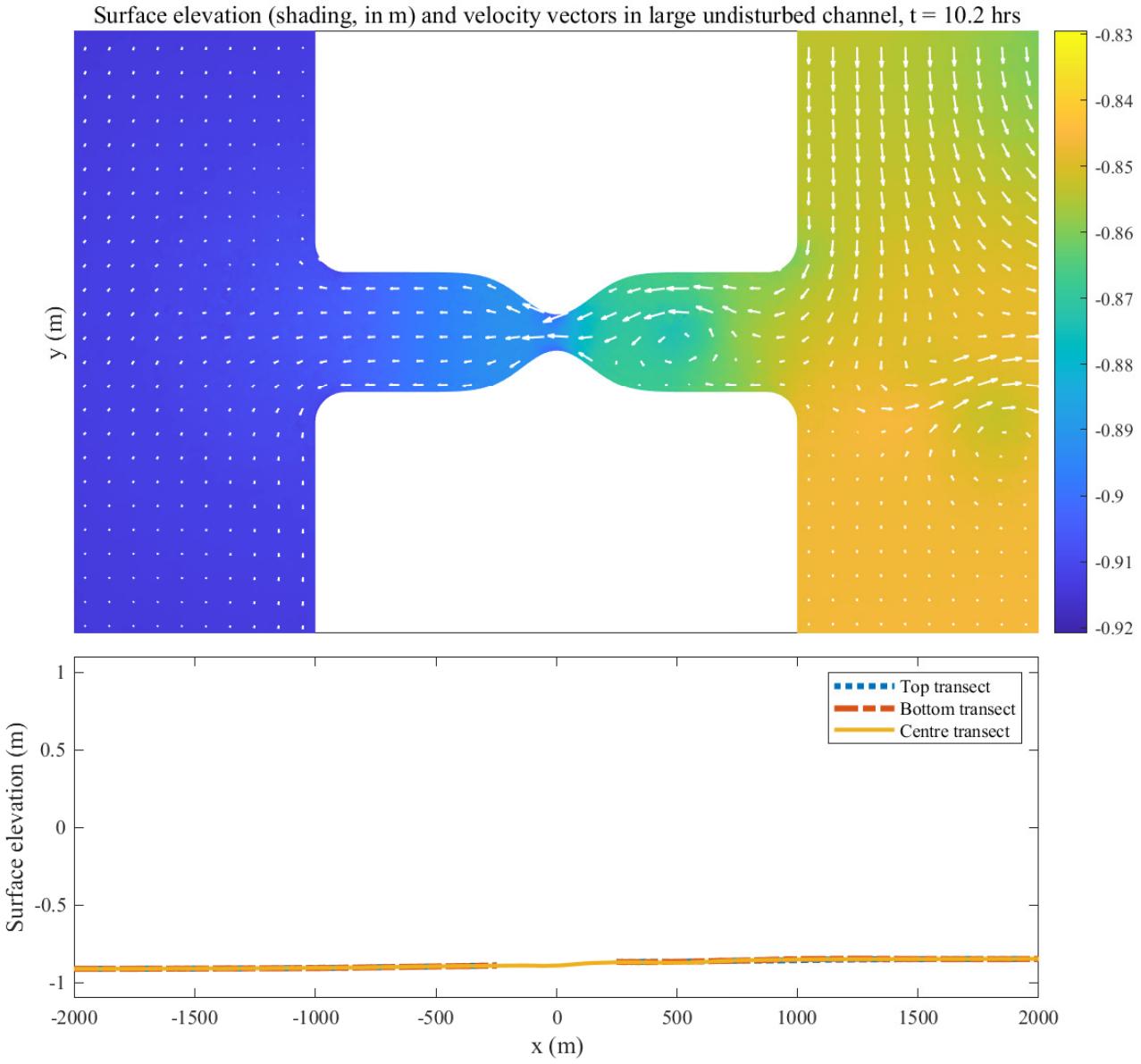

Figure 4.15: Snapshot 4 (bird's eye view) of highly constricted small channel dynamics. Shading in upper figure corresponds to surface elevation and arrows are velocity vectors. The lower line plot shows the surface elevation across three horizontal transects.

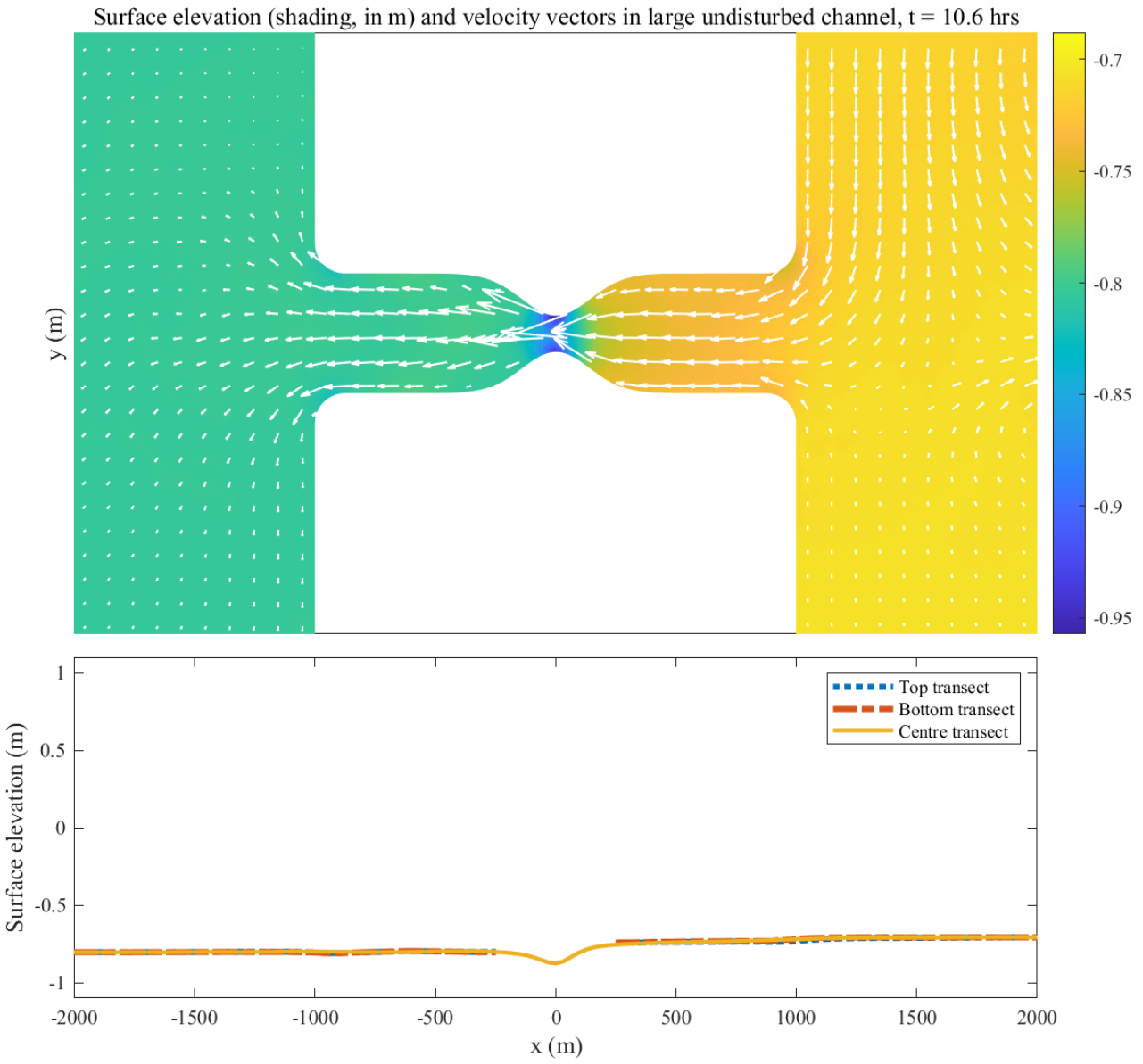

Figure 4.16: Snapshot 5 (bird's eye view) of highly constricted small channel dynamics. Shading in upper figure corresponds to surface elevation and arrows are velocity vectors. The lower line plot shows the surface elevation across three horizontal transects.

4.4.3 Comparison to real channels (Cook Strait and Minas Passage)

Figures 4.17 and 4.18 below show the modelled 2-D depth-averaged velocity fields and bathymetry of Minas Passage and Cook Strait. Flow and bathymetry described in the sections precedent for the idealised channels here share several similarities with these real channels. for instance, the eddies forming on the bottom side of Minas Passage that then forces the constriction jet to flow on the opposite side of the channel is a feature seen in both the large and small channel examples above (Sections 4.4.1 and 4.4.2). Smaller eddies are also present on the downstream

side of the constriction in Cook Strait. These two real channels also have a deep channel running through their centre. Bathymetry here also has the deepest part of the channel in the centre; however, the transition from the wall to the deepest part of the channel is achieved over a much smaller distance in the idealised channels of this thesis. These real channels are more complicated in terms of flow and bathymetry than the test channels used here. However, the degree of similarity between the test cases and these real channels suggests that results from this work can be applied to real channels, particularly at the macro-scale which is the focus of this investigation.

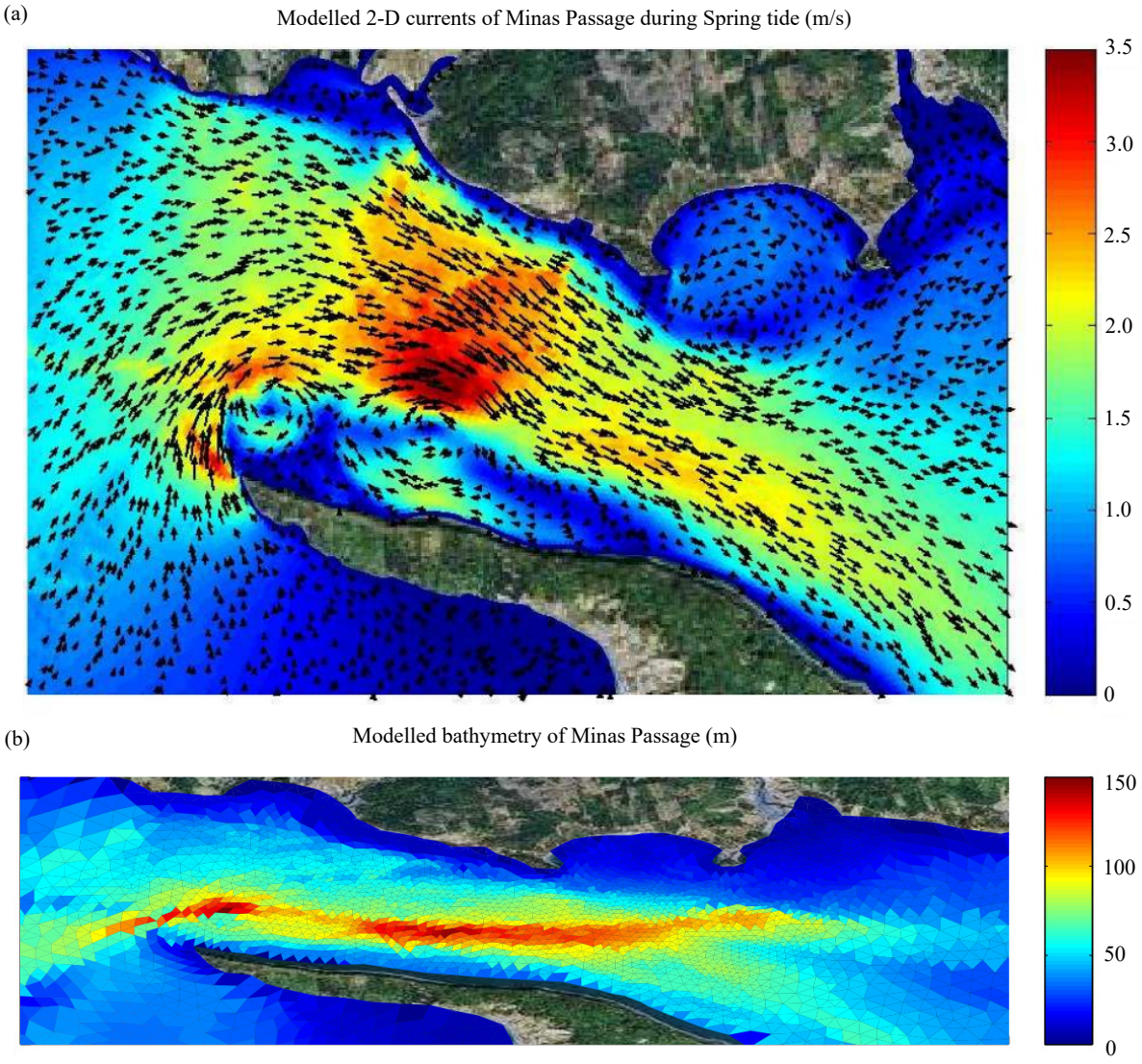

Figure 4.17: Example velocity field and bathymetry of Minas Passage, Canada (modified from Karsten *et al.* (2011)

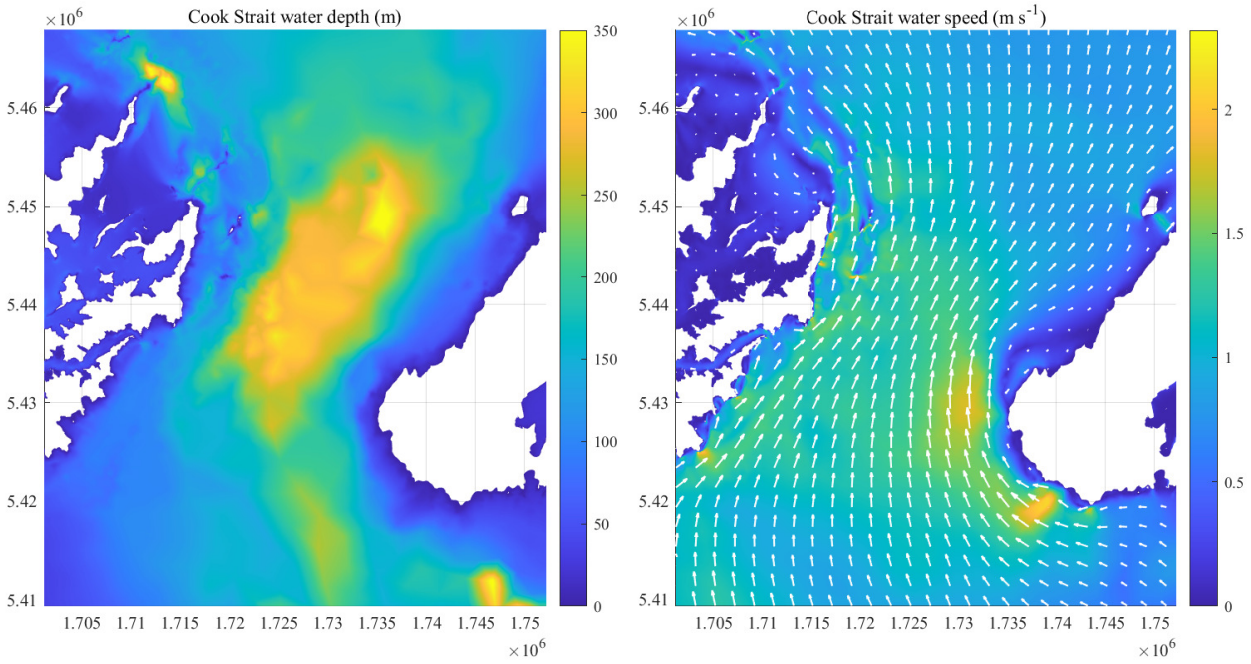

Figure 4.18: Example bathymetry and velocity field of Cook Strait, New Zealand (taken from MetOcean Solutions 2019)

4.5 Power generation from a single row of turbines

4.5.1 Power generation from a single row inside/outside of the constriction

Figure 4.19 shows the array power (a,b), turbine power (c,d) and average load per turbine (e,f) for a single row of turbines for both the inside and outside cases (solid lines and dashed lines respectively) and different constriction factors (colours). Key findings are discussed in the following sub-sections. It is re-iterated that failing to tune turbines causes them to create too much drag in the channel, which reduces the power output from the whole array. Turbines must be tuned to maximise power output which can cause the force per turbine to reduce but the output of the array to still increase.

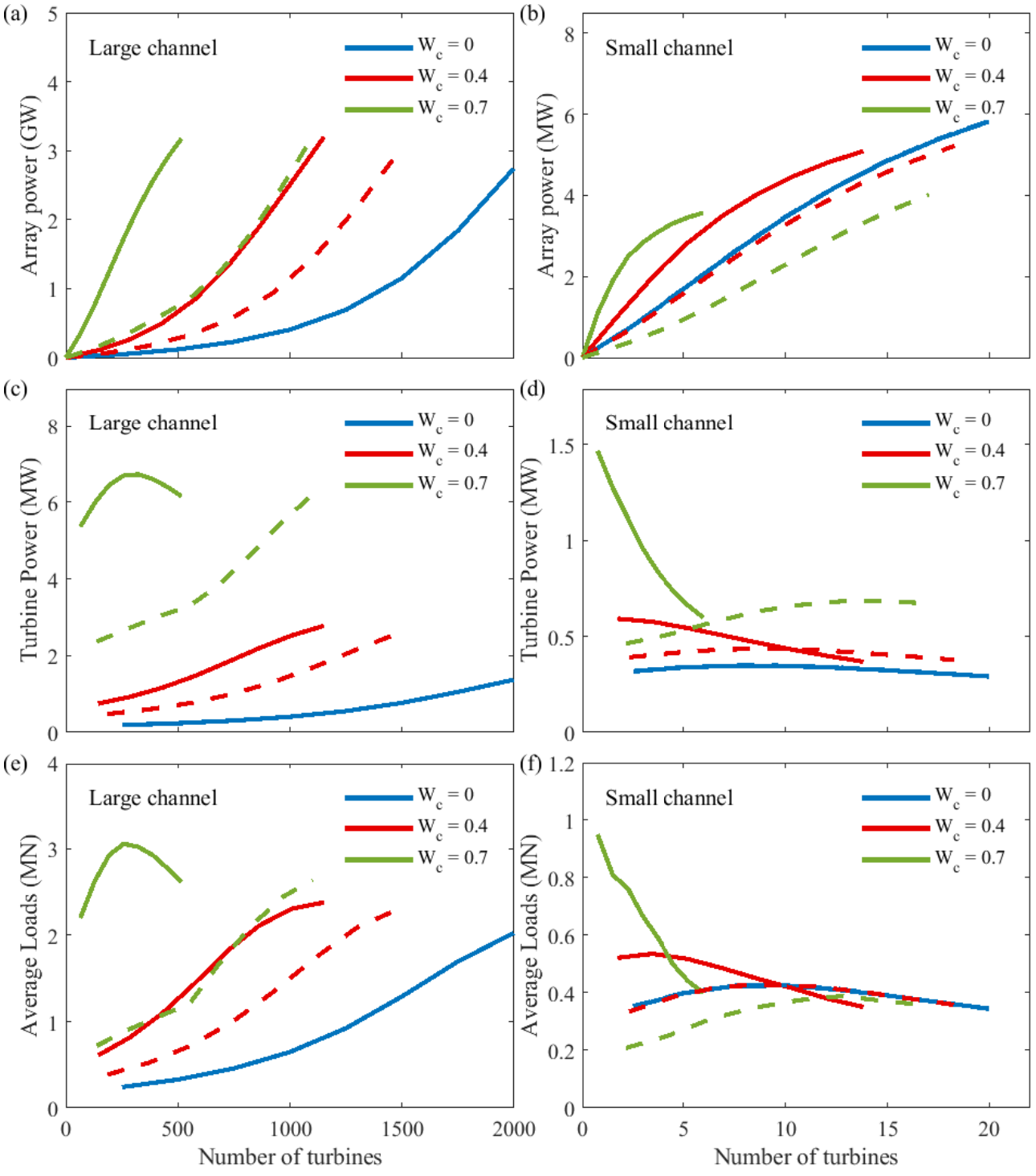

Figure 4.19: Array power (a,b), power per turbine (c,d) and average load per turbine (e,f) for a single row both inside (solid) and outside (dashed) of the constricted zone for the large and small channels with the three constriction factors tested

4.5.1.1 More power can be generated using fewer turbines in the smallest cross-section

1-D theory presented in the past chapter predicted arrays in constricted channels will generate more power from fewer turbines but eventually be limited by their potentials at high blockage. Results from the 2-D model confirm that using the constricted area allows more power to be generated from significantly fewer turbines. For all cases except the most constricted small channel, the same total array power can be achieved by both the inside and outside row configurations using a different amount of turbines.

At high blockage ratio in the highly constricted small channel, the outside row generates slightly more power due to excessive flow reduction occurring from the inside row configuration (Section 4.8.2). A row of turbines in the most constricted zone benefits from the velocity advantage and subsequently turbines here generate more power but exert more drag on the flow (drag is quadratically proportional to velocity). The smallest, most constricted channel is an extreme case and the drag forces are so profound at high blockage that flow is choked to the point of limiting power generation. For highly constricted drag-dominated channels, these results suggest it may be beneficial to generate power outside of the constriction to avoid this - especially if a proposed turbine array is intended to block a large portion of channel cross-section. It should be noted that this difference in generation is small. The cost of the additional turbines required to achieve the additional power of the outside design may make it unfeasible.

Although the result that the most power is generated by using the smallest cross-section may be obvious, Figure 4.19 quantifies how this power scales with the number of turbines and the size of the constriction.

4.5.1.2 Power per turbine increases according to blockage ratio and channel dynamics

In line with findings of the past chapter, adding turbines to an array always increases power generation but the size of this increase varies with blockage ratio and channel size. Array power for the large channels has positive concavity which means initially adding turbines to the array has less effect on total power growth. Beyond a given blockage ratio, these curves steepen and the

power return on additional turbines to arrays in these channels increases significantly. The concave down nature of the lesser-constricted small channels means enhanced array growth occurs when the number of turbines in the array is few. In the most constricted small channel, there are diminishing returns on all additional turbines to the array. The delay in enhanced power return for the large channels occurs at a much smaller number of turbines for the constricted cases due to the threshold blockage ratio being more readily achieved. However, perhaps the main driver of this high power return phenomenon occurring at different development stages across all channels is that the addition of turbines (and therefore drag) is causing a shift in these channels' dynamics.

The dual concavity of the most constricted large channel was observed by the 1-D model and is particularly good at highlighting how total channel drag is the main driver of power curve concavity. Both increased constriction (therefore higher velocities, therefore more drag) and the addition of turbines to the large highly-constricted channel increase drag in the channel to the point where it starts behaving like the small drag-dominated channels at low blockage. The channel test cases can be placed on a continuum of drag with the undisturbed, large unconstricted channel at one end and the highly constricted, highly blocked small channel at the other (Figure 4.20). The non-dimensional total drag can be used as an indicator as to where these channel and arrays sit on the continuum. Array configuration alters the position of each test case slightly, the location of each test case is primarily based on the size and degree of constriction in each channel. The outside row cases all result in less drag than the inside row cases and shift the test case slightly to the left of positions shown in Figure 4.20. Midway along this continuum is the drag balance that results in enhanced power growth from increases in turbines and is roughly sketched on the figure, corresponding to total drag values of approximately 1 to 11.

4.5.1.3 Potential limitations are important in the small channel but not in the large one

The potential limitation [more constricted channels have lower potentials (Smeaton *et al.*, 2016)] is clear for the small channel examples. Array powers at high blockage ratios in the constricted small channels are significantly lower than the unconstricted small channel (Figure 4.19(b)).

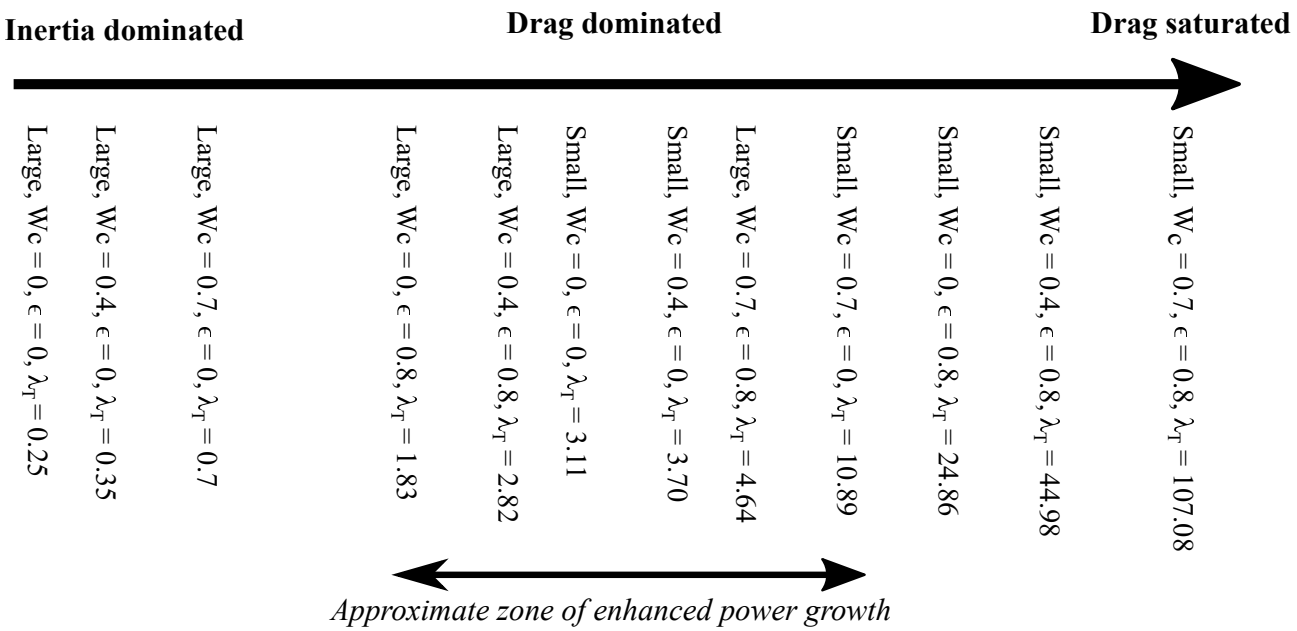

Figure 4.20: Drag continuum representation of channels and test cases. Constriction factor and blockage ratio cause dominance of drag to increase. There is a zone of "drag dominance" that results in enhanced power growth of the array with the addition of more turbines: the *zone of enhanced power growth zone*, which corresponds to a total drag value between about 1 and 11. Having rows in more constricted cross-sections and adding rows to the array shifts the case positions to the right.

This limitation is less obvious in the large channel examples (Figure 4.19(a)). The limiting effect is less obvious but still detectable for the large channel cases in Figure 4.19. It is possible that it may become more obvious at higher blockage ratios than those tested here. When using the 1-D model in the last chapter, the potential limitation did not become significant until approximately $\epsilon = 0.8$. Blockage ratios this high are unrealistic, at least in the near future, especially for the large channel due to the shear number of turbines required to achieve them. It could be argued then that, for all practical purposes, the limitation of channel potential in large channels is unimportant.

4.5.1.4 Using the smallest cross-section requires stronger turbines

The power output per turbine in the row is significantly higher for rows placed within the constriction due to the greater velocities and hence greater forces on the turbines. For all cases in the large channel except the highly constricted inside case, the power from each turbine increases as more turbines are added to the row which is line with findings of Vennell (2012). The most constricted large channel, is near the drag dominance transition point in Figure 4.20 and beyond a certain blockage ratio ceases to behave like an inertial channel. There is a

clear turning point in the power per turbine curve (Figure 4.19(e)) after which the addition of turbines to the inside row causes it to behave more like a drag-dominated channel e.g. the small channel examples. Turbine power and turbine loads are closely related (e.g. $P = Fu$).

Turbines placed in the narrowest cross-section are subject to significantly greater loads than those in the outside case and will need to be built to withstand these forces. Whether it is preferable to use fewer stronger turbines within the most constricted area instead of using more less-robust turbines outside of this zone becomes a question of economics. An initial insight into this provided in Section 4.7.2 by looking at the power-to-force ratio. With no knowledge of capital costs or economies of scale it is impossible to say for certain whether using fewer turbines in the fast flowing constricted area will be worthwhile. This question is more important for the large channel where the bulk of the array power is gained at high blockage ratios, which due to channel size, will necessitate a vast number of turbines. In the small channel, the majority of power is generated from the first turbines added to the channel and fewer are required to significantly block the channel's cross-section.

4.5.2 Effects of the jet on the generation cycle

Downstream of a constriction, an adverse pressure gradient can form. The fast velocities exiting the constriction have lower pressure than the rest of the flow downstream due to the Bernoulli effect. This lower pressure flow results in an adverse lateral pressure gradient. Surrounding higher pressure water flows inwards to try to equilibrate the pressure field which results in flow separation and the formation of eddies.

Figures 4.21 and 4.22 show the power time-series for blockage ratios of $\epsilon = 0.1$ and $\epsilon = 0.7$. Array configurations shown are the inside and outside cases (single rows placed solo - solid blue and green lines respectively) and the odd case scenario (the same rows operating together - plotted as individual rows using dashed blue and green lines respectively). The black curve in the figures denotes the total output from the two-row array. The discussion here pertains to all test cases but, for the sake of brevity, results presented herein are for the small channel only where the key points of the discussion are more prominent.

4.5.2.1 Adding turbines dampens the effects of the jet

Rows of turbines placed outside of the constricted area experience an asymmetric power cycle due to the presence of the exit jet on the downstream side of the constriction whereas rows within the constriction produce the same amount of power during both flood and ebb. While the turbines are downstream of the constriction they experience greater power production from the increased velocities of the jet (power is a function of u^3). However, these rows are also subject to eddies due to being placed within the shear zone of the jet. These effects are, of course, more prominent in the most constricted case where the jet is strongest (Figure 4.21(c)). Here, jagged spikes occur in the power time-series of the outer row during the half cycle when it is downstream of the constriction jet and to a lesser degree, in the central row. This is likely due to turbulent features such as those described in Section 4.4. These effects are only present at low blockage and only for the single row cases.

Both increasing blockage and adding another row of turbines to an array dampen the jagged peaks in the power cycle. In general terms, an increase in drag dampens the effects of the jet by reducing flow through the channel and taking power from the jet to convert into electricity.

Results for the even two-row case are not shown and were excluded for the sake of brevity. They are similar to those for the odd two-row case presented here except both have asymmetric power time-series due to both, at some point, being downstream of the jet. The differences in output between the two-rows in the even case were less stark as both rows were in slower-flowing, larger cross-sections.

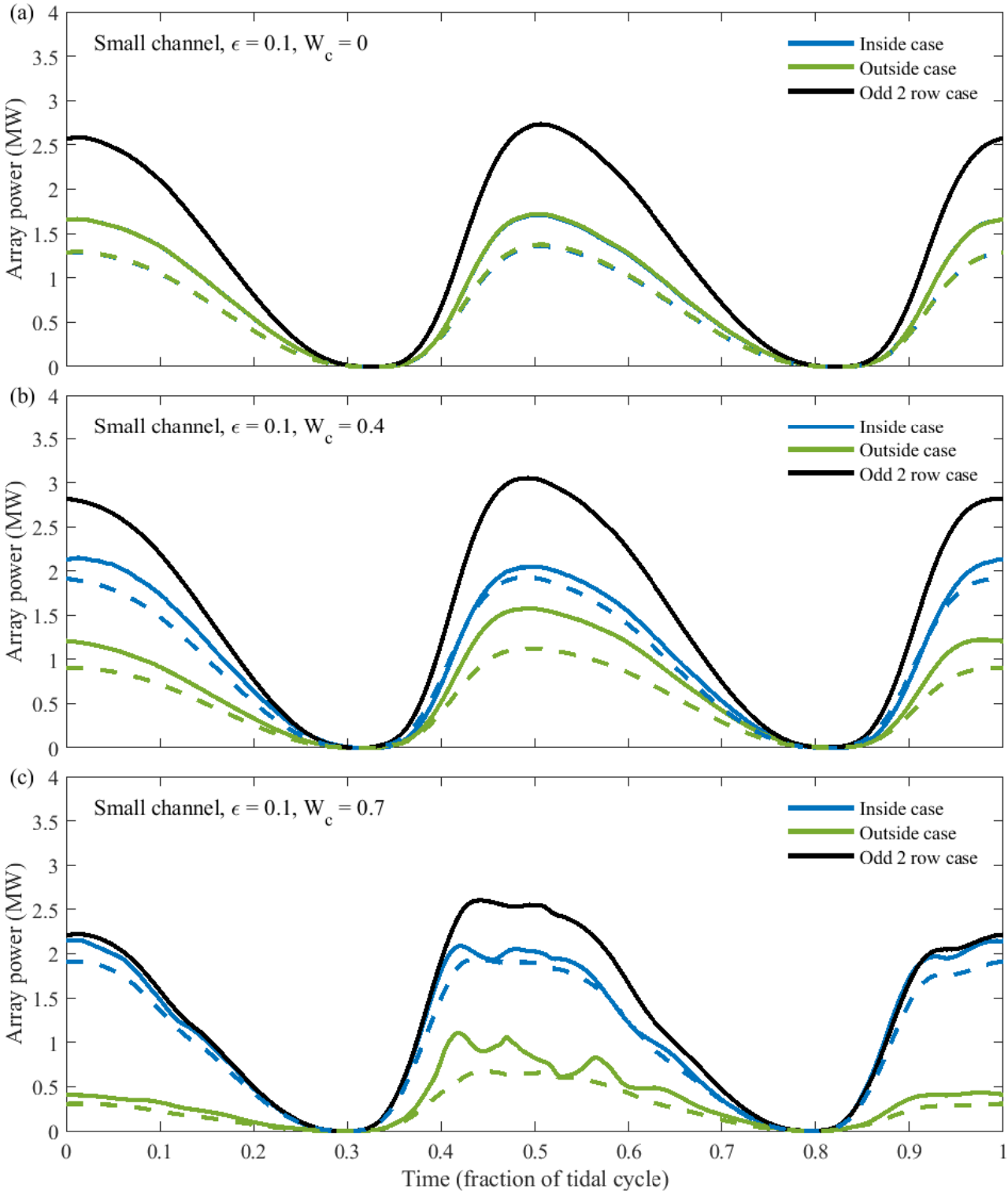

Figure 4.21: Power time-series for rows in isolation (solid coloured) and as part of a two-row array (dashed coloured). The combined power of the two-row array is depicted by the black solid line. These power curves are for the most constricted ($W_c = 0.7$) small channel at low blockage ($\epsilon = 0.1$)

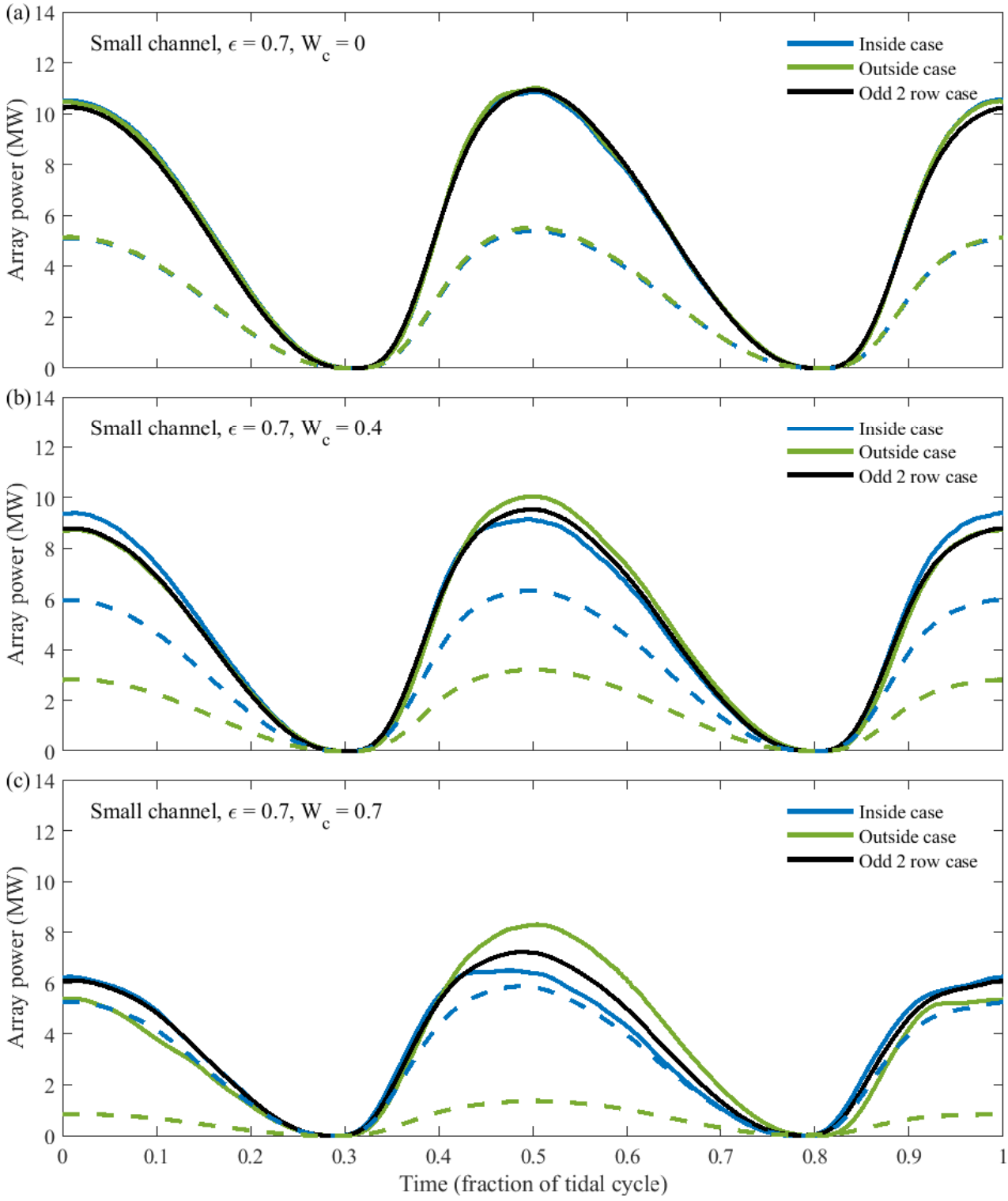

Figure 4.22: Power time-series for rows in isolation (solid coloured) and as part of a two-row array (dashed coloured). The combined power of the two-row array is depicted by the black solid line. These power curves are for the most constricted ($W_c = 0.7$) small channel at high blockage ($\epsilon = 0.7$)

4.5.2.2 The jet causes a net loss of kinetic energy in the small channel

Power generation in the small channels was significantly less than generation predicted by the 1-D model (6 MW versus 25 MW for the worst case). The 1-D model predicted that turbines would be subject to forces in the order of mega-newtons whereas findings here suggest an order of magnitude less - only in the hundreds of kilo-newtons. This disparity is due to both the attenuation of head over the ocean boundaries (discussed in Section 4.8.1); but mostly because of the way constriction jet impacts on the energy balance of the channel. The most constricted small channel, where the change in cross-sectional area (dA/dx) is most rapid, is the most affected.

The jet created on the downstream side of the constriction expels vast amounts of kinetic energy from the channel into the ocean that cannot be captured by the turbines (Figure 4.23). While a jet exists in the large channels also, these channels are sufficiently long and the constriction sufficiently gentle, that the jet is less intense. Subsequently, flow is able to recover before the channel ends. The bottom graphs of Figure 4.23 show the average kinetic energy lost in the large channel is two orders of magnitude smaller than the power generated by the turbines e.g. negligible. In the small channel, the array power and jet-related energy loss are of the same order of magnitude. Increasing the number of turbines in both channels reduces the kinetic energy loss of the jet by converting energy within it to electricity but also by reducing flow throughout the channel (and thereby reducing the intensity of the jet). This kinetic energy loss is significant for small channels and is something that is not captured by 1-D modelling.

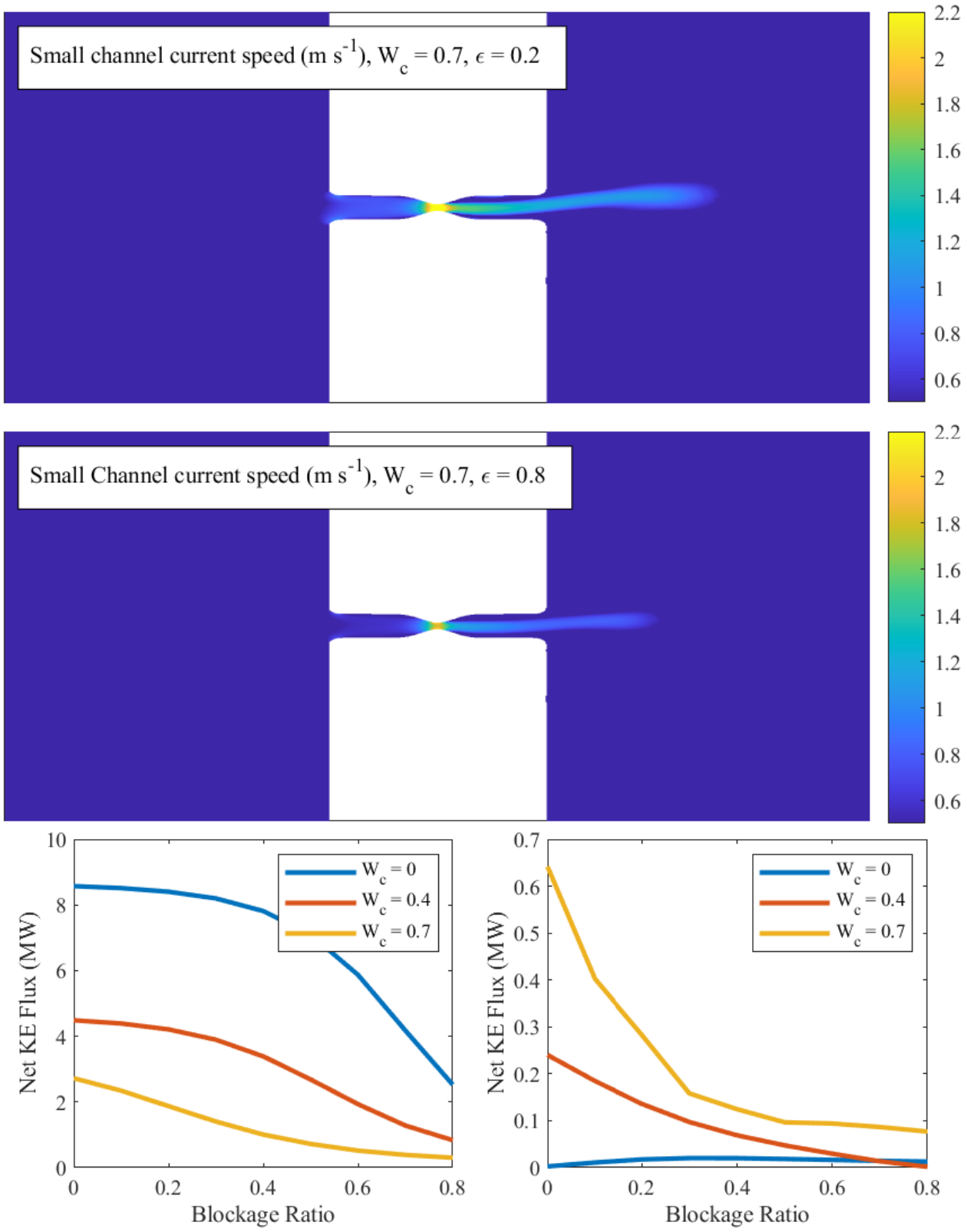

Figure 4.23: The presence of the jet causes an efflux of energy that is significant in the small channel. Flow heat maps show a bird's eye view of the extent and magnitude of the exit jet for low blockage ratio (top figure) and high blockage ratio (middle figure). The lower two plots show the average kinetic energy flux leaving the channel for the "inside" cases. Energy loss is insignificant for the large channel relative to the turbine array generation but important for the small channel.

4.6 Performance of two-row arrays

Turbine rows behave differently when part of an array relative to when they are in isolation. Figure 4.24 compares the average power from the single row cases to the two-row cases. Solid lines correspond to total array output while dashed lines correspond to the individual contributions of the rows in the two-row case as a function of the number of turbines. The black solid line is the sum of the two dashed lines; note that points on the x-axis do not line up between the two dashed lines as the number of the turbines in the array is the sum of the number of turbines in each row and the rows are filled simultaneously.

4.6.0.1 Adding a second row reduces the output of the first row

Individual rows produce significantly less power when acting as part of a two-row array. For few turbines (relative to the maximum amount on the axis), placing them all in a central row will always result in the greatest power production. It is only in the large channel, and at very high blockage that it becomes worthwhile to place down a second row of turbines. The reason this is worthwhile in the large channel is because the potential of the channel is not realised for a single row at 80% blockage (the value to which we have modelled) and so some power remains to be harnessed by the second row. Except for the most constricted channels, placing turbines in an outside row is also competitive if not superior to using a two-row array. Indeed, in the small channel, the two individual rows outperform the two-row array even at high blockage.

4.6.0.2 Most power is generated by the inside row (odd configuration)

The central row does the majority of the generation in all cases - due to the higher flow speeds in the constriction and due to being immune from the asymmetric effects of the jet during the tidal cycle. The discrepancy between the power contributions of the inside and outside rows becomes increasingly profound as the degree of constriction in the channel is increased. Particularly for the small channels, but also to some degree in the large channels, the addition of the outside row to the two-row array is hardly worthwhile because (a) it reduces the output of the central row, which when in isolation out-performs a two-row array with the same number of turbines, (b) it requires significantly more turbines to generate a similar amount of power than

the outside row and (c) the additional capital infrastructure will probably make it unfeasible.

In a hypothetical scenario where a central row has been built and filled with 300 turbines in the most constricted large channel, placing a second row of equal blockage will necessitate an additional 1,700 turbines to increase the power output of the array by less than 20%. This has implications for channels where multiple companies may be developing because if one company has built a row of turbines, a new row of turbines built by a second company will affect the output and feasibility of the initial development. Additionally, the constricted region has considerably more value than anywhere else in the channel. Note that rows have been optimised with the same r_3 tuning in this study and a different tuning strategy may allow for more balanced power generation across rows or increase output from the array as a whole. Results from the past chapter suggest that tuning both rows of the array individually would result in the outside row contributing even less power to the total array output.

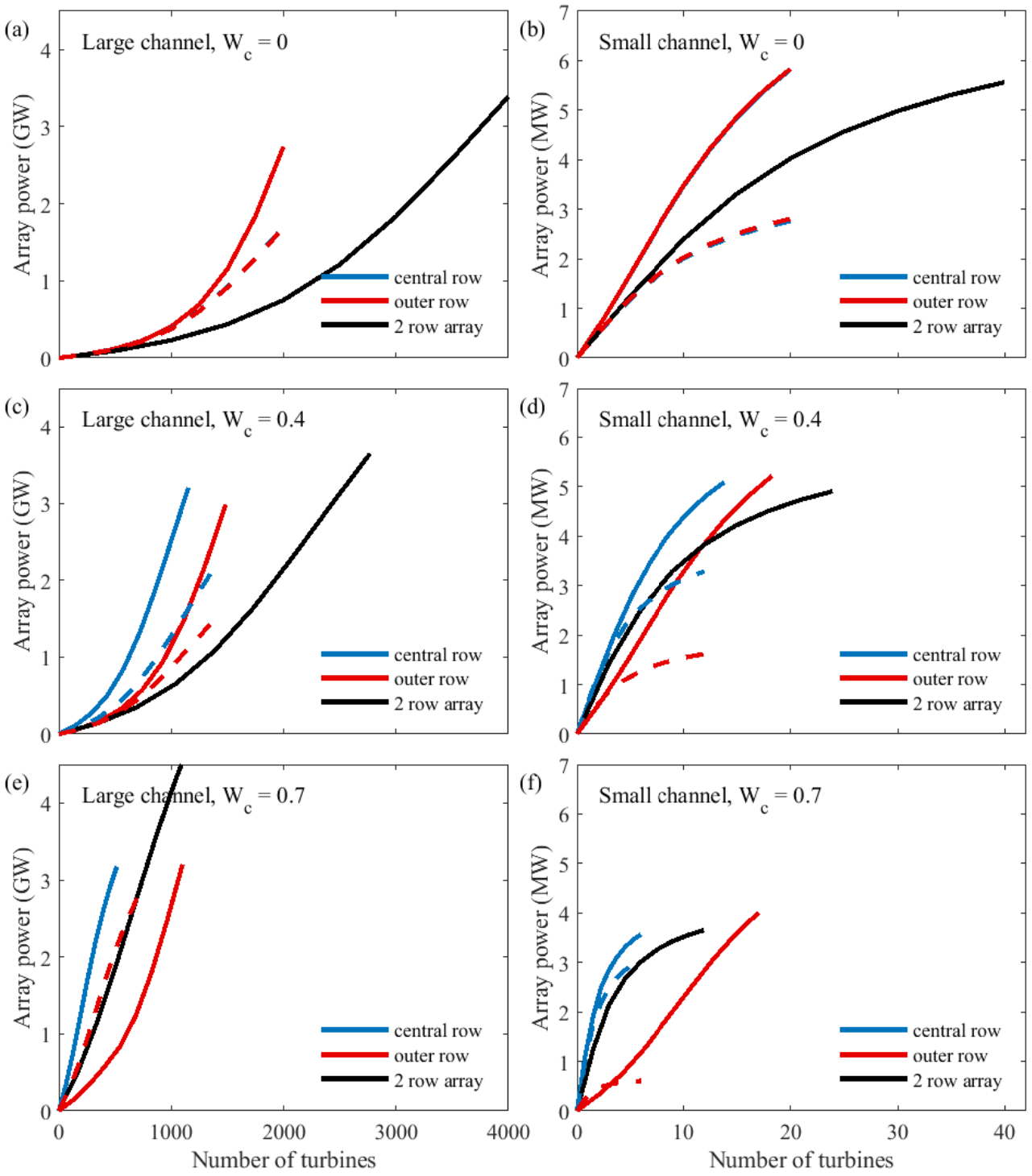

Figure 4.24: Array power curves for the inside and outside rows in isolation (solid coloured) and when the two-rows are part of a two-row array (dashed coloured). The black solid line is the sum of the two dashed lines, note that points on the x-axis do not line up between the two dashed lines as the number of the turbines in the array is the sum of the number of turbines in each row and the rows are filled simultaneously.

4.6.0.3 The even configuration has some advantages over the odd configuration

Figure 4.25 compares power outputs for the odd and even configurations. The odd configuration makes use of the smallest cross-section while the even configuration places rows either side of it. Unlike the odd configuration, rows in the even configuration had equal power output. Although these rows were subject to an exit jet over one half of the tidal cycle, the channel is symmetrical and thus while one row produces less power during one half of the tidal cycle, the other produces more. Arrays built using the even configuration, for the most part, matched the total array power from the odd configuration. In highly constricted channels, the even configuration actually produced more power. If the rows were to be developed by separate companies, the even arrangement would be a significantly fairer means of sharing the total energy available in the tidal channel. The downside of the even arrangement is that the low hanging fruit, that is the smallest cross-section, could not be exploited by the first developer in the channel. Once the most constricted part of the channel is developed, findings in this thesis suggest there is little gain from building a second row of turbines (if they are optimally tuned to maximise total power extracted from the channel). Thus it should be decided before any development takes place how many rows will eventually be permitted in a channel and policy should be created to regulate promising development areas.

4.6.0.4 Adding rows increases r_3 and reduces loads

Although not shown here for brevity, the act of adding a second row to an array in all channels studied was to increase the optimal tuning of the rows of turbines for any given blockage e.g. r_3 increases. An increase in r_3 reduces the difference in velocity upstream and downstream of the turbine rows and thus reduces the load on the turbines. This is consistent with findings for rectangular unconstricted channels in Vennell (2010, 2011b).

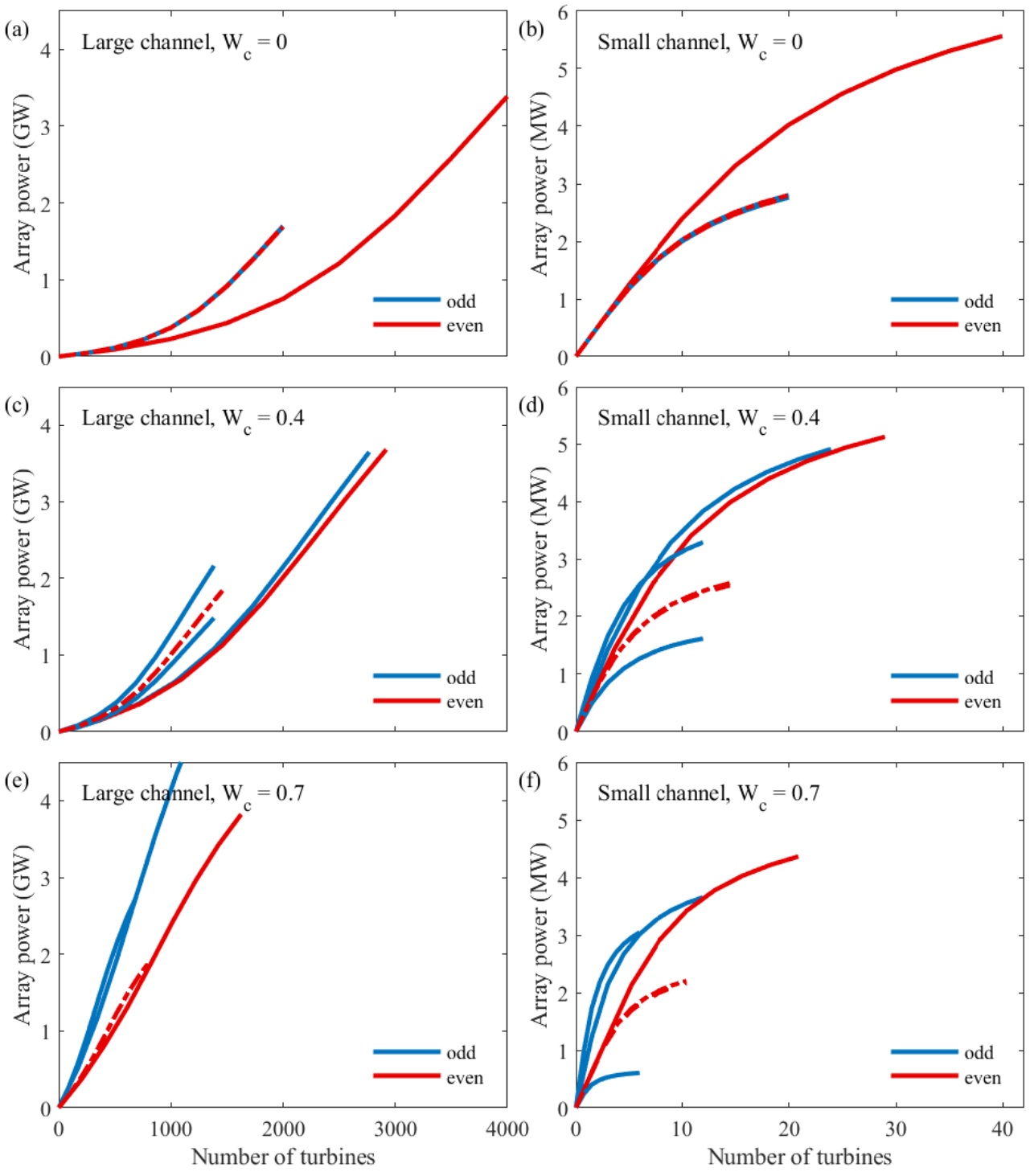

Figure 4.25: Power curves for the odd and even arrays. Individual power curves for the individual rows are given by dashed lines while the combined power output of the two-row array is drawn with the solid lines

4.7 Performance indicators

4.7.1 Array performance indicator: turbine power vs array power

A useful indication of array performance is the total array power versus the power of each turbine in the array. Arrays with both high array power and high turbine power are indicative that fewer turbines are being used to generate a large amount of energy. This indicates the resource is being exploited efficiently. Figure 4.26 shows scatter plots for all the cases tested in this chapter. Blue crosses (X) and circles (O) represent the two single row cases for the inside and outside case respectively. Red crosses and circles represent these rows in the odd two-row array design while green circles are for the even two-row array. With respect to this indicator, the best configurations will be in the top right of the plots.

In all instances, the single row within the constriction is the best configuration. The outside row performs well as does the inside row of the odd two-row array. However, the performance of the inside row of the odd two-row array should be penalised by the second row being the worst performing row in all cases (not shown in Figure 4.26). The even configuration rows sit between those of the odd configuration although relative to the two single row cases, does not perform particularly well.

As was seen in other figures, the development (shape) of these curves is indicative of the dominance of drag in the channel. Inertially dominated channels show an upwards trend while drag dominated channels have negative gradients and show a decrease in performance with the addition of more turbines.

4.7.2 PFR: increased power from constriction compensates for increased loads

Power-to-force ratio (PFR) offers an initial indication of how economics and engineering may influence array design based on the assumption that turbines of equal dimensions must be built using stronger materials to withstand greater loads. A full description of this is given in Chapter 3, Section 3.4.5. A turbine that is subject to high loads but generates little power should be avoided and will have low PFR. Figure 4.27 shows the PFR of all rows in all array

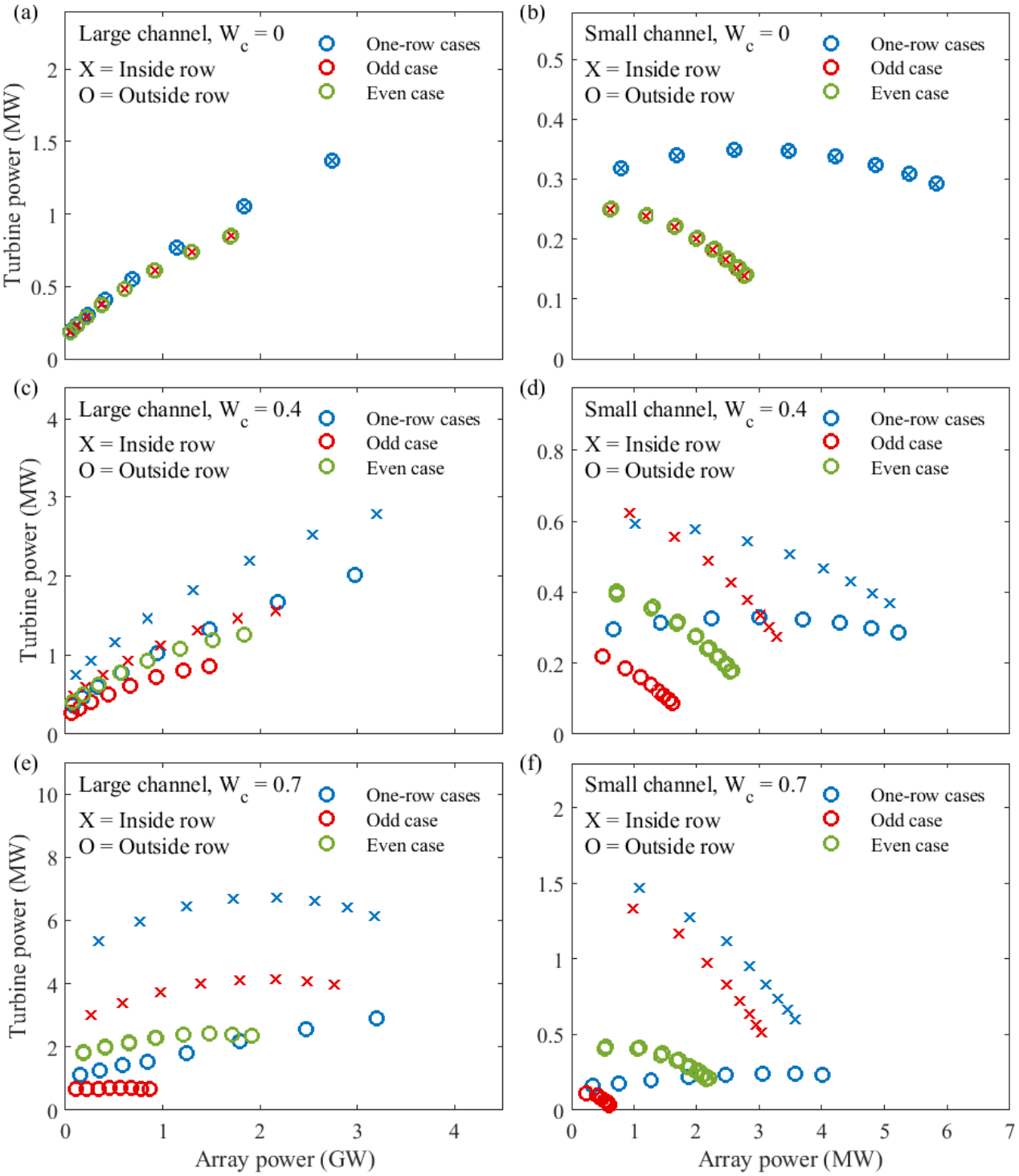

Figure 4.26: Power per turbine and array power for all array configurations and all channels. High performing array configurations appear in the upper right of each subplot

configurations tested. In these plots, an ideal row has high power to force ratio as well as high array power generation and thus is positioned in the top right of the plots. Rows marked with crosses (X) are rows placed in the most constricted cross-section of the channel while rows outside of the constriction are marked with circles (O). The rows within the most constricted cross-section are the best performers in Figure 4.27. PFR is seemingly proportional to the cross-section within which the row is situated. The two outside rows (both the solitary outside row and the outside row in the two-row odd case) have the lowest PFR. This is followed by the even case where the rows are in cross-sections smaller than the outside rows, but larger than the most constricted cross-section. The inside row, that utilises the smallest cross-section have the highest PFR. Figure 4.27 suggests that using the most constricted cross-section is the best decision economically although this should be explored with comprehensive economic modelling.

The importance of drag is yet again relevant to this performance indicator. Inertia-dominated channels show an initial decrease in PFR versus array power before increasing as the number of turbines in the array becomes many. Drag dominated channels show a similar trend, however drag-saturated channels (Figure 4.20) have near constant gradient and show little variation in PFR with array power as turbines are added to the array. This suggests near equal feasibility with addition of more turbines. This was predicted with 1-D modelling in the most constricted small channel in the past chapter (Figure 3.7).

4.8 Effects of turbines on the channel

4.8.1 Head difference

In the 2-D model, a disparity exists between the head difference set at the outer ocean boundaries and the ends of the channel area in the domain. The maximum channel head difference (Δ) was calculated by interpolating the surface elevation across the channel width at the two ends of the channel. This was averaged over the y-axis to give the time-varying mean elevations at each end of the channel. Subtracting one mean elevation from the other and taking the amplitude of the remainder gives the maximum head difference across the channel ends, Δ.

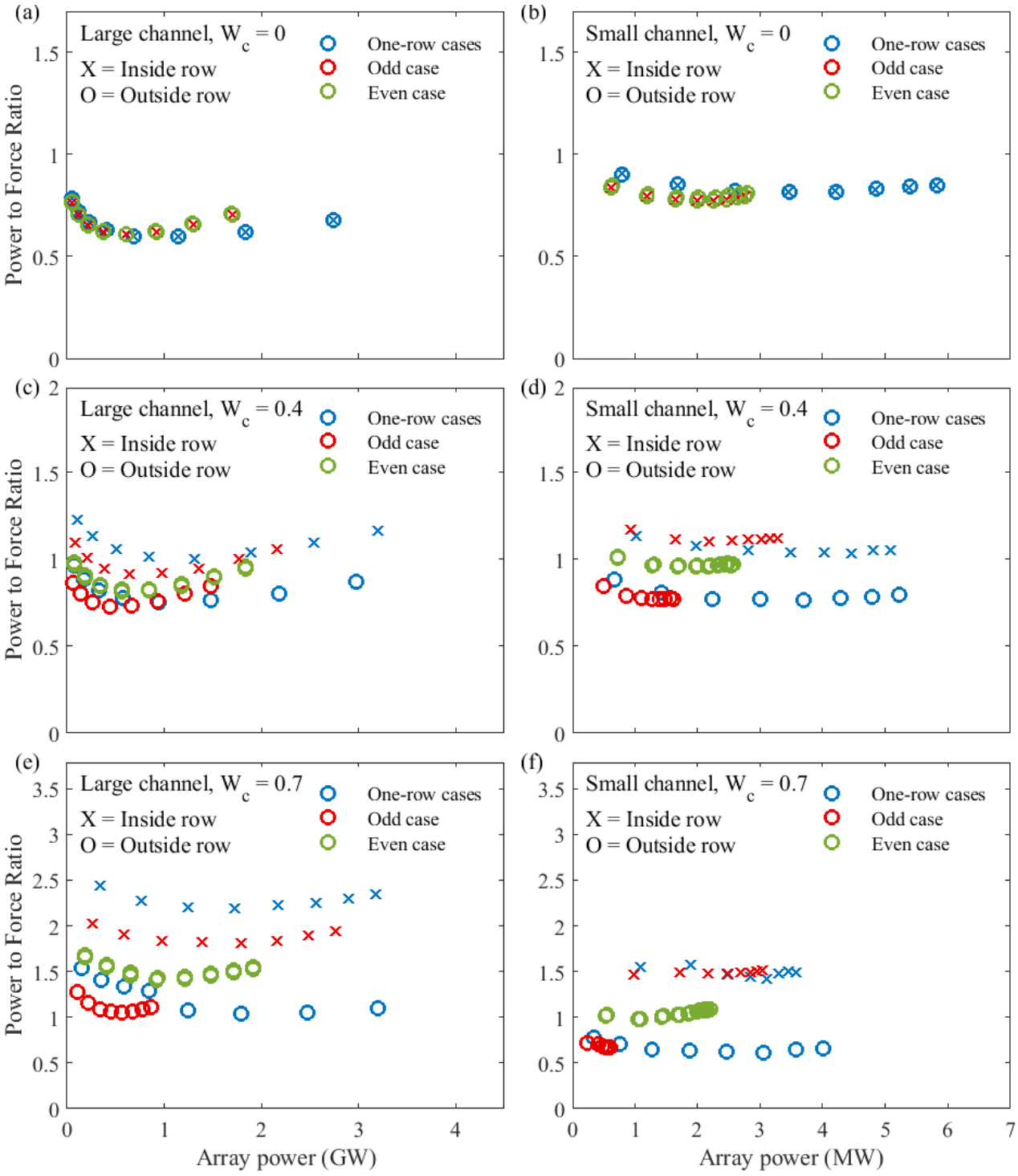

Figure 4.27: Power to force ratio for all array configurations and all channels. High performing array configurations appear in the upper right of each subplot

The tidal forcing conditions applied to the outer ocean boundary were Δ= 1.4 m and Δ= 0.17 m for the large and small channels which, in these 2-D simulations, translated to channel head differences 1.07 m and 0.10 m respectively. The channel head difference was assumed to be constant in the 1-D model at the ends of the channel. In the 2-D simulations, this was not the case. In these 2-D simulations, several factors caused the head difference across the channel ends to differ from that at the ocean boundaries.

4.8.1.1 Head difference decreases during propagation from ocean to channel

As flow travels towards the channel from the outer boundary it accelerates due to the shallowing sea bed. By conservation of energy, an increase in flow velocity must be countered by a decrease in pressure head and thus a decrease in tidal elevation. From the forcing boundary to the channel entrance, the ocean depth decreases by a factor of 4 in the large channel, and 2 in the small channel over distances of 165 km and 28 km respectively. By continuity, this results in an increase in velocity. But also, during this journey, the tide is attenuated. This distance is large, much larger than the channel lengths. Energy losses during this journey are significant and appear as a decrease in hydrostatic pressure, and therefore, tidal elevation.

4.8.1.2 The exit-jet causes an increase in head difference

Exit jet effects partially counter this head loss. Due to Bernoulli, the high speeds of the exit jet are countered by low pressure and therefore a decrease in free surface elevation. This effect always occurs in the downstream section of the channel, which is always the end with lower free surface elevation. Further lowering the free surface here acts to increase the head difference across the channel. In the small channel, where the exit jet impinges on the channel ends - the amplification effects of the jet can be observed even in the absence of turbines by comparing head differences at $n_T = 0$ in Figures 4.28 (b, d, f). In Figure 4.28 (f), the effect is strong enough to counter the head loss due to propagation.

4.8.1.3 Adding turbines causes the head difference to increase

Figure 4.28 shows that the addition of turbines to a channel also acts to increase the channel's head difference. The intensity of this increase depends on the dominance of drag forces already

present in the channel. In the inertial cases (Figure 4.28 (a, c) at low n_T), the addition of turbines has little or no impact on head difference. In cases where drag has started to dominate (Figure 4.28(b,d) for all blockage ratios and (a, c, e) at high blockage only), the head difference increases as turbines are added. This increase may be due to the effect of water back logging behind the row. Once the level of drag has increased beyond a certain point (Figure 4.28(d) at high n_T and all cases in Figure 4.28 (f)) the addition of turbines appears to no longer influence the head difference (Figure 4.28(f) and (b,d) at high blockage).

4.8.2 Flow rate reduction

As the degree of flow rate reduction may be an indicator of some environmental effects, one can use Figure 4.29 as an environmental performance indicator. According to this indicator, top performing arrays should generate more power for less flow reduction which is indicated by being in the upper right of each plot. A two-row array in the small unconstricted channel, for example, causes more flow reduction for less power and it would therefore be best to use only a single row if flow reduction was of concern.

Velocities were interpolated along multiple slices of the channel and the time-varying, cross-sectional area was calculated by integrating the sum of the water depth and free surface deviation over slices in the channel width. Velocities were then averaged over the y-axis at each slice and the time-varying flow rate of each slice was calculated by multiplying the mean velocity by the total area. These respective flow rate values were then averaged to give the time-varying flow rate of the channel. Channel transport should be near constant across slices (Vennell, 1998a,b) and a check was done to ensure this was the case.

4.8.2.1 Flow rate decreases quasi-linearly with power production

In line with findings of not only Vennell (2011a, 2012) for unconstricted channels but also work presented in the past chapter for constricted channels; the addition of turbines to all test channels resulted in a decrease in overall transport through the channels. The degree to which flow rate was reduced was proportional to the amount of power extracted by the array of turbines. Figure 4.29 shows the relative reduction in flow rate with respect to the total power

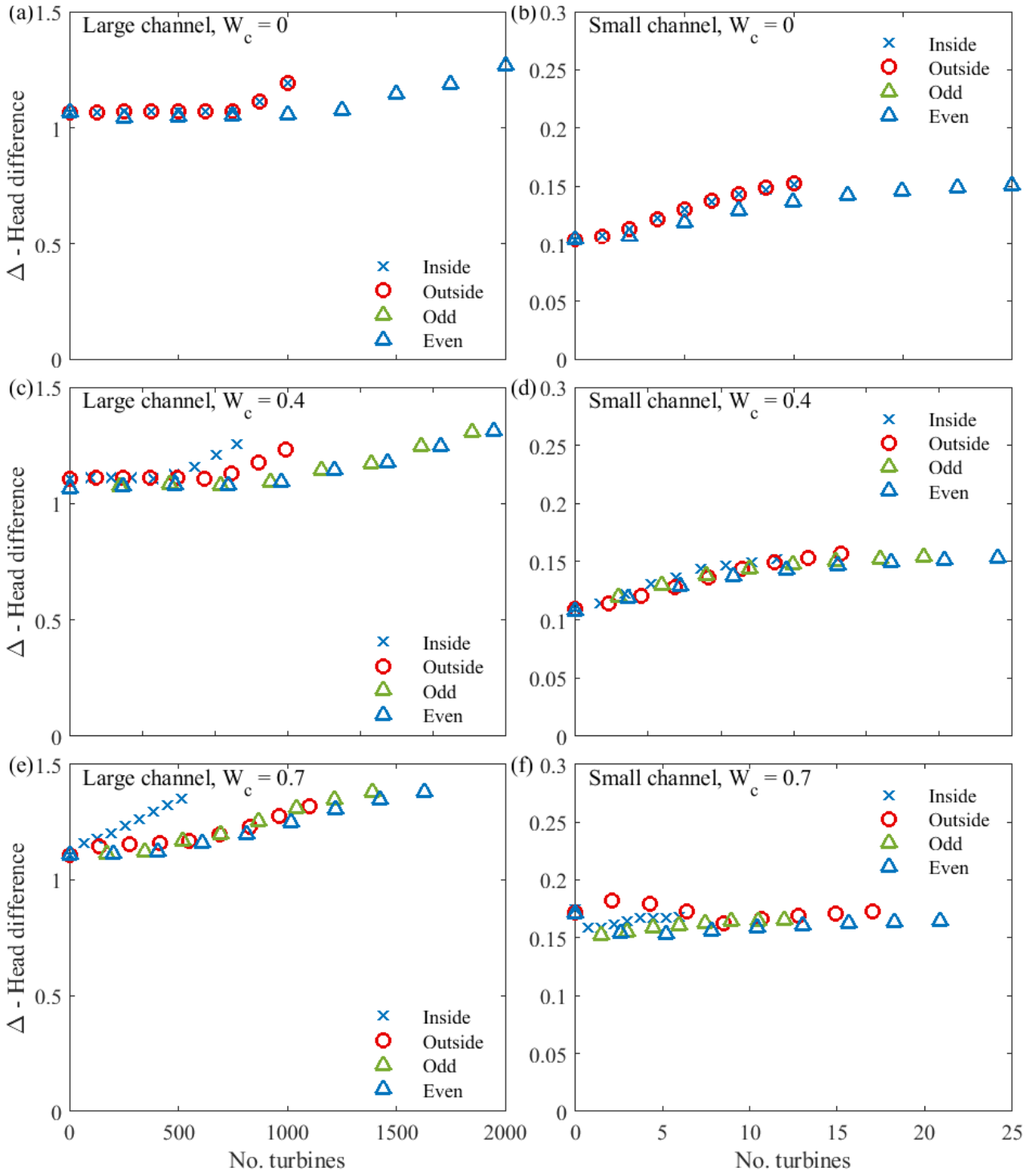

Figure 4.28: Maximum head differences across the channel ends for all turbine configurations and all channels

generated by the array for all cases tested. The degree to which flow rate is reduced relative to the amount of power taken from the channel is in good agreement with results presented in Chapter 3 (ranging from 0 to 40%). Results for high blockage ratios ($\epsilon > 0.8$) were not simulated in SUNTANS and could not be compared. While adding turbines to the channel increases the head difference across the channel-ends in most cases, the effect of this on flow rate is offset by the increased drag associated with their addition.

4.8.2.2 Arrays can be designed to minimise flow reduction depending on channel dynamics

Contrary to findings in the past chapter which used a 1-D model, results here indicate the way in which turbines are arranged has an effect on flow rate reduction. Furthermore, results suggest this sensitivity is more profound as the dominance of drag in the channel increases. Flow rate reduction is relatively insensitive to array design for the more inertial channels shown in Figure 4.29 (a, c). But, as drag begins to dominate the channel, the flow reduction per unit of power starts to vary between array configurations. Figure 4.29 suggests that there is not one overarching rule to designing turbine arrays that minimises the likely negative effect on flow speed. The optimal array configuration in this respect appears to be specific to the channel. That said, at the higher end of drag-dominated channels (b, d, f), the single row positioned outside of the constriction appears to be preferential. This would likely negatively impact on economic feasibility due to requiring more turbines. There is potential for this to be a source of tension between environmentalists and developers.

In some instances, the flow of the channel is increased above its undisturbed levels, this is the case in Figure 4.29(d, e) with few turbines in the array and only for some array configurations. There is no clear common factor between the few simulations that show this. It is speculated that this may be due to the turbine configurations of interest being large enough to cause an increase in head difference but not large enough to cause significant flow reduction.

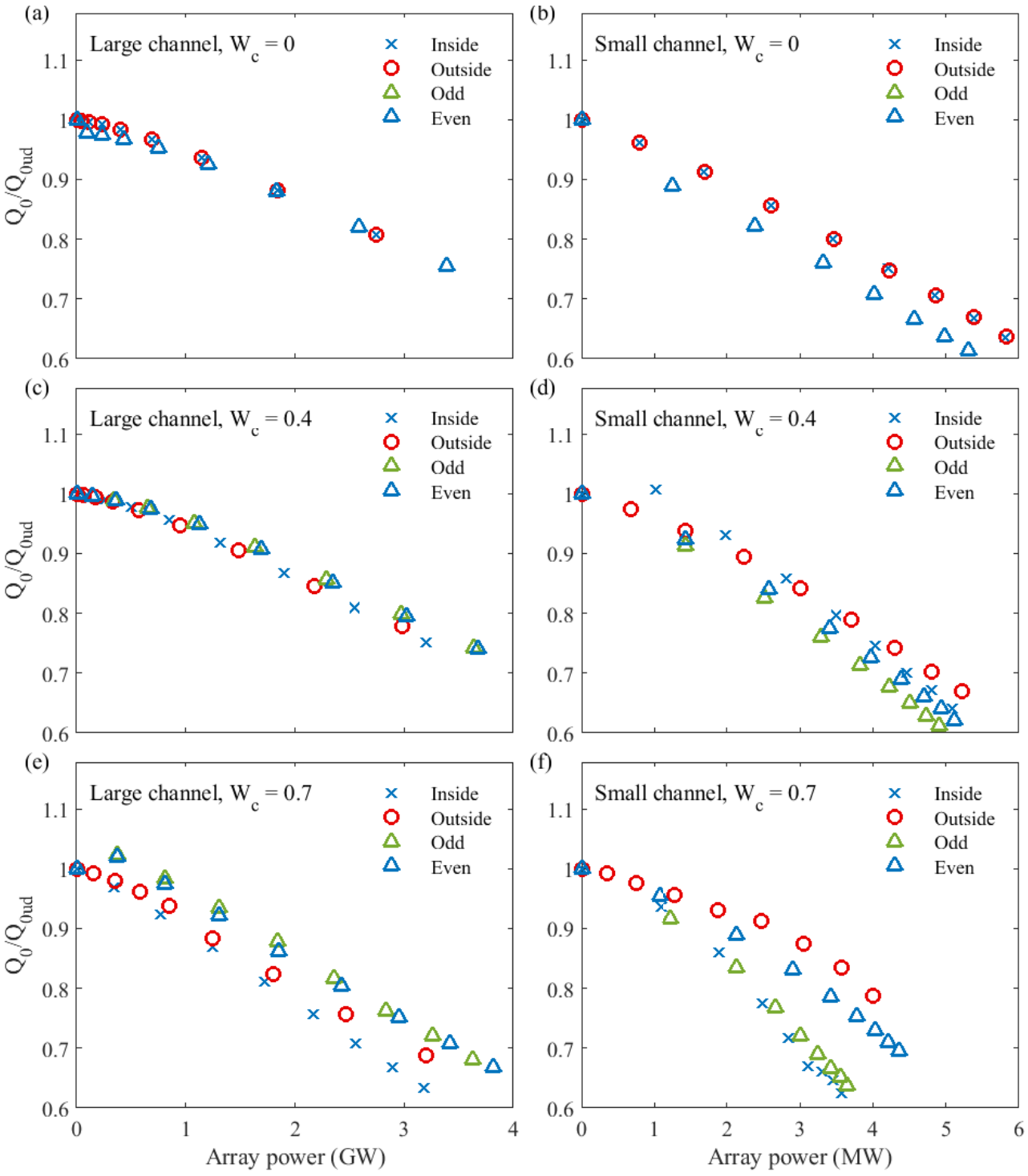

Figure 4.29: Relative flow rate reduction as a function of array power. Arrays that generate more power with lesser effects on channel flow are indicated by their proximity to the upper right corner of each subplot.

4.9 Comparison to 1-D model

The 1-D model used here is similar to models that have been used to build the foundations of tidal energy theory for unconstricted channels. This section seeks to validate not only findings presented from Chapters 2 and 3 but also to validate the existing body of literature that has made use of 1-D modelling.

The 1-D model requires the mean head difference between the channel ends as a fixed input value. As discussed in Section 4.8.1, values obtained from the more realistic model here showed this variable is by no means constant. The 1-D power formula (Equation 4.23) has cubic dependence on the channel head difference (Δ) and thus results are highly sensitive to the value used for this parameter 4.23.

$$\overline{P}_{\text{avail}} = \frac{2\rho Q_{IU}^3}{3\pi\hat{\alpha}A_0^2}\overline{P}'_{\text{avail}}, \tag{4.23}$$

where

$$Q_{\text{IU}} = \frac{g\Delta A_0}{\omega L}.$$

Initial checks were performed using the 1-D model without correcting for head difference at the forcing boundaries. These showed the 1-D model was overestimating power as the 2-D head differences were much lower.

The undisturbed head differences (e.g. $\epsilon = 0$) from each simulation, as calculated using the 2-D model, were then used in the 1-D model but were assumed to be constant with the addition of turbines. This showed the 1-D model was underestimating results. This makes sense as findings from our 2-D model show that adding turbines to the channel increases the channel head difference which is still not being accounted for in the 1-D model framework.

Using the head difference from each 2-D array simulation to drive the 1-D model resulted in excellent agreement between the two models and these results are presented below. This suggests a head difference correction needs to be applied to the 1-D model to account for the effect of increasing head difference with the addition of turbines to the channel. It also suggests

that the 1-D model head difference should be chosen carefully, ensuring measurements are close to the channel ends.

For work presented in Chapter 3, the r_3 tuning factors of different rows were allowed to vary between rows. For the sake of model validation, the 2-D simulation condition that both rows must have the same tuning factor was applied to the 1-D model for the purposes of this comparison.

It should be noted that this section compares one model against another model. It is assumed that because the 2-D model is more sophisticated that it is more realistic and so the 2-D results are used as a benchmark to evaluate the performance of the 1-D model. In reality, there is no way to know if either are closer to a true system without real world data (for which there is none). The 2-D model could be validated for small arrays that have been built in real locations although these arrays will be too small to observe the feedback mechanisms predicted to occur at high blockage ratios.

4.9.1 Transport and peak speeds show reasonable agreement

Channel transport calculated using both the 1-D and 2-D models for the duration of one tidal cycle is shown in Figure 4.30 for the large channel (top) and small channel (bottom). Transport calculated by the 1-D model shows very good agreement with the more realistic 2-D model for the large channel. 1-D transport for the small channel is larger than the 2-D transport by almost a factor of 2. This is likely due to the exit jet from the constriction which is significantly long in the small channel but in the large channel is dwarfed by the channel's total length. The 1-D channel model used here has assumed that the velocity at the entrance and exit of the channel is the same, if a jet is still present at the channel boundary this would not be the case. Partially re-arranging the equations of Garrett and Cummins (2005) with non-equal entrance/exit speeds gives:

$$\left(\int_0^L \frac{dx}{A}\right)\frac{dQ}{dt} = g\left[\eta_0 - \eta_\mathrm{L}\right] - \left(C_\mathrm{D}\left(\int_0^L \frac{dx}{hA^2}\right) + \frac{C_\mathrm{F}}{A_\mathrm{R}^2}\right)|Q|\,Q - \frac{1}{2}\left[u_L^2 - u_0^2\right].$$

which shows that the channel transport is driven by the head difference and dissipated from drag forces as well as a kinetic energy loss term. Building this loss term into the 1-D model in a future work could improve the performance of the 1-D model for constricted channels.

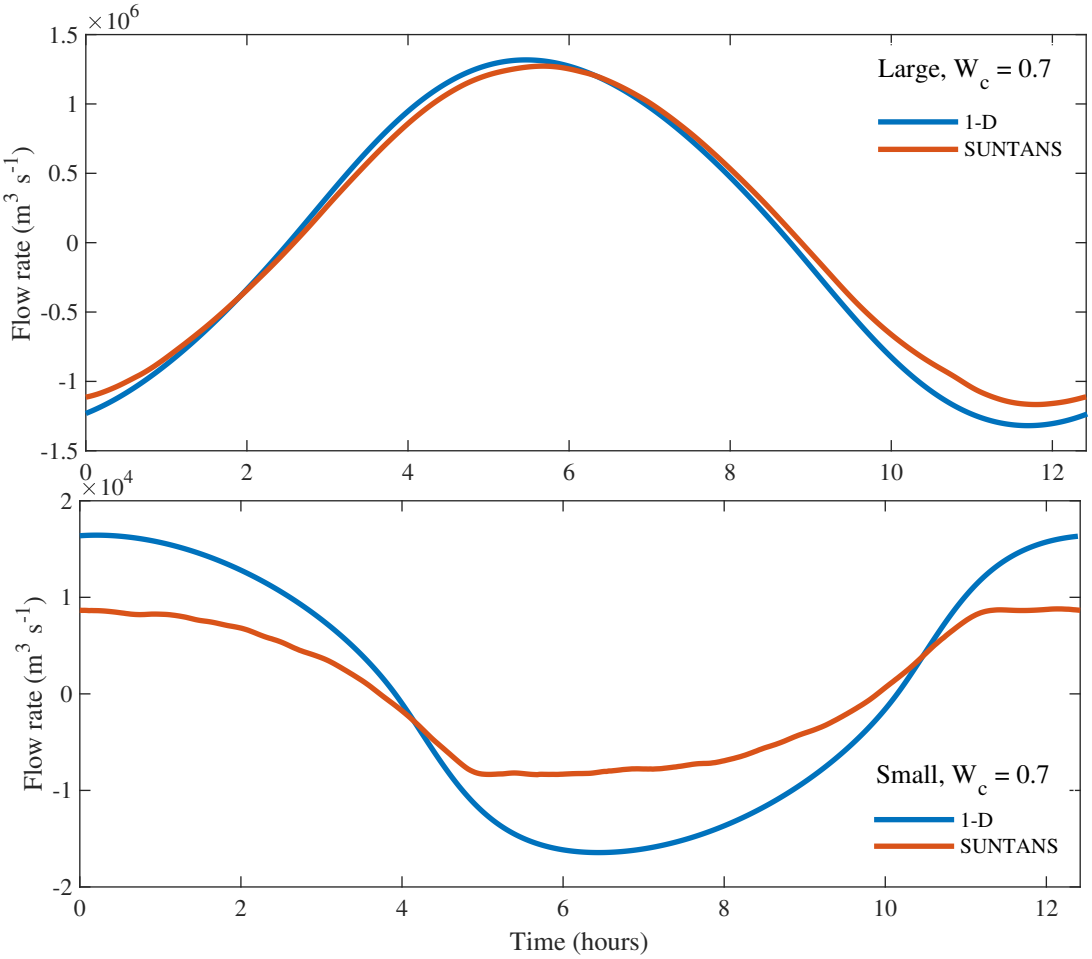

Figure 4.30: Undisturbed flow rate through mean tidal cycle calculated using both the 1-D model (blue) and the SUNTANS model (orange)

Figure 4.31 shows the mean velocity (averaged over each cross-section along the channels' lengths) calculated by both models. Velocities calculated using the 1-D model are larger in the small channel which is unsurprising as the channel transport was almost twice as high. Comparison of the 1-D and 2-D curves show that the 1-D model is not resolving the small fluctuations in velocity seen along the channel using the 2-D model - mostly downstream of the constrictions. These fluctuations are likely the consequence of 2-D effects such as the eddies seen in Section 4.4 that form downstream of the constriction (or sometimes exist upstream as remnants of the last tidal cycle). These effects are more dominant in the small channel.

For its simplicity, the 1-D model does a reasonable job of reproducing the correct flow rate and velocity profile of the example channels.

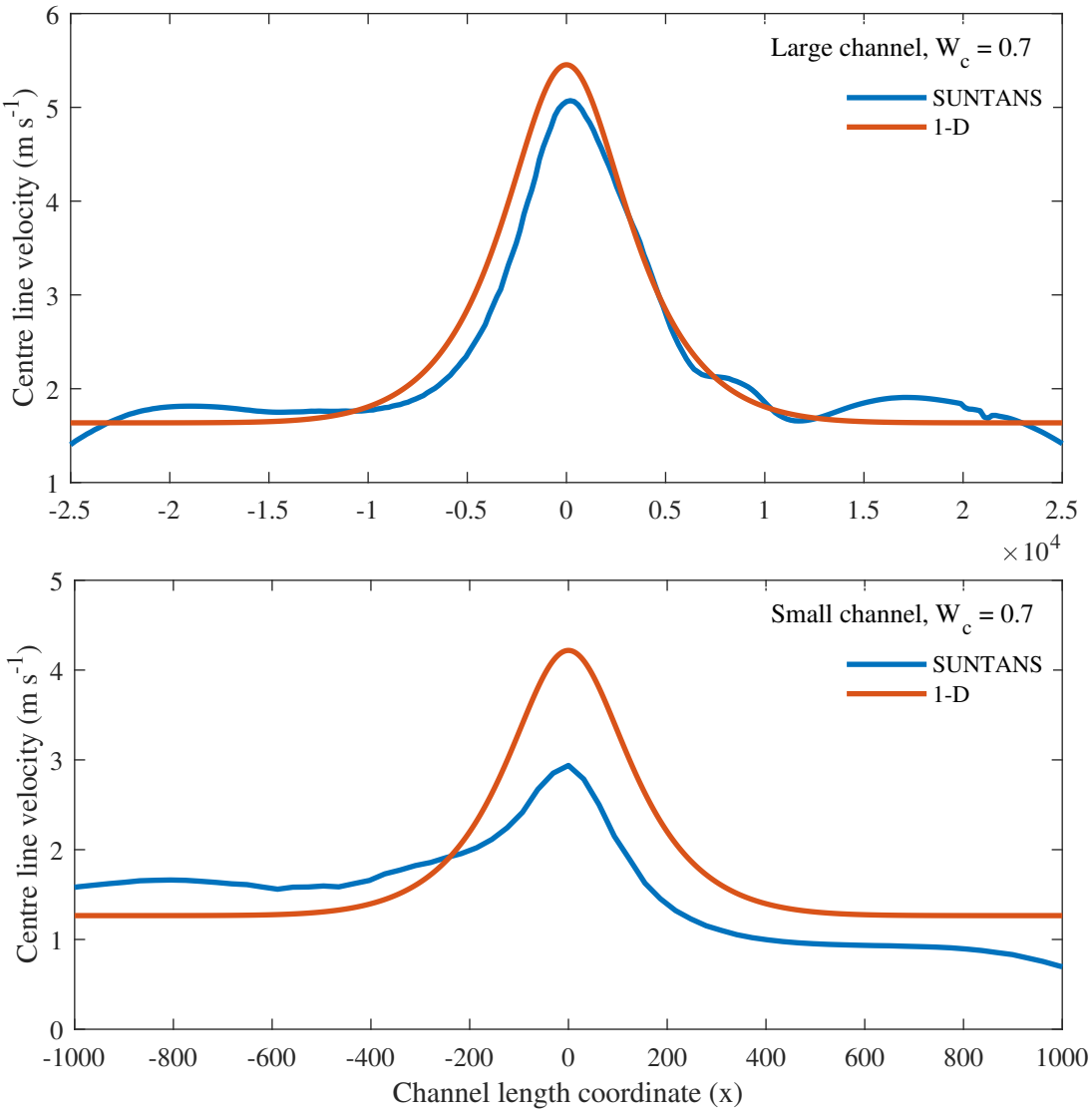

Figure 4.31: Maximum centre line velocity along channel length as calculated using the 1-D (orange) and the SUNTANS model (blue)

4.9.2 Power curves show excellent agreement

A comparison between power curves from the 2-D model and those from the 1-D model used in Chapter 3 are shown in Figure 4.32.

Excellent agreement between model outputs can be seen in the large channel cases (Figure 4.32 left-hand column). The 1-D model ever so slightly underpredicts power in the two-row simulations for the highly constricted large channel. Agreement is still reasonable for the small channel in terms of curve shape but the 1-D model overestimates power by up to approximately 40% for the most constricted channel. This is due to the 1-D model's inability to account for the efflux of energy in the constriction jet which brings down the channel flow rate (see discussion in Section 4.9.1) as well as not being able to account for the smaller variations in flow resulting from the subsequent eddies borne from this process. The large channel is sufficiently long that the jet is able to mix in with the surrounding flow before leaving the channel exit and so the 1-D model is a more satisfactory tool for predicting array power output in the large channel examples. Results here are pleasing as they suggest that the 1-D model, for all its simplicity, has correctly predicted the dominant trends in how power scales with channel constriction and how row placement in the channel affects power output (when the channel head difference is corrected).

Additionally, this comparison has outlined two significant caveats of the 1-D model which must be considered when adopting its use in research. Firstly, adding turbines to a channel will cause the head difference (Δ) across the channel ends to increase. This suggests results for unconstricted channels provided in (Vennell, 2010, 2011b, 2012) may be underestimating the power available for generation, particularly for large channels. Conversely, and more importantly, the energy loss associated with a constriction jet can be important if the degree of constriction is high and the channel length is small - resulting in the 1-D model significantly overestimating power output.

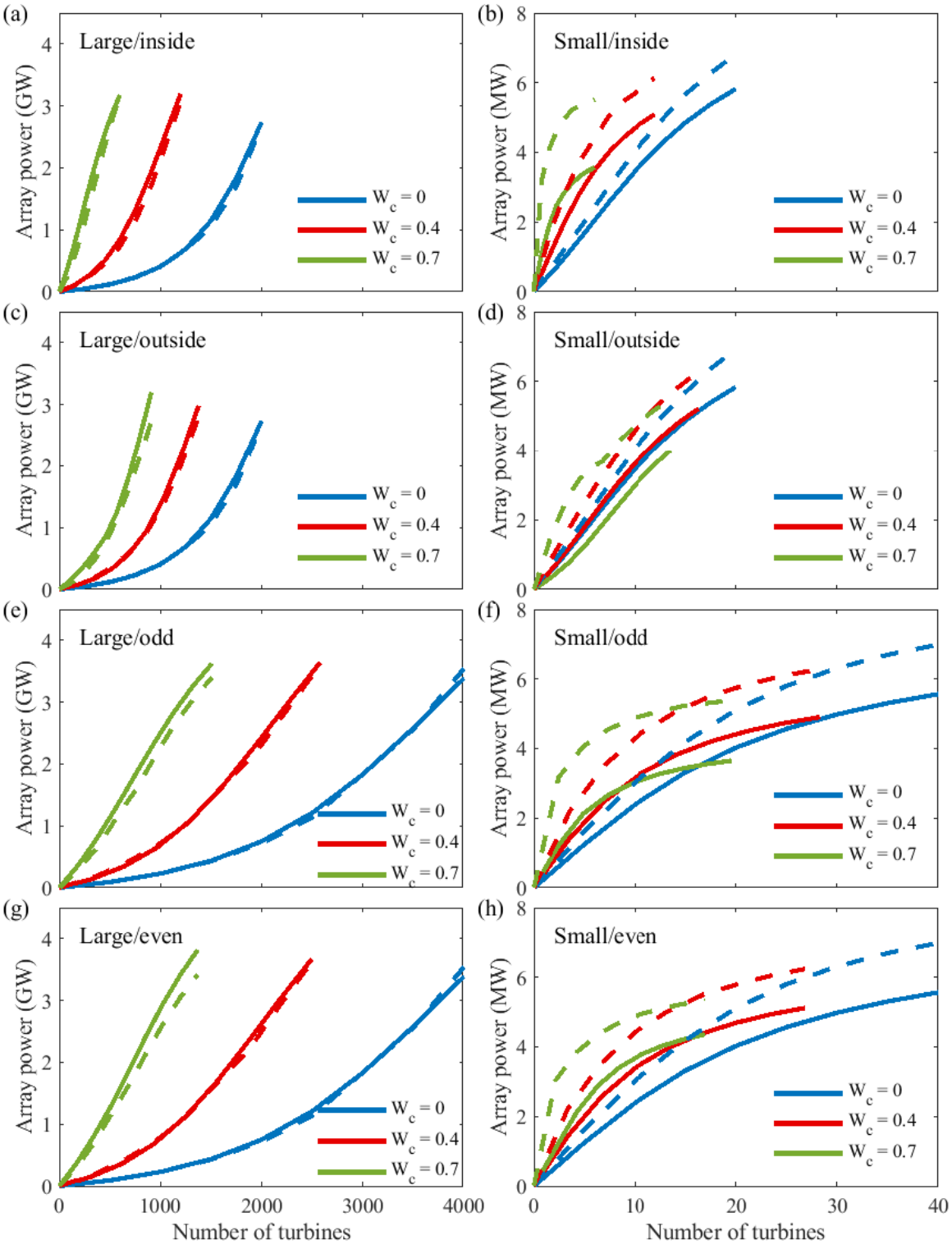

Figure 4.32: Array power curves generated using the 2-D model presented here (solid lines) and the 1-D model presented in the previous chapter (dashed curves). 1-D power curves were calculated using the corrected head differences presented in Figure 4.28

4.9.3 SUNTANS model predicts less flow reduction than the 1-D model

Comparison between the two model outputs (Figure 4.33 below) shows that the 1-D model provides a reasonable estimate of flow-rate reduction while array power is low (e.g. fewer turbines) but as the array gets larger, the 1-D model can overpredict or underpredict the flow rate reduction from tidal energy generation. The 1-D model usually overpredicts flow rate reduction in the large channel. In the small channel, the 1-D model both underpredicts and overpredicts flow-rate reduction. The fact that these inconsistencies are limited to the small channel and appear more prominent for constricted channels suggests that it may somehow be related to the effects of the exit jet. The overarching reason behind this disagreement of reported flow reduction may come down to the 2-D model being a more realistic model of the hydrodynamics of the constricted channels and therefore may be a truer representation of the real physical process. This would need to be validated against other hydrodynamic/turbine models.

4.9.4 Optimal tuning values differ between models

Figure 4.34 shows the difference in optimised r_3 tuning factors calculated by the 2-D model (solid) and the 1-D model (dashed). Interestingly the 1-D model predicts a higher optimal r_3 tuning in all instances. A more realistic flow model has been used in the 2-D case and the disparity seen in tuning parameters may be due to the physics of the 1-D model being overly simplified and thus an incorrect tuning factor is found during optimisation. Interestingly, this has not really affected the agreement in power output of the two models which is likely because the increased channel head difference and therefore lower flow rate reduction predicted in the 2-D model compensates for this.

4.10 Conclusion

This chapter has systematically explored turbine array theory in constricted channels using a 2-D numerical model (SUNTANS) with the actuator disc model for the same idealised channels

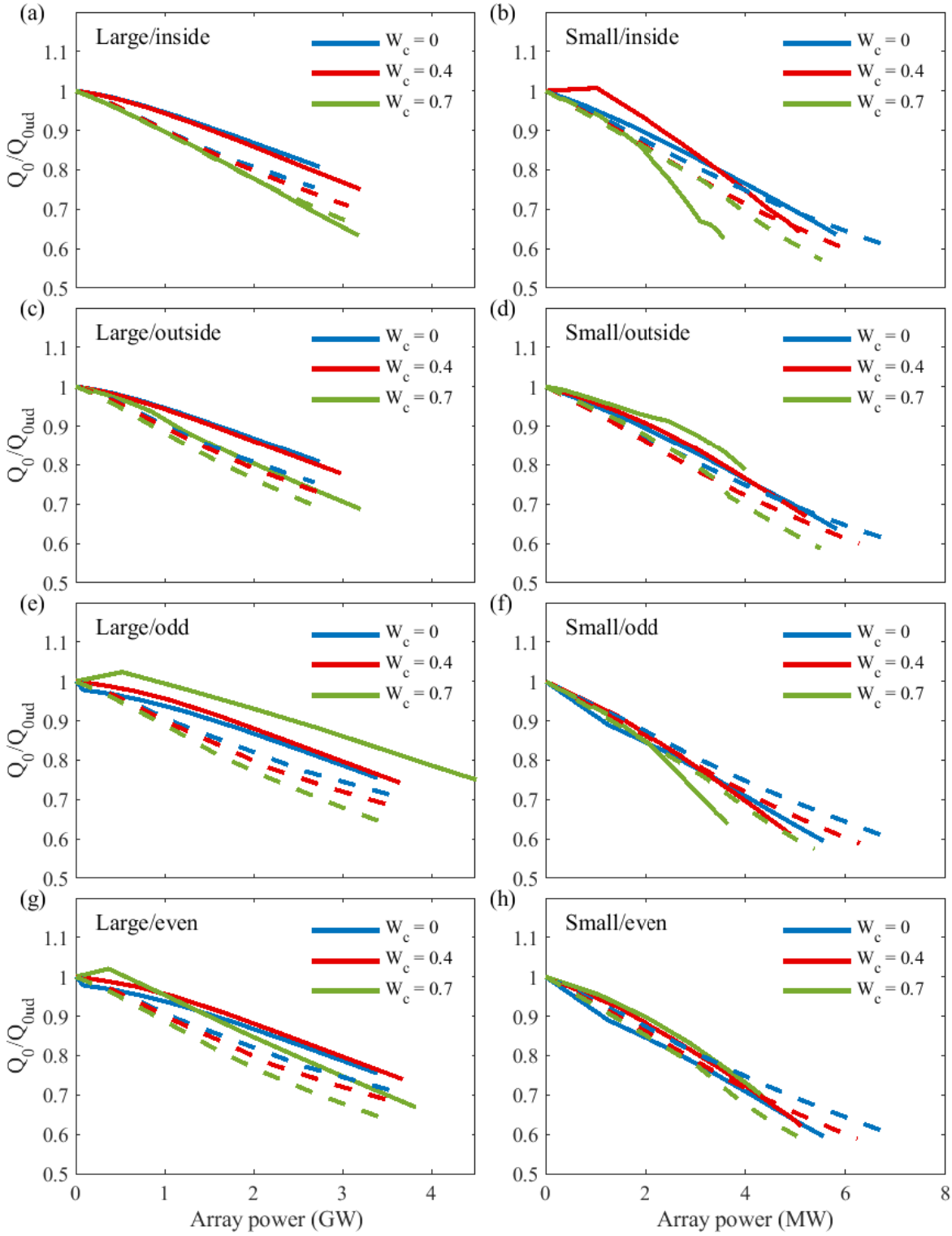

1-D results were calculated using the corrected head differences presented in Figure 4.28

Figure 4.33: Flow rate reductions calculated using the 2-D model presented here (solid lines) and the 1-D model presented in the previous chapter (dashed curves). 1-D results were calculated using the corrected head differences presented in Figure 4.28

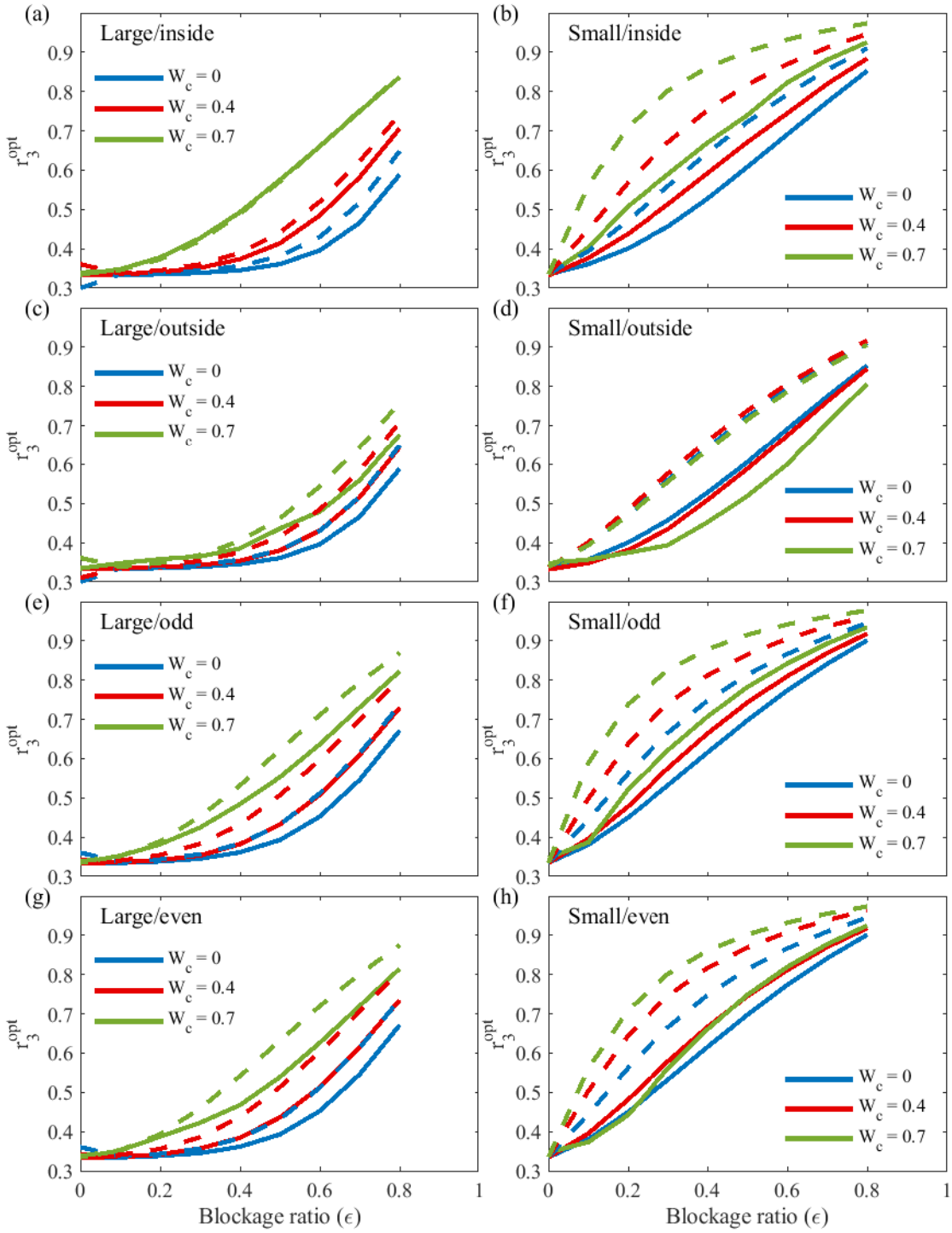

Figure 4.34: Optimal r_3 tunings calculated using the 2-D model presented here (solid lines) and the 1-D model presented in the previous chapter (dashed curves). 1-D results were calculated using the corrected head differences presented in Figure 4.28

as the past chapter - although with more realistic geometries. This model provides a more realistic representation of tidal channel flow and tidal forcing.

Instinct suggests that the best place to put turbines in a constricted channel is in the most smallest cross-section due to the highest channel velocities being at this point. For most realistic blockage ratios, placing turbines in the smallest cross-section does result in the greatest power output from both the array as a whole as well as on a per turbine basis. This comes at the requirement of the turbines being able to withstand significantly greater loads. Depending on the level of drag already in a channel, increasing the number of turbines in the row may increase or decrease the output of turbines already present in the row. Power generation in constricted channels is limited by these channels having lower potentials. This limitation is more important for small channels where the number of turbines required to reach potential is fewer. Work here suggests that even at very high blockage ratios (equating to arrays of 1000s of turbines) this limitation is unimportant in large inertia dominated channels.

Adoption of this 2-D model allowed for investigation of the exit jet that forms on the downstream side of a constriction. The effects of the jet were detectable but less significant in the large channel example where the constriction geometry was gentle and the channel was sufficiently long that the jet could mix in with the surrounding flow before leaving the channel. In the smaller channel, the effects of the jet had a significant impact on the energy balance of the channel and caused a net efflux of energy out the channel end that could not be captured by the array of turbines. Turbines positioned outside of the constriction, and therefore in the jet path, were able to take advantage of its high flow velocities on one half of the generation cycle. This resulted in an unpredictable and jagged power output over the generation cycle - it was found that adding turbines to the channel dampened these effects and tended the power cycle back towards a pure sinusoid.

Two different two-row array designs were tested - one made use of the smallest cross-section at the cost of placing the second further away while the second design placed two-rows of turbines equidistantly from the most constricted cross-section. In the first case, the row placed in the smallest cross-section generated the vast majority of power and produced the same amount of power each tidal cycle due to being immune from the effects of the jet. Adding a second row of turbines to an array reduces the power output of the first row and results here indicate that

the addition of a second row of turbines to a channel that already has turbines in the smallest cross-section is likely not worthwhile. This will have implications for ocean space management if multiple developers are trying to generate power from the same channel.

The second case, where neither row made use of the smallest cross-section, resulted in near identical power output relative to the first case albeit through the use of more turbines. In the highly constricted channels, these arrays actually produced more power. Both rows experienced a jet on one half of the tidal cycle although neither row was as productive as the row in the smallest cross-section of the first example. If tidal energy generation in constricted channels is to be pursued by multiple entities then restricting use of the most constricted cross-section would allow for fairer competition between developers as once the smallest cross-section is developed there is little reason to build a second row of turbines.

Array power versus turbine power was used to compare performance of the array configurations tested here. Top performing configurations would ideally have high overall array power from fewer turbines (and thus have high turbine power). In all cases, a single row placed in the most constricted cross-section was the best performer. Power-to-force ratio versus array power was used as an initial indicator of economic performance on the basis that turbines of identical dimensions must be built stronger to withstand greater loads and will thus be more expensive. Results here suggested that despite being subject to increased loads which affects the cost of manufacture, a single row of turbines in the smallest cross-section would still be the best choice. This last result should be taken crudely as true array economics will depend on multiple additional factors.

The flow reducing effect of tidal energy generation is well documented and quantified in previous chapters and literature. Work here suggests that flow rate reduction values predicted in our past chapter are slightly conservative but also confirm that the degree of flow rate reduction is nearly linearly proportional to the amount of power extracted. Comparing the flow rate reduction of our various test cases indicates that for the same amount of power generated, certain array designs will cause less of a reduction in flow and therefore may be of lesser environmental impact. Little consistency between array design and flow rate reduction existed across channels and findings therefore suggest that developers and policymakers should assess multiple turbine array layouts to try and minimise the effects of this industry on the natural channel dynamics.

An effect not accounted for by past 1-D modelling was the impact of tidal energy extraction on the head difference across the channel. The addition of turbines to a channel can cause the amplitude of the head difference at the channel ends to increase. The magnitude of this effect depends on the dominance of drag present in the channel. Additionally, the importance of accurately setting tidal head forcing in channel scale models was highlighted by a significant disparity between the head difference occurring at the ocean boundary and that occurring at the channel ends. Power predictions from the 1-D model used in past chapters and throughout literature were highly sensitive to the head difference parameter and this identifies that for this model to be used accurately, the feedback between energy extraction and head difference needs to be considered.

Finally, a comparison was made between the more realistic and sophisticated SUNTANS model and the 1-D model used in the previous chapter and throughout literature. Using the head differences calculated from the SUNTANS model to drive the 1-D model resulted in excellent agreement between the two in terms of power output - particularly for the large channel. The 1-D model overpredicts the power output of arrays in the small channel and this is likely due to its inability to account for the effects of the exit jet. Optimal r_3 tunings predicted by SUNTANS were lower than those predicted by the 1-D model and predicted flow rate reduction was slightly less.

Chapter 5

Conclusions, Limitations and Future Work

Electricity generation from strong flows through tidal channels could make a significant contribution to the world's renewable energy supply (Vennell, 2011a; Karsten *et al.*, 2008; Draper and Nishino, 2014). Constricted channels are potentially lucrative sites for energy development due to enhanced flow velocities in the narrowest section. It is possible, in these high velocity zones, to generate the same amount of power using fewer turbines than would be required outside of the channel's constriction. This can also be economically, socially and environmentally beneficial in some cases. Little electricity is generated from tidal currents at present due to high initial investment costs and a reasonable degree of uncertainty surrounding the future of the industry. Enhanced understanding of the tidal resource and improved resource assessment methods can help reduce some of this uncertainty and increase investor confidence. This thesis builds on the existing body of tidal energy theory with the aim of helping the industry develop.

This thesis has used a combination of mathematical models to investigate how constrictions affect basic tidal stream energy theory in constricted channels. This has largely been done by taking a thorough and systematic approach - testing and optimising macro-scale array design aspects in order to maximise the power produced by tidal stream turbines.

5.1 Addressing the thesis research questions

5.1.1 Limits on tidal energy generation in constricted channels

Research Question 1: How are theoretical limits on tidal energy generation such as channel potential and maximum available power affected by channel constriction?

The addition of a constriction to a tidal channel causes the undisturbed flow rate of the channel to decrease due to an increased amount of energy being lost to seabed drag (Figure 2.4(c, d)). A consequence of this is that less energy is available for electricity generation. For channels of similar size, those with more severe constrictions will have lower potentials (Figure 2.4(a, b)). The potential limitation of constricted channels is relevant for cases where the channel cross-section is completely blocked by turbines. 2-D modelling suggests that at more realistic blockage ratios, the penalty of having a smaller potential is not a limiting factor on maximum available power.

Conversely, the increased loss of energy to the seabed in channel constrictions can be exploited for tidal energy (Figure 3.6). If more energy is lost to the seabed in constrictions due to higher flows, it follows that more energy can be lost to turbines in these regions. Utilising the high flow speeds within constrictions results in more power being lost by the flow to the turbines (the velocity advantage) and secondly, turbines placed in this smaller cross-section can achieve greater blockage-ratio which forces more of the flow through the turbines (the blockage advantage). Findings from both a simple 1-D model (Figure 3.6) and a more complicated 2-D model confirm that significantly higher power generation can be achieved by exploiting the constricted passage.

5.1.2 Flow reduction in constricted channels

Research Question 2: How does channel constriction affect the extent of tidal energy related flow reduction?

Arrays in constricted channels cause greater flow reduction per unit of power than unconstricted channels of similar scale. The actual degree of flow reduction that one can expect varies between methods tested here with the more realistic 2-D model predicting lesser reduction in flow than

the 1-D model. This disparity is likely due to the 2-D model accounting for the effect of increasing head difference with the addition of turbines. This suggests that flow rate reduction estimates given in existing tidal energy literature, which has predominantly used 1-D models, may be overestimates.

Both models used in this thesis confirm that flow rate reduction is nearly linear with respect to the amount of power generated by the array. The relationship between flow rate reduction and power extraction in the 2-D model results became less linear as the channel reached a drag-saturated state which was not predicted by the 1-D model.

Results from the 2-D model show that the way in which turbines are arranged within arrays can impact the amount of flow reduction. Percentage flow reduction per unit power generated by the array was used as an environmental performance indicator. No best overall array design was observed for the cases tested here which suggests that optimising this will be specific to a channel's dynamics. It can be concluded from these findings that the best array configuration for electricity generation is not always the best design environmentally. Ideally developers will design arrays to have as little impact on flow per unit of power generated.

5.1.3 Array design for maximum power

Research Question 3: How should arrays be arranged in constricted channels to maximise energy output?

In all instances, for an array containing M turbines, placing these turbines in a single row in the smallest cross-section of the channel will maximise energy output. If the smallest cross-section is unavailable then the smallest available cross-section should be used instead. Turbines should be added to a single row until it blocks as much of the cross-section as possible. If some constraint (such as a navigable strip) restricts filling this row beyond a certain blockage ratio and turbines must be placed in additional rows then the problem becomes more complicated. The best layout in this instance depends on the total number of turbines and rows in the final version of the planned array and it must consider any other arrays that will be operating within the channel.

If power is to be generated by two-rows only, then utilising the smallest cross-section of a

constriction for one row will require the second row to be further away and, in the case of our idealised channel design, in a larger cross-section. Findings from both models suggest the row in the smallest cross-section will generate the majority of the total array power (provided the array is optimally tuned to maximise total array power). Diminishing returns on adding rows to a turbine array (with respect to additional power generated) is a well documented effect in existing turbine array theory for unconstricted rectangular channels. Assuming turbine arrays will be developed in stages, this will have implications on the feasibility of adding a second row of turbines to an already operational array. Perhaps more importantly, this finding infers that if multiple developers have rights granted to build arrays in the same constricted channel, the developer who builds in the smallest cross-section can generate significantly more power than their competitors.

Conversely, the addition of the second row of turbines in the channel will cause the power output of the existing row to decrease (as will a third row and so on). This can be translated into a scenario where an existing tidal energy developer will have their power generation reduced if a new developer decides to build in the same channel. That is, allowing new developers into a channel will impact the feasibility of existing developments. Financial planning should account for this and policy should endeavour to ensure the most efficient use of the entire resource. To be effective, this policy (and also financial decisions) should consider how many turbines will be present, and how they will be arranged, in the final version of the developed channel. From this, an appropriate subdivision of the channel may be required to encourage fairness and competition.

The most powerful turbine array configuration is not necessarily the most economic. Economics may change with scale and time. According to a simple economic indicator (power-to-force ratio or PFR), it turns out that the most constricted section of the channel is still the best place to build a turbine array. This is good, as this is in line with the most efficient use of the resource. Using PFR as an economic indicator is basic. True economics will be site-dependent and must consider both the local environment and the proposed turbine design(s) for the array. Additional infrastructure such as cabling and local electricity demand will affect decision-making and planning. Exploring this topic at this level of detail is beyond the scope of a broad systematic theoretical study such as this one. Economic decisions must be made on

a site by site basis however findings from this work can inform them.

5.1.4 How power scales with number of turbines

Research Question 4: How do channel constrictions affect how power scales with the number of turbines in an array or across multiple arrays in the same channel?

As turbines in arrays are likely to be installed over an extended period of time, knowing how array power scales with additional turbines is useful and will be a governing factor when assessing project feasibility. The way in which array output grows is dependent on the natural dynamical balance of the channel and the degree of constriction, but also how many other turbine arrays or devices are already in the channel. The driving factor behind how power scales in tidal channels appears to be how dominant drag forces are in the dynamical balance of the channel. Both channel constriction and turbines increase the degree of drag in channels. Constrictions create regions of high velocity which causes more severe drag loss while turbine devices are additional sources of drag loss. All channel and array scenarios can be placed on a drag continuum (Figure 4.20).

At one end of this continuum are unconstricted, large inertia-dominated channels. These channels experience a period of enhanced power return only when the array is so large it blocks a significant portion of the channel's cross-section. In the middle of the spectrum are large constricted channels containing large arrays and small unconstricted channels. Arrays in these channels experience enhanced power return early on in their development e.g. when the number of turbines in the array is few. This makes them particularly favourable for early-stage developments of tidal energy. At the far end are highly constricted small channels with large arrays. These channels are effectively drag-saturated and experience diminishing returns on every turbine added to the channel.

Constricted channels contain high velocity flow in the constricted region which results in increased drag loss through the channel. This causes these channels to have lower potential. Simultaneously though it allows them to generate significantly more power using fewer turbines because turbine devices, as additional pieces of drag, can take advantage of these flows (the velocity advantage). Smaller cross-sections allow for turbines to block more of the channel

which prevents flow from bypassing the array and forces it through the turbines (the blockage advantage). Placing turbines away from these boosting effects results in slower growth and in the case of a two-row array especially, lower power output.

Adding additional rows to an array is detrimental to efficient use of the tidal resource but likely necessary due to various constraints (physical and regulatory). There is a diminishing return on power from every row added and when the degree of constriction is high and larger cross-sections must be used, even the return on a third row can be not worthwhile. If a row of turbines already exists in the smallest cross-section of a constricted channel, it may not be worthwhile building a second row which may result in a monopoly if not regulated.

5.1.5 Jet effects

Research Question 5: How might flow separation and jet formation downstream of a constriction influence energy output and array design?

Findings from the 2-D model suggest that flow separation and jet formation do not impact significantly on results in large channels for the cases tested here. The rate of change in channel width relative to channel length in the large test channels was sufficiently small that effects of the jets were small. Furthermore, the channel was sufficiently long that the jet could mix in with the surrounding flow before leaving the channel.

Jet effects were found to be significant in the small channel and resulted in less power being generated by the array relative to findings derived using the 1-D model. The presence of a jet causes an asymmetric power generation cycle if turbines are placed outside of the narrowest cross-section. More power is generated from turbines when they are downstream of the jet due to the high velocities of the jet. Additionally, at low blockage the power cycle deviates from a traditional sinuosoid and becomes jagged in appearance, this is likely due to the turbulent nature of the jet. Adding turbines to the row dampens this effect and the power time-series curve becomes more sinusoidal.

The most significant effect of the jet is that it results in a net efflux of kinetic energy from the small channels. The jet is unable to mix with the surrounding flow before the channel exit and as a result a large amount of energy is expelled in the jet that cannot be captured by

turbines. This effect is demonstrated by comparing the available power averaged over a tidal cycle calculated using the 1-D and 2-D models.

5.1.6 Suitability of 1-D modelling

Research Question 6: How suitable are 1-D models for performing exploratory studies on tidal energy resource assessment relative to 2-D modelling?

In the way it has been used to date, our findings suggest that 1-D modelling underpredicts the amount of power extracted from turbine arrays because it does not consider the effect that turbines have on the head difference across the channel ends. Adding turbines to a channel as a form of seabed drag causes a backlog of water upstream of the devices which increases the head-difference of the channel. This partially counteracts some of the flow rate reduction that is also incurred from adding turbines. Existing systematic turbine array studies completed for unconstricted channels have not considered this feedback loop e.g. Vennell (2010). These have, instead, assumed that the head difference over the channel is constant. While this does not greatly affect the general trends published in these works, it does mean they have overestimated power output. Future 1-D modelling works could account for this by applying a nested model that adjusts the head difference parameter (Δ) accordingly as turbines are added to the array. Due to time and resource constraints, this is beyond the scope of this thesis.

When the corrected head difference taken from the 2-D model was used to drive the 1-D channel model, the array power calculated from both models showed excellent agreement. The optimal tuning required to array output differed significantly. This was put down to using more realistic and thus more complicated hydrodynamics. The flow rate reduction associated with certain levels of power production was lower in the more realistic 2-D model than in the 1-D model. This may have also affected the optimal tuning parameter as the arrays would have responded differently to changes in channel dynamics.

The 1-D model was less effective at predicting the power output of smaller constricted channels due to its inability to account for the effects of the constriction jet. There is a place for this to be incorporated into the 1-D model by not assuming equal entry and exit velocities although this would require rebuilding the 1-D framework with this extra term present and as such is

deemed out of scope for this thesis. For the most severe case, the 1-D model overpredicted power by about 40%. The main effects of the jet on turbine array design are to alter the head difference across the channel ends and also to efflux a large amount of kinetic energy that can no longer be captured by turbine devices. Kinetic energy losses are smaller as turbine devices are added due to the subsequent reduction in flow rate and thus weakening of the jet.

5.2 General limitations and possible future work

5.2.1 Analytical turbine representation

The greatest difficulty in modelling tidal stream energy extraction is the range of scales over which the problem spans. It is computationally unfeasible to model blade-scale turbulence in a domain the size of an ocean basin. This thesis presents a systematic overview of turbine array design in constricted channels and has tried to be as general as possible. While it has aimed to span as many scales as possible it is impossible to capture all of them. The actuator disc model used for the purposes of this work has many limitations.

Firstly, the model is only applicable if turbines are evenly distributed within rows that span the channel cross-section. It is possible that for real arrays, turbines will not be arranged in rows like they are in the test scenarios of this thesis. Partial row theory (Nishino and Willden, 2012, 2013) would allow for the testing of rows that block only part of the channel's cross-section but this model has greater computational cost of optimising additional variables to tune the turbines. Additional work could be completed using partial row theory to test this or the drag application methods used in Chapter 4 could be weighted with an additional function in the y-direction.

Additional and more realistic information could have been obtained if a more sophisticated turbine representation was used. However, this would have come at the cost of making this work less generally applicable. Current speeds are usually lowest near the seafloor which is where many available turbine devices will be located (e.g. the OpenHydro turbines deployed in Minas Passage, Canada) but methods used here do not consider where in the water-column turbines are located. Some turbine devices are designed to float from the sea-surface which

means turbines sit in faster flows and also experience wind-driven surface currents and wave motion. The actuator line method (Churchfield *et al.*, 2013) gives more realistic information for one particular device (this method requires empirical data) but this would limit this work to a particular turbine design and other turbine designs that are similar. The tidal energy industry at the time of writing is young and there is no champion device on the market. Furthermore, this thesis aims to be far-reaching in terms of relevance and broadly applicable to all tidal energy developments. Subsequently, these methods were not used.

While the turbine representation used here is appropriate for the arrays in the test scenarios and the relevant scale of the problem being explored (large arrays that extract significant fractions of the channel potential), it is less useful for smaller arrays. Arrays being built at present are much smaller than those tested in this thesis. Turbine devices and related infrastructure are, at the time of writing, costly and the tidal energy industry is far from fully developed. The large channel in this thesis is loosely based on Cook Strait, New Zealand; which, at its narrowest point is 22 km wide. Building a row to extend this width would require just under 1,000 hypothetical turbines used in this study arranged blade-to-blade. As these smaller arrays are unlikely to significantly impact on channel dynamics, a higher-order model used over a smaller domain could be used at a similar computational cost to this work.

The tuning methods used in this thesis are not the best method for maximising power output. Chapter 2, using the 1-D model, optimised a constant tuning parameter for each row individually to use time-variable tuning which maximises the average power output over a full tidal cycle. Chapter 3, using the 2-D model, used a less sophisticated method of a constant tuning parameter for all rows in an array to maximise the average power generated over a tidal cycle. Vennell (2016) showed that while the method in Chapter 2 is better than the method in Chapter 3, the best tuning method for a turbine array is to maximise the tuning of turbines in real-time, to maximise the average power over the tidal cycle. To do this, Vennell (2016) represented the tuning as a Fourier series in time and optimised the Fourier coefficients via adjoint methods. While adjoint methods are fast - this tuning method would have been much more computationally demanding than that used here. For this reason, and the complexity of the process, this approach was considered beyond the scope of this thesis.

5.2.2 Test case scenarios and idealised geometry

Modelling in this thesis has been limited to a handful of idealised geometries and channel sizes. It is simply not feasible to test all geometric possibilities. In reality, bathymetry will vary and constrictions will not be Gaussian-shaped. There is a myriad of additional cases that could be tested which may produce interesting data e.g. multiple constrictions in the same channel. As the level of detail in the model developed, certain cases were dropped from the study e.g. depth constrictions after Chapter 2 and lagoon channels during Chapter 3. In a world with no resource constraints these could have been explored and may have produced interesting information.

In addition, it would be interesting to complement this work with real channel examples.

5.2.3 Hydrodynamics

The 1-D hydrodynamic representation of channel flow used in Chapters 2 and 3 has obvious limitations. Namely, tidal energy generation is a 3-D process and this model considers flow to be a 1-D process. That said, a comparison between the 1-D channel model and the 2-D hydrodynamic model indicated that for the purposes of this study, the 1-D model is satisfactory provided the caveats of kinetic energy loss in the constriction jet and feedback of turbines on the channel head-difference are addressed. One is unlikely to develop a turbine array based solely on 1-D modelling. One should complete higher-order modelling of the array development in a domain representative of the proposed location. As the 1-D model has been validated in Chapter 4 in terms of agreement to the 2-D model, this section will discuss only the limitations of the SUNTANS model.presented in the previous chapter (dashed curves).

Amongst other things, the depth at which turbines are placed in the water column will certainly affect the amount of power they generate. The influence of wind on near-surface currents and waves as well as the boundary layer at the seafloor will cause power generation to be sensitive to the depth at which turbines are operating. The depth-averaged hydrodynamic model used in Chapter 4 cannot be used for exploring how deployment depth affects results. In defence of not modelling turbine depth, doing so would have diverted the focus of this work from producing general turbine array design guidelines to producing guidelines specific to one type of turbine

devices.

The RANS and MY2.5 approach to dealing with turbulence, although widely used for geophysical studies, is not as realistic as a large eddy simulation (LES) or direct numerical simulation (DNS) approach. A 2-D RANS does account for turbulent loss of energy at a sub-grid scale but its ability to truly describe turbulent structures is limited by its mesh size. In unison with the actuator disc model that does not allow for partial turbine fences, there has been no analysis of turbine wakes or turbine wake mixing processes in this thesis because the focus is on the macro scale. The turbine model that represents turbines as a continuous row of turbines does not allow for flow around the turbines, so cannot model partial fences or individual turbines. Resolving relevant features properly in these cases would require a significantly larger number of cells and a different turbulence method. This is computationally expensive, and focus was instead placed on the macro-scale aspects of array design. As such, looking at these features was deemed beyond the scope of this work. Harang *et al.* (in prep) use methods similar to those here to address this limitation.

Further work could be done to investigate the increase in head difference associated with the addition of turbines to a channel. The addition of some kind of feedback loop between the turbine model and the channel model would greatly increase the predictive efficacy of the one-dimensional model for unconstricted and constricted channels. If this broader topic could be understood, then a simplified forcing could be applied to the channel ends.

5.2.4 Improvement of 1-D model

Chapter 3 provided a comparison between the 2-D model and 1-D model used in this thesis that outlined two major improvements that could be made to the 1-D the model. These were (1) accounting for the effect that turbine devices have on channel head difference and (2) accounting for the kinetic energy flux loss associated with a constriction jet in a small channel. These could be accounted for using nested models within the existing 1-D framework. These nested models may not necessarily be straightforward as the channel head difference response to the addition of turbine devices appears to depend on the channel dynamics e.g. the dominance of drag in the channel. Figure 4.28 shows the channel head difference for the six example channels tested.

As the level of drag increases, the head difference curve behaviour changes from concave up, to concave down and finally almost flat when the channel is drag saturated.

Accounting for kinetic energy flux loss is likely a function of jet velocities and channel length. 2-D simulations could be used to inform the development of an approximate model that could be nested within the 1-D model framework or further exploration of the 1-D equations without the assumption of equal entry and exit velocities may yield a convenient and useful result. Many other factors regarding the specific turbine device used, the downstream wake dynamics and existing turbulence in the channel dynamics will also impact jet length and will be likely more difficult to incorporate into a 1-D model.

5.3 Closing comment

This thesis has extended the existing body of tidal energy and turbine array theory to include effects of channel constriction. Specifically this work has looked at the limitations of tidal energy in constricted channels and how this energy can be efficiently exploited using turbine devices. A systematic exploration of turbine array design was done using a 1-D and 2-D model. The 1-D model allowed for efficient exploration of a multitude of different scenarios. The 2-D model allowed for exploration of fewer, but still a reasonable number, of different scenarios in greater detail with a more realistic representation of the ocean. While current industry is at the stage of building an array containing ten turbine devices, this work has looked at arrays containing sometimes thousands. If we are to efficiently utilise the tidal energy resource it is imperative that we plan for the future to encourage intelligent use of resources, healthy competition and minimal environmental impact. Work presented in this thesis shows that arrays built in channels now should consider the long term plan for tidal energy generation in the channel as arrays will almost certainly interact and different parts of the channel are far more lucrative than the rest. Most promising tidal energy sites in the world contain constrictions and this work can inform developers, financiers, researchers and engineers how to best design turbine arrays in these channels.

Appendices

Appendix A: Alternative problem formulation

In this work we constricted channels while keeping the head difference constant between the two terminal water bodies. This results in peak velocities of 4.4 ms^{-1} and 5.8 ms^{-1} in the narrows of the large inertial strait and small drag dominated channel with $W_c = 0.7$ respectively which are on the verge of being unrealistically high. Another way of approaching this problem would be to hold the peak velocity constant while allowing the head difference to vary as the channel is constricted. In order to achieve constant peak velocity, the head difference of the channels must diminish as the constriction factor is increased. These constant velocity channels (Table 5.1) have even lower potentials compared to the constant head channels. This results in a greater difference in power output resulting in a greater difference between power curves of different constriction factors (Figure 5.1). Despite this, the curves for these constant velocity channels exhibit the same trends and concavities as the constant head channels shown in this work.

Table 5.1: Channel data for constricted channels with constant head and constant velocity

Parameter	**Large Channel** ($W_c = 0$)		**Small Channel** ($W_c = 0$)	
u_{max}	1.9 ms^{-1}		2.7 ms^{-1}	
Δ	1.4 m		0.17 m	
$B\lambda_0$	0.30		4.5	
Potential	5.7 GW		3.7 MW	
Parameter	**Large Channel** ($W_c = 0.4$)		**Small Channel** ($W_c = 0.4$)	
	Constant Δ	**Constant** u_{max}	**Constant** Δ	**Constant** u_{max}
u_{max}	2.7 ms^{-1}	1.9 ms^{-1}	3.8 ms^{-1}	2.7 ms^{-1}
Δ	1.4 m	0.94 m	0.17 m	0.09 m
$B\lambda_0$	0.40	0.27	6.1	3.2
Potential	4.1 GW	2.2 GW	2.5 MW	1.4 MW
Parameter	**Large Channel** ($W_c = 0.7$)		**Small Channel** ($W_c = 0.7$)	
	Constant Δ	**Constant** u_{max}	**Constant** Δ	**Constant** u_{max}
u_{max}	4.4 ms^{-1}	1.9 ms^{-1}	5.8 ms^{-1}	2.7 ms^{-1}
Δ	1.4 m	0.57 m	0.17 m	0.046 m
$B\lambda_0$	0.71	0.29	10.8	2.9
Potential	1.9 GW	0.59 GW	1.2 MW	0.35 MW

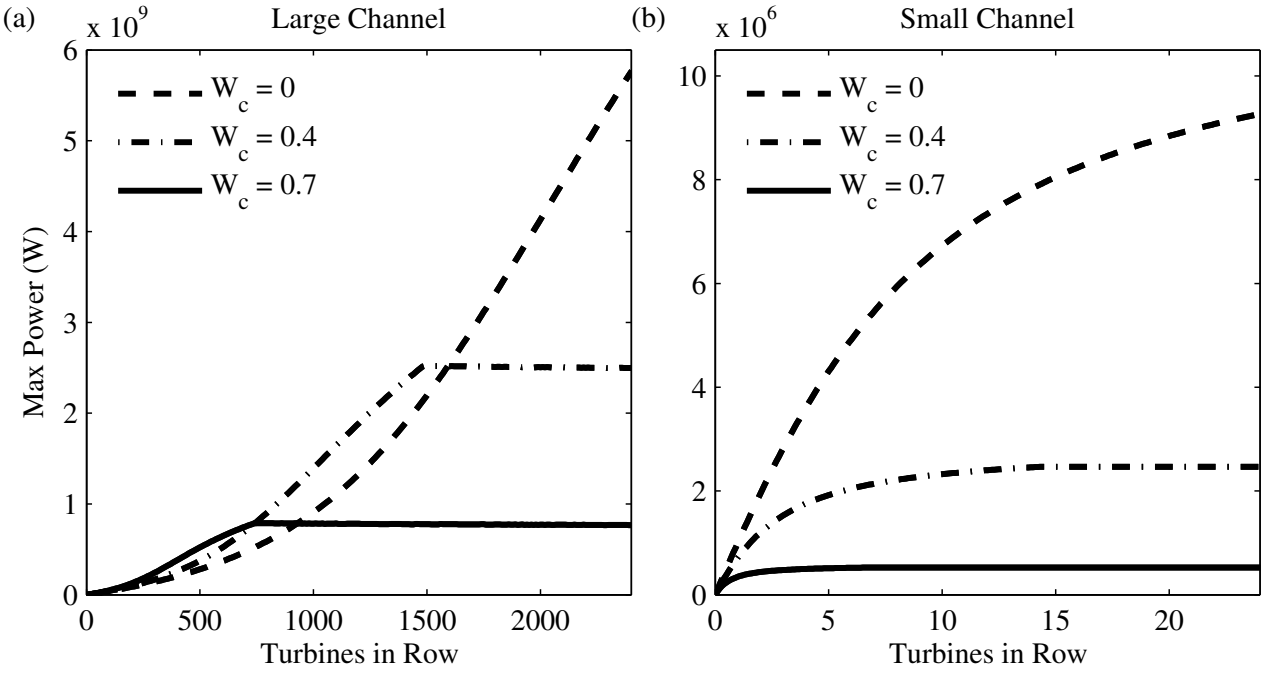

Figure 5.1: Power curves obtained using constant velocity data as opposed to constant head data which was used throughout the analysis of this study

Appendix B: Non-zero Froude number sensitivity

The model derived above in Section 3.3 assumes the Froude number is small e.g. $\mathrm{Fr} = u/\sqrt{gh} \ll 1$. In some extreme instances, the Froude number of the flow may approach or exceed a value of 1, inferring critical flow. This is most likely to occur in the bypass flow of a row of turbines placed in the most constricted part of the channel. (Whelan *et al.*, 2009; Houlsby *et al.*, 2008) derive actuator disc models for non-zero Froude number. These models involve solving a quartic equation for r_4 with respect to both r_3 and Fr and then eliminating answers outside of the solution domain by applying a set of conditions. Applying this model to the r_3 optimization problem becomes complicated because the addition of turbines (and thus drag) retards the flow through the channel and changes the Froude number of the channel. Additionally, the model of Houlsby *et al.* (2008) subsequently requires solving a cubic equation for the free surface deformation across the turbine. Due to the complicated nature of this process and the computational time required, we have chosen not to adopt this model for the purposes of our study. However, we have used the optimal data for the most constricted cross-section in the large channel with a width constriction factor of $W_\mathrm{c} = 0.7$ (e.g. where non-zero Froude effects will be most prominent) and run this through both models to test the sensitivity of our results to this effect (Figure 5.2).

It is clear in Figure 5.2(a) that the consideration of non-zero Froude number has little impact on the power generated from a single row of turbines and the relative flow velocity through the turbines (r_1) across all blockage values. Figure 5.2(c) and (d) however show that at high blockages, the drag coefficient of the row (C_R) is underestimated using our simple model which in turn leads to the transport through the channel being overestimated. Thus the increased drag losses from the row of turbines are counterbalanced by the decrease in channel transport that they cause resulting in the power predicted by all three models being the same. Note that the models of (Whelan *et al.*, 2009; Houlsby *et al.*, 2008) have strong agreement for all parameters despite being slightly different in their formulation. Based on this sensitivity analysis, Froude effects appear to become significant at blockage ratios above that of $\epsilon = 0.6$. This is a reasonably high value and it is unlikely a row of turbines will be built to exceed this blockage in the near future. We conclude that our model is satisfactory for the purposes Sensitivity of our optimal results to non-zero Froude number effects for a row of turbines in the most constricted cross-

section of the large channel with . The thick black curve Sensitivity of optimal results from 1-D model to non-zero Froude number effects for a row of turbines in the most constricted cross-sectionof this study and note that in the future, pursuing further work for high blockage ratios may become worthwhile.

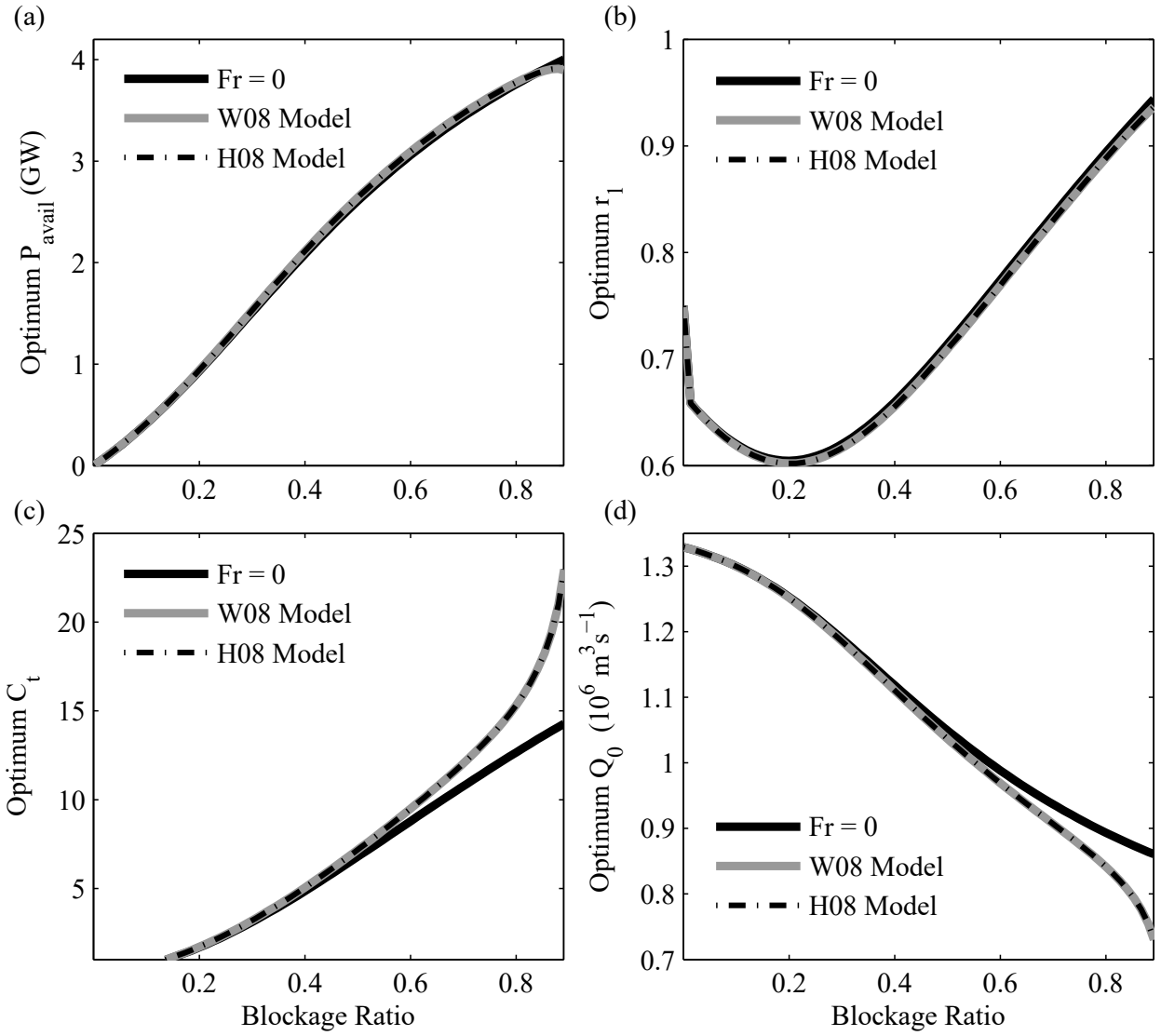

Figure 5.2: Sensitivity of optimal results from 1-D model to non-zero Froude number effects for a row of turbines in the most constricted cross-section ($x = 0.5L$) of the large channel with $W_c = 0.7$. The thick black curve corresponds to the model used in this paper where Fr = 0. While the thick grey curve and the dashed black curve correspond to the models of Whelan *et al.* (2009) and Houlsby *et al.* (2008) respectively.

Appendix C: Mesh resolution figures

The following figures show the relative mesh sizes of the large, moderately constricted channel from Chapter 4. Circles denote the Voronoi points of each cell.

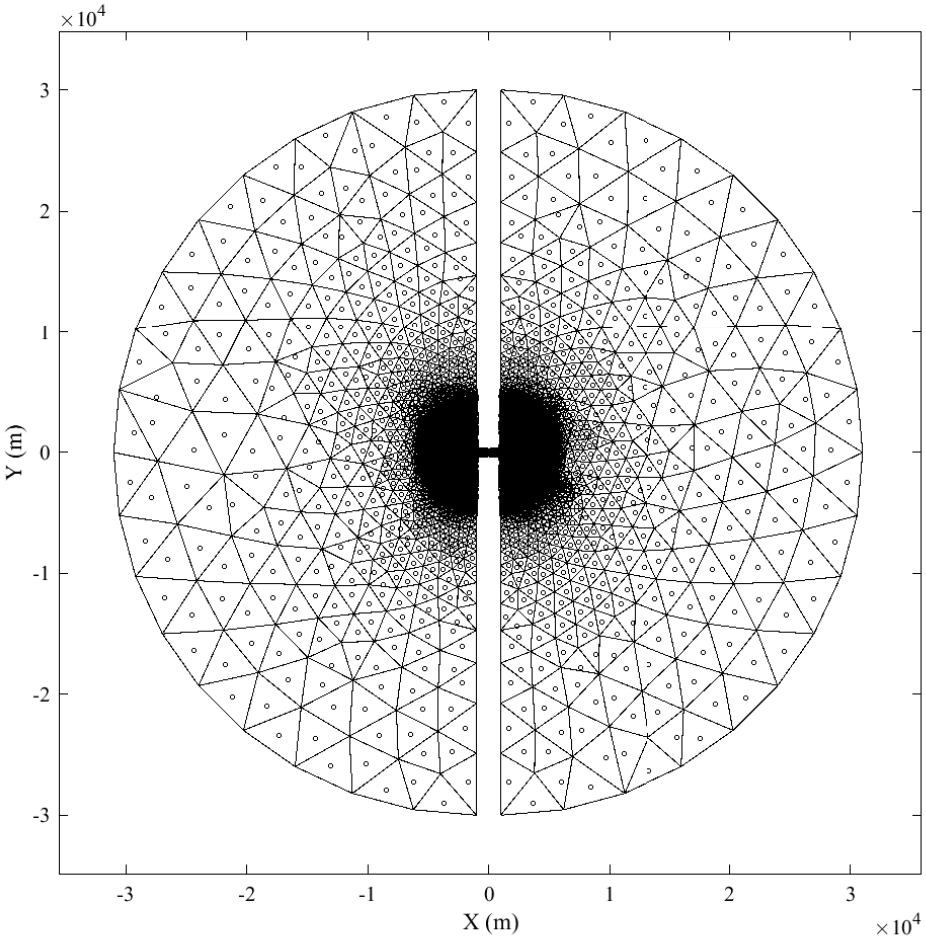

Figure 5.3: Fully zoomed out bird's eye view of mesh across whole domain for the small channel with $W_c = 0.4$. Circular dots depict the position of Voronoi points

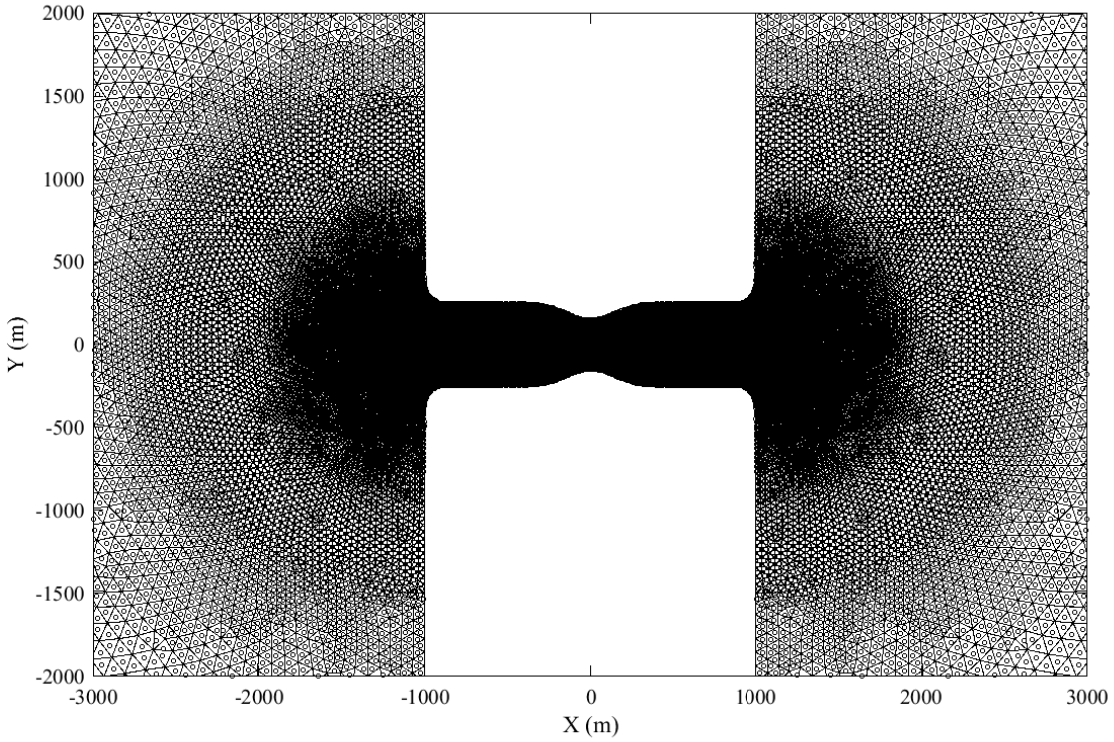

Figure 5.4: Mid-zoomed bird's eye view of mesh showing channel and near surroundings for the small channel with $W_c = 0.4$. Mesh resolution was increased to resolve the effects of jets in the channel and at the channel mouths

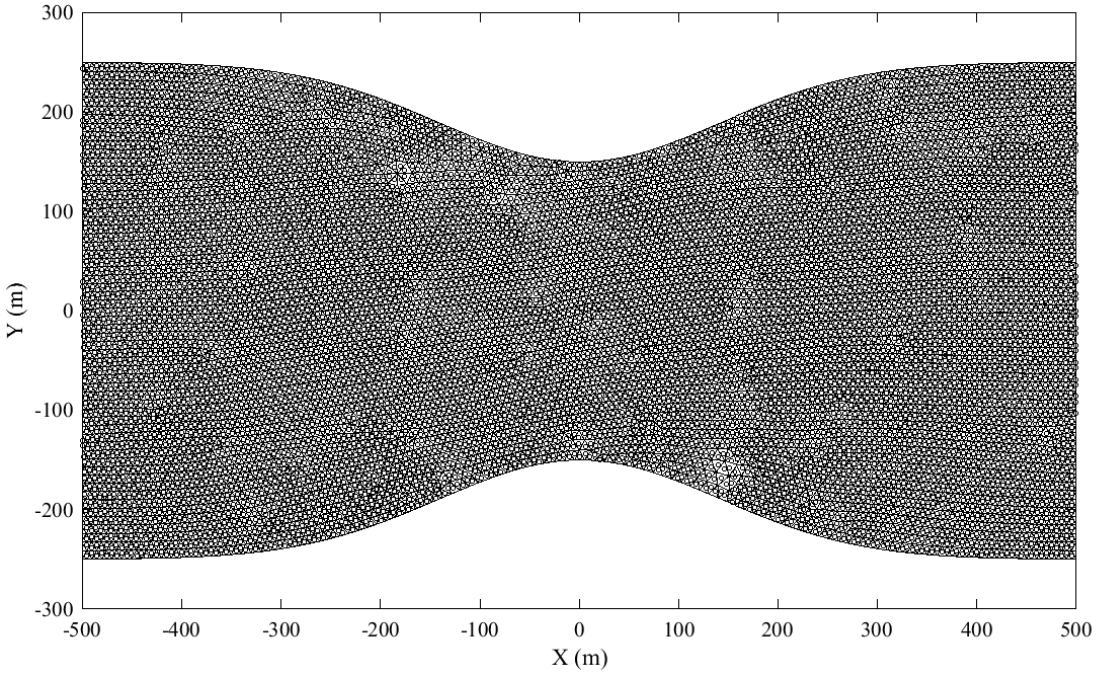

Figure 5.5: Zoomed in bird's eye view of mesh showing the whole channel area for the small channel with $W_c = 0.4$

Appendix D: Additional misc. figures

An additional plot (Figure 5.6) was produced to show the power per turbine from arrays with rows inside/outside (solid/dashed) the constriction using the 1-D model.

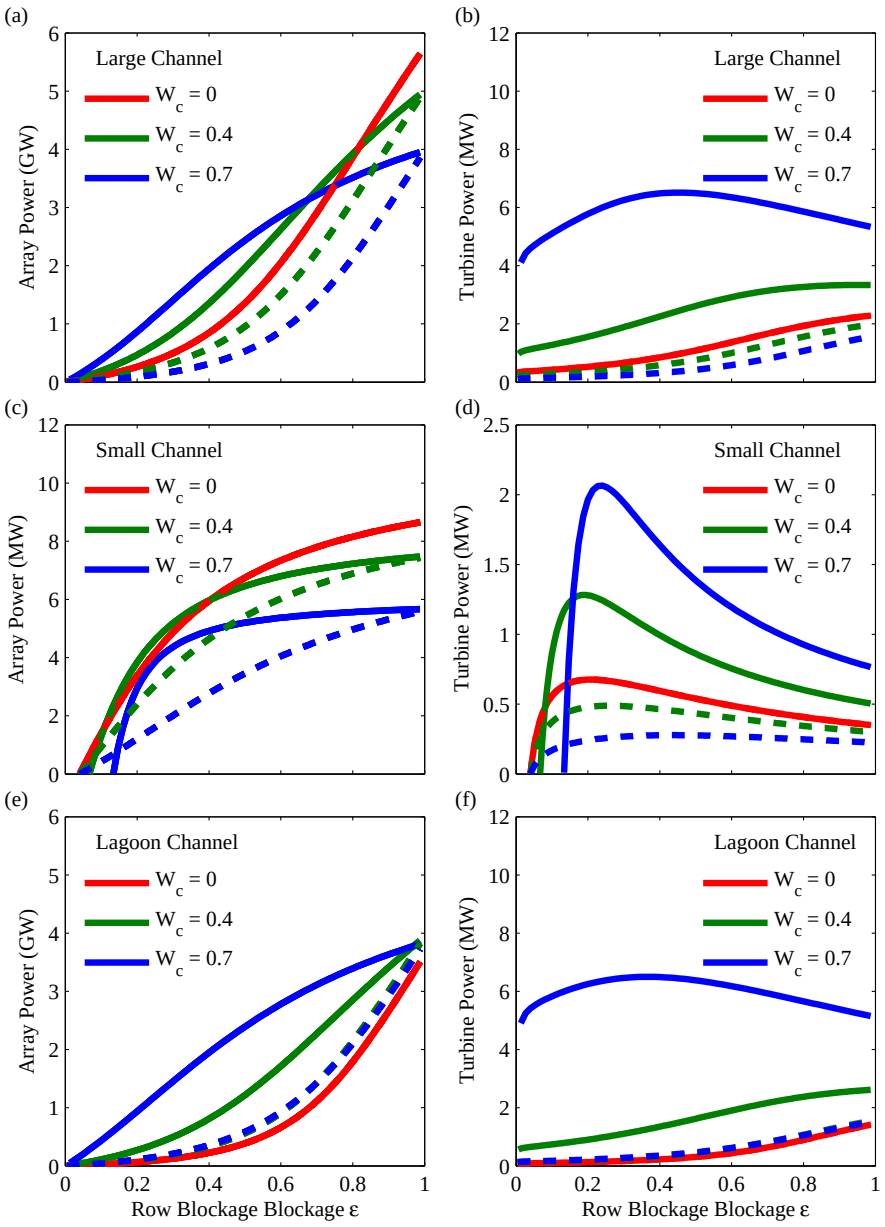

Figure 5.6: Examples of array power and turbine power curves as calculated using the 1-D model.

The velocity profiles for the small channel with $W_c = 0.4$ are provided below in Figure 5.7 both using the velocity deficit model (blue dashed line) and with no velocity deficit model applied (black line). The model was built to achieve the optimal r_3 value at a distance of four turbines downstream from the first row (which is placed at $x' = 0.5$ here). Values within this 4 diameter

zone were not required when calculating power outputs or velocities.

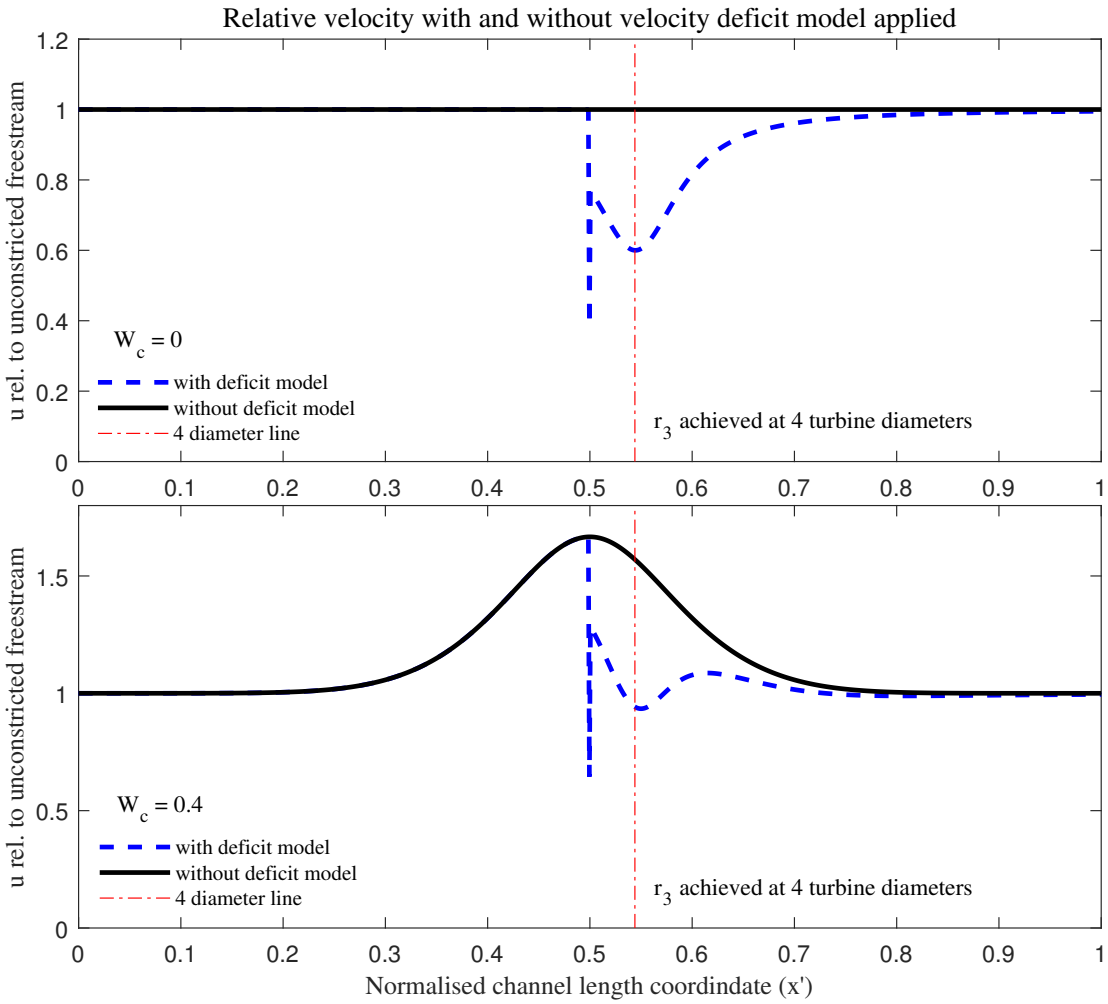

Figure 5.7: Relative velocities for the unconstricted small channel (top) and the moderately constricted small channel (lower, $W_c = 0.4$) with and without the velocity deficit model applied

Bibliography

Adcock, T. A., Draper, S., and Nishino, T. (2015). Tidal power generation–a review of hydrodynamic modelling. *Proceedings of the Institution of Mechanical Engineers, Part A: Journal of Power and Energy*, *229*(7), 755–771.

Adcock, T. A. A. and Draper, S. (2014). Power extraction from tidal channels - Multiple tidal constituents, compound tides and overtides. *Renewable Energy*, *63*, 797–806.

Adcock, T. A. A., Draper, S., Houlsby, G. T., Borthwick, A. G. L., and Serhadlıoğlu, S. (2013). The available power from tidal stream turbines in the Pentland Firth. *Proceedings of the Royal Society of London A: Mathematical, Physical and Engineering Sciences*, *469*(2157).

Afgan, I., McNaughton, J., Rolfo, S., Apsley, D., Stallard, T., and Stansby, P. (2013). Turbulent flow and loading on a tidal stream turbine by LES and RANS. *International Journal of Heat and Fluid Flow*, *43*, 96–108.

Ahmed, U., Apsley, D., Afgan, I., Stallard, T., and Stansby, P. (2017). Fluctuating loads on a tidal turbine due to velocity shear and turbulence: Comparison of CFD with field data. *Renewable Energy*, *112*, 235 – 246.

Bahaj, A., Batten, W., Molland, A., and Chaplin, J. (2005). Experimental investigation into the hydrodynamic performance of marine current turbines. *Sustainable Energy Series*, *3*, 1747–0544.

Betz, A. (1920). Das Maximum der theoretisch möglichen Ausnutzung des Windes durch Windmotoren. *Zeitschrift fur das gesamte Turbinenwesten*, *20*.

Blanchfield, J., Garrett, C., Wild, P., and Rowe, A. (2008). The extractable power from

a channel linking a bay to the open ocean. *Proceedings of the Institution of Mechanical Engineers, Part A: Journal of Power and Energy*, *222*(3), 289–297.

Blunden, L. S. and Bahaj, A. S. (2007). Tidal energy resource assessment for tidal stream generators. *Proceedings of the Institution of Mechanical Engineers, Part A: Journal of Power and Energy*, *221*(2), 137–146.

Butikov, E. I. (2002). A dynamical picture of the oceanic tides. *American Journal of Physics*, *70*(10), 1001–1011.

Carballo, R., Iglesias, G., and Castro, A. (2009). Numerical model evaluation of tidal stream energy resources in the Ria de Muros (NW Spain). *Renewable Energy*, *34*(6), 1517–1524.

Carlson, J. T. and Adams, M. (2020). Assessing the consistency of in-stream tidal energy development policy in Nova Scotia, Canada. *Marine Policy*, *113*, 103743.

Carter, G. S. and Merrifield, M. A. (2007). Open boundary conditions for regional tidal simulations. *Ocean Modelling*, *18*(3-4), 194–209.

Casulli, V. (1999). A semi-implicit finite difference method for non-hydrostatic, free-surface flows. *International Journal for Numerical Methods in Fluids*, *30*(4), 425–440.

Churchfield, M. J., Li, Y., and Moriarty, P. J. (2013). A large-eddy simulation study of wake propagation and power production in an array of tidal-current turbines. *Philosophical Transactions of the Royal Society A: Mathematical, Physical and Engineering Sciences*, *371*(1985), 20120421.

Consoli, S., Recupero, D. R., and Zavarella, V. (2014). A survey on tidal analysis and forecasting methods for Tsunami detection. *arXiv preprint arXiv:1403.0135*.

Cornett, A., Toupin, M., and Nistor, I. (September, 2015). Appraisal of IEC technical specification for tidal energy resource assessment at Minas Passage, Bay of Fundy, Canada. In *Proceedings of the 11th European wave and tidal energy conference. Nantes, France.*

Divett, T. (2013). *Channel scale tidal stream array layout optimisation: a thesis submitted for the degree of Doctor of Philosophy.* Ph. D. thesis, University of Otago.

Divett, T., Vennell, R., and Stevens, C. (2013). Optimization of multiple turbine arrays in a channel with tidally reversing flow by numerical modelling with adaptive mesh. *Philosophical Transactions of the Royal Society A: Mathematical, Physical and Engineering Sciences*, *371*(1985), 20120251.

Douglas, C. A., Harrison, G. P., and Chick, J. P. (2008). Life cycle assessment of the Seagen marine current turbine. *Proceedings of the Institution of Mechanical Engineers, Part M: Journal of Engineering for the Maritime Environment*, *222*(1), 1–12.

Draper, S., Adcock, T. A. A., Borthwick, A. G. L., and Houlsby, G. T. (2014). Estimate of the tidal stream power resource of the Pentland Firth. *Renewable Energy*, *63*, 650–657.

Draper, S., Borthwick, A. G. L., and Houlsby, G. T. (2013). Energy potential of a tidal fence deployed near a coastal headland. *Philosophical Transactions of the Royal Society A: Mathematical, Physical and Engineering Sciences*, *371*(1985).

Draper, S., Houlsby, G. T., Oldfield, M. L. G., and Borthwick, A. G. L. (2010). Modelling tidal energy extraction in a depth-averaged coastal domain. *IET Renewable Power Generation*, *4*(6), 545.

Draper, S. and Nishino, T. (2014). Centred and staggered arrangements of tidal turbines. *Journal of Fluid Mechanics*, *739*, 72–93.

Easton, M. C., Woolf, D. K., and Bowyer, P. A. (2012). The dynamics of an energetic tidal channel, the Pentland Firth, Scotland. *Continental Shelf Research*, *48*, 50–60.

Feng, D., Hodges, B. R., Socolofsky, S. A., and Thyng, K. M. (2019). Tidal eddies at a narrow channel inlet in operational oil spill models. *Marine Pollution Bulletin*, *140*, 374–387.

Fleisher, S. (2016). A study into commercial and technical considerations for the future use of marine energy in New Zealand. 5th IET Conference on Renewable Power Generation. London, UK.

Fringer, O. B., Gerritsen, M., and Street, R. L. (2006). An unstructured-grid, finite-volume, nonhydrostatic, parallel coastal ocean simulator. *Ocean Modelling*, *14*(3-4), 139–173.

Funke, S. W., Farrell, P. E., and Piggott, M. D. (2014). Tidal turbine array optimisation using the adjoint approach. *Renewable Energy*, *63*, 658–673.

Funke, S. W., Kramer, S. C., and Piggott, M. D. (2016). Design optimisation and resource assessment for tidal-stream renewable energy farms using a new continuous turbine approach. *Renewable Energy*, *99*, 1046–1061.

Garner, D. (1969). The seasonal range of sea temperature on the New Zealand shelf. *New Zealand Journal of Marine and Freshwater Research*, *3*(2), 201–208.

Garrett, C. (1972). Tidal resonance in the Bay of Fundy and Gulf of Maine. *Nature*, *238*(5365), 441.

Garrett, C. and Cummins, P. (2005). The power potential of tidal currents in channels. *Proceedings of the Royal Society A: Mathematical, Physical and Engineering Sciences*, *461*(2060), 2563–2572.

Garrett, C. and Cummins, P. (2007). The efficiency of a turbine in a tidal channel. *Journal of Fluid Mechanics*, *588*, 243–251.

Garrett, C. and Greenberg, D. (1977). Predicting changes in tidal regime: the open boundary problem. *Journal of Physical Oceanography*, *7*(2), 171–181.

Gebreslassie, M. G., Tabor, G. R., and Belmont, M. R. (2013). Numerical simulation of a new type of cross flow tidal turbine using OpenFOAM–Part I: Calibration of energy extraction. *Renewable Energy*, *50*, 994–1004.

Gorlov, A. *et al.* (2001). Tidal energy. *Elements of Physical Oceanography*, 103–108.

Hasegawa, D., Sheng, J., Greenberg, D. A., and Thompson, K. R. (2011). Far-field effects of tidal energy extraction in the Minas Passage on tidal circulation in the Bay of Fundy and Gulf of Maine using a nested-grid coastal circulation model. *Ocean Dynamics*, *61*(11), 1845–1868.

Houlsby, G. T., Draper, S., and Oldfield, M. L. G. (2008). Application of linear momentum actuator disc theory to open channel flow. *Report no. OUEL*, *2296*(08).

Hunter, W., Nishino, T., and Willden, R. H. (2015). Investigation of tidal turbine array tuning using 3D Reynolds-averaged Navier–Stokes simulations. *International Journal of Marine Energy*, *10*, 39–51.

IPCC (2013). *Climate Change 2013: The Physical Science Basis. Contribution of Working Group I to the Fifth Assessment Report of the Intergovernmental Panel on Climate Change*. Cambridge, United Kingdom and New York, NY, USA: Cambridge University Press.

Kang, S., Yang, X., and Sotiropoulos, F. (2014). On the onset of wake meandering for an axial flow turbine in a turbulent open channel flow. *Journal of Fluid Mechanics*, *744*, 376–403.

Karsten, R., Greenberg, D., and Tarbotton, M. (2011). Assessment of the potential of tidal power for the Minas Passage and Minas Basin. *Report to OEER/OETR*.

Karsten, R. H., McMillan, J. M., Lickley, M. J., and Haynes, R. D. (2008). Assessment of tidal current energy in the Minas Passage, Bay of Fundy. *Proceedings of the Institution of Mechanical Engineers, Part A: Journal of Power and Energy*, *222*(5), 493–507.

Katic, I., Højstrup, J., and Jensen, N. O. (1986). A simple model for cluster efficiency. In *European wind energy association conference and exhibition. Rome, Italy.*, 407–410.

Kowalik, Z. (2004). Tide distribution and tapping into tidal energy. *Oceanologia*, *46*(3), 291–331.

Lanchester, F. W. (1915). A contribution to the theory of propulsion and the screw propeller. *Journal of the American Society for Naval Engineers*, *27*(2), 509–510.

Le Provost, C. and Lyard, F. (1997). Energetics of the M2 barotropic ocean tides: An estimate of bottom friction dissipation from a hydrodynamic model. *Progress in Oceanography*, *40*(1-4), 37–52.

Lee, S. H., Lee, S. H., Jang, K., Lee, J., and Hur, N. (2010). A numerical study for the optimal arrangement of ocean current turbine generators in the ocean current power parks. *Current Applied Physics*, *10*(2), S137–S141.

Liang, D., Xia, J., Falconer, R. A., and Zhang, J. (2014). Study on tidal resonance in Severn Estuary and Bristol Channel. *Coastal Engineering Journal*, *56*(01), 1450002.

Lloyd, B. (2007). The commons revisited: the tragedy continues. *Energy Policy*, *35*(11), 5806–5818.

Malki, R., Masters, I., Williams, A. J., and Croft, T. N. (2014). Planning tidal stream turbine array layouts using a coupled blade element momentum - computational fluid dynamics model. *Renewable Energy*, *63*, 46–54.

Malki, R., Williams, A. J., Croft, T. N., Togneri, M., and Masters, I. (2013). A coupled blade element momentum–Computational fluid dynamics model for evaluating tidal stream turbine performance. *Applied Mathematical Modelling*, *37*(5), 3006–3020.

Manins, R. (2008). Project Hayes wind farm hearing to resume in January. *Otago Daily Times*.

Manins, R. (2009). Wind farm could attract tourists: witness. *Otago Daily Times*.

Manwell, J. F., McGowan, J. G., and Rogers, A. L. (2010). *Wind energy explained: theory, design and application*. John Wiley & Sons.

Masters, I., Williams, A., Croft, T., Togneri, M., Edmunds, M., Zangiabadi, E., Fairley, I., and Karunarathna, H. (2015). A comparison of numerical modelling techniques for tidal stream turbine analysis. *Energies*, *8*(8), 7833–7853.

MBIE (2017). Energy in New Zealand. Technical report, Ministry of Business, Innovation and Employment. Available from: https://www.mbie.govt.nz/assets/bc14c2778b/energy-in-nz-2017.pdf.

Mellor, G. L. and Yamada, T. (1982). Development of a turbulence closure model for geophysical fluid problems. *Reviews of Geophysics*, *20*(4), 851–875.

Myers, L. and Bahaj, A. (2012). An experimental investigation simulating flow effects in first generation marine current energy converter arrays. *Renewable Energy*, *37*(1), 28–36.

Nishino, T. and Willden, R. H. J. (2012). The efficiency of an array of tidal turbines partially blocking a wide channel. *Journal of Fluid Mechanics*, *708*(OCTOBER 2012), 596–606.

Nishino, T. and Willden, R. H. J. (2013). Two-scale dynamics of flow past a partial cross-stream array of tidal turbines. *Journal of Fluid Mechanics*, *730*(SEPTEMBER 2013), 220–244.

Old, C. P. and Vennell, R. (2001). ADCP measurements of the velocity field of an ebb tidal jet. *Journal of Geophysical Research*, *106*(C4), 7037–7050.

Plew, D. R. and Stevens, C. L. (2013). Numerical modelling of the effect of turbines on currents in a tidal channel–Tory Channel, New Zealand. *Renewable Energy*, *57*, 269–282.

Polagye, B. L. and Malte, P. C. (2011). Far-field dynamics of tidal energy extraction in channel networks. *Renewable Energy*, *36*(1), 222–234.

Pond, S. and Pickard, G. L. (1983). *Introduction to dynamical oceanography.* Pergamon Press, New York.

Pugh, D. T. (1987). *Tides, surges and mean sea-level: a handbook for engineers and scientists.* John Wiley, Hoboken, NJ.

Quon, A. (2018). Cape Sharp Tidal turbine was 'damaged beyond repair' in September. *Global News. Available from: https://globalnews.ca/news/4644316/cape-sharp-tidal-turbine-damaged/*.

Sanchez, M., Carballo, R., Ramos, V., and Iglesias, G. (2014). Energy production from tidal currents in an estuary: A comparative study of floating and bottom-fixed turbines. *Energy*, *77*, 802–811.

Scott, D. B. and Greenberg, D. A. (1983). Relative sea-level rise and tidal development in the Fundy tidal system. *Canadian Journal of Earth Sciences*, *20*(10), 1554–1564.

Shields, M. A., Woolf, D. K., Grist, E. P. M., Kerr, S. A., Jackson, A. C., Harris, R. E., Bell, M. C., Beharie, R., Want, A., Osalusi, E., Gibb, S. W., and Side, J. (2011). Marine renewable energy: The ecological implications of altering the hydrodynamics of the marine environment. *Ocean and Coastal Management*, *54*(1), 2–9.

Signell, R. P. and Geyer, W. R. (1991). Transient eddy formation around headlands. *Journal of Geophysical Research*, *96*, 2561.

Smeaton, M., Vennell, R., and Harang, A. (2016). The effect of channel constriction on the potential for tidal stream power. *Renewable Energy*, *99*, 45–56.

Sorensen, J. N. and Shen, W. Z. (2002). Numerical modeling of wind turbine wakes. *Journal of Fluids Engineering*, *124*(2), 393–399.

Stallard, T., Collings, R., Feng, T., and Whelan, J. (2013). Interactions betweem tidal turbine wakes: Experimental study of a group of 3-bladed rotors. *Philosophical Transactions of the Royal Society of London: A*, *371*(1985), 1471–2962.

Stansby, P. and Stallard, T. (2016). Fast optimisation of tidal stream turbine positions for power generation in small arrays with low blockage based on superposition of self-similar far-wake velocity deficit profiles. *Renewable Energy*, *92*, 366–375.

Stevens, C. L., Smith, M. J., Grant, B., Stewart, C. L., and Divett, T. (2012). Tidal energy resource complexity in a large strait: The Karori Rip, Cook Strait. *Continental Shelf Research*, *33*, 100–109.

Sutherland, G., Foreman, M., and Garrett, C. (2007). Tidal current energy assessment for Johnstone strait, Vancouver Island. *Proceedings of the Institution of Mechanical Engineers, Part A: Journal of Power and Energy*, *221*(2), 147–157.

Toffoli, A. and Bitner-Gregersen, E. M. (2017). Types of Ocean Surface Waves, Wave Classification.

Turnock, S. R., Phillips, A. B., Banks, J., and Nicholls-Lee, R. (2011). Modelling tidal current turbine wakes using a coupled RANS-BEMT approach as a tool for analysing power capture of arrays of turbines. *Ocean Engineering*, *38*(11-12), 1300–1307.

Vaughan, A. (2019). Swansea tidal lagoon plan revived - without government funding. *The Guardian*.

Venayagamoorthy, S. K., Ku, H., Fringer, O. B., Chiu, A., Naylor, R. L., and Koseff, J. R. (2011). Numerical modeling of aquaculture dissolved waste transport in a coastal embayment. *Environmental Fluid Mechanics*, *11*(4), 329–352.

Vennell, R. (1998a). Observations of the Phase of Tidal Currents along a Strait. *Journal of Physical Oceanography*, *28*(8), 1570–1577.

Vennell, R. (1998b). Oscillating barotropic currents along short channels. *Journal of Physical Oceanography*, *28*(8), 1561–1569.

Vennell, R. (2010). Tuning turbines in a tidal channel. *Journal of Fluid Mechanics*, *663*, 253–267.

Vennell, R. (2011a). Estimating the power potential of tidal currents and the impact of power extraction on flow speeds. *Renewable Energy*, *36*(12), 3558–3565.

Vennell, R. (2011b). Tuning tidal turbines in-concert to maximise farm efficiency. *Journal of Fluid Mechanics*, *671*, 587–604.

Vennell, R. (2012). The energetics of large tidal turbine arrays. *Renewable Energy*, *48*, 210–219.

Vennell, R. (2013). Exceeding the Betz limit with tidal turbines. *Renewable Energy*, *55*, 277–285.

Vennell, R. (2016). An optimal tuning strategy for tidal turbines. *Proceedings of the Royal Society A: Mathematical, Physical and Engineering Science*, *472*(2195), 20160047.

Vennell, R., Funke, S. W., Draper, S., Stevens, C., and Divett, T. (2015). Designing large arrays of tidal turbines: A synthesis and review. *Renewable and Sustainable Energy Reviews*, *41*, 454–472.

Wang, B., Fringer, O., Giddings, S., and Fong, D. (2009). High-resolution simulations of a macrotidal estuary using SUNTANS. *Ocean Modelling*, *26*(1-2), 60–85.

Waters, S. and Aggidis, G. (2016). A world first: Swansea Bay tidal lagoon in review. *Renewable and Sustainable Energy Reviews*, *56*, 916–921.

Whelan, J. I., Graham, J. M. R., and Peiro, J. (2009). A free-surface and blockage correction for tidal turbines. *Journal of Fluid Mechanics*, *624*, 281–291.

Willden, R. H., Nishino, T., and Schluntz, J. (2014). Tidal stream energy: designing for blockage. In *3rd Oxford Tidal Energy Workshop*, 7–8.